Dissertation

submitted to the

Combined Faculty of Natural Sciences and Mathematics

of Heidelberg University, Germany

for the degree of

Doctor of Natural Sciences

Put forward by

Karan Molaverdikhani

born in: Rasht, Iran

Oral Examination: February 5^{th}, 2020

Characterization of Planetary Atmospheres

Referees:
Prof. Dr. Thomas Henning
Prof. Dr. Cornelis Dullemond

Abstract

After the discovery of the first exoplanet in 1990's and a fast growing number of discoveries since then, there have been many attempts to observe and characterize their atmospheres. In particular, water and methane have been the focus of many investigations due to their relevance to the origin of life and habitability, as well as their major roles to shape the structure of planetary atmospheres. Abundances retrieved for these species can be also used as a tracer of carbon-to-oxygen ratio (C/O) and metallicity of these atmospheres; hence potentially linking the formation scenarios with the observations. Water's spectral signature is everywhere, but despite many efforts, there has been only one robust detection of methane and only recently. The question is,

"*where is methane?*".

By applying a hierarchical modelling approach (utilising more than 177,000 thermochemical equilibrium cloud-free, disequilibrium cloud-free, and thermochemical equilibrium cloudy models) we predict that there are four classes of irradiated gaseous planets; two of them (Class-I and Class-II; $T_{\rm eff} \lesssim 1650$ K) likely to show signatures of CH_4 in their transmission spectra, if cloudy-free and C/O above a certain threshold (aka the "Methane Valley"). The effect of disequilibrium processes on the classification found to be modest with a more continuous transition between Class-II and III planets. Clouds, however, heat-up the deeper parts of Class-I and Class-II planets; removing CH_4 from the photosphere. Simultaneously, clouds obscure any molecular features; hence making the observation of methane even more challenging.

تقدیم به خانواده‌ام

Contents

List of Figures

List of Tables

List of Abbreviations

0D, 1D, 2D, 3D zero-, One-, two- or three-dimensional

ARIEL . . . . Atmospheric Remote-sensing Infrared Exoplanet Large-survey

AU . . . . . Astronomical Unit

C/O . . . . . Carbon-to-Oxygen ratio

ChemKM . . . Chemical Kinetic Model

CHEOPS . . . CHaracterising ExOPlanets Satellite

CN . . . . . Condensation Nuclei

CoRoT . . . . Convection, Rotation and planetary Transits

CV, gCV . . . Coefficient of Variation, geometric Coefficient of Variation

DLSODE . . . Double precision Livermore Solver for Ordinary Differential Equations

DVODPK . . Double precision Variable-coefficient method for Ordinary Differential equations using Preconditioned Krylov method

ELT . . . . . Extremely Large Telescope

Eri . . . . . Eridani

ExoMol . . . . Exoplanet Molecular database of line lists

GCM . . . . . General Circulation Model

GCRs . . . . . Galactic and solar cosmic rays

GJ . . . . . Gliese-Jahreiss

GPI . . . . . Gemini Planet Imager

HabEx . . . . . The Habitable Exoplanet Imaging Mission

HARPS . . . . The High Accuracy Radial Velocity Planet Searcher

HAT . . . . . The Hungarian-made Automated Telescope

HD . . . . . Henry Draper; Henry Draper Catalogue

HITEMP . . . The high-temperature molecular spectroscopic database

IR . . . . . Infrared (spectrum)

IRAC . . . . . The Infrared Array Camera

JWST . . . . . James Webb Space Telescope

KELT . . . . . The Kilodegree Extremely Little Telescope

LIMP . . . . . Local interplanetary medium

LTE . . . . . Local Thermal Equilibrium

LUVOIR . . . The Large UV/Optical/IR Surveyor

MASCARA . The Multi-site All-Sky CAmeRA

NASA . . . . . The National Aeronautics and Space Administration

NIR . . . . . Near Infrared (spectrum)

ODE . . . . . Ordinary differential equation

petitCODE . . Pressure-Temperature Iterator and Spectral Emission Calculator for Planetary Atmospheres (PETIT) code

Pic . . . . . Pictoris

PLATO . . . . PLAnetary Transits and Oscillations of stars

RV . . . . . Radial Velocity

SN . . . . . Signal-to-Noise Ratio

SPHERE . . . Spectro-Polarimetric High-contrast Exoplanet REsearch instrument

TD . . . . . Transit Depth

TESS . . . . . Transiting Exoplanet Survey Satellite

TOA . . . . . Top of the atmosphere

TP . . . . . Temperature-Pressure profile

TTV . . . . . Transit timing variation

UV . . . . . Ultra Violet (spectrum)

VIS . . . . . Visible (spectrum)

VLT . . . . . Very Large Telescope

WASP . . . . . Wide Angle Search for Planets

WFIRST . . . The Wide Field Infrared Survey Telescope

There will come a time when you believe everything is finished. That will be the beginning...

— *Louis L'Amour* (L'Amour 1984)

1 Introduction

Contents

1.1 Planetary bodies in the Solar System

It all began about 4.5 billion years ago when a fraction of a giant molecular cloud started to collapse under its gravity (e.g. Glavin et al. 2018) ; resulting in the formation of the Sun and smaller bodies. Eight planets, five dwarf planets, 181 moons, 3,083 comets, and 552,894 asteroids have been detected in the solar system so far[1]; suggesting diversity of these planetary bodies in this system.

[1] https://theplanets.org/solar-system/

Among the planets, Venus, Earth, Mars, Jupiter, Saturn, Uranus, and Neptune are known to possess substantial atmospheres. Pluto is the only explored dwarf planet with an atmosphere. It is, however, tenuous in comparison to the atmosphere of other terrestrial planets in the solar system (e.g. Gladstone et al. 2016). In contrast, Titan, as the largest moon of Saturn, is the only moon in the solar system that is covered by a considerable atmospheric envelope that is comparable to the planetary atmospheres (e.g. Vuitton et al. 2019).

How unique or frequent these atmospheres are in other planetary systems can not be addressed unless first we shape an understanding of the solar system's planetary atmospheres. In what follows we summarize our current understanding about the atmosphere of gaseous planets in the solar system; as they are the main focus of this thesis.

1.1.1 Jupiter

The largest, the most massive planet in the solar system: Jupiter. It is a hydrogen dominated planet with molecular hydrogen and helium being the most abundant atmospheric constituents. The helium to hydrogen ratio (He/H) is measured to be 0.807±0.02 on Jupiter, which is slightly lower than its solar counterpart by a value around 0.0975 (e.g. Atreya et al. 2003). This suggests that the Jovian atmosphere has most likely formed from the Solar System's primordial materials and has not underwent a significant evolution. The slightly lower He/H is not fully understood but possibility could be the depletion of helium from the atmosphere through, e.g., rain-out mechanism (e.g. Atreya et al. 2003).

Other detected atmospheric species include H_2O, CH_4, CH_3 H_2S, NH_3, PH_3, S_2, CS_2, CO, CO_2, C_2H_2, C_2H_4, C_2H_6, C_3H_4, C_3H_8, C_4H_2, and C_6H_6. The hydrocarbons are likely locally produced by the photolysis of CH_4. The presence of CO and CO_2 requires a source of oxygen. Complex organic components within the ablated dust grains that also bear oxygen-bearing silicate or metal-oxide compounds could result in CO and CO_2 from the gas-phase chemistry (Lellouch et al. 2002). Water is also believed to be an outcome of dust grain ablation at the upper atmosphere of

Jupiter. Upon removal of the external source(s) of water, it would condense and sink in the cold-region of the tropopause (cold-trap); demanding the necessity of such external source.

According to its thermal structure, Figure 1.1, the atmosphere of Jupiter can be divided into four layers: the troposphere, stratosphere, thermosphere and exosphere. The troposphere is the deepest layer; connecting the interior to the upper atmosphere. There is no sharp boundary to separate the troposphere from the interior, but the intermediate region rather comprises an environment with gradual transition from the troposphere to the interior materials (e.g. Guillot 1999). The 1 bar pressure is commonly referred to as the reference pressure of Jupiter, mostly for the purpose of numerical simulations (e.g. Guillot 1999). The visible cloud decks (mostly NH_3 clouds) are also typically located at this pressure; making it more convenient to define it as a "surface" for Jupiter (e.g. Seiff et al. 1998). The lower boundary of the troposphere can be defined with respect to this reference pressure, as an altitude that is 90 km below the reference pressure. The altitude of troposphere-thermosphere boundary varies with local conditions but it is located roughly at 1 μbar. The thermosphere continues outward until it gradually diffuses into the interplanetary medium (e.g. Miller et al. 2005).

1.1.2 Saturn

Similar to Jupiter, Saturn is also a gas giant since they both mainly composed of hydrogen and helium. Helium is deficient on Saturn too; presumably due to a similar rain-out mechanism as on Jupiter. In addition to H_2 and He, other constituents have also been detected on Saturn CH_4, CH_3, NH_3, PH_3, CO, CO_2, H_2S, HD, C_2H_2, C_2H_6, C_3H_8, H_2O, and NH_4SH (e.g. Guerlet et al. 2008; Guillot et al. 2009). The abundance measurements of PH_3, CO, and CO_2 provided an early indication of disequilibrium processes in the upper tropospheres and stratospheres of Saturn and their vertical distribution do not represent their thermochemical equilibrium values. (Atreya et al. 1999). These disequilibrium species are most likely the upward convection from the deep interiors or ablation and mixing from

the upper boundary. The abundance of the hydrocarbons and NH_3 are also likely to be a result of loss processes and photolysis in the stratosphere; suggesting that the upper atmosphere of Saturn (and Jupiter) to be driven away from their thermochemical equilibrium states.

NH_3 cloud base is observable and is estimated to be vertically located at around 750 mbar (Banfeld et al., 1998), Figure 1.1. The distribution and composition of deeper clouds are difficult to directly assess through remote sensing, which can change both temporally and spatially. The vertical extension of the clouds are therefore being estimated mostly through a combination of observations and numerical simulations (Atreya et al. 1999). NH_4SH clouds are thought to take place at pressure around 1-2 bar, and H_2O clouds at pressures larger than a few bar (e.g. West et al. 2009).

1.1.3 Uranus

Uranus is one of the two discovered ice-giants in the solar system. It orbits the Sun at a distance of 19.8 AU on average. Hence its atmosphere is expected to be colder than that of gas-giants. The Uranian thermal structure suggests four main vertical layers, namely the troposphere, the stratosphere, and the thermosphere, and the exosphere. The 1 bar pressure is defined to be the reference pressure (nominal surface) of Uranus and the altitude is commonly measured from that pressure (e.g. Lunine 1993). The troposphere covering a region roughly between 100 and 0.1 bar, that corresponds to altitudes of -600 and 50 km on Uranus respectively. The stratosphere extends above this layer and has a diffused upper boundary at around 10^{-4} μbar (corresponding to an altitude of around 4000 km). The thermosphere and exosphere layers are above the stratosphere and extend to the interplanetary medium at several Uranian radii.

Similar to the gas-giants, Uranus is also mainly composed of molecular hydrogen and helium. Measurements of its atmospheric He/H indicates its proximity to the protosolar helium to hydrogen ratio. This hints that unlike Jupiter and Saturn, the helium at the upper atmosphere of Uranus has not settled towards the interior of the planet (e.g. Conrath et al. 1987).

Methane is the most abundant atmospheric species after hydrogen and helium. Strong absorption features in the spectrum of CH_4 resulted in the early discovery of this species with the ground-based observations (e.g. Lunine 1993). CH_4, C_2H_2, C_2H_6, CH_3C_2H, C_4H_2, H_2O, CO and CO_2 are among the most prominent additional constitutes that have been discovered on Uranus (Orton et al. 2014). The hydrocarbons are believed to form through the photolysis of CH_4 at around 5 μbar regime. Eddy diffusion transports these hydrocarbons to the deeper layers where the temperature is cold enough for polymerization to occur more efficiently (e.g. Lunine 1993). Measurements of CH_4 mixing ratio at 1 bar suggests that the deeper parts of Uranian atmosphere is most likely enriched in carbon relative to the solar values. However, at the lower pressures, where the atmosphere is colder, the CH_4 can freeze-out and its abundance decreases (e.g. Bishop et al. 1990).

Uranus temperature structure creates a cold-trap for most of the observed hydrocarbons and H_2O. Thus the abundance of H_2O, CO, and CO_2 in the stratosphere of Uranus requires an external source (e.g. Burgdorf et al. 2006); similar to the Saturn and Jupiter upper atmosphere. There are some hypothesis regarding the origin of source(s), which can be tested by more accurate measurements of relative abundance of H_2O in comparison with CO and CO_2 (Orton et al. 2014).

The CH_4 cloud deck is located at around 1.2 bar. H_2S cloud forms at deeper layers where the pressure reaches around 6 bar and temperature around 100 K. NH_3 cloud form at a similar atmospheric condition if $H_2S + NH_3 \longrightarrow NH_4HS$ would not proceed. This reaction, however, proceeds due to the adequate sulfur abundance and presumably lack of nucleation sites (solid particles) at these pressures (e.g. de Pater et al. 1991). Therefore, the NH_3 clouds is likely removed from the atmosphere if the solid particles are efficiently, e.g., settled down from these layers. H_2O and NH_4HS may also form at deeper pressures, e.g. at 20 bar (e.g. Lunine 1993).

1.1.4 Neptune

Although Neptune is similar to Uranus in many regards, orbiting at a distance of around 30 AU but having an effective temperature resembling that of Uranian hints

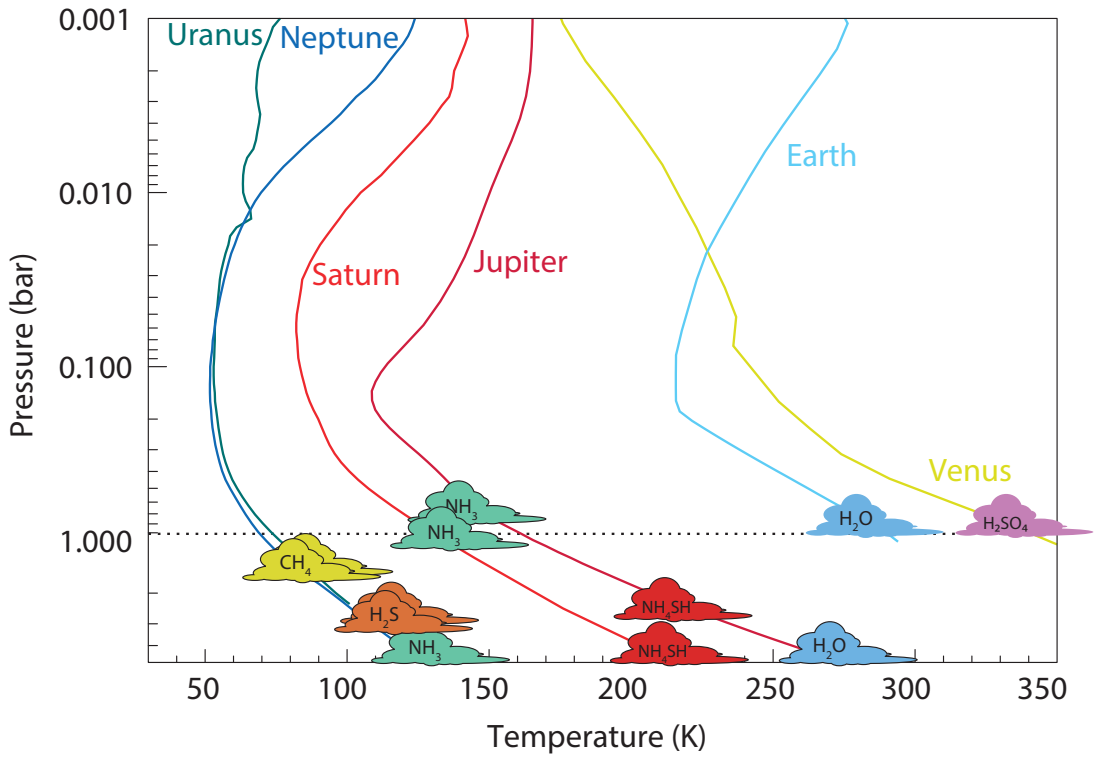

Figure 1.1: Temperature profiles and cloud composition in the solar system gaseous planets. Earth's and Venus's profiles are included for reference. The temperature profiles are adapted from Robinson & Catling (2014).

for significant differences in terms of dynamic and composition. This excess source of energy is believed to be a significant internal heat flow that is not associated with solar irradiation (e.g. Pearl & Conrath 1991). The origin of this heating is unknown but one explanation could be a radical and oblique collision that changed the cooling history of Neptune, as well as its tilt angle (e.g. Podolak & Helled 2012).

Similar to Uranus, Neptune's atmosphere can be divided into four layers: the troposphere, the stratosphere, the thermosphere, and the exosphere (e.g. Lunine 1993). In the troposphere temperature decreases with altitude and in the stratosphere it increases with altitude. The boundary of these regions, i.e. the tropopause, is located at around 0.1 bar. The stratopause lies at a pressure of 10-100 μbar where most of photochemical reactions take place.

Like other gaseous planets in the solar system, Neptune is also dominated by molecular hydrogen and helium. CH_4, CH_3, C_2H_2, C_2H_4, C_2H_6, and C_4H_2 are some of other detected species at the upper atmosphere of Neptune. Vertical distribution

of cloud layers on Neptune is expected to be largely similar to the clouds' structure on Uranus. A summary of the temperature profiles and cloud composition in the solar system gaseous planets are shown in Figure 1.1.

In summary, the atmospheric temperature of gaseous planets in the solar system at 1 bar is somewhere between 50 to 150 K. The mostly comprise of the molecular hydrogen and helium and show roughly similar chemical products at their upper atmospheres; with subtle differences as discussed. In the light of new discoveries, we now know that there are other types of gaseous planets in the galaxy that are significantly different from the gaseous planets in the solar system. we briefly overview how these extrasolar planets, "exoplanets", have been discovered and the techniques that have been used to study their atmospheres.

1.2 Beyond the Solar System

The news was short: "*The Nobel Prize in Physics 2019 was awarded "for contributions to our understanding of the evolution of the universe and Earth's place in the cosmos" with one half to James Peebles "for theoretical discoveries in physical cosmology", the other half jointly to Michel Mayor and Didier Queloz "for the discovery of an exoplanet orbiting a solar-type star."*"[2]. This illustrates the significance of this discovery and the impact of this branch of astronomy on the scientific community.

Michel Mayor and Didier Queloz discovered the first exoplanet orbiting a main-sequence star through the Radial Velocity (RV) technique (Mayor & Queloz 1995). Since then thousands of exoplanets have been discovered through verity of detection methods[3].

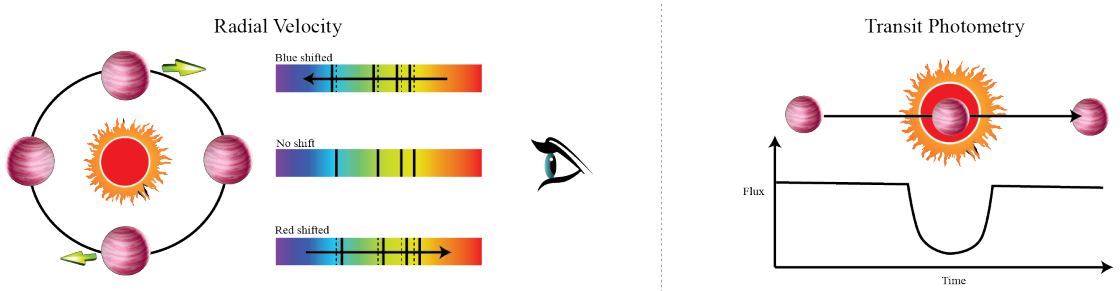

Figure 1.2: Schematic of two of the main exoplanet detection methods: the radial velocity and transit photometry.

1.2.1 Detection methods

Radial Velocity (Doppler spectroscopy)

In a binary system, both objects orbit around their center of mass. In the case of a planet orbiting a star, the center of mass usually resides within the stellar radius. But the movement of the star can be detected if the gravitational pull of the planet is strong enough to cause a detectable Doppler shift in the spectral lines of the star, Figure 1.2. In 1952, Struve (1952) proposed to use this technique to estimate the frequency of planet-like objects in the galaxy. He estimated that for a planet of 10 times mass of the Jupiter orbiting a solar-mass star at a distance of 1/50 AU, the radial velocity would oscillate with a range of ± 2 km/sec. This oscillation was predicted to be achievable by the modern spectrographs back in time.

It was not until 1990s that the instruments became advance enough to reach the resolution that was necessary to measure the predicted radial velocities. Mayor & Queloz (1995) discovered 51 Pegasi b by using such spectrograph, ELODIE (Baranne et al 1996). Until 2010, 77% of exoplanets were discovered through this technique (Molaverdikhani 2010). Since then, the transit photometry method has become the dominant technique to discover exoplanets by almost 80% of planets being discovered through this method (e.g. Deeg & Alonso 2018).

[2]https://www.nobelprize.org/prizes/physics/2019/summary/
[3]https://exoplanetarchive.ipac.caltech.edu

Transit photometry

In 1952, Struve (1952) also proposed to use the dimming in the stellar light when a planet crosses the disk of the star to discover and study the planet-like objects, Figure 1.2. He estimated the loss of light in the stellar magnitude to be around 0.02 for a planet with a density approximately five times of the stellar density. He pointed that one advantage of using this technique would be the accessibility to the fainter stars in comparison to the radial velocity that he also proposed. His estimations were remarkably accurate as in the case of HD 209458, the star dims by about 1.7%. In 2000, HD 209458 b was the first observed exoplanet transiting its host star (Charbonneau et al. 1999).

CoRoT (Convection, Rotation and planetary Transits) was the first space mission to look for transiting planets. It discovered its first planet in 2007, COROT-1b (Barge et al. 2008), and continued operating until 2013 with 600 candidate planets to be confirmed[4]. In 2009, Kepler mission was launched with a yield estimation of about 2000 planets in 3.5 years (e.g. Molaverdikhani 2010). This yield was quickly achieved and by 2013 the number of planet candidates increased to 3,278. The successful demonstration of transit photometry method led to further ground-based and space missions using the same technique. This includes the Transiting Exoplanet Survey Satellite (TESS) mission – launched in 2018 and currently operating, CHEOPS (CHaracterising ExOPlanets Satellite) – launched is planned for December 2019, and PLAnetary Transits and Oscillations of stars (PLATO) – for a launch in 2026. To take a part in this exciting era of discoveries, I am involved with the project EDEN to "discover and explore the habitable planets closest to us."[5]. These planets would be the best candidates to characterize their atmospheres put Earth's atmosphere in a broader context in the near future.

[4]https://cnes.fr/en/web/CNES-en/9897-gp-corot-s-haul-of-25-exoplanets.php
[5]http://project-eden.space

Pulsar timing

Pulsars are highly magnetized rotating neutron stars that emit beams of radio-frequency radiation. This radio emission is so regular that can be used as a tool to investigate any anomaly in their timing due to gravitational perturbations by other companion. This is a powerful technique that can characterize very small planetary objects (as small as 10% of Earth's mass) and planets orbiting far from the pulsar. In fact, the first exoplanet discovered by using this technique in 1992 (Wolszczan & Frail 1992). But pulsars are not frequent and the formation of planets around these objects are thought to be inefficient. Therefore this method is not suitable for discovering a large number of exoplanets; let alone the habitable ones that are as of a growing interest.

Gravitational microlensing

About a decade ago, I started my studies on exoplanets that were discovered by this technique. Back then the radial velocity method was the main method to discover exoplanets but the status was expected to change drastically by Kepler (transit photometry) in the coming years. As discussed, both methods (radial velocity and transit photometry) are sensitive to relatively bright and nearby stars and gravitational microlensing was one of a few techniques that would give access to the planetary objects across the galaxy.

In short, the gravity of a star can act as a magnifier to intensify the light of a background star. If the foreground star has a companion, it can contribute in the light-curve of the background star. The lensing events last for days or weeks and the contribution from a low mass companion appears only for a small fraction of this time. Therefore the best regions to look for planets with this technique is toward the galactic center as it provides a large number of background stars (e.g. Molaverdikhani & Tabeshian 2009).

Direct imaging

As the name suggests the direct imaging technique aims to directly take the image of planets. While the concept seems to be simple, it is technically very challenging due to a verity of reasons. The planet should be detectable in the vicinity of its bright host star, and this poses a challenge as the planets are usually much fainter that their host star. Thus planets having the following characteristics may help for their detection through this method: 1) A wider star-planet separation, 2) the planetary system to be closer to the Sun, 3) higher reflected starlight from the planet; e.g. a larger cloudy planet, and 4) higher emission light from the planet; this usually means the younger the system is the easier planet can be detected (e.g. Keppler et al. 2018; Müller et al. 2018).

In addition to these, using chronographs can reduce the starlight significantly, which provides access to the smaller angular separations from the host star. The thermal emission of planets peak at the Infrared wavelengths while the radiation form the hot stars tend to peak at shorter wavelengths. Hence directly imaging at longer wavelengths (IR/NIR) increases the contrast between the starlight and planet's emission.

Phase Curve (Orbital brightness modulation)

The planetary thermal emission and the reflected light from the planets can be observed through other methods as well. In particular this can be achieved when the planet's orbital plane is not face-on with respect to the observer. As the planet revolves around the star in this geometry, the observer observes a variation in the planetary signal; similar to the variation of lunar phases throughout of a lunar month. This "modulation" can be an indication of an orbiting planet around a star. Two example of exoplanets detected by using this technique are Kepler-70b and Kepler-70c (Charpinet et al. 2011).

This method is expected to contribute more in the detection of exoplanets in the coming years as several space missions (such CHEOPS, PLATO, and ARIEL) will join TESS to precisely measure these modulations. This method (along with

a few others) can be also used to study the atmosphere of exoplanets, which will be discussed later.

Other techniques

There are also other techniques that have been used or are proposed to detect planets beyond the solar system. **Transit timing variation (TTV)** is one of them. In the multi-planetary systems the gravitational pull can cause a variation on the transit timing of the transiting planets. This variation has been used to estimate the maximum mass of tight planetary systems with small planets, which is usually difficult for the radial velocity to measure. TTV has been also used to discover new planets in the planetary systems. The Kepler-19 system is an example where a non-transiting planet was discovered using this method (Ballard et al. 2011).

Astrometry is another method for the detection of exoplanets. It uses the change in the position of the host star in the sky as it is being pulled around by the planet(s) in the system. These changes, however, are very small cause by a planetary companion and usually ground-based observations are not precise enough to disentangle the atmospheric and systematic distortions from a planetary signal. So far there has been no confirmed detection of an exoplanet using this method, but the space mission Gaia is expected to change this view by finding thousands of planets via astrometry.

Similar to pulsar timing method, the **Variable star timing** can be used in the case of regular pulsating variable stars. The radial velocity then can be estimated based on the Doppler shift of the pulsation frequency. One advantage of using this technique (in comparison to the radial velocity) is that the RV can be measured photometrically instead of spectroscopically.

Polarimetry is yet another promising method that can be sued to detect exoplanets thanks to the fact that the stellar light is un-polarized but the reflected light from the atmosphere of planets are polarized (Schmid et al. 2005). Although this method may be limited to the planets owning an atmosphere, the majority of characterized exoplanets have shown to possess some sort of atmosphere (e.g.

Tsiaras et al. 2018). This technique can be also used in conjunction with the transit method as, e.g., described by Oklopčić et al. (2019).

There are also other detection techniques, but either they have not been established yet as a method for massive discovery of exoplanets or the technology requirement has not reached to the required level to perform those methods. Some of these methods are: Relativistic beaming, Ellipsoidal variations, Transit duration variation, Transit imaging, Eclipsing binary minima timing, Flare and variability echo detection, Magnetospheric radio emissions, Auroral radio emissions, Optical interferometry, and Modified interferometry.

1.2.2 Observed populations of exoplanets

Discovering thousands of exoplanets in the last 30 years has opened the path to start addressing some of the questions regarding the demographics and properties of exoplanets. In this section we briefly summarize the findings achieved by each detection technique mentioned in the last section.

Out of 4093 confirmed planets, 779 (∼20%)[6] are discovered by **radial velocity**. The technique responds better to the systems with larger planet-to-star mass ratios and for the detection of planets at shorter orbital distances. The discovery of hot jupiters was indeed one of the consequences of RV sensitivity to such planetary systems. In contrast, not so many brown dwarfs have been discovered at such close distances from their host stars (Wright et al. 2012); demanding further studies to investigate the underlay physics and formation scenarios.

Hot jupiters are more frequently formed around the metal-rich stars (e.g. Fischer & Valenti 2005), with a tendency to increase in their occurrence rate as their orbital period increases (Cumming et al. 2008) with a maximum rate at around 3 days; see Figure 1.3. This "pile-up" of hot jupiters is observed only for the metal-rich stars where the hot jupiters show higher eccentricities in general; which may suggest the current location of such planets are largely affected by planet-planet interactions (Dawson & Murray-Clay 2013). On the other hand, hot jupiters are less frequent

[6] exoplanetarchive.ipac.caltech.edu retrieved on Nov 14, 2019

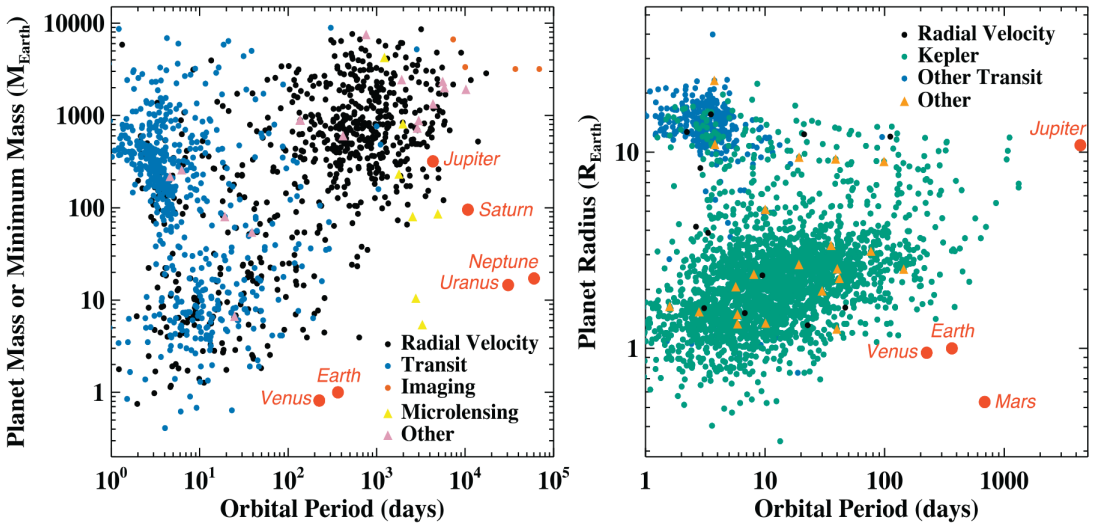

Figure 1.3: The distribution of mass, radius, and orbital periods of known exoplanets. Planets are color-coded by their method of detection. The solar system planets are superimposed for comparison. Source: National Academies of Sciences (2018).

around M dwarfs; suggesting a critical role of stellar metallicity and protoplanetary disk mass in the formation of close-orbiting gas giants (e.g. Wang & Fischer 2014). Radial velocity has been also successful with the discovery of smaller planet orbiting close to their host stars (Mayor et al. 2011), small planets in the habitable zones (e.g. Bonfils et al. 2018) and gas-giants at larger orbital distances (e.g. Giguere et al. 2015), which illustrates the power of this technique to map a demographic of exoplanets over a large parameter-space.

Transit photometry is the by far the most successful method to detect exoplanets. About 76% of all exoplanets has been discovered through this method. This many exoplanets (3131[7]) covers a variety of exoplanets, ranging from ultra-hot jupiters (e.g. Hebb et al. 2009) to temperate rocky planets (e.g. Dressing & Charbonneau 2015). Maybe the most exciting results from the transit surveys is that the probability of finding a terrestrial planet in the habitable zone of solar-type stars is about 10%; given the uncertainties (e.g. Burke et al. 2015). This value increases to about 25% for M dwarfs (e.g. Dressing & Charbonneau 2015). The existence of a population of planets that has no analogue in the solar system was a surprise. The

[7]exoplanetarchive.ipac.caltech.edu retrieved on Nov 14, 2019

radius of these planets lies somewhere between the Earth's and Neptune's radius and they are the found to be the most frequent type of planets so far. In fact, it is estimated that 50% of the stars in the galaxy harbor such a planet at a close orbit (e.g. Dressing & Charbonneau 2015; Burke et al. 2015). Moreover, Fulton et al 2017 reported a paucity of planets in the range of 1.5-2.0 Earth radius that splits the population of small planets into two size regimes. This has been hypothesized to be a result of mass loss due to photoevaporation (e.g. Owen & Wu 2017).

While the transit photometry and radial velocity are sensitive to the close-orbiting planets, **microlensing** can probe the regions far from the host star and beyond the snow-line; a complementary technique to extend exoplanets demographics. The discovery of cold giant planets around M dwarfs suggested that they are not uncommon, while are less common in comparison to the cold giants orbiting solar-type stars (e.g. Clanton & Gaudi 2014, 2016). Gould et al. (2006) found that cold low-mass planets (Neptune-like or smaller) are more common than cold giants orbiting M Dwarfs. In fact, Neptune-mass objects may be the most common cold planets orbiting M dwarfs; although cold super-Earth objects are also abundant around this type of stars (e.g. Suzuki et al. 2016).

In summary, planetary systems are found to be extremely diverse and our solar system appears to be a rare system among them. We have found that planets, and in particular small planets, are frequent in the galaxy. Terrestrial planets in the habitable zone of stars are not rare, and there are some evidence in the demographics of observed exoplanets that support planet migration scenarios.

1.2.3 Observation of exoplanet atmospheres

Currently, there are two major goals in the exoplanet science (National Academies of science 2018):

1. "*To understand the formation and evolution of planetary systems as products of the process of star formation, and characterize and explain the diversity of planetary system architectures, planetary compositions, and planetary environments produced by these processes.*"

2. "*To learn enough about the properties of exoplanets to identify potentially habitable environments and their frequency, and connect these environments to the planetary systems in which they reside. Furthermore, scientists need to distinguish between the signatures of life and those of non-biological processes, and search for signatures of life on worlds orbiting other stars.*"

In both goals, observation and characterization of exoplanet atmospheres (exoatmospheres) is a pivotal part. In what follows, we briefly summarize the techniques that have been used to study the exoatmospheres.

Transmission spectroscopy

Transmission spectroscopy is a type of absorption spectroscopy in which the absorption of stellar radiation is measured as a function of wavelength after it passes through the atmosphere of an exoplanet. The theory of this method was introduced by Seager & Sasselov (2000) and it is the most frequently used technique for the observation of exoatmospheres (e.g. National Academies of Sciences 2018). The principle of the method is similar to that of the transit photometry, except spectroscopic measurements are made instead of the photometric ones. As the planet crosses the disk of the star, its atmospheres absorbs a fraction of the stellar light. This absorption depends on the properties of the atmosphere such as its composition, scale height, and its dynamic; hence generally varies with wavelength.

The transit depth (TD) of a bare planet with no atmosphere and a radius of R_p is:

$$TD\left(\lambda\right) = \left(\frac{R_p}{R_s\left(\lambda\right)}\right)^2, \tag{1.1}$$

where R_s is the radius of the star at a given wavelength (λ). Note that the radius of the planet does not change with wavelength in this case. The effective altitude (H_p) of a planetary atmosphere can be defined at a pressure at which the atmosphere becomes optically thick. The reference radius (R_{ref}) of a planet with an atmosphere can be thus defined at a pressure at which the atmosphere becomes optically thick at all wavelengths. Their relationship can be simply written as follow:

$$R_p(\lambda) = R_{ref} + H_p, \tag{1.2}$$

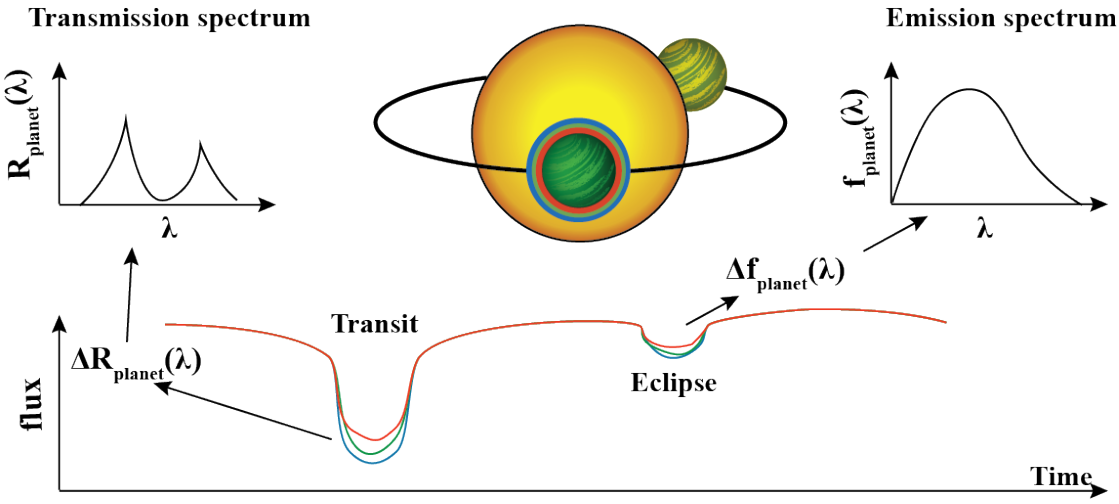

Figure 1.4: Schematic of transmission and emission spectroscopy. Adapted from Sing (2018)

where the planetary radius changes with wavelength in this case. Therefore the "atmospheric signal" can be estimated as below:

$$\delta(TD(\lambda)) = \left(\frac{R_p(\lambda)}{R_s(\lambda)}\right)^2 - \left(\frac{R_{ref}}{R_s(\lambda)}\right)^2 = \left(\frac{2R_{ref}H_p(\lambda) + H_p(\lambda)^2}{R_s(\lambda)^2}\right). \tag{1.3}$$

For hot jupiters, H_p is generally 30 to 3000 times smaller than R_{ref} (e.g. Lecavelier des Etangs et al. 2008). Hence the second term in Eq. 1.3 can be neglected for an order of magnitude estimation:

$$\delta(TD(\lambda)) \approx \left(\frac{2R_{ref}H_p(\lambda)}{R_s(\lambda)^2}\right). \tag{1.4}$$

A typical radius of a hot-jupiter is roughly 10% of its host star[8]. A quick calculation therefore shows that the atmospheric signal is on the order of 0.07%-0.0007% depending on the scale height and other properties of the atmosphere.

Eclipse spectroscopy

As a "transiting exoplanet" orbits around its host star, it passes behind it and becomes occulted by the stellar disk. Therefore the flux contribution by the planet, F_p, will be blocked by the star and can be separated from that of the star, F_s, (e.g. Sing 2018):

$$\frac{\Delta f}{f} = \frac{F_s + F_p}{F_s + F_p} - \frac{F_s}{F_s + F_p} = \frac{F_p}{F_s + F_p} \tag{1.5}$$

[8]For the Jupiter and the Sun this ratio is 0.1028

where generally $F_p \ll F_s$, and hence

$$\frac{\Delta f}{f} \approx \frac{F_p}{F_s}. \tag{1.6}$$

The planetary flux, F_p, has two reflected and emitted components that dominate the planetary spectrum at different wavelengths. In general, we have:

$$\frac{\Delta f}{f} \approx \frac{F_p}{F_s} \times \left(\frac{R_p}{R_s}\right)^2 + A\left(\frac{R_p}{a}\right)^2 \tag{1.7}$$

where A is the planetary geometric albedo and a is the semi-major axis. At larger wavelengths (NIR/IR) the emission flux from the dayside of the planet dominates (first term in the right hand side). At optical wavelengths, the emission contribution becomes low and the reflected stellar flux from the planet dominates (second term in the right hand side). The eclipse depth signal is usually much smaller than the transit depth signal, with 0.001% and 0.1% for order of magnitude values of the this signal due to the reflected light and planetary emission flux, respectively[9]. Similar to the transit signal, the eclipse signal also depends on the composition, scale height and other properties of the planetary atmosphere and hence in general depends on the wavelength as well. Figure 1.4 shows a schematic of transmission and eclipse spectroscopy.

As the planet is being eclipsed by the star, different parts of the dayside of the planet is become covered. This encoded spatial information can be used to construct a 2D map of the reflected and emission flux on the dayside of the planet. Such 2D mapping usually requires high cadence high signal to noise ratio observations of the eclipse, and are challenging to obtain. The phase curve spectroscopy, however, can be used to construct a 1D longitudinal map.

Phase curve spectroscopy

Phase curve spectroscopy is similar to the eclipse spectroscopy, expect that the information is collected from all orbital phases and not only the eclipse (e.g. Knutson et al. 2009, 2012). As the planet orbits around its host star, the dayside and nightside

[9]Recall that the transit depth signal is on the order of 1%

contribution of the visible disk of the planet with respect to the observer changes. A time series spectroscopy then provides sufficient amount of information to extract the differential flux contribution at different orbital phases. One advantage of this method over the transit and eclipse spectroscopy is that it can also be used to observe non-transiting planets; as long as their flux contribution modulate with phase.

In addition to the small atmospheric signal, dedicated and long observational campaigns are usually needed to perform this method. Such observations at the moment are scarce but with JWST and ARIEL mission in 2020's this method is expected to provide pivotal information regarding the composition and dynamic of planetary atmospheres.

High-resolution spectroscopy

Ground-based observations are generally complementary to the space-based observations (e.g. Brogi et al. 2017). While the telluric removal is an added challenge with respect to the space-based observations (e.g. Shulyak et al. 2019), larger light collecting area and higher resolving power are advantageous in the ground-based observations (e.g. Kneer 1987).

In general there are two strategies to study the atmosphere of exoplanets from the ground: 1) resolving individual and strong spectral lines (e.g. Redfield et al. 2008), and 2) using the position of the lines (line list) and combine the information through the cross-correlation technique (e.g. Snellen et al. 2010).

When studying a resolved spectral line, the shape of the line usually contains the information regarding the vertical structure of the atmosphere. The wings are generally sensitive to lower optical depths while the line core probes higher altitudes. The sodium doublet lines are very strong and are placed in the optical regime at 5889.95 and 5895.92 Å. Hence the atomic Na has become one of the most frequently studied line in the spectra of exoplanet atmospheres for probing a wide altitude-pressure range (e.g. Snellen et al. 2010; Jensen et al. 2011; Huitson et al. 2012; Casasayas-Barris et al. 2017).

Many other spectral features have also been detected by using the ground-based spectroscopy (most of which through the cross-correlation technique), including He triplet (Nortmann et al. 2018), Hα (Yan & Henning 2018), CaII (Yan et al. 2019), FeII, the Balmer series of H (Hα, Hβ, and Hγ) (Casasayas-Barris et al. 2019), neutral and singly ionized atomic iron (Fe and Fe^+) and singly ionized atomic titanium (Ti^+) (Hoeijmakers et al. 2018), and CrII, ScII and YII, MgI, FeI, FeII, and TiII (Hoeijmakers et al. 2019).

The detection of "atmospheric lines" both re-confirms the existence of a planet and provides additional information on the dynamic of its upper atmosphere. Doppler shift in these spectral features and in the rest frame of the planet hints for the detection of non-stationary atmospheres. The magnitude of the atmospheric velocity and its direction maps the dynamic of an atmosphere into these Doppler shifts (e.g. Snellen et al. 2008, 2010).

The high-resolution spectroscopy of exoplanetary atmospheres can be also used to study the host star itself. Understanding the stellar spectral features is an essential key because the exoplanet atmosphere can be understood only as good as its host star's atmosphere (e.g. Yan et al. 2017).

Direct imaging spectroscopy

All mentioned techniques to explore the atmosphere of exoplanets are based on time series observations; means that the observations are usually time critical and are performed through a series of observations in a time interval. These techniques are also mostly suitable for studying close-orbiting exoplanets; the wider separation gets the weaker signal becomes. Direct imaging spectroscopy, on the other hand, can be performed both as a time series observations or not. The method is similar to the photometric direct imaging except spectroscopy being performed instead of the photometry. This method, as discussed in Section 1.2.1, is mostly suitable for observing the atmosphere of young planets with large separation from their host stars (Biller & Bonnefoy 2017).

Assuming a temperature of 400-2000 K for young planets, their thermal emission spectra peak around 1-5 μm. At these wavelengths the star-planet contrast ratio is generally around 10^4 to 10^7 (e.g. Beuzit et al. 2008; Macintosh et al. 2014). Moreover, the directly imaged around nearby planetary systems usually show a projected angular separation of 0.05" to 1". The current observational facilities, such as SPHERE at VLT (e.g. Beuzit et al. 2008) and GPI at Gemini (e.g. Macintosh et al. 2014), are capable of reaching such contrasts and resolutions. To name a few, β Pic b (e.g. Bonnefoy et al. 2014b; Chilcote et al. 2017), HR 8799 b,c,d, and e (e.g. Skemer et al. 2012; Oppenheimer et al. 2013), 51 Eri b (e.g. Macintosh et al. 2015; Samland et al. 2017), and PDS 70 b (Müller et al. 2018) are among the planets that have been studies using this method.

Atmospheric inhomogeneities can be also observed through time series and photometric or spectral modulations (e.g. Apai et al. 2013). Although generally an ill-posed problem, these modulations can be translated to longitudinal maps using similar principles as in the tomography techniques (e.g. Biller & Bonnefoy 2017). Instrument instability and limited number of bright and fast rotating nearby exoplanets are the main challenges for exploring exoatmospheres through this method.

This is a growing field and in the future we might be able to observe the atmosphere of terrestrial planets in the habitable zone with upcoming facilities such as JWST, ELT, WFIRST, HabEx, and LUVOIR (e.g. Biller & Bonnefoy 2017).

1.3 Characterization of planetary atmospheres

To characterize the planetary atmospheres we need to understand the connection between their spectra and underlying atmospheric properties. The connection goes two ways: 1) construction of a synthetic spectrum given a set of physics and atmospheric properties, called forward modelling, and 2) interpretation of the atmospheric properties given an observed spectrum, called atmospheric retrieval methods. Both of these approaches require the development of theoretical models of planetary atmospheres that we discuss in following sections.

1.3.1 Forward modeling

Atmospheric spectral forward modelling is the simulation of atmospheric spectra based on a given set of atmospheric parameters. These parameters can interplay with each other or not. If these parameters are physicochemically consistent, then they are called "self-consistent" models, and when they are not consistent, called "parametric" forward models (e.g. Fortney 2018).

The main ingredients to synthesize a planetary spectrum are the pressure-temperature (PT) profile and the chemical composition of the atmosphere (e.g. Madhusudhan et al. 2011; Waldmann et al. 2015; Mollière et al. 2019). In a parametric setup, the PT profile can have any shape; usually defined as an analytical function which is controlled by a number of other parameters (e.g. Madhusudhan & Seager 2009). The chemical composition of the atmosphere is also parameterized and any desired atmospheric constituent could be assigned with any value for their mixing ratio. Then with a radiative transfer solver, and for a given observational mode, the synthetic spectra can be calculated; in emission, transmission, or reflected light as desired (e.g. Mollière et al. 2019).

On the other hand, in a self-consistent setup, the atmospheric processes are assumed to be known. These assumptions generally include spherically symmetric atmosphere, thermochemical equilibrium, hydrostatic equilibrium, and radiative-convective equilibrium. In most cases local thermodynamic equilibrium (LTE) and homogeneous cloud formation are also assumed (e.g. Fortney et al. 2003; Fortney 2005; Mollière et al. 2015, 2017). Under such setup, the input are generally the planetary properties such as its mass, radius, the distance from the host star, and the spectral type of the host star. The temperature-pressure profile as well as the chemical composition of the atmosphere are being calculated self-consistently and are not given as a priory.

1.3.2 Retrieval

Atmospheric retrievals are observationally driven techniques that generally employ parametric forward models to robustly interpret the atmospheric properties from

observed spectra through an optimization algorithm. The optimization algorithm is generally a statistical inference method to efficiently sample the model parameter space given the observed spectrum. In simple words, a retrieval fits the models into the data and estimates the posterior probability distributions of the model parameters (e.g. Madhusudhan 2019).

The first step is thus computing the atmospheric structure. For a given grid of pressures, a corresponding grid of temperatures is calculated. If some physicochemical processes are assumed (such as thermochemical equilibrium or disequilibrium chemistry) then the concentration of atmospheric species can be calculated, as well as the mean molecular weight and total number density. If no physicochemical process is assumed, the retrieval follows a free parameterization in this regard and the concentrations must be provided as input. These calculations can be expanded to the liquid and solid phases too, when could/haze formation is considered in the forward model.

After obtaining the atmospheric properties, the spectrum should be calculated. For simplifications, atmospheric retrievals generally assume a 1D plane-parallel planetary atmosphere (e.g. Seager 2010; Madhusudhan & Seager 2009; Line et al. 2013). One key element in the radiative transfer codes is the opacities. In the planetary atmospheres, molecules and clouds usually play the main roles in the total opacity. Molecular spectral features are consistent of millions to billions lines in the range of optical to IR (e.g. Tennyson & Yurchenko 2012). Some retrieval codes compute the opacities line-by-line (e.g. Madhusudhan & Seager 2009; Line et al. 2013; Benneke & Seager 2013; Madhusudhan et al. 2014c). However, this is computationally expensive and other methods, such as correlated-K, are replaced for speeding up the retrieval of low-resolution retrievals[10].

While retrieval are invaluable for interfering the atmospheric properties, they generally burden some assumptions. For instance, the vertical abundances of the atmospheric species are usually assumed to be constant or divided into two layers (e.g. Changeat et al. 2019). This is an intrinsic limitation of retrieval methods,

[10] An exoplanetary low resolution spectrum is usually referred to a spectrum with $\frac{\Delta\lambda}{\lambda} \leq 10^3$.

because the number of free parameters can not be increased arbitrarily due to the limited information content in the atmospheric spectra. Any additional free parameter decreases the degree of freedom; hence, increasing the intrication of degeneracies between the retrieved parameters.

1.4 Open Questions and Thesis Outline

In recent years, the modelling of exoplanet atmospheres has progressed significantly. Substantial gaps between the models and observations (as well as among the models), however, has remained. Consequently, any planning in the direction of future opportunities (such as observing the exoatmospheres by the next generation facilities or interpretation of such data) demands addressing the shortcomings of current modeling efforts (e.g. National Academies of Sciences 2018).

One example of differing approaches in the planetary atmospheric modelling is the the chemistry treatment. Usually hot jupiters are assumed to be at their thermochemical equilibrium. This assumption provides a chemically-based yet fast approximation of the amount of constituents in the atmosphere. The atmosphere of colder planets, however, are not guaranteed to remain at thermochemical equilibrium. Under these conditions reaction rates are usually slower and the timescale of disequilibrium processes (such as mixing and photolysis) could become shorter than the chemical timescales for some species. Hence disequilibrium processes are expected to dominate. Chemical kinetic codes are then used to perform time-dependent calculation of disequilibrium abundances until they reach a steady state. These kinetic models are usually computationally expensive and have been applied only on limited cases. The same is also true for the self-consistent models; they are computationally much more expensive than parameterized forward models and only a limited number of studies have explored relatively a wide range of parameter space.

These approaches are generally performed in 1D setup for above mentioned reasons. But planets are 3D objects and a more realistic approach could be simulations in higher dimensions, such as 3D general circulation models (GCMs; e.g., Cooper & Showman 2006; Parmentier et al. 2013; Parmentier & Guillot

2014). A simplified chemical scheme is usually considered to compensate for higher dimensionality of these models. Thermochemical equilibrium, chemical relaxation schemes, and chemical kinetic with reduced chemical network are a few of these methods to couple the chemistry with 3D simulations (e.g. Drummond et al. 2018a).

Including all physics and chemistry in the atmospheric models is therefore impossible with our current computational capabilities. Inevitably, some of the physics and chemistry must be left out. The question is, which physics and chemistry dominates a planetary atmosphere and which modelling approach is valid for that atmospheric condition?, and more generally, what are the dominant physics and chemistry in the planetary atmospheres across the full parameter space? The present thesis represents a step to address these questions from an observation-oriented perspective. In particular, we focus on water and methane because of their relevance to the origin of life and habitability, as well as their major roles to shape the structure of planetary atmospheres. Abundances retrieved for these species can be also used as a tracer of carbon-to-oxygen ratio (C/O) and metallicity of these atmospheres; hence potentially linking the formation scenarios with the observations. More specifically, water's spectral signature is everywhere, but despite many efforts, there has been only one robust detection of methane and only recently. Therefore, the question is, "where is methane?". In what follows, we shortly describe the content of each chapter in this work:

- In **Chapter 2**, we present the results of our extensive thermochemical cloud-free self-consistent simulations with more than 28,000 models. We propose a new classification scheme for the irradiated gaseous planets based on their dominant chemistry at their photospheric levels.

- In **Chapter 3** we describe a `Chemical Kinetic Model`, called `ChemKM`, that we implemented to investigate the importance of kinetics in the planetary atmospheres.

- We present the results of these simulations in **Chapter 4** where 112,000 chemical kinetic models with full chemical network are performed and presented

to cover the same parameter space as in our thermochemical simulations. Covering the same parameter space allows me to quantitatively estimate the importance of each chemical processes.

- In **Chapter 5**, we isolate and discuss the role of cloud formation in the exoplanetary atmospheres by performing 37,800 self-consistent cloudy models (i.e. considering the radiative feedback of the clouds).

- In **Chapter 6**, we investigate how 3D geometry of exoplanet can affect their chemical composition. In particular we study the fingerprints of disequilibrium chemistry on the atmospheric composition of an ultra-hot jupiter that are believed to remain at thermochemical equilibrium due to their extremely hot environment.

- We summarize our findings in **Chapter 7** where we also describe the next steps that we plan to take in the future of this research.

Alles Gescheite ist schon gedacht worden.
Man muss nur versuchen, es noch einmal zu denken.

All intelligent thoughts have already been thought;
what is necessary is only to try to think them again.

— Johann Wolfgang von Goethe (Goethe 1821)

2

Classification of Planets

Contents

[1]The first classification of planets from a modern scientific point of view was proposed by Alexander von Humboldt and his colleagues in their book "Cosmos" (Humboldt et al. 1852). They categorized the solar system planetary objects into three classes of inner, central, and outer planets based on their apparent orbital configuration

[1]This chapter was published as a refereed article "From cold to hot irradiated gaseous exoplanets: Toward an observation-based classification scheme", Molaverdikhani et al. (2019b), for which I am the lead author and has been adapted for this thesis.

and noted the disparity of the inner (terrestrial) and outer (giant) planets densities. Remarkably, they also suggested different internal density distributions for these two classes; deduced from their different degree of oblateness.

Adequate and accurate observations of these objects to examine these hypotheses did not take place until the 20^{th} century. Even then the early studies on the constitution of the giant planets in the solar system were based on a few observations only. Wildt (1934) summarized these studies and crystallized the dominant role of hydrogen in their make-up. He further developed this idea and proposed the presence of a core for these planets similar in structure to the terrestrial planets, covered by ice and a layer of solid hydrogen on top of it (Wildt 1938, 1947). However, it was not until a few years later when Brown (1950) suggested the composition of Uranus and Neptune differ from Jupiter and Saturn and proposed that they are mainly composed of solid methane and ammonia. Later studies by Demarcus & Reynolds (1963) and Zapolsky & Salpeter (1969) significantly improved our understanding of "ice giants"[2] to make the first step toward the classification of gaseous planets.

This classification did not remain unmitigated after the detection of the first Hot-Jupiter (Mayor & Queloz 1995) and demanded new investigations. Motivated by the apparent diversity of the solar system planetary objects, Sudarsky et al. (2000) proposed a classification of H/He dominated gaseous planets based on their albedo and reflection spectra with five classes namely "Jovians" ($T_{eff} \lesssim 150$ K), "water cloud" objects, "clear" objects, and class-IV/V "roasters" (i.e. close orbiting planets with $T_{eff} \gtrsim 1500$ K). Although most of the observed exo-atmospheres appear to be cloudy, observations of their reflected light have proven to be challenging due to their faint signal and contamination by stellar noise (Martins et al. 2013, 2015; Angerhausen et al. 2015; Kreidberg 2017).

In contrast, transmission and emission spectroscopy have found to be among the best techniques to study exoplanetary atmospheres. By considering the benefits of these techniques and extricating from the orbital configuration point of view,

[2]In early 70's the terminology became popular in the science fiction community, e.g. Bova (1971), but the earliest scientific usage of the terminology was likely by Dunne & Burgess (1978) in a NASA report.

Fortney et al. (2008) argued that orbital period is a poor discriminator between "hot" and "very hot" Jupiters and proposed two classes of irradiated gaseous giants by highlighting the importance of the insolation level and TiO/VO opacities for these objects. Despite the cloudy nature of exoplanets they ignored the cloud opacities due to their weak effects on the temperature structures and spectra (Fortney et al. 2005). By using cloud-free models they concluded that these two classes of planets are somewhat analogous to the M- and L-type dwarfs and hence named them "pM Class" and "pL Class" planets according to their similarities. Ti and V in the colder objects, i.e. pL Class, are thought to be predominantly in solid condensates and neutral alkalis absorption lines were predicted to cause the dominant optical spectral features both in transmission and emission. On the other hand, the hotter objects, i.e. pM Class, were predicted to present molecular bands of TiO, VO, H_2O and CO in emission due to their hot stratospheres (temperature inversion) and the presence of these molecules in the gas phase at photospheric pressures. They reported HD 149026b and HD 209458b as prototypical exoplanets for atmospheric thermal inversions, and classified them as pM Class planets. However, further observations and newer data reduction techniques provided evidence against an inversion in the case of HD 209458b (Diamond-Lowe et al. 2014), and therefore the onset of pM Class is thought to begin at higher temperatures.

Along this line of thought, another class of gaseous giant planets with T_{eff}>2500 K was recently proposed by Lothringer et al. (2018). The chemistry of these extremely irradiated hot Jupiters is thought to be fundamentally different in comparison to the cooler planets. For instance, the presence of strong inversions due to the absorption by atomic metals, metal hydrides and continuous opacity sources such as H^-, and significant thermal dissociation of H_2O, TiO and VO on the dayside of these planets are predicted. As will be addressed in Section 2.1.2, we exclude this range of temperature (and hence this class of ultra-hot Jupiters) from our study.

The complexity of irradiated planets classification is not limited to the effect of their insolation level. Seager et al. (2005b) studied HD 209458b to place a stringent constraint on the H_2O absorption band depths. They proposed a new scenario where

an atmospheric carbon-to-oxygen ratio C/O≥1 explains the very low abundance of water vapor. The carbon-rich atmosphere scenario was in contrast to the solar C/O ratio of 0.55 (Asplund et al. 2009) that was used in the exoplanets models prior to their study. The chemistry of such atmospheres were also predicted to be significantly different in comparison to the atmospheres with solar or sub-solar C/O ratios. Hence the spectral differences were predicted to be observable (Kuchner & Seager 2005). However, there has not been a robust detection of a carbon-rich exoplanet yet.

Madhusudhan (2012) integrated and expanded these ideas into a two-dimensional classification scheme with four classes of irradiated gaseous planets, with the effective temperature of the planet and the C/O ratio as the two key factors on their atmospheric characteristics. Madhusudhan reported strong H_2O features for the models with a C/O ratio of 0.5. This was in contrast to the models with C/O≥1 in which their spectra showed enhanced CH_4 absorption at near-infrared wavelengths. Therefore, he noted that in this scheme a natural boundary between C-rich and O-rich atmospheres is plausible at C/O=1. He also concluded that the strength of methane spectroscopic features depends on the C/O ratio and the temperature of the observable atmosphere, but did not investigate this quantitatively and only for limited parameter space. His conclusions can be understood from the following net reaction (e.g. Kotz et al. 2014; Ebbing & Gammon 2016), assuming thermo-chemical equilibrium:

$$CH_4 + H_2O \underset{\lesssim 1000K}{\overset{\gtrsim 1000K}{\rightleftharpoons}} 3\,H_2 + CO\,. \tag{2.1}$$

For effective temperatures $T_{eff} \gtrsim 1000$ K Reaction 2.1 is in favor of CO production and thus in a C/O<1 atmosphere (i.e. oxygen-rich) the excess oxygen is being sequestered in the water molecules with almost no methane in the atmosphere. In the case of a C/O>1 atmosphere (i.e. carbon-rich) the extra carbon is bound in the methane molecules and the atmosphere is depleted of water molecules. For $T_{eff} \lesssim 1000$ K the net Reaction 2.1 is in the direction of CO depletion and therefore both H_2O and CH_4 are expected to be present in the atmosphere (see e.g. Mollière et al. 2015). However, a transition from water- to methane-dominated spectrum

might still occur as C/O increases, where the CH_4 spectral features become stronger than the strongest H_2O features. While exoplanets, and in particular colder ones, are expected to be cloudy, Madhusudhan (2012) used cloud-free atmospheric models and argued that the gas phase chemistry and corresponding spectroscopic signatures resulting from cloud-free simulations are also applicable to cloudy atmospheres (Madhusudhan et al. 2011).

Following this line of thought, Mollière et al. (2015) studied an extensive grid of 10,640 self-consistent cloud-free equilibrium chemistry models investigating how stellar type, T_{eff}, surface gravity (log(g)), metallicity ([Fe/H]) and C/O ratio affect the emission spectra of hot H_2-dominated exoplanets. They inspected the synthetic emission spectra and found that the water- to methane-dominated atmosphere transition occurs at C/O$\sim$ 0.9 for relatively hot planets with T_{eff}>1750 K. This is approximately consistent with a natural boundary between these two atmospheres at C/O$\sim$1, as was predicted by Madhusudhan (2012). However, Mollière et al. (2015) reported a smaller value of C/O$\sim$ 0.7 for planets with an effective temperature of 1000 K<T_{eff}<1750 K mainly due to oxygen being partially bound in enstatite ($MgSiO_3$) and other oxygen bearing condensates. They also predicted transition C/O ratios [3] as low as 0.7 for colder planets, i.e. T_{eff}<1450 K, with strong dependency on the surface gravity and atmospheric metallicity.

Given the lack of a quantitative study on the transition C/O ratios dependency on the atmospheric parameters and its importance in the classification of irradiated exoplanets, we aim to quantitatively investigate a 5D model parameter space to translate the photospheric chemistry into the spectra of irradiated planets. We explore how these spectra change with the variation of planetary effective temperature, surface gravity, metallicity, carbon-to-oxygen ratio and spectral type of the host star. In this chapter, as the first step, we present the results of our self-consistent cloud-free simulations, and in the forthcoming chapters we address the effects of non-equilibrium chemistry and cloud opacities on these

[3] From now on we call these C/O ratios, “transition" C/O ratio, $(C/O)_{tr}$

results to shape a consistent observationally driven theoretical framework on the classification of gaseous planets.

In what follows, we describe the most up-to-date version of our model (*petitCODE*) and the parameter space that we have investigated in Section 2.1. In Section 2.2, we present the results on $(C/O)_{tr}$ ratios. In Section 2.3, we discuss how our chosen parameters influence the transition C/O ratios and propose a classification scheme for irradiated planetary spectra between 400 and 2600 K with four classes, and how they fit to Spitzer color-diagrams. We summarize and conclude our results and findings in Section 2.4.

2.1 Methods

In order to investigate the influence of mentioned parameters on the atmospheric properties, we have synthesized a population of 28,224 self-consistent planetary atmospheres by using *petitCODE* (Mollière et al. 2015, 2017). This code and the grid are described in the following subsections, and the grid is publicly available[4].

2.1.1 petitCODE

petitCODE is a 1D model that calculates planetary atmospheric temperature profiles (TP structures), chemical abundances, and emission and transmission spectra (which includes scattering), assuming radiative-convective and thermochemical equilibrium. It was introduced in Mollière et al. (2015), and is described in its current form in Mollière et al. (2017) (general capabilities) and (Mollière & Snellen 2018) (opacity updates).

The basic physical inputs are the stellar effective temperature and its radius, planetary effective temperature or distance to the star, planetary internal temperature, planetary radius and mass (or surface gravity), atomic abundances, and the irradiation treatment (it is possible to calculate the dayside average, planetary average, or to provide incidence angle for the irradiation).

[4] www.mpia.de/homes/karan

There are two options to treat clouds: one is by following the prescription by Ackerman & Marley (2001) and introducing the settling factor (f_{sed}), the width of the log–normal particle distribution (σ_g) and the atmospheric mixing K_{zz}; the other is by providing the cloud particle size and setting the maximum cloud mass fraction (see Mollière et al. 2017).

Depending on the case of interest, some of the inputs may not be required. For instance, the current chapter presents our results on the irradiated gaseous planets without clouds to provide a cloud-free framework, which can also be used to explore the atmosphere of cloud-free planets or as a diagnostic tool to identify cloudy/partially-cloudy atmospheres. As will be discussed in our following chapter, our non-equilibrium chemistry study will be built upon this framework as well.

The chemical inputs of the code are the lists of atomic species (H, He, C, N, O, Na, Mg, Al, Si, P, S, Cl, K, Ca, Ti, V, Fe, and Ni) with their mass fractions and reaction products (H, H_2, He, O, C, N, Mg, Si, Fe, S, Al, Ca, Na, Ni, P, K, Ti, CO, OH, SH, N_2, O_2, SiO, TiO, SiS, H_2O, C_2, CH, CN, CS, SiC, NH, SiH, NO, SN, SiN, SO, S_2, C_2H, HCN, C_2H_2, CH_4, AlH, AlOH, Al_2O, CaOH, MgH, MgOH, PH_3, CO_2, TiO_2, Si_2C, SiO_2, FeO, NH_2, NH_3, CH_2, CH_3, H_2S, VO, VO_2, NaCl, KCl, e^-, H^+, H^-, Na^+, K^+, PH_2, P_2, PS, PO, P_4O_6, PH, V, VO(c), VO(L), $MgSiO_3$(c), Mg_2SiO_4(c), SiC(c), Fe(c), Al_2O_3(c), Na_2S(c), KCl(c), Fe(L), Mg_2SiO_4(L), SiC(L), $MgSiO_3$(L), H_2O(L), H_2O(c), TiO(c), TiO(L), $MgAl_2O_4$(c), FeO(c), Fe_2O_3(c), Fe_2SiO_4(c), TiO_2(c), TiO_2(L), H_3PO_4(c) and H_3PO_4(L)) to be considered in the equilibrium chemistry network. The lists of gas opacity species (CH_4, H_2O, CO_2, HCN, CO, H_2, H_2S, NH_3, OH, C_2H_2, PH_3, Na, K, TiO and VO) and cloud opacity species (Al_2O_3, $MgAl_2O_4$, Mg_2SiO_4, $MgSiO_3$, $MgFeSiO_4$, Fe, KCl and Na_2S) should be also provided for the calculations. In addition, whether or not to include H_2-H_2 collision induced absorption (CIA) and H_2-He CIA in the model must be specified.

The abundances in petitCODE follow from true chemical equilibrium, i.e. no "rain-out" of condensates is assumed (Burrows & Sharp 1999; Lodders & Fegley 2002). However, alkalis are not allowed to condense into feldspars, as Si atoms

tend to be sequestered in rained-out silicates; see Line et al. (2017) for a discussion. In this way, the choice of allowed condensates effectively mimics the process of rain-out for the alkalis. This treatment of rain-out in petitCODE was found to be sufficient, as there is only very small differences found between the spectra and P-T structure solutions of petitCODE and Exo-REM (Baudino et al. 2017), the latter of which includes rain-out.

The code begins with an initial guess of the TP structure, that can be either user-provided or calculated from the Guillot (2010) analytical solution. The code then uses a self-written Gibbs-minimizer (see Mollière et al. 2017), resulting in chemical equilibrium abundances, as well as the adiabatic temperature gradient of the gas mixture. This chemical composition is then used to compute the opacities at each pressure level. Finally, the code computes the temperature profile assuming radiative-convective equilibrium (both emission/absorption and scattering are taken into account, see paragraph below) and considers the new TP profile to iterate the procedure until convergence is reached. Finally, the code outputs emission and transmission spectra of the converged model at a resolution of $\lambda/\Delta\lambda = 1000$.

The temperature iteration method used in *petitCODE* is a variable Eddington factor method. For this, the radiation fields of planet and star are both solved over the full wavelength domain (110 nm to 250 μm), for rays along 40 different angles (20 up and 20 down) with respect to the atmospheric normal. The angles ϑ are chosen for carrying out a 20-point Gaussian quadrature over $\mu = \cos(\vartheta)$. For the radiative transfer solution the Feautrier method is used. Scattering can be naturally included in the Feautrier method, and the scattering source function in *petitCODE* is converged using both ALI (Olson et al. 1986) and Ng (Ng 1974) acceleration. In order to speed up calculations, scattering is assumed to be isotropic, but the scattering cross-sections are reduced by $(1 - g)$, where g is the scattering anisotropy factor. This ensures a correct scattering treatment in the diffusive limit (see, e.g., Wang & Wu 2012).

As reported in (Mollière et al. 2017), the scattering implementation was tested by comparing the atmospheric bond albedo as a function of the incidence angle of the

stellar light to the values predicted by Chandrasekhar's H functions (Chandrasekhar 1950). For this test the appropriate simplifying assumptions were made (like vertically constant opacities). Excellent agreement was found. Because both the planetary and stellar radiation field are solved within the same, full wavelength regime, and along 40 rays, the radiative transfer is superior when compared to the often-used two-stream method. No assumptions have to be made for the direction that radiation is propagating into, or the wavelength range that the stellar or planetary radiation field typically populate, as long as both are within 110 nm to 250 μm. The only sense in which *petitCODE* calculations may be considered as "two-stream" is the fact that they treat planet and stellar radiation independently. This in no way restricts the generality of the *petitCODE* solutions, however, as the radiative transfer equation is linear in nature.

petitCODE as described above, has been recently successfully benchmarked against the state-of-the-art *ATMO* (Tremblin et al. 2015) and *Exo-REM* (Baudino et al. 2015) codes, see Baudino et al. (2017). Recent applications of the code include Mollière et al. (2015); Mancini et al. (2016); Mollière et al. (2017); Southworth et al. (2017); Baudino et al. (2017); Samland et al. (2017); Tregloan-Reed et al. (2017); Müller et al. (2018), and Mollière & Snellen (2018).

2.1.2 Grid properties

For modeling irradiated exoplanets, the main parameters of interest are typically the effective temperature ($T_{\rm eff}$), surface gravity (log(g)), metallicity ([Fe/H]), carbon-to-oxygen-ratio (C/O) and stellar type; for a recent review see Fortney (2018). In addition to these parameters, some other factors might be of significance as well, such as interior temperature, atmospheric thickness, eddy and molecular diffusion, photochemistry and the presence of clouds. The effect of non-equilibrium chemistry and clouds will be presented in two follow-up chapters where we will also introduce our *Chemical Kinetic Model (ChemKM)* and our extensive self-consistent cloudy grid of models.

The chosen parameters and their ranges are discussed in the following subsections.

Effective temperature (T_{eff})

Unless a planet is highly inflated, young, or far from its host star, the flux contribution from the planetary interior has a minimal effect on the atmospheric TP profile (e.g. Mollière et al. 2015; Fortney 2018). This can be understood by a simple relation: $T_{eff}^4 = T_{eq}^4 + T_{int}^4$, where T_{eff}, T_{eq} and T_{int} are the effective, equilibrium and interior temperatures of the planet, respectively. In the limit of $T_{eff} \gg T_{int}$, the relation becomes $T_{eff}^4 \approx T_{eq}^4$, and hence the flux contribution from the interior can be neglected.

We set the interior temperature at 200 K to be consistent with the Fortney (2005) and Mollière et al. (2015) simulation setup so we can compare the effects of additional physics in the updated *petitCODE* (such as extra reactants as well as including multiple scattering). Therefore the lowest T_{eff} in our grid was selected to be 400 K to keep the effect of interior temperature on the energy budget at a minimum.

To take a computationally pragmatic approach, we only studied planetary structures and spectra under the assumption of isotropic incident flux (i.e. planetary average). However, very hot planets are expected to display inefficient redistribution of the insolation energy to the night side due to the domination of radiative cooling over advection (Perez-Becker & Showman 2013; Komacek & Showman 2016; Keating & Cowan 2018). For instance, Kepler-13Ab with $T_{eff} \sim 2750$ K (Shporer et al. 2014) and WASP-18b with $T_{eff} \sim 3100$ K (Nymeyer et al. 2011) are shown to have low energy redistribution efficiencies, resulting in their large day-night temperature contrasts. Therefore, we set the upper limit of T_{eff} at 2600 K, and investigate T_{eff} from 400 K to 2600 K with an increment of 200 K. This choice of temperature range also keep our parameter space away from the extremely irradiated hot Jupiters where the atmospheric chemistry is thought to be fundamentally different (Lothringer et al. 2018).

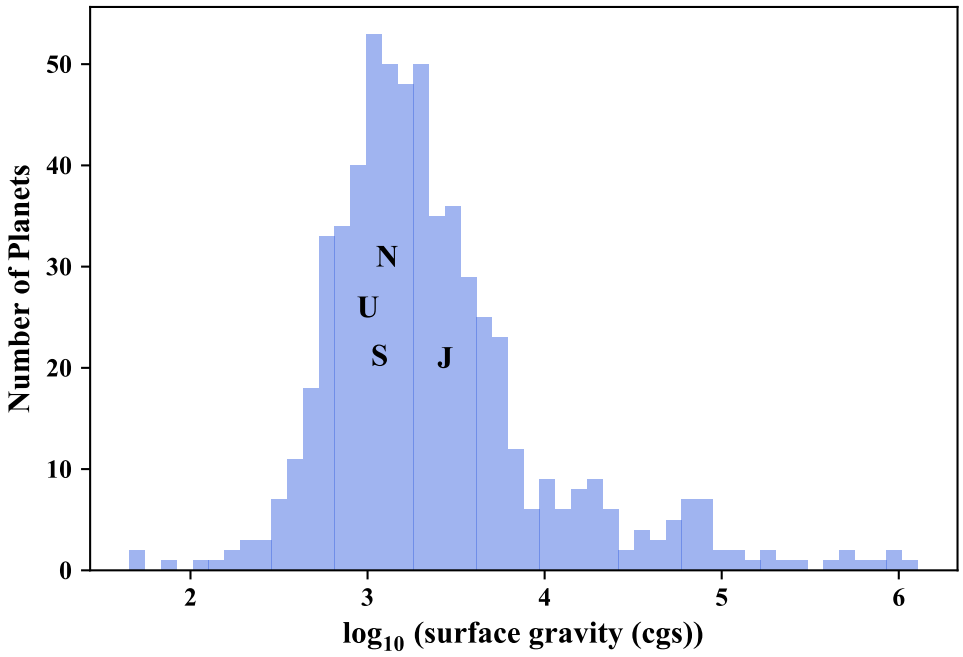

Figure 2.1: Distribution of log(g) for known exoplanets. Values are estimated based on the retrieved radius and mass values from the NASA exoplanet archive. Log(g)s of the solar system's gas-ice giants (J: Jupiter, S: Saturn, U: Uranus, and N: Neptune) are also shown for comparison.

Surface gravity (log(g))

In the solar system, radii of gas and ice giants are measured from the center up to an altitude where the pressure is 1 bar (see e.g. Simoes et al. 2012; Kerley 2013; Robinson & Catling 2014). For exoplanets we determine the radius by photometry and estimating where their atmospheres become optically thick. This radius is called the *photospheric radius*. Applying the photometric approach on the Solar System,s gas and ice giants does not provide us with the same values, but it is still a valid approach to estimate their radii. Discrepancies of the two methods however remain within a few percent.

Nevertheless, in most cases the mass or the radius of an exoplanet are not well constrained and one can use surface gravity as a combined quantity to explore the effect of these two quantities by one combined parameter (see e.g. Fortney 2018). In addition, the temperature structure calculations depend only on the

surface gravity and not the planetary radius and mass as two separated parameters. Therefore, the selection of surface gravity over radius and mass of the planet remains a plausible choice.

Figure 2.1 illustrates the distribution of log(g) based on radius and mass values retrieved from the *NASA exoplanet archive* [5]. Log(g) ranges from 1.5 to 6.1 with only a few objects at the extreme values. Note that high log(g) values are mostly associated with the objects having masses larger than $13M_{Jupiter}$ and hence, by definition (see e.g. Homeier et al. 2005), are Brown dwarfs. We thus explored this parameter from 2.0 to 5.0 with increment of 0.5.

Metallicity ([Fe/H])

The metallicities of solar system gaseous planets range from around 3 times to 100 times of solar metallicity. There is a trend of higher metallicity for lower-mass objects. Observations suggest that this trend holds true for exoplanets as well (Miller & Fortney 2011; Thorngren et al. 2016; Wakeford et al. 2017a; Sing 2018), but it should be kept in mind that this conclusion is only based on a few estimations with large uncertainties. Furthermore the metallicities of these different exoplanets have been estimated using different definitions and techniques, and thus it is difficult to make a fair comparison between them (Heng 2018).

Nevertheless, we chose to explore a wide range of metallicities from sub-solar, [Fe/H]=-1.0, to super-solar [Fe/H]=2.0 with increment of 0.5. [Fe/H] denotes the metallicity in log-scale where [Fe/H]=-1.0 represents an atmosphere with 10 times lower *metal* abundances than in the Sun; here *metal* refers to all elements except H and He.

Carbon-to-oxygen-ratio (C/O)

As briefly discussed in the introduction, varying C/O alters the TP structure as well as the abundance distribution of species in the atmosphere. The highest sensitivity of TP and chemical abundances to C/O variations is expected to occur around C/O$\sim$1 where the natural boundary between methane- and water-dominated atmospheres

[5] exoplanetarchive.ipac.caltech.edu

is predicted and reported. For this reason we selected irregular parameter steps spanning from 0.25 to 1.25 with smaller steps around unity: C/O=[0.25, 0.5, 0.7, 0.75, 0.80, 0.85, 0.90, 0.95, 1.0, 1.05, 1.10, 1.25]. Unlike the definition of metallicity, C/O represents the number ratio of carbon to oxygen elemental abundances and is not scaled to the solar value of ∼0.55.

In principle, there are three ways to alter C/O ratio: by changing the oxygen abundance but keeping the carbon abundance fixed, by changing the carbon abundance but keeping the oxygen abundance fixed, and changing both but keeping the total oxygen and carbon abundance constant. The compositional outcome of these scenarios can be quite different. Lodders (2010) discussed the first two scenarios and reported the different compositional outcome of these two cases. Changing the oxygen abundance (to alter C/O ratio) represents the accretion of gas or planetesimals with different water contents onto a forming planet. Similar to Madhusudhan (2012); Mollière et al. (2015) and Woitke et al. (2018), we also follow this school of thought.

Stellar type

Irradiated atmospheres are susceptible to their parent star,s spectral type. As the temperature of the host increases its spectral peak,s wavelength decreases toward the blue region of the spectrum, affecting the optically active parts of the planetary atmospheres. The effect of stellar spectral type on irradiated atmospheres has been investigated by a number of authors (see e.g. Miguel et al. 2014; Mollière et al. 2015; Fortney 2018). In this work we chose the same values for this parameter as in Mollière et al. (2015), i.e. M5, K5, G5 and F5, to cover a wide range of stellar types and make the models directly comparable with their grid of models.

Reactants and Opacity sources

We kept all *petitCODE*'s atomic species and reaction products (including TiO/VO) in our models except one reactant, $MgAl_2O_4$(c), due to the poor convergence of some of the models. We discuss this common problem in the forward models and our solution to it in Appendix 2.5. We considered these gas opacity species: H_2O, CO,

CO_2, OH (HITEMP, see Rothman et al. 2010), CH_4, HCN (ExoMol, see Tennyson & Yurchenko 2012), as well as H_2, H_2S, C_2H_2, NH_3, PH_3 (HITRAN, see Rothman et al. 2013), Na, K (VALD3, see Piskunov et al. 1995) and H_2-H_2 and H_2-He CIA Borysow et al. 1989; Borysow & Frommhold 1989; Richard et al. 2012), but no cloud opacity. We shall present and discuss the effects of TiO/VO and cloud opacities on planetary atmospheres in a follow-up chapter.

2.2 Results

Given our grid setup and parameters of choice, we calculated 28,224 forward self-consistent models of planetary atmospheres and their transmission and emission spectra. For calculating the transmission spectra we set the reference pressure 1 R_{jup} at 10 bar, following Fortney et al. (2010) prescription. In order to quantitatively discriminate spectral features and how they vary from one spectrum to another, we introduced a technique to decompose a spectrum to its individual opacity sources. This technique is discussed in the following section.

2.2.1 Spectral Decomposition Technique

Thermal emission at any given wavelength comes from a range of pressures, but the contribution of emission flux from each pressure level in the final emergent emission spectrum is not equal. A common practice is to define a *contribution function* and evaluate how sensitive the emission spectrum is to different pressure levels (see e.g. Selsis 2002; Swain et al. 2009a; Mollière 2017; Cowan & Fujii 2017; Dobbs-Dixon & Cowan 2017; Fortney 2018). Similarly, the contribution function can be calculated for the transmission spectra.

While this method combines information of all atmospheric constituents to provide the spectral contribution at each pressure, another approach could be taken to define a *contribution coefficient* for each species to approximate its contribution in the spectrum, integrated over all pressures. This would allow us to study the relative importance of individual species in a given spectrum and to investigate the dominant net chemical reactions at the photospheric levels of the planet that

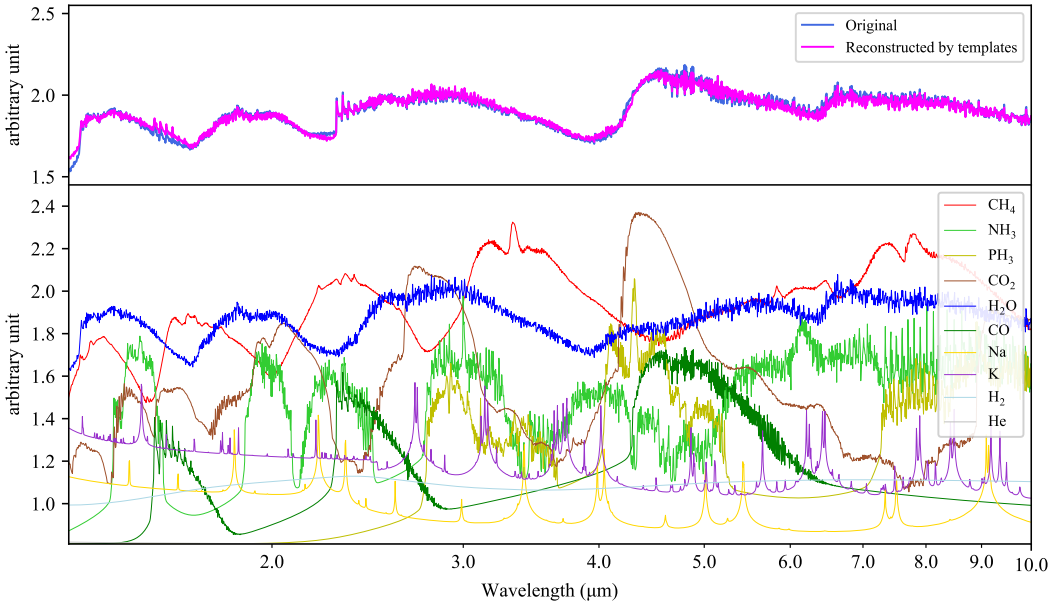

Figure 2.2: Reconstruction of a transmission spectrum by the *Spectral Decomposition Technique*. Top) Transmission spectrum of a planet with an effective temperature of 1600 K, log(g)=3.0, [Fe/H]=1.0, C/O=0.85 orbiting a central G5 star (blue) and its reconstruction by the Spectral Decomposition Technique (magenta). Bottom) The templates of major opacity sources in the reconstructed model.

cause those spectral signatures. We call this method the *Spectral Decomposition Technique* and develop it for the decomposition of transmission spectra.

This technique was motivated by the fact that opacities contribute logarithmically to the transmission spectra, and major atmospheric opacity sources (such as H_2O, CO_2, NH_3, CH_4, HCN, CO, C_2H_2) have distinct signatures in the range of optical to IR wavelengths:

$$z(\lambda) = H_p \log\left[\sum_i \kappa_i(\lambda)\right] + cst, \tag{2.2}$$

(Fortney 2005; Lecavelier des Etangs et al. 2008), where $z(\lambda)$ is the photometric radius at the wavelength λ, H_p is the atmospheric scale height and κ_i is the opacity of the i^{th} species above a reference pressure (or a reference radius, interchangeably). This technique has been employed before, but only graphically. For example, in a study of hot-Jupiters spectra by Rocchetto et al. (2016), they provided several synthetic transmission spectra along with the contributions of the major opacity

sources to illustrate how much they contribute to the spectrum qualitatively. For additional examples see Tinetti et al. (2010); Shabram et al. (2011); Encrenaz et al. (2015) and Kreidberg (2017).

The first step to decompose a spectrum to its individual opacity sources is to produce a template of every species, $\Gamma_i(\lambda)$. For a transmission spectrum, this can be achieved by assuming the template spectra to contain only a given species each; e.g. the water template has only H_2O in the atmosphere and the methane template has only CH_4 and so on. The TP profile in the templates can be adopted directly from the self-consistently calculated TP structure of each model. However, if the decomposition is intended for an extensive number of transmission spectra, a reasonable approximation would be to employ an isothermal TP and calculate the templates only once. Here we followed the latter and set the temperature at 1600 K for the calculation of templates. It is then possible to estimate the contribution coefficient of each opacity source, c_i, using Equation 2.3.

$$\mathcal{S}(\lambda) = \left(\sum_i c_i \Gamma_i^p(\lambda) \right)^{\frac{1}{p}}, \tag{2.3}$$

where $\Gamma_i(\lambda)$ is the spectral template of the i^{th} species, p is an arbitrary exponent that can be adjusted to achieve the best result over a wide range of parameter space (here we chose it to be 10; higher values make stronger spectral features more pronounced), and $\mathcal{S}$ is the total spectrum.

After creating a spectral template for each opacity source, as shown for example in Figure 2.2, bottom panel, we can raise the templates to the p^{th} power, multiply them by some coefficients, add them up and then take the p^{th} root of the summed spectrum to calculate the total spectrum, $\mathcal{S}$. We explored different combinations to find the best linear combination of the templates that could represent the spectrum, Figure 2.2, top panel. The coefficients of this best linear combination are the *contribution coefficient* of species.

To perform the decomposition, a wavelength range should be chosen. Using wider wavelength ranges generally results in a more accurate estimation of contribution coefficients; However, depending on the species of interest not all wavelengths

have the same information content. In the current study, the aim is to estimate the transition C/O ratios by the use of H_2O and CH_4 contribution coefficients. Therefore a choice of 1.3-10 μm sufficiently provides the spectral information content needed for the spectral decomposition to achieve the same results as a choice of 0.4-20 μm, the latter of which is the wavelength span of our synthetic spectra.

While not the focus of our current study, one could similarly perform the spectral decomposition on a cloudy transmission spectrum. Since clouds and hazes may obscure or mute spectral features, it is therefore important to introduce a template for the cloud/haze species to estimate the contribution coefficients. This will be discussed in a forthcoming work describing the decomposition of our self-consistent cloudy grid.

The illustrated example in Figure 2.2 presents a case with an effective temperature of 1600 K, log(g)=3.0, [Fe/H]=1.0, C/O=0.85 and G5 to be the host star's spectral type. The transmission spectrum (blue curve in the top panel) shows clear signatures of both H_2O and CO molecules between 1-4 μm. Small excess absorption at longer wavelengths, and particularly at $\sim$4.2 μm, might hint the presence of CO_2, but CH_4 has almost no contribution in the spectrum. By using the spectral decomposition technique the contribution coefficients of H_2O, CH_4, CO and CO_2 were found to be 0.88, 0.03, 1.25 and 0.08, respectively, consistent with our visual interpretation of the spectrum.

The ratio of contribution coefficients provides a quantitative estimation of spectral contrast for different species as a measure of species' relative detectability. For instance as c_{CH_4}/c_{H_2O} increases, methane features become more pronounced in the spectrum with respect to the water features and hence the probability of CH_4 detection increases. This ratio can then be used to determine the dominance of observable atmosphere by water or methane. In the next section we show how to apply this method on the models with different C/O ratios in order to estimate the *transition* C/O ratios.

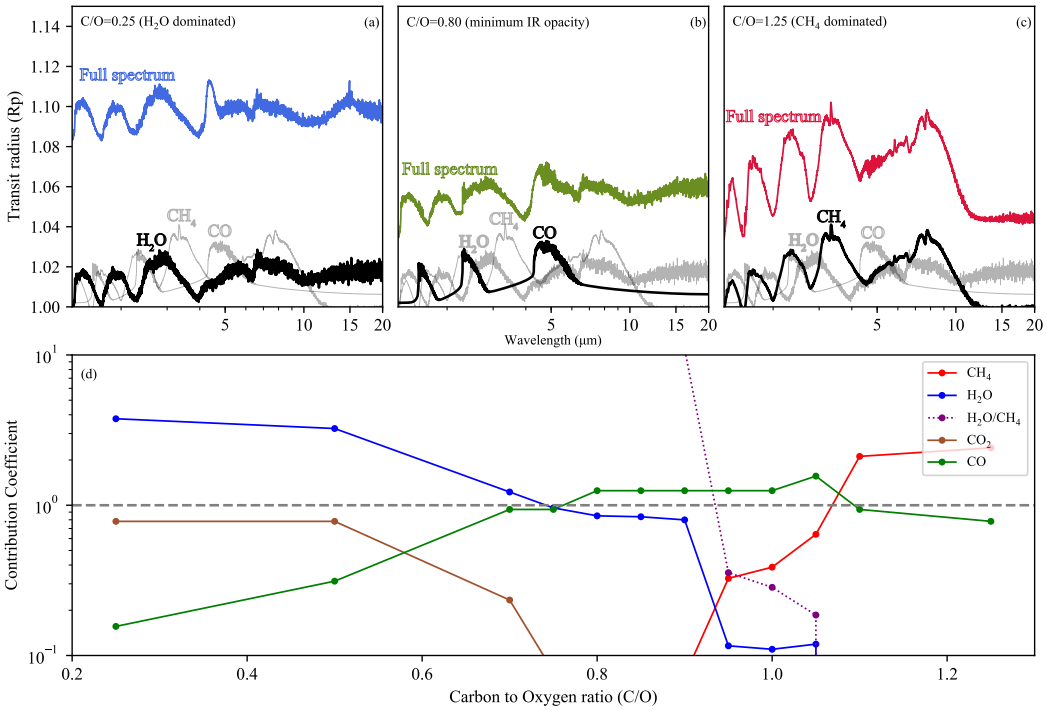

Figure 2.3: Top panels) Transition of water- to methane-dominated transmission spectrum for a planet with T_{eff}=1600 K, log(g)=3.00, [Fe/H]=1.00 orbiting an G5 star. (a) At low C/O ratio, H_2O dominates the spectrum (blue). (b) Higher C/O ratio decreases H_2O abundances and hence the transit radius decreases (green). (c) By increasing C/O ratio CH_4 abundance increases and hence contributes more in the spectrum and the transit radius increases (red). Black and gray lines represent H_2O, CO, and CH_4 templates with an arbitrary offset to graphically illustrate which of them have a higher contribution into the spectrum (black). Bottom) Variation of contribution coefficients of H_2O, CH_4, CO_2 and CO at different C/O ratios. As the ratio of H_2O to CH_4 contribution coefficient (dotted purple line) passes the unity (gray horizontal dashed line), the spectrum transitions from water- to methane-dominated one; resulting in a quantitative estimation of $(C/O)_{tr}$.

2.2.2 Estimation of transition C/O ratios

Following our previous example of a planet with an effective temperature of 1600 K, log(g)=3.0, [Fe/H]=1.0 and a central G5 star, we explore a variety of C/O ratios and estimate the contribution coefficients of major opacity species. At C/O=0.25 the H_2O, CH_4, CO and CO_2 contribution coefficients are equal to 3.8, 0.0, 0.14 and 0.79 respectively: a clear indication of a water-dominated spectrum and no trace of CH_4, see Figure 2.3a. At C/O=0.5, these coefficients change to 3.2, 0.0, 0.31 and 0.79, suggesting more CO and less H_2O spectral contributions. The trend continues at C/O=0.7 with 1.23, 0.0, 0.93 and 0.23 values for the coefficients.

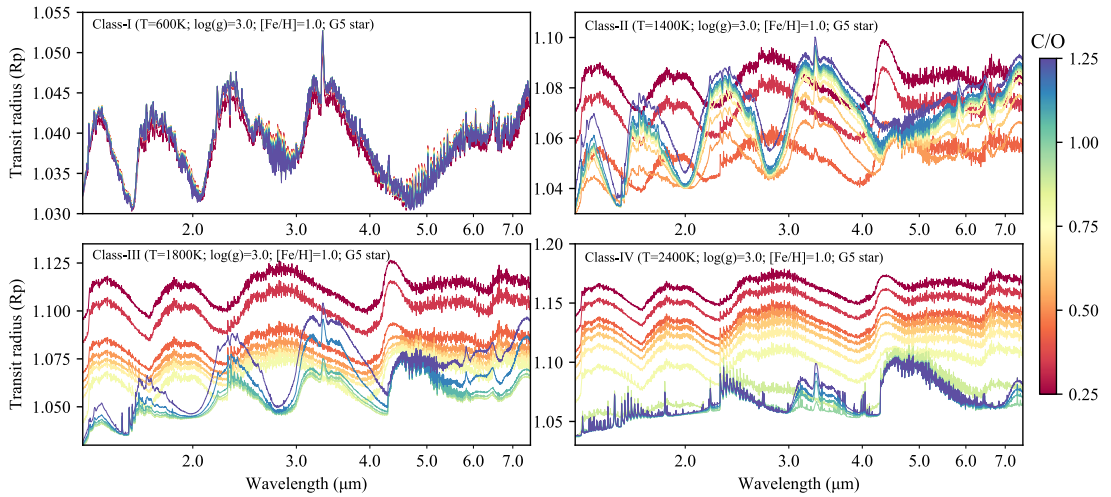

Figure 2.4: Examples of spectral variation in four planetary *Classes* as C/O increases from 0.25 (blue) to 1.25 (red), with the steps described in Section 2.1.2. In *Class-I* (upper left), higher C/O ratios result in slightly more CH_4 abundant atmospheres but water features are also remain noticeable. More CH_4 also cause the planets to appear larger and a transition from H_2O- to CH_4- dominated spectrum does not coincide with a minimum IR opacity condition as it is the case for the *Class-II* (upper right). In *Class-II* and *Class-III* (lower left) the transition occurs at the minimum IR opacity, where the planet appears to be smaller relative to other similar cases but with different C/O ratio. In *Class-IV* (lower right), a higher C/O results in a smaller radius for planets since larger C/O ratio leads to a stronger removal of water from the atmosphere, but the condition is in favor of CH_4 destruction and hence there is no significant opacity sources in IR to make the planet larger.

In all of these models, CO_2 closely follows the water features' diminishing trend, i.e. CO_2,s contribution coefficient is strongly correlated with H_2O,s contribution coefficient; brown and blue curves in Figure 2.3d respectively, implying they are both part of the same net chemical reaction.

CH_4 begins to contribute at C/O=0.90 by $c_{CH_4} = 0.02$, see Figure 2.3b, and at C/O=0.95 its contribution surpasses water,s; leading to a methane dominated spectrum. A linear interpolation suggests the transition occurs at $(C/O)_{tr}$=0.96 where $c_{CH_4}/c_{H_2O} = 1$; consistent with the value reported by Mollière et al. (2015) for the planets with $T_{eff} \geq 1750$ K. At this transition C/O ratio, both water and methane opacities contribute very little to the spectrum and carbon monoxide has the highest contribution, see the green curve in Figure 2.3d. CO is not a significant IR opacity source compared to H_2O and CH_4 and therefore diminished contributions of H_2O and CH_4 result in a minimum atmospheric IR opacity such that an inversion

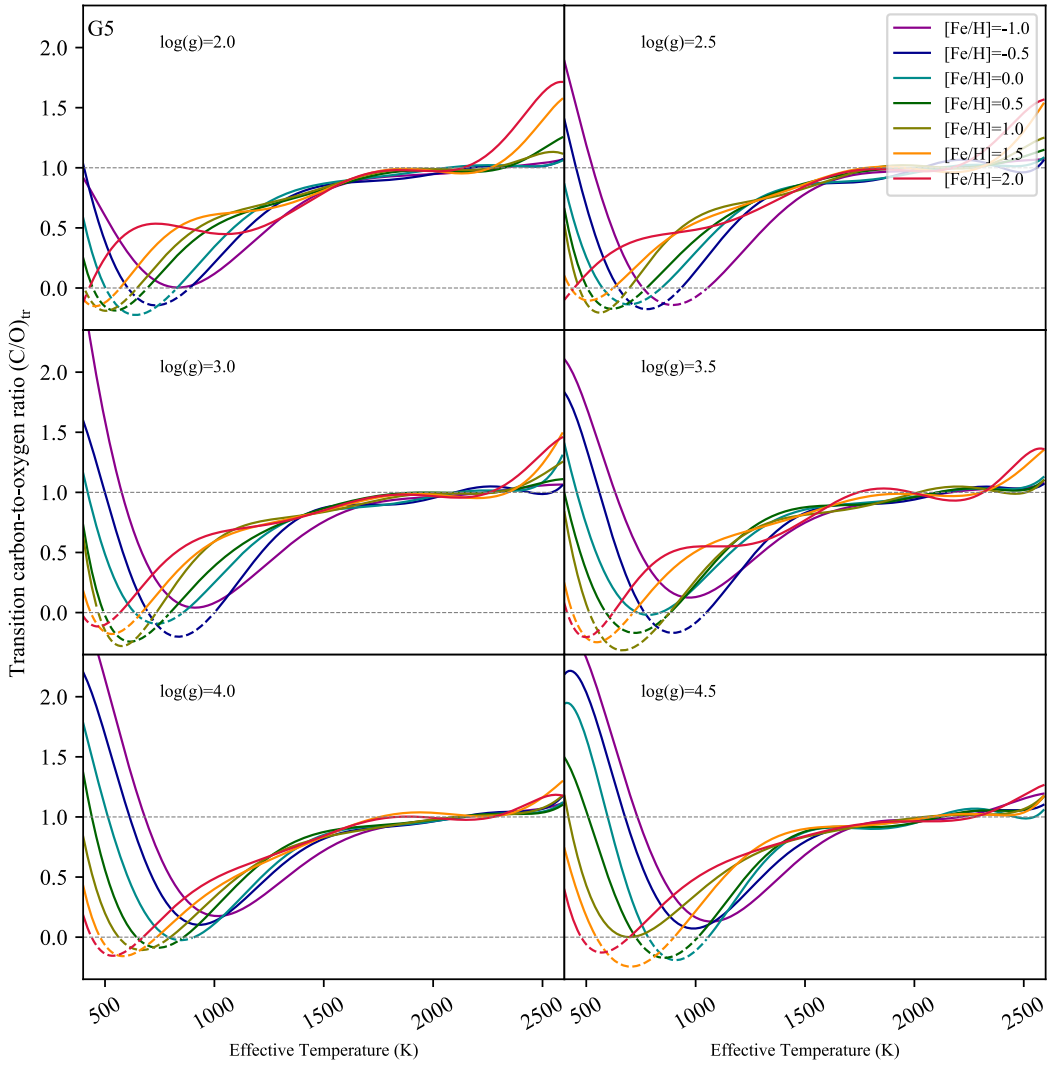

Figure 2.5: Transition carbon-to-oxygen ratios, $(C/O)_{tr}$, for planets around a G5 star. $(C/O)_{tr}$ marks the condition where the atmospheric spectrum transits from water- (regions under the transition lines) to methane-dominated features (regions above the transition lines). Sub-panels show the values at different surface gravities, log(g). $(C/O)_{tr}$ values below 0.25 and above 1.25 are outside of our parameter range and are linearly extrapolated from the neighboring points. $(C/O)_{tr} \leq 0$ means for that particular log(g) and [Fe/H] the spectrum is predicted to be always methane-dominated regardless of C/O ratio, assuming equilibrium chemistry (colored dashed curves below C/O=0).

is expected to form for hot planets with host stars of type K and earlier (Mollière et al. 2015). Equilibrium chemistry maintains methane,s spectral dominance at all higher C/O ratios for the case that we studied here, Figure 2.3c,d.

Decomposing the spectra for a similar case but with lower metallicity [Fe/H]=-1.0 results in a lower transition C/O ratio of 0.83 relative to the case of [Fe/H]=1.0. This can be understood by considering Equation 2.4 for relatively hot planets, (Mollière et al. 2015):

$$\frac{d\gamma}{d[Fe/H]} > 0, \tag{2.4}$$

where $\gamma = \kappa_{\rm vis}/\kappa_{\rm IR}$ and $\kappa_{\rm vis}$ and $\kappa_{\rm IR}$ are the mean opacities in the visual and IR wavelengths in the atmosphere, respectively. Therefore, the cooling efficiency of the atmosphere is expected to increase as [Fe/H] decreases. A colder environment, in turn, is in favor of more CH_4 production and thus the transition occurs at lower C/O ratios in this case.

The spectral dominance of methane features over water features does not mean a complete lack of water features in the spectrum, but rather it is the relative strength of methane features in comparison to the water features. For instance, exploring somewhat colder planets ($T_{\rm eff} \lesssim 1000$ K) reveals that both water and methane features are present in the spectra, see e.g. $T_{\rm eff}$=600 case in Figure 2.4.

Calculating the transition C/O ratios for all 28,224 models reveals similar trends to the predicted trends by Mollière et al. (2015). As an example, Figure 2.5 shows calculated transition C/O ratios for planets around a G5 star. Although, the general trend remains similar to the prediction by Mollière et al. (2015), the details of the trends differ for different log(g) and [Fe/H] values. We extrapolated the transition C/O ratios when they occurred outside of our C/O parameter range, i.e. C/O<0.25 or C/O>1.25. Because of this, it is possible to also numerically find $(C/O)_{\rm tr} < 0$. These negative $(C/O)_{\rm tr}$ values indicate the parameter space where the spectrum is expected to be always methane-dominated and has no other physical interpretation; colored dashed curves below C/O=0 in Figure 2.5 show these regions. Negative ratios notwithstanding, we draw the extrapolated trends to aid the eye since the

location of minimum $(C/O)_{tr}$ in this temperature range is key to separate the first two atmospheric classes as will be discussed in the next section.

2.3 Discussion

2.3.1 Four classes of atmospheric spectra

Trends of $(C/O)_{tr}$ values at different temperatures suggest four classes of distinct chemically driven planetary spectra in a cloud-free context. Hence we propose a spectral classification scheme of irradiated planets based on these classes as a preparatory step to comprehend an observationally driven classification scheme with additional physics. Follow-up studies are needed to confirm and refine this classification framework.

The first class contains cold planets with T_{eff} lower than ∼600-1100 K. Their $(C/O)_{tr}$ ratios have a quasi-linear relation with the effective temperature, i.e. for a given metallicity and surface gravity, $(C/O)_{tr}$ linearly decreases as temperature increases. This can be traced back to the dominant net reactions in this temperature range (Pirie 1958; Atreya et al. 1989):

$$CO + 3\,H_2 \longrightarrow H_2O + CH_4 \tag{2.5}$$

$$CO + H_2O \longrightarrow CO_2 + H_2 \tag{2.6}$$

where oxygen and carbon atoms are mostly bond in water and methane molecules, but CO_2 can lock up a fraction of oxygen atoms, too. Since Reaction 2.5 is strongly pressure sensitive, the chemical equilibrium abundances are thus highly temperature and pressure dependent. Consequently $(C/O)_{tr}$ ratios are expected to change significantly, depending on the metallicity and surface gravity of the planet. This can be noticed in the diversity of $(C/O)_{tr}$ values at low temperatures. We stress again that both CH_4 and H_2O features are expected to be present in the spectra of these planets since the overall temperature-pressure at the photospheric level of this class favors production of both CH_4 and H_2O, see *Class-I* in Figure 2.4. In reality, however, non-equilibrium chemistry and cloud formation are expected to

obscure or mute some of the spectral features in the spectra of this class (see e.g. Sing et al. (2016)). Since photosphere of planets with higher metallicity and lower surface gravity extends to lower pressures, the spectra of this kind of class-I planets are expected to be quite vulnerable to the non-equilibrium chemistry and presence of clouds. We will examine this prediction in the forthcoming chapters.

The second class contains intermediate-temperature planets, i.e. T_{eff} higher than *Class-I* but lower than ∼1800 K. For this class, $(C/O)_{tr}$ highly depends on the surface gravity and metallicity, see Figures 2.5 and 2.6. The main net reaction is similar to the dominant chemical reaction in *Class-I* but toward the other direction due to higher temperatures. Therefore:

$$H_2O + CH_4 \longrightarrow CO + 3\,H_2 \tag{2.7}$$

where the condition is in favor of CO production. Due to the presence of oxygen-containing condensates in this temperature range, the transition of water-to-methane-dominated-spectra depends on how much condensates are evaporated, which in turn depends on the metallicity and log(g) of the planet. Theoretical predictions (see e.g. Ackerman & Marley (2001); Fortney (2005); Helling (2008); Moses et al. (2011); Heng & Demory (2013); Venot & Agúndez (2015); Wakeford & Sing (2015); Drummond et al. (2016); Kempton et al. (2017)) and observations (see e.g. Madhusudhan & Seager (2011); Knutson et al. (2012); Sing et al. (2016)) suggest that non-equilibrium chemistry and clouds could be present even in hotter exoplanets, although less likely comparing with class-I (Wakeford & Sing 2015; Stevenson 2016; Wakeford et al. 2017c). These can also potentially alter the oxygen and carbon abundances in this class, and as a result, the dominant chemistry at the photospheric levels and therefore the spectra can change as well. We will briefly discuss the observational evidence in the next section.

As the effective temperatures of the planets increase, condensates are completely evaporated. The net Reaction 2.7 still dominates the chemical equilibrium but the lack of silicates and other oxygen carrier condensates from the spectrally active regions of the atmosphere at these temperatures, T_{eff}>1800 K, forces the transition

to be almost independent of log(g) and [Fe/H] (Mollière et al. 2015). Therefore, $(C/O)_{tr}$ remains at around a constant value, see Figure 2.5 and Figure 2.6, and *Class-III* of planets emerges. Although the presence of clouds is expected to be less probable for this class, due to the lack of condensates, the importance of dynamics and cooling mechanisms on the nightside of these planets can not be neglected. Therefore, clouds and out-of-chemical-equilibrium atmospheric constituents can be transported to the dawn terminator from the nightside and alter the transmission spectrum, but the dayside emission spectrum is likely to remain unaffected.

At even higher temperatures, i.e. *Class-IV* with T_{eff}>2200 K, HCN dominates the atmosphere as the main carbon-bearing compound through three possible net reactions, also see Mollière et al. (2015):

$$CH_4 + NH_3 \longrightarrow HCN + 3\,H_2 \tag{2.8}$$

$$2\,CH_4 + N_2 \longrightarrow 2\,HCN + 3\,H_2 \tag{2.9}$$

$$NH_3 + CO \longrightarrow H_2O + HCN \tag{2.10}$$

Bimolecular reaction rates of Reaction 2.8 increase by one order of magnitude from 700 to 1400 K, at around one millibar (Hasenberg & Schmidt 1987) and the condition at high temperatures progresses in favor of CH_4 and NH_3 destruction as well as HCN production. This results in the reappearance of the $(C/O)_{tr}$ dependency on log(g) and [Fe/H] and a mild increase in $(C/O)_{tr}$ at higher temperatures that will be discussed in the following section.

Altogether, four spectral classes can be defined based on their dominant chemical reactions and major IR spectral characteristics within the parameter space of this study. Figure 2.4 shows some example spectra in each *Class* where the dominant spectral features change as C/O ratios increase from 0.25 to 1.25 (blue to red colors in the Figure).

Three out of four classes, i.e. first, second and fourth classes, show dependency of the transition $(C/O)_{tr}$ ratios on log(g) and [Fe/H] which is discussed in the next section.

2.3.2 Effect of log(g) and [Fe/H]

At any given temperature of the first class, increasing the metallicity decreases $(C/O)_{tr}$ ratio, see Figures 2.5 and 2.6. This can be understood by considering the net Reactions 2.5 and 2.6. By combining those two reactions we arrive at a new net reaction:

$$CO_2 + 4\,H_2 \rightleftharpoons 2\,H_2O + CH_4 \tag{2.11}$$

The net Reaction 2.11 establishes a one-to-one relation between H_2O and CO_2 where it favors CO_2 production at high pressure and high metallicity conditions. As metallicity increases, oxygen can be locked up in CO_2 more readily in comparison to CO (see e.g. Heng & Lyons 2016). This enhances the reduction of water abundance at the photosphere and results in a decreased $(C/O)_{tr}$ ratio.

Likewise, decreasing the surface gravity decreases the $(C/O)_{tr}$ ratio. A simple relation between the optical depth (τ) and pressure (P) of a planetary atmosphere is established, assuming a gray opacity:

$$\tau = \kappa/gP, \tag{2.12}$$

where κ is the gray opacity and g is the gravitational acceleration. Therefore decreasing the surface gravity is expected to mimic the effects of increasing metallicity (which is logarithmically related to the opacity) on the optical depth, up to some degree. It is more convenient to combine the metallicity and log(g) parameters with a linear relation and introduce a modified β-factor (Mollière et al. 2015) as follow:

$$\beta = \log(g) - c_\beta[Fe/H], \tag{2.13}$$

where c_β is a constant and represents relative importance of log(g) over metallicity (for a detailed description of the β-factor see appendix 2.6). Hence a decreasing β-factor lowers $(C/O)_{tr}$ ratio for *Class-I* planets. Figure 2.6 illustrates the calculated $(C/O)_{tr}$ ratios for all models and the described trend is evident for the cold planets.

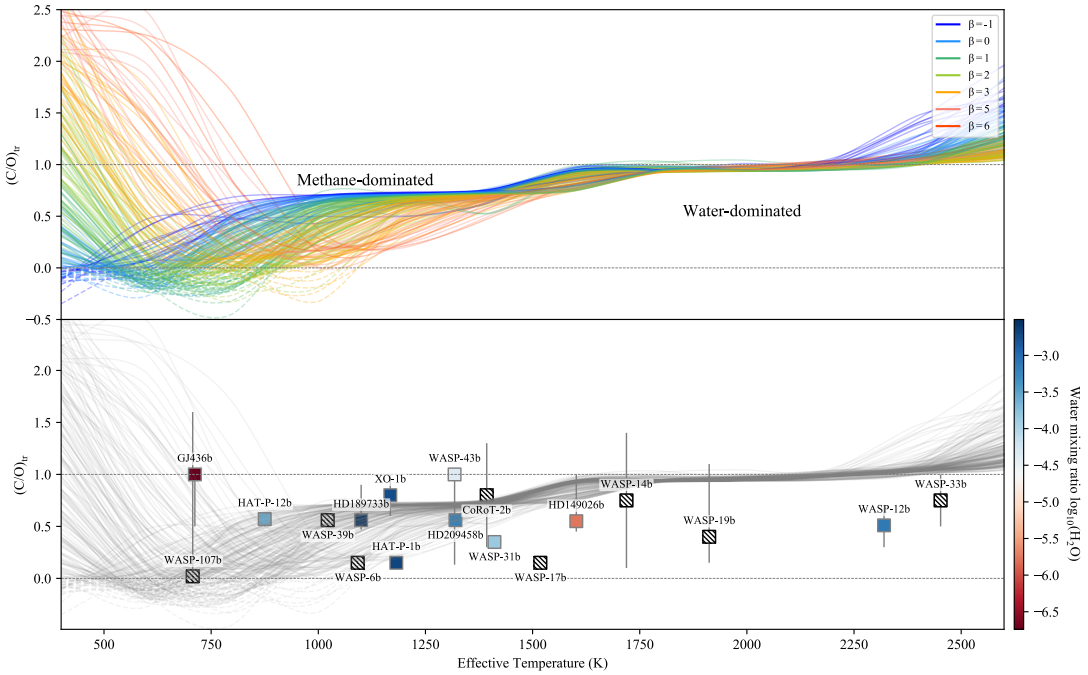

Figure 2.6: Top) Mapping all water-to-methane transition curves reveals a region between 800 and 1500 K with C/O>0.7 (*the Methane Valley*) where methane spectral features are always the dominant features in the planetary spectra, given the assumptions used in this study. Exploring this region could enhance the probability of methane detection. The lack of such detection could alternatively provide a suitable road-map to study out of thermochemical, out of radiative-convective hydrostatic equilibrium, or the effect of clouds on the presence of water/methane abundances in planetary atmospheres. Bottom) Estimated C/O ratios for several planets tentatively suggest departure from cloud-free equilibrium chemistry conditions since the observed planets within or close to this region (i.e. WASP-43b, XO-1b, HD 189733b, and HAT-p-12b) all contain significant water abundances in their photosphere Tsiaras et al. (2018). More precise C/O measurements are needed to observationally constrain the Methane Valley properties.

The $(C/O)_{tr}$ ratios for *Class-II* planets (with intermediate temperatures), however, demonstrate a completely different trend with respect to the *Class-I*, where $(C/O)_{tr}$ ratios increase with higher metallicity and lower log(g), i.e. lower β-factor, at any given temperature. As briefly discussed, this is mainly due to the presence of oxygen-bearing condensates. Higher [Fe/H] and lower log(g) pull the photosphere toward lower pressures while keeping the corresponding temperatures at the photospheric level almost the same. This lower pressure environment enhances the partial evaporation of the condensates, such as $MgSiO_3$(c), $MgSiO_3$(L), Mg_2SiO_4(c), Mg_2SiO_4(L), Fe_2O_3(c) and Fe_2SiO_4(c), which results in a decreased

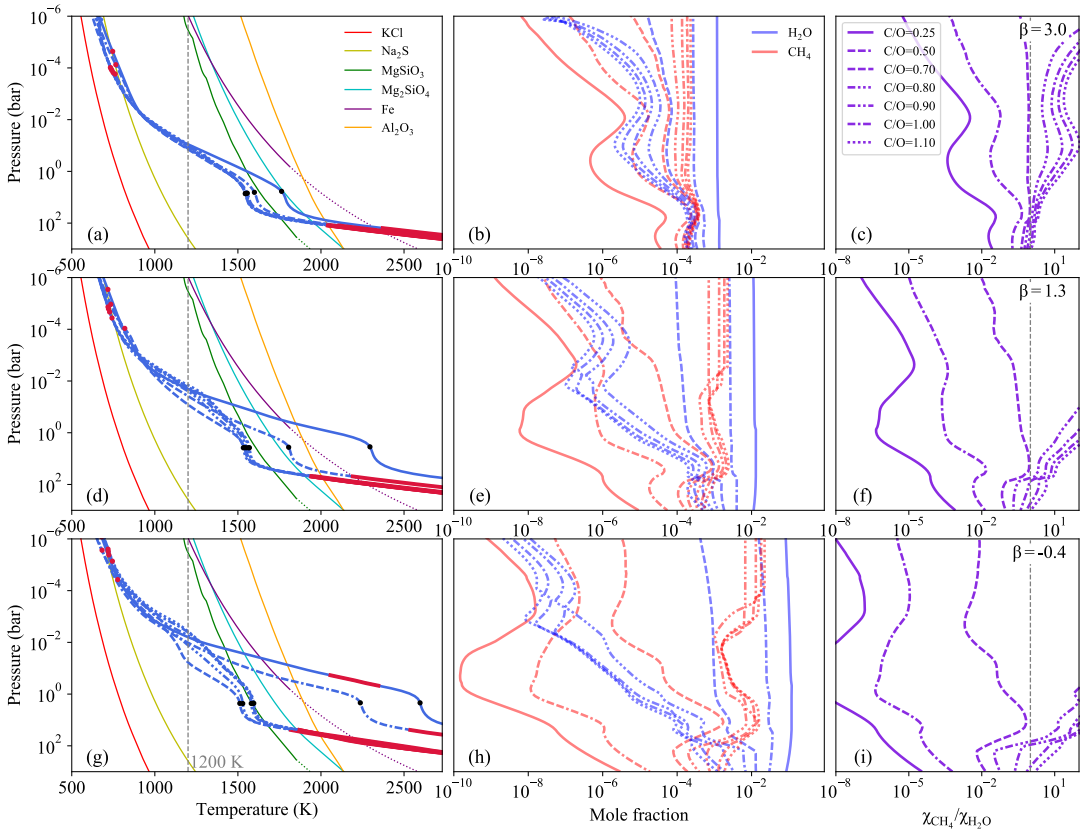

Figure 2.7: Decreasing the β-factor increases the transition C/O ratio of Class-II planets. (a) TP structures for a planet with T_{eff}=1200 K (gray dashed line), log(g)=3.00, [Fe/H]=0.00 (β=3.0) orbiting an F5 star at different C/O ratios (blue lines); shaded red lines are convective regions; red and black dots represent 0.1% and 99% absorption levels of stellar flux respectively, i.e. the approximate location of the photosphere; Condensation curves are shown for solar metallicity. (b) H_2O and CH_4 mole fractions at different C/O ratios. (c) CH_4 to H_2O mole fraction ratios at different C/O ratios; a mole fraction ratio of unity (gray dashed line) at photospheric levels roughly coincides with the transition C/O ratio. The mole fraction ratios for C/O=0.7 model is about unity which suggests the transition C/O ratio should be close to this value. (d, e, f) Similar to (a, b, c) but with [Fe/H]=1.00 (β=1.3). (f) CH_4 to H_2O mole fraction ratios decreased which hint at a higher transition C/O ratio compared with (c). (g, h, i) Similar to (a, b, c) but with [Fe/H]=2.00 (β=-0.4). (i) Mole fraction ratios continue to decrease and so do their associated transition C/O ratios.

CH_4 but increased H_2O abundances at the photospheric levels. Therefore the transition to a methane-dominated spectra happens at higher C/O ratios, see Figure 2.7. The effect of cloud opacity and non-equilibrium chemistry on this trend yet remain to be investigated.

It is noticeable that this trend is more monotonic at the lower log(g)s rather than high log(g)s due to more isothermal-like TP structures under lower surface gravities.

As a less variant TP structure, i.e. more isothermal, crosses the condensation curves, the partial evaporation of condensates changes monotonically. In the case of higher log(g)s the deep atmosphere is cooler and condensate evaporation is more susceptible to the exact shape of the temperature profile and condensation curves.

The mentioned role of CO_2 formation in *Class-I* and partial evaporation of condensates in *Class-II* are not Class-specific and both mechanisms are in action at the boundary of these two Classes and hence influence the spectral appearance. Moreover, the temperature at which this boundary occurs, i.e. the $(C/O)_{tr}$ minima in Figures 2.5 and 2.6, depends on the β-factor with the *Class-I*-to-*Class-II* transition happening at hotter planets for higher β-factors, see Figure 2.8.

In *Class-III*, $(C/O)_{tr}$ ratios show no substantial dependency on metallicity and surface gravity, but at higher temperatures, i.e. *Class-IV*, HCN captures most of the carbon atoms in the upper atmosphere and imposes a significant depletion of remaining CH_4 at high temperatures. However, this CH_4 depletion increases the transition carbon-to-oxygen values only slightly. As the photosphere rises to lower pressure at higher metallicities, water and methane abundances and the TP structure are also consistently moved to the lower pressures, and thus the contributions of water and methane features in the spectra remains alike.

At T>2500 K H_2O also starts to dissociate at low-pressure levels and in turn makes the oxygen atoms available to other stable molecules under these conditions. This mostly occurs at high metallicities and low C/O ratios and appears in the spectra when log(g) is adequately high. Altogether we should expect a mixed dependency of the transition on log(g) and metallicity in *Class-IV*. Table 2.1 provides a summary of $(C/O)_{tr}$ dependency on the model parameters.

2.3.3 Impact of stellar type

In addition to the surface gravity and metallicity of the planets, the spectral type of their host star also affects the $(C/O)_{tr}$ ratios and hence the boundary of different classes.

Temperature (K) (Classes)	Influencing parameter	$(C/O)_{tr}$	Dominant cause of dependency
< 600-1100 K	Lower log(g)	Decreases	Formation of CO_2
(Class-I)	Higher [Fe/H]	Decreases	at photosphere
600-1100 to ∼1650 k	Lower log(g)	Increases	Evaporation of condensates
(Class-II)	Higher [Fe/H]	Increases	at photosphere
∼1650 to ∼2200 K	Lower log(g)	Almost invariant	Lack of
(Class-III)	Higher [Fe/H]	Almost invariant	condensates
>∼2200 K	Lower log(g)	Increases	Lifting up the photosphere to lower pressure and dominance of HCN;
(Class-IV)	Higher [Fe/H]	Almost invariant	Water dissociation at lower pressures

Table 2.1: A summary table on the effect of log(g) and FEH

We found the boundary of *Class-I* and *Class-II* planets by locating the minimum $(C/O)_{tr}$, for *Class-II* to *Class-III* by setting $(C/O)_{tr}$= 0.9 and likewise for *Class-III* to *Class-IV* by estimating the temperatures at which $(C/O)_{tr}$= 1.0. We then estimated the β-factor by minimizing the scatter (see appendix 2.6) and separate the boundaries according to their stellar types. We found c_β∼1.7 which is an indication of metallicity to be more influential than surface gravity for the classification. Figure 2.8 maps the boundaries of these four classes through a β-T_{eff} diagram.

The boundary between *Class-I* and *Class-II* is influenced by the stellar spectral type with the earlier types moving the boundary toward hotter planets. The effect is less pronounced at the lower β-factors which results in a cut-off temperature at around 550 K where all spectral types appear to have similar transition temperature from *Class-I* to *Class-II* and no dependency to the stellar spectral type. The temperature at which the transition occurs can be estimated by Equation 2.14.

$$T_{ClassI-ClassII} = \left(\sum_{i=0,2} a_i(T_s)\beta^i \right) \tag{2.14}$$

where $a_0 = 535 + 0.005T_s$, $a_1 = -84 + 0.002T_s$, $a_2 = 20 - 0.003T_s$, T_s is the host star's temperature in Kelvin and β can be calculated through Equation 2.13 by

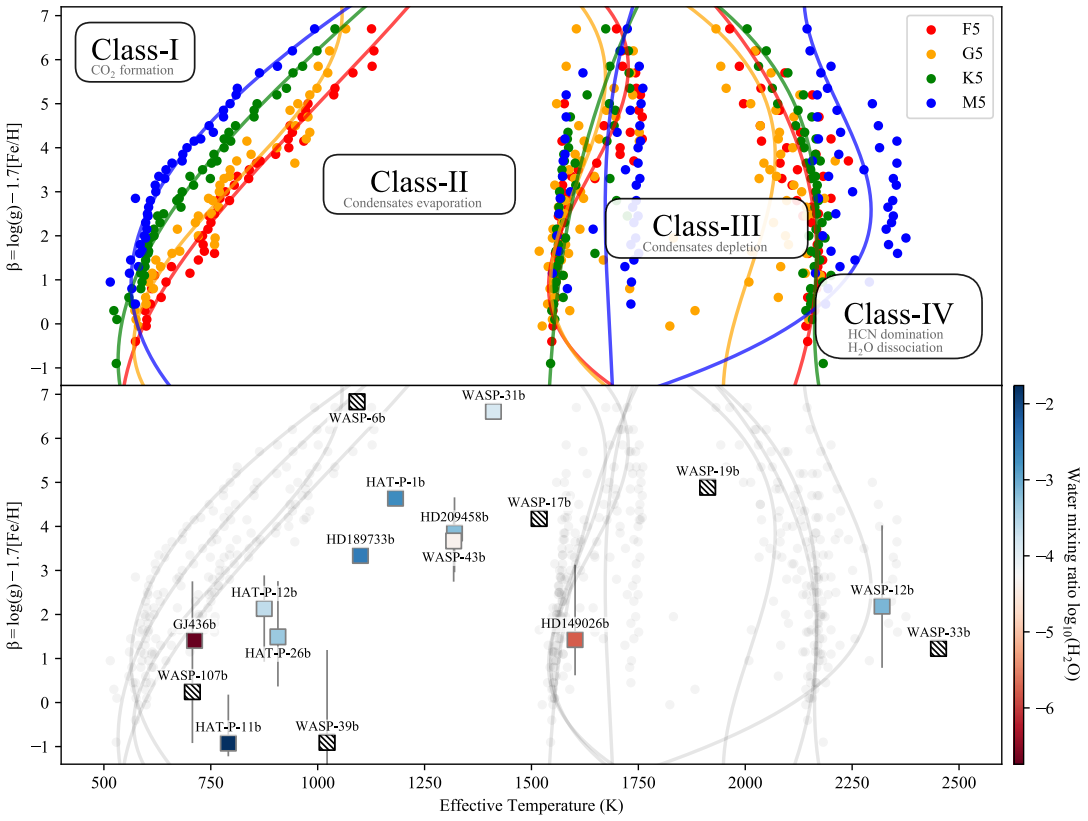

Figure 2.8: Top) β-T_{eff} diagram: Mapping the effect of stellar type in four atmospheric classes. Bottom) the position of observed exoplanets with estimated metallicity and β-factor. Observational points are color-coded by the retrieved water abundances from Tsiaras et al. (2018). Planets without estimation of their water content are shown by hatches. The dominant chemical mechanism at the photospheric levels of the irradiated planets vary with their effective temperature, and hence influences their spectral appearance. Note that there has been no estimation of metallicity and β-factor for Class-I planets, likely due to the presence of clouds and muted spectral features, e.g. GJ 1214b's flat transmission spectra (Berta et al. 2012; Kreidberg et al. 2014a).

setting c_β=1.7. At any given β-factor hotter host stars make the boundary occur at hotter planets, mostly due to their ability to heat the atmosphere of *Class-I* planets more efficiently than the late types. This leads to decreasing CH_4 and increasing H_2O abundances which leads to higher transition C/O ratios at the photospheric levels. Interestingly, the transition C/O ratios are more sensitive to the β-factor than to the stellar type, as demonstrated in Figure 2.9. Higher $(C/O)_{tr}$ values for earlier types results in pushing the *Class-I*/*Class-II* transition to higher planetary effective temperatures.

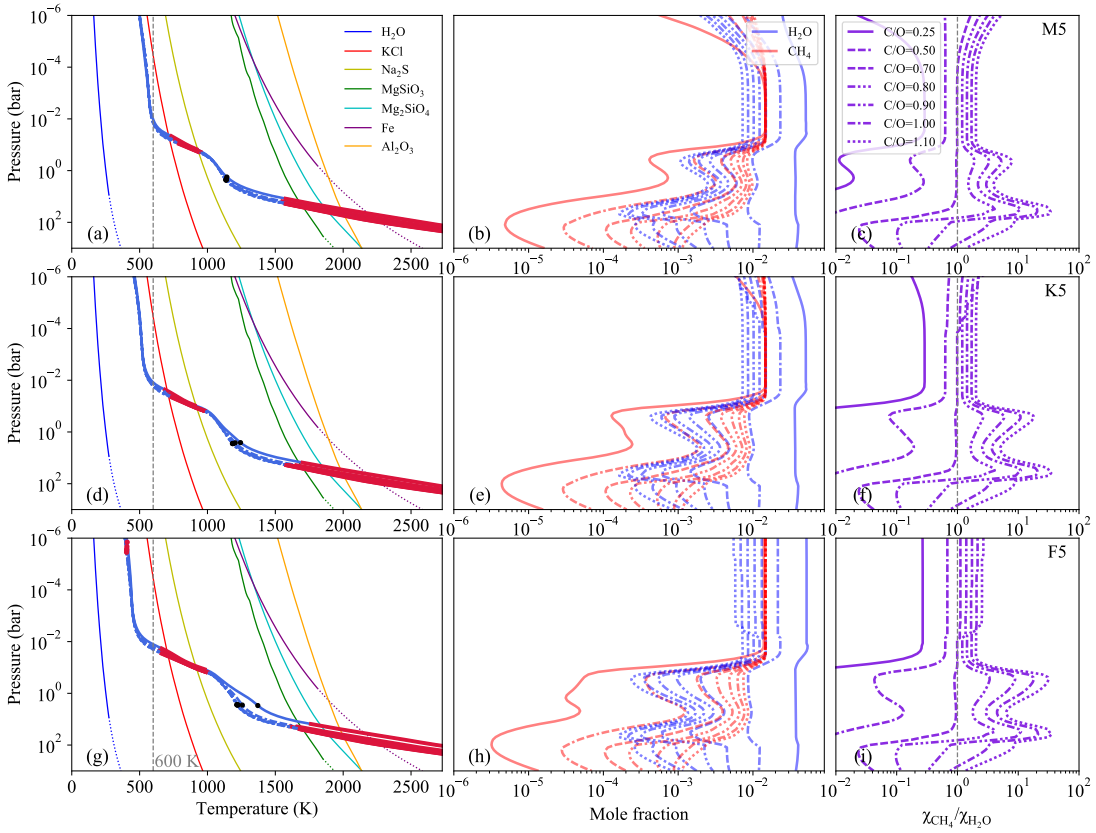

Figure 2.9: Hotter host stars increase the transition C/O ratios in Class-I planets. (a) TP structures for a planet with T_{eff}=600 K (gray dashed line), log(g)=3.00, [Fe/H]=1.50 orbiting an M5 star at different C/O ratios (blue lines); shaded red lines are convective regions; red and black dots represent 0.1% and 99% absorption levels of stellar flux respectively; Condensation curves are shown for solar metallicity. (b) H_2O and CH_4 mole fraction. (c) CH_4 to H_2O mole fraction ratios; a mole fraction ratio of unity at photospheric levels roughly coincides with the transition C/O ratio which is about 0.7 in this case. (d, e, f) Similar to (a, b, c) but for K5 star. (e) CH_4 abundance decreased while H_2O increased relative to M5 case; resulting in a higher transition C/O ratio. (g, h, i) Similar to (a, b, c) but for F5 host star. (h) CH_4 abundance decreases while H_2O increases relative to K5 case; resulting in a slightly higher transition C/O ratio. Note that the β-factor is more dominant than the stellar type in its effect on the transition C/O ratio.

Although a slight correlation between *Class-II/Class-III* transition and the β-factor can be found, a specific effect of stellar type is difficult to deduce due to our coarse temperature step size of 200 K. Nevertheless, the transition moves slightly to hotter planets as the β-factor increases because the photosphere moves to higher pressures in the atmosphere under these conditions, i.e. the surface gravity increases or metallicity decreases.

The stellar type has a somewhat different effect on the *Class-III/Class-IV* transition relative to *Class-I/Class-II*: the earlier types move the boundary to colder planets as a consequence of their efficient destruction of CH_4 and H_2O by thermal dissociation.

If these trends continue to higher β-factors, all transitions converge to one transition region at T_{eff}~1750K at β ~10, where the transition occurs from *Class-I* to *Class-IV* directly. Observing the atmosphere of such planets with extreme surface gravity and metallicity is very difficult, if not impossible, due to their small scale height. The question arises if such planets exist at all.

The bottom panel of Figure 2.8 illustrates the location of some of the observed planets for which metallicities have been estimated. The data are summarized in Table 2.2. The metallicities are not always well constrained and, in some cases, are only reported to be consistent with the observations. Clearly, a coherent analysis of available data and additional observations are needed to draw any conclusions.

Nevertheless, the Figure shows that none of the observed planets are characterized as *Class-I*, mostly due to their smaller scale heights and possible cloud coverage in the case of transmission spectroscopy (e.g. GJ 1214b's flat transmission spectra (Berta et al. 2012; Kreidberg et al. 2014a)), and lower emergent flux in the case of emission spectroscopy. Most of the observed planets in fact belong to the *Class-II*; this is mainly a consequence of the higher number of detected planets in this temperature range.

Since emission spectra probe deeper than transmission spectra into the atmosphere one might ask how the boundaries of four classes would change if the analysis was based on the emission spectra. Applying the spectral decomposition technique

Planet	$T_{eq}(K)$	log(g)	[Fe/H]	β	C/O	Ref.
CoRoT-2b	1393	$3.60^{+0.03}_{-0.03}$	–	–	$0.8^{+0.5}_{-0.5}$	Madhusudhan (2012)
GJ436b	712	$3.09^{+0.05}_{-0.05}$	1.0	1.41	$1.0^{?}_{-0.5}$	Madhusudhan & Seager (2011); Line et al. (2014)
HAT-P-1b	1182	$2.90^{+0.02}_{-0.02}$	-1.0	4.64	0.15	Goyal et al. (2017)
HAT-P-11b	791	$3.07^{+0.06}_{-0.06}$	$2.30^{+0.18}_{-0.65}$	$-0.92^{1.1}_{-0.3}$	–	Fraine et al. (2014); Wakeford et al. (2017b)
HAT-P-12b	875	$2.77^{+0.04}_{-0.04}$	$0.37^{+0.7}_{-0.45}$	$2.1^{+0.75}_{-1.2}$	$0.57^{+0.06}_{-0.07}$	Goyal et al. (2017); Yan et al in prep.
HAT-P-26b	907	$2.68^{+0.10}_{-0.09}$	$0.70^{+0.66}_{-0.74}$	$1.48^{+1.27}_{-1.13}$	–	Wakeford et al. (2017b)
HD149026b	1602	$3.25^{+0.05}_{-0.05}$	$1.0^{+0.48}_{-1.0}$	$1.43^{+1.7}_{-0.8}$	$0.55^{+0.45}_{-0.1}$	Fortney et al. (2006); Line et al. (2014); Zhang et al. (2018)
HD189733b	1100	$3.37^{+0.03}_{-0.03}$	0.0	3.34	$0.56^{+0.34}_{-0.09}$	Line et al. (2014); Goyal et al. (2017)
HD209458b	1320	$2.97^{+0.02}_{-0.02}$	$-0.52^{+0.52}_{-0.48}$	$3.85^{+0.81}_{-0.89}$	$0.56^{+0.44}_{?}$	Line et al. (2014, 2016); Goyal et al. (2017)
WASP-6b	1092	$2.94^{+0.04}_{-0.04}$	-2.30	6.83	0.15	Goyal et al. (2017)
WASP-12b	2320	$3.08^{+0.06}_{-0.05}$	$0.48^{+0.82}_{-1.08}$	$2.19^{+1.83}_{-1.40}$	$0.51^{+0.19}_{-0.21}$	Stevenson et al. (2014); Line et al. (2014); Kreidberg et al. (2015); Wakeford et al. (2017a); Goyal et al. (2017)
WASP-14b	1719	$4.06^{+0.06}_{-0.06}$	–	–	$0.75^{+0.65}_{-0.65}$	Madhusudhan (2012)
WASP-17b	1518	$2.50^{+0.05}_{-0.05}$	-1.0	4.18	0.15	Goyal et al. (2017)
WASP-19b	1912	$3.17^{+0.02}_{-0.02}$	-1.0	4.89	$0.40^{+0.70}_{-0.25}$	Madhusudhan (2012); Line et al. (2014); Goyal et al. (2017)
WASP-31b	1411	$2.72^{+0.04}_{-0.04}$	-2.30	6.61	0.35	Goyal et al. (2017)
WASP-33b	2452	$3.33^{+0.02}_{-0.02}$	1.48	1.23	$0.75^{+0.25}_{-0.25}$	Madhusudhan (2012); Zhang et al. (2018)
WASP-39b	1022	$2.65^{+0.05}_{-0.06}$	$2.08^{+0.40}_{-1.23}$	$-0.90^{+2.10}_{-0.68}$	0.56	Goyal et al. (2017); Wakeford et al. (2017a)
WASP-43b	1318	$3.69^{+0.02}_{-0.02}$	$0.00^{+0.54}_{-0.40}$	$3.67^{+0.68}_{-0.92}$	$1.0^{?}_{-0.87}$	Line et al. (2014); Kataria et al. (2015); Wakeford et al. (2017a)
WASP-107b	707	$2.55^{+0.04}_{-0.04}$	$1.34^{+0.69}_{-1.47}$	$0.25^{+2.50}_{-1.17}$	$0.02^{+1.58}_{-0.01}$	Anderson et al. (2017); Kreidberg et al. (2018b)
XO-1b	1168	$3.21^{+0.03}_{-0.03}$	–	–	$0.80^{+0.20}_{-0.20}$	Madhusudhan (2012)

Table 2.2: A summary of estimated metallicity and carbon to oxygen ratio for 20 exoplanets. One should be cautious about the [Fe/H] and C/O values summarized in this Table due to different data reduction, assumptions in the forward simulations or retrieval techniques. Here we report them only to provide a qualitative picture of the current status of our understanding regarding these parameters in the context of locating their positions on the planetary classification map, Figures 2.8 and 2.6.

(Section 2.2.1) on emission spectra is technically challenging, mostly due to the necessity of making different templates for each model based on their exact TP structure. However, Figure 2.12 could provide some insight. The pressure of a given photospheric level increases as β-factor increases. Therefore if we employ emission spectra instead, we would probe higher pressures for a given photospheric level. Consequently, a lower β-factor would be required to keep a given photospheric level at the same pressure for both transmission and emission spectra. Thus a slight shift of the β-T_{eff} diagram (Figure 2.8) toward lower β values is expected if our analysis was based on the emission spectra.

2.3.4 A Parameter Space for CH_4

The lack of a robust methane detection in the spectra of irradiated exoplanets (see e.g. Madhusudhan & Seager 2011) immediately rises a question: *Does there exist a parameter space preferential for the detection of CH_4?*

Espinoza et al. (2017) studied C/O ratios of 50 cold planets with T_{eff}<1000 K. They found C/O>1 to be highly unlikely for these planets and concluded that this is likely to be a universal outcome for gas giants. By extending this conclusion to hot planets one could expect the spectra of *Class-IV* planets to be always water-dominated with no room for a methane dominated spectrum. This reduces the probability of CH_4 detection at high temperatures, i.e T_{eff}>1500 K, significantly.

However, Figure 2.6 reveals a region between 800 and 1500 K with C/O>0.7 where the CH_4 molecule is predicted to always be the dominant spectral feature. We therefore call this region *the Methane Valley* and anticipate higher probability of CH_4 detection over H_2O spectral features when exploring this parameter space.

The lack of such a detection would likely to be an indication that cloud-free models are incapable of capturing exoatmosphere characteristics within that parameter space. Hence, studying the methane valley could potentially provide a suitable road-map to study departures from thermochemical equilibrium, departures from radiative-convective hydrostatic equilibrium, or the effect of clouds on the presence of methane in planetary atmospheres. Mapping the observed planets

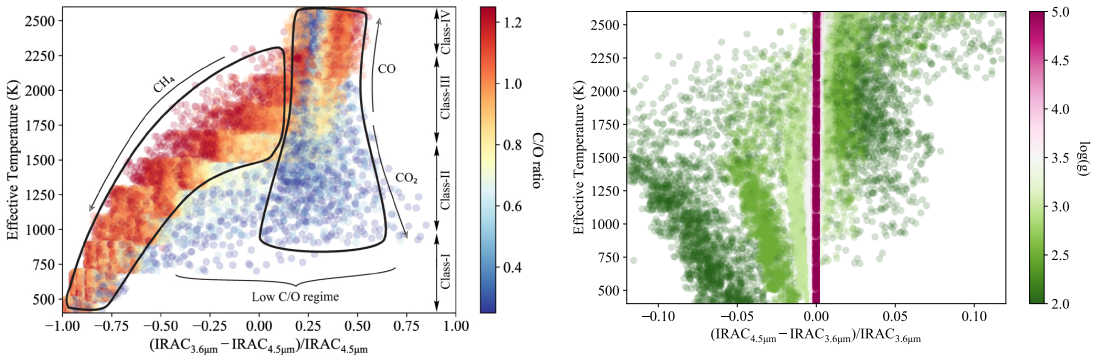

Figure 2.10: Synthetic IRAC color-temperature diagrams for cloud free atmospheres under equilibrium chemistry condition. Left) Color diagram based on emission spectroscopy, i.e. IRAC data describes the secondary eclipse depth at λ (μm). Right) The same for transmission technique, i.e. IRAC data describes the transit depth at λ (μm).

with estimated C/O on Figures 2.6, tentatively suggest such departure from cloud-free equilibrium chemistry conditions where the observed planets within or close to this region (i.e. WASP-43b, XO-1b, HD 189733b, and HAT-p-12b) all have shown significant water features in their transmission spectra. More precise C/O measurements are needed to observationally constrain the Methane Valley properties.

2.3.5 Color-Temperature Diagrams

Color-diagrams have been used as a method of characterization of self-luminous objects for more than a century, see e.g. Rosenberg (1910) for stars, Tsuji & Nakajima (2003) for cool dwarfs and brown dwarfs, and Bonnefoy et al. (2014a); Keppler et al. (2018); Batalha et al. (2018) for directly imaged planets. Triaud et al. (2014) and Triaud (2014) studied color-magnitude diagrams of known transiting exoplanets. Their investigations, therefore, were limited to the systems with known parallaxes. They compared irradiated planets with very low mass stars and field brown dwarfs and concluded that further measurements are required to confirm or reject whether irradiated gas giants form their own sequence on the color-magnitude diagrams.

Inspired by these works, we investigated the possibility of introducing a color-diagram for the characterization of irradiated planets, using their effective tempera-

ture instead of their absolute magnitude. The effective temperature can be used as a proxy for the luminosity/absolute magnitude, because the reference radius assumed to be constant, see Section 2.2. To take an even more practical approach we chose a normalized color parameter based on the Spitzer's Infrared Array Camera (IRAC) (Fazio et al. 2004; Allen et al. 2004) as a commonly used photometer for the observation of exoplanets (see e.g. Charbonneau et al. (2005); Deming et al. (2007); Todorov et al. (2009); Sing et al. (2016)). The IRAC photometric channels 1 and 2 are centered at 3.6 and 4.5 μm, respectively. Channel 1 (3.6 μm) is more suited to study CH_4/H_2O spectral features while channel 2 (4.5 μm) is more sensitive to CO/CO_2 features (see e.g. Swain et al. 2009b; Désert et al. 2009; Swain et al. 2009a). Depending on the type of spectroscopy, i.e. transmission or emission, the ratio of the transit depth or the ratio of the secondary eclipse depth at these channels could potentially provide an information regarding the relative presence of these molecules in the atmosphere of a planet. For transmission spectroscopy, we define this ratio as:

$$R_{tr} = (IRAC_{4.5\ \mu m} - IRAC_{3.6\ \mu m})/IRAC_{3.6\ \mu m} \tag{2.15}$$

where $IRAC_\lambda$ is the transition depth observed at wavelength λ (μm) channel. In transmission spectroscopy absorption features appear as positive signals in the unit of transit depth. This is not the case for emission spectroscopy where absorption features are negative signals with respect to a blackbody curve. As a result, we rearrange the terms and define this ratio of channels for emission spectroscopy as follows:

$$R_{em} = (IRAC_{3.6\ \mu m} - IRAC_{4.5\ \mu m})/IRAC_{4.5\ \mu m} \tag{2.16}$$

where $IRAC_\lambda$ is the secondary eclipse depth observed at wavelength λ (μm) channel. By applying IRAC's spectral response curves on our 56,448 synthetic spectra we estimated these ratios for the two spectroscopy methods. Figure 2.10 shows the IRAC synthetic color-temperature diagrams for cloud-free atmospheres under equilibrium chemistry conditions.

The general shape of the “emission" color-temperature diagram (Figure 2.10, left panel) is very similar to that of self-luminous dwarfs and directly imaged planets, with two distinct populations at the first glance. One population is associated with colder planets and negative R_{em} values, which means the planetary emission flux at 4.5 μm is stronger than at 3.6 μm. This in turn indicates that the absorption at 3.6 μm is stronger and, hence, suggests the presence of strong CH_4 over CO/CO_2 features. In contrast, the second hotter population has positive R_{em} values and, therefore, indicates pronounced CO/CO_2 spectral features. A typical uncertainty of observed R_{em} by IRAC is on the order of $\sim$0.25 and, consequently, the two populations should be distinguishable. Any deviation from these two populations could be a consequence of eddy diffusion, the presence of clouds or sub-solar C/O in the visible atmosphere of exoplanets. The case of low C/O is evident for the planets with an effective temperature between 750 and 1750 K, and C/O<0.4 in the left panel of Figure 2.10, which shows significant scatter.

From the transmission color-temperature diagram (see Figure 2.10, right panel), a new pattern emerges, but the two populations are still distinguishable: the population of colder planets with negative R_{em} values (with stronger CH_4 spectral features) and the population of hotter planets with positive R_{tr} values (with stronger CO/CO_2 features). The diagram is color-coded by surface gravity values, because the amplitude of transmission spectral features is strongly correlated with this parameter, i.e. higher log(g) results in smaller features (see e.g. Lecavelier des Etangs et al. (2008)). A typical uncertainty of observed R_{tr} by IRAC is on the order of $\sim$0.05. However only planets with log(g)$\leq$ 3.0 result in a $R_{tr} \geq 0.05$. Therefore, any significant deviation from $R_{em} \sim 0$ for planets with log(g)$\geq$ 3.0 should be due to the effects of non-equilibrium chemistry or clouds on their transmission spectra. This could be used as a diagnostic tool to indicate such planets as suggested by Baxter et al. (2018).

2.4 Summary & Conclusion

In this chapter we have studied the dominant chemistry in the photosphere of irradiated gaseous exoplanets by calculating a large grid of self-consistent cloud-free atmospheric models, as a preparatory step toward a framework for an observationally driven classification scheme.

The Spectral Decomposition Technique enabled us to quantitatively estimate the contribution of H_2O and CH_4 in the synthetic transmission spectra and hence we were able to find the transition C/O ratios at which the water-dominated spectrum flips to a methane-dominated one. We find that C/O<1 is not a global indicator of water-dominated spectra, and C/O≥1 is not a ubiquitous indication of methane-dominance, see e.g. Figure 2.6. However, the separation at C/O=1 still provides a rough approximation for the water-methane boundary for adequately hot planets.

Mapping all the transition C/O ratios revealed four spectral populations of planets in the C/O-T_{eff} diagram. Hence a “four-class" classification scheme emerged for irradiated planets; spanning from cold (400 K) to hot (2600 K) planets. The spectra within the temperature range of 600 K to 1100 K, i.e. the boundary of *Class-I* and *Class-II.*, is found to be quite diverse and a slight variation of the physical parameters, such as metallicity or surface gravity, could lead to another chemistry and hence to another spectral class. This parameter space is thus well-suited for studying the diversity of physics and chemistry of exoplanetary atmospheres. Such study potentially opens the path to the study of colder planets.

We have also predicted a region (*The Methane Valley*) where methane always remains the cause of dominant spectral features, under the assumptions of this study. The temperature range to look for CH_4 features spans from 800 to 1500 K and requires C/O≥ 0.7. Although CH_4 is expected to be more present in the atmosphere of colder planets, the temperature range of the Methane Valley is expected to be in favor of less cloudy and less vertically quenched atmospheres, which increases the probability of CH_4 detection in turn. CH_4 detection in the Methane Valley, or the lack of it, could hint the prevalence of cloud formation or

non-equilibrium chemistry within this parameter space and provides a diagnostic tool to identify these conditions.

We constructed two Spitzer IRAC color-diagrams; one from the synthetic transmission and one from emission spectra. In both cases two populations of planets can be interpreted. One population highlights the planets with a stronger CH_4 photometric signature at 3.6 μm (mostly associated with *Class-I*, *II* and *III*) and the other one shows a stronger CO/CO_2 signal at 4.5 μm (mostly associated with *Class-II*, *III* and *IV*). Future photometric analysis could reveal whether irradiated planets follow the location of these populations on the color-maps or they would deviate from the predictions and hence mark the possibility of cloud presence or non-equilibrium chemistry in their photosphere.

As mentioned, the results of this chapter is based on cloud-free equilibrium-chemistry assumptions. Including additional physics (such as non-equilibrium chemistry or clouds) or opacities (such as TiO/VO; see e.g. Mancini et al. (2013),Haynes et al. (2015),Evans et al. (2016), and Nugroho et al. (2017)) can potentially change the results. Therefore, our classification scheme might lead to biased conclusions in cases where the cloud formation or disequilibrium chemistry are expected to occur, e.g. colder planets, and should be taken only as an initial step toward an observationally driven characterization scheme for exoplanet atmospheres.

2.5 Appendix A) Problematic parameter space

With five parameters to explore, the number of models exceeds 28,000. It then should not be a surprise that some models demanded extra attention as a result of their poor convergence. In particular, models with high metallicity, but low C/O turned out to be quite problematic. By examining a wider range of metallicities and C/O ratios the trend became more prominent, see Figure 2.11.

This problem has been noticed before by Paul Mollière and Pascal Tremblin [private communication, 2018] and it is thought to be a numerical issue with the Gibbs free energy minimization algorithm. Their investigation have shown that excluding $MgSiO_3$(c), $MgSiO_3$(L), $MgAl_2O_4$(c) and Fe_2SiO_4(c) from the chemistry

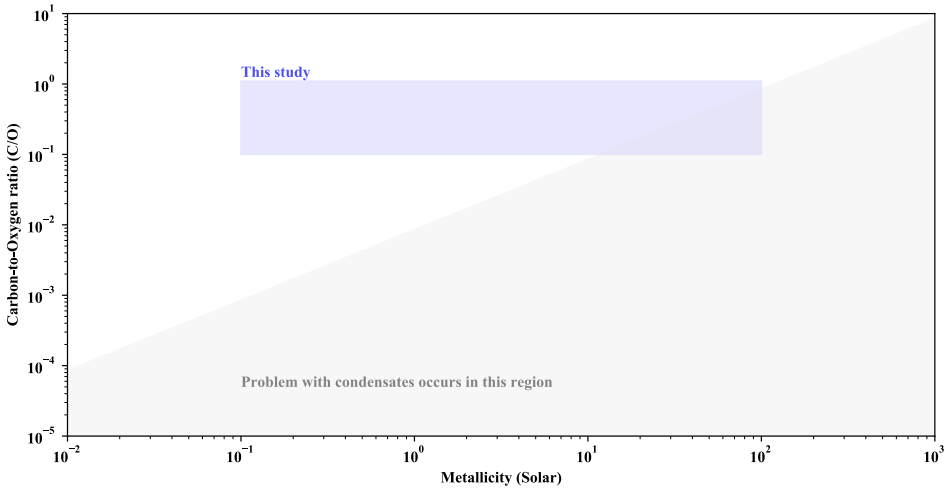

Figure 2.11: Problematic parameter space at high metallicities and low C/Os

network solves the numerical problem and hence they concluded there are possibly some linear combinations of condensates that make the abundance matrix in the Gibbs minimization problem rank-deficient. Two examples of such net reactions are:

$$\mathrm{MgAl_2O_4(c) + MgSiO_3(c) \rightleftharpoons Mg_2SiO_4(c) + Al_2O_3(c)} \tag{2.17}$$

$$\mathrm{Fe_2SiO_4(c) + MgAl_2O_4(c) \rightleftharpoons 2\,FeO\,(c) + MgSiO_3(c) + Al_2O_3(c)} \tag{2.18}$$

The presence of these condensates have a prominent effect in the planetary atmospheres as they bind oxygen from the atmosphere and change the water content along with other compositional variations. As a result the TP structure and resulting spectra change too. The spectral difference between the models with and without these four condensates was explored quantitatively and more than 10% of our models were found to show a deviation larger than 10ppm in their transmission spectrum (assuming Jupiter-sized planets and solar-sized host stars). All these models had very low log(g), i.e. 2.0-2.5, in the grid. Planets with log(g)=2.0-2.5 are not common, see Figure 2.1, and also 10ppm is likely below the expected JWST noise floor (e.g. Ferruit et al. 2014; Beichman et al. 2014; Batalha et al. 2017) but nevertheless it is important to understand how removing the condensates can improve the numerical convergence by keeping the change in the spectra to a minimum.

We explored the problematic models from our grid by excluding the condensates one-by-one and found removing either of these condensates can solve the problem of our grid: Fe_2SiO_4(c), $MgAl_2O_4$(c), FeO(c), Mg_2SiO_4(c) and Al_2O_3(C). The following net reaction can be a possible linear combination, which results in a rank deficiency:

$$Fe_2SiO_4(c) + 2\,MgAl_2O_4(c) \rightleftharpoons 2\,FeO\,(c) + Mg_2SiO_4(c) + 2\,Al_2O_3(C) \quad (2.19)$$

We extended our investigation beyond our parameter space to explore this numerical issue in more detail and found that excluding Mg_2SiO_4(c) can solve the problem while keeping the spectral change to a minimum. In conclusion less than 0.7% of our entire models have spectral change on the level of 10ppm or above if we exclude Mg_2SiO_4(c), and thus we removed this condensate from the problematic models to compute the grid of models.

2.6 Appendix B) β: the scaling factor

The relationships between TP structures, abundances and spectra to the surface gravity and metallicity have been reported by previous studies (see e.g. Mollière et al. 2015). They all reported low log(g) imitates high [Fe/H] and high log(g) emulates low metallicity effects. This can be understood by assuming gray opacities in an atmosphere and deriving a simple relation between the optical depth (τ) and pressure (P) as noted in Equation 2.4. Mollière et al. (2015) suggested $\beta = log(g) - [Fe/H]$ as a factor to map the optical depth-pressure in the planetary atmospheres. This linear relation is inspired by the dependency of log(p) to the surface gravity and metallicity at any given optical depth: $\tau = \kappa/gP \Rightarrow P = \tau g/\kappa$

$$\tau_{phot} \approx 1 \Rightarrow P \approx P_{phot} = g/\kappa \Rightarrow \log(P_{phot}) \approx \log(g) - \log(\kappa) \approx \log(g) - [Fe/H] + cst$$
$$\Rightarrow \log(P_{phot}) \approx \beta + cst \quad (2.20)$$

where P_{phot} is the pressure at photospheric levels. Molecular and atomic opacities are non-gray in nature and thus the defined relation holds true only over a narrow pressure level (or optical depth, alternatively). Hence from a broader perspective the

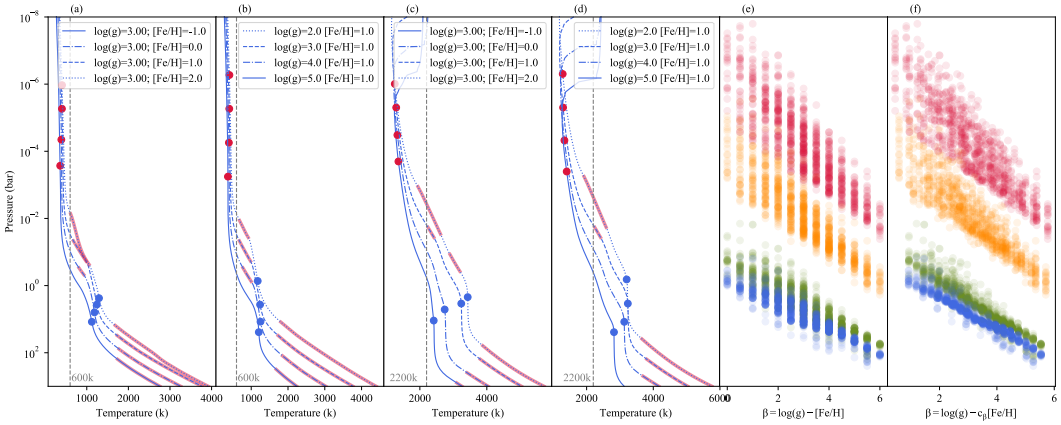

Figure 2.12: The effect of surface gravity and metallicity on the temperature structures of planetary atmospheres. (a) TP structures for planets with T_{eff}=600 K (gray dashed line), log(g)=3.00, C/O=0.5 orbiting an F5 star at different metallicities [Fe/H]=-1.0,0.0,1.0 and 2.0 (blue lines); Shaded red lines are convective regions; red and blue dots represent 0.1% and 99% absorption levels of stellar flux, respectively; (b) similar to (a) but for a fixed [Fe/H]=1.0 and varying log(g)=2.0, 3.0, 4.0, and 5.0; (c, d) similar to (a, b) but for a hot planet T_{eff}=2200 K. These values are chosen to represent similar β-factor for both sets and hence TP profiles are expected to change similarly. (e) Color dots are 0.1% (red), 5% (orange), 95% (green) and 99.9% (blue) absorption levels of stellar flux drawn from 1000 randomly chosen models with their representative β-factor using $\beta = \log(g) - [\text{Fe/H}]$. (f) Finding c_β values by minimizing the scatter of absorption levels using $\beta = \log(g) - c_\beta[\text{Fe/H}]$. See the text for more details.

β-factor can be expressed as a function of pressure or can be defined for a specific feature in the atmosphere such as the location of convective-radiative boundary in the atmosphere and how it varies with β.

Figure 2.12a shows the effect of increasing metallicity on the TP structure of a cold planet with an effective temperature of 600 K at a fixed C/O ratio of 0.5, orbiting around a F5 star. In contrast, increasing the surface gravity pushes the TP structure to higher pressures, Figure 2.12b. Figure 2.12c and d similarly demonstrate these trends but for a hot planet with an effective temperature of 2200 K. We locate the pressure levels at which the stellar flux is absorbed by 0.1% (red dots) and 99.9% (blue dots) on the TP structure of these models to investigate how their photosphere vary with the beta factor. In these two cases, where the stellar type and C/O are fixed, the location of photosphere is almost invariant to the planets' temperatures.

1000 random models are drawn from all 28,224 simulations, regardless of their

input parameters, and their 0.1%, 5%, 95% and 99.9% stellar absorption levels are shown in Figure 2.12e with respect to their beta factor. At lower beta values, i.e. lower log(g) with higher [Fe/H], the data are more scattered around a linear trend due to the pressure dependence of the atomic and molecular opacities and the effect of C/O on the shape of TP structure and abundances, vertical distribution. In addition, each absorption level has slightly different dependency on the β factor: low pressure regions have steeper linear slopes but more scattered in general. This suggests the relationship between the pressure levels of spectrally active regions, and metallicity and surface gravity is possibly not a one-to-one association. Constructing a complex function for the β-factor is possible, however we aim to keep this modification at a minimal level. We therefore introduce a modified relation for the beta factor as follows:

$$\beta = \log(g) - c_\beta[Fe/H] \tag{2.21}$$

where c_β is a constant and represents relative importance of log(g) over metallicity. We define c_β in a way to make log(g) and c_β[Fe/H] terms comparable. Therefore, if c_β<1 then log(g) is influencing that specific layer of the atmosphere more than [Fe/H], and otherwise for c_β>1. When c_β=1, surface gravity and metallicity are equally important for the region under study.

An approach to find c_β could be to minimize the scatter at each region of interest, for instance through χ^2 minimization. By following this approach we estimate c_β for the β factor at 0.1%, 5%, 95% and 99.9% stellar absorption levels to be 0.774, 0.733, 0.706, 0.534, 0.530 and 0.538, respectively. All evaluated c_β are less than 1.0, pointing at the surface gravity to be more influential than the metallicity on the TP structures in the spectrally active regions, but in particular at the optically thicker layers where c_β is the minimum. It is also noticeable that the deeper regimes are less influenced by other parameters such as planet's effective temperature, stellar type or carbon to oxygen ratio. This can be seen in the less scattered β-factor in Figure 2.12f for the region with 99.9% light absorption in comparison to the highly scattered values at 0.1% stellar absorption layer. This simple method could

be also applied to estimate the sensitivity of other parameters such as spectral features to β-factor, as is discussed in Section 2.3 .

"The meeting of two personalities is like the contact of two chemical substances: if there is any reaction, both are transformed."

— Carl Jung.

3

ChemKM: The Chemical Kinetic Model

Contents

3.1 Implementing the chemical kinetics scheme

[1] To study the effects of disequilibrium chemistry on the composition and atmospheric spectra of irradiated exoplanets I developed a 1D Chemical Kinetic Model (`ChemKM`).

3.1.1 The continuity equation

The implementation of `ChemKM` closely follows the photochemical model described in Venot (2012) and Agúndez et al. (2014a). As the first step, the abundances of atmospheric constituents are governed by numerically solving the equations of chemical kinetics (also known as the altitude-dependent continuity–diffusion equation) which describe the formation and destruction of species, equation 3.1 (e.g. Allen et al. 1981):

$$\frac{\partial n_i}{\partial t} = P_i - n_i L_i - \frac{\partial \Phi_i}{\partial z}, \tag{3.1}$$

where n_i is the number density (cm^{-3}), P_i is the total production rate (cm^{-3} s^{-1}), L_i is the total loss rate (s^{-1}), and Φ_i is the net vertical flux (cm^{-2} s^{-1}) of species i at altitude z (with respect to a reference level; usually 1 bar for gaseous giants as discussed in Chapter 1). These quantities are all functions of time t and altitude z (or alternatively pressure). In spherical coordinate, the continuity equation can be rewritten as follow:

$$\frac{\partial f_i}{\partial t} = \frac{P_i}{n_T} - f_i L_i - \frac{1}{n_T r^2}\frac{\partial (r^2 \Phi_i)}{\partial r}, \tag{3.2}$$

where n_T is the total number density of species, f_i is the mixing ratio of species i and is defined as $f_i = n_i/n_T$, and r is the distance to center of planet. The vertical flux transport terms include molecular and eddy diffusion, $\Phi_i = \Phi_{i,mol} + \Phi_{i,eddy}$ where the latter is commonly parameterized by an eddy diffusion coefficient K_{zz}. The vertical

[1] Parts of this chapter was published as a refereed article "From cold to hot irradiated gaseous exoplanets: Fingerprints of chemical disequilibrium in atmospheric spectra", Molaverdikhani et al. (2019a) and "Understanding the atmospheric properties and chemical composition of the ultra-hot Jupiter HAT-P-7b: II. Mapping the effects of kinetic gas composition", (Molaverdikhani et al. sub.), for which I am the lead author and has been adapted for this thesis.

flux transport terms can be estimated through equations 3.3 and 3.4, respectively (see e.g. Moses (1991) and references therein).

$$\Phi_{i,mol} = -n_T D_i \left(\frac{\partial f_i}{\partial z} - \frac{f_i}{H_a} + \frac{f_i}{H_i} + \frac{\alpha_i f_i}{T} \frac{dT}{dz} \right) \tag{3.3}$$

$$\Phi_{i,eddy} = -n_T K_{zz} \left(\frac{\partial f_i}{\partial z} \right), \tag{3.4}$$

where K_{zz} is the eddy diffusion coefficient ($cm^2\ s^{-1}$), D_i is the molecular diffusion coefficient ($cm^2\ s^{-1}$), H_a is the mean scale height of the atmosphere, H_i is the scale height of species i, T is the gas kinetic temperature (K), and α_i is the thermal diffusion factor of species i. The thermal diffusion factor is usually set to zero, except for light species such as H, H_2, and He, that can be estimated with -0.25 (e.g. Marshall & Plumb 2013).

We use Lennard-Jones calculations for the estimation of molecular diffusivity of species, as discussed in the next section. Note that D_i scales inversely with pressure and will become important at very low pressures. Therefore this term's contribution is no longer negligible at the pressures probed by transmission observations, i.e. above ∼1 bar. The effect becomes more pronounced when the atmosphere is probed by high resolution spectroscopy. We discuss this in more detail in Section 4.2.1.

One approach to estimate K_{zz} is using general circulation models (GCMs) to calculate wind velocity fields (e.g. Moses et al. (2011)) or to compute the advection of passive tracers (Parmentier et al. 2013). Due to large uncertainties in these approaches an alternative method could be to treat the eddy diffusion coefficient as a free parameter in the model (e.g. Miguel & Kaltenegger 2014). We use the latter approach, in our parametric study, Section 4.

3.1.2 Approximation of Molecular Diffusion Coefficients

So far, we described the essence of our chemical kinetic modelling. Now we expand on how we approximate the molecular diffusion coefficients using the Chapman

and Enskog equation (Poling et al. 2000):

$$D = \frac{3}{16}\frac{(4\pi kT/M_{AB})^{1/2}}{n\pi\sigma_{AB}^2\Omega_D}f_D \tag{3.5}$$

where M_{AB} is defined as $2[(1/M_A) + (1/M_B)]^{-1}$ (M_A, M_B being the molecular weights of species A and B, respectively), Ω_D is the collision integral for diffusion, σ_{AB} is the characteristic length of the intermolecular force law, f_D is a correction term (usually of order unity), n is number density of molecules in the mixture, k is the Boltzmann's constant, and T is the gas temperature of the mixture. Among them, Ω_D and σ_{AB} demand extra steps to be approximated.

Ω_D can be estimated by following the relation of Neufeld et al. (1972):

$$\Omega_D = \frac{A}{(T^*)^B} + \frac{C}{exp(DT^*)} + \frac{E}{exp(FT^*)} + \frac{G}{exp(HT^*)} \tag{3.6}$$

where A=1.06036, B=0.15610, C=0.19300, D=0.47635, E=1.03587, F=1.52996, G=1.76474, H=3.89411, and $T^*=kT/\varepsilon_{AB}$. ε_{AB} can be estimated as:

$$\varepsilon_{AB} = (\varepsilon_A\varepsilon_B)^{1/2} \tag{3.7}$$

where ε_A and ε_B are the characteristic Lennard-Jones energy of molecule A and B respectively, which their values are usually tabulated and in-hand (see e.g. Poling et al. 2000, Appendix B).

Similarly, σ_{AB} can be estimated as below:

$$\sigma_{AB} = \frac{\sigma_A + \sigma_B}{2} \tag{3.8}$$

where σ_A and σ_B are the characteristic Lennard-Jones length of molecule A and B respectively, which their values are also tabulated (see e.g. Poling et al. 2000, Appendix B). Using these approximations the molecular diffusion coefficients can be estimated in the chemical kinetic models.

3.1.3 Implementation of photochemical dissociation

Photodissociation is one of the most important processes in the atmosphere of irradiated planets. As the temperature of the atmosphere decreases, the chemical kinetic timescale becomes longer with respect to the photolysis timescale. Hence photodissociation affects the atmospheric properties more at lower temperatures. A photolysis reaction takes place when a high energy photon ($h\nu$) hits an atmospheric constituent. Through this process, generally, a species (e.g. **A**) goes into an excited state, or being dissociated into one or more species (e.g. **B, etc.**).

$$\mathbf{A} \xrightarrow{h\nu} \mathbf{B} + \dots \tag{3.9}$$

The products of the dissociation and their production rates depend on the energy of the absorbed photon. This "branching" of the photodissociation pathway is generally shown by "branching ratios". Here, we show two major photodissociation pathways of ethylene (C_2H_4):

$$Path - I) C_2H_4 \xrightarrow{h\nu} C_2H_2 + H_2 \tag{3.10}$$

$$Path - II) C_2H_4 \xrightarrow{h\nu} C_2H_2 + H + H \tag{3.11}$$

In one pathway, Path-I, C_2H_4 is dissociated to acetylene (C_2H_2) and molecular hydrogen. In Path-II, it is dissociated to acetylene (C_2H_2) and two atomic hydrogen. At the Lyman α, the branching quantum yields ($q_k(\lambda)$) are 0.58 and 0.42 for these two pathways, respectively (Hébrard et al. 2012). This means at the wavelength of ∼122 nm, 58% of the products come from the Path-I and the rest (42%) are produced from the Path-II.

Photodissociation rate, J_A, is the probability of species **A** being dissociated and can be related to the loss rate as below:

$$L_i^{photo} = \frac{d[A]}{dt} = -J_A[A] \tag{3.12}$$

where [A] is the concentration of the species **A** in the unit of molecule·cm^{-3}. Photodissociation rate has a unit of s^{-1} and its inverse represents the photodissociation

lifetime and it is a measure of photodissociation timescale of species A:

$$t_A^{photo} = \frac{1}{J_A} \tag{3.13}$$

In addition to its dependency to the frequency (energy) of the absorbed photons, photodissociation rate also depends on the flux of the photons, $F(\lambda, z)$, and the cross-section of the species, $\sigma_A(\lambda)$, at any given wavelength. As photons penetrate into the deeper layers of the atmosphere, the photon flux drops. Thus the photodissociation rate is a function of altitude, z, too. All together, for each branching pathway (m) we can write:

$$\frac{d[A]}{dt} = -J_A[A] = \int \sigma_A(\lambda) q_m(\lambda) F(\lambda, z) d\lambda \tag{3.14}$$

where the wavelength dependent cross-section of species **A** has a unit of (cm^2·molecule), and its spectral actinic flux density has a unit of (#/cm^2/s). The total photodissociation rate of species **A** is thus a summation of the photodissociation rates over all branching pathways.

The attenuation of the actinic flux at a given wavelength, $dF(\lambda)$, and through a slab of atmosphere with a path length of dl can be expressed by using Beer-Lambert law:

$$dF(\lambda) = -\kappa(\lambda) F(\lambda, z) dl \tag{3.15}$$

where κ is the extinction coefficient and can be expressed as a linear combination of absorption ($k(\lambda)$) and scattering ($\alpha(\lambda)$) coefficients:

$$\kappa(\lambda) = k(\lambda) + \alpha(\lambda) \tag{3.16}$$

where the extinction coefficient is related to the absorption ($\sigma_{abs}(\lambda)$) and scattering ($\sigma_{sct}(\lambda)$) cross-sections as follow:

$$\kappa(\lambda) = \left(\sigma_{abs}(\lambda) + \sigma_{sct}(\lambda)\right) n(l) \tag{3.17}$$

where $n(l)$ is the number density (cm^{-3}) within the atmospheric slab that the flux of photons experience. Putting all together, a general solution to the Equation 3.15 is therefore:

$$F(\lambda, l) = F^{TOA}(\lambda) e^{-\int_l^{TOA} ((\sigma_{abs}(\lambda) + \sigma_{sct}(\lambda)) n(x) dx} \tag{3.18}$$

where F^{TOA} is the photon flux at the top of the atmosphere. The integral in Equation 3.18 can be defined as a new term, called optical depth:

$$\tau(\lambda, l) = \int_{l}^{TOA} \left(\left(\sigma_{abs}(\lambda) + \sigma_{sct}(\lambda)\right) n(x) dx \right. \tag{3.19}$$

hence:

$$F(\lambda, l) = F^{TOA}(\lambda) e^{-\tau(\lambda, l)} \tag{3.20}$$

Given a plane-parallel atmosphere the radiative transfer equation can be further simplified by relating the slab length, l, with altitude, z, as $z = l \cdot Cos(\theta)$; where θ is the irradiation zenith angle. Thus:

$$F(\lambda, z) = F^{TOA}(\lambda) e^{-\tau(\lambda, z, \theta)} \tag{3.21}$$

where θ is a constant value and not an independent variable to be considered, for instance, in the actinic flux function. For the absorption, we consider the flux extinction due to the photodissociation, and for the scattering I include the Rayleigh scattering. The Rayleigh scattering cross-section is given by Rayleigh (1871) and (Cabannes & Rocard 1929):

$$\sigma_A^{Ray}(\lambda) = \frac{8\pi}{3} \left(\frac{2\pi}{\lambda}\right)^4 \alpha_p^2 \frac{6 + 3\delta}{6 - 7\delta} \tag{3.22}$$

which is an averaging of the cross-section over all scattering angles. α_p is the polarizability of the compound and δ is the depolarization factor. The last term of the expression makes it possible to take into account the anisotropy of the molecules. The polarizability can be calculated by:

$$\alpha_p = \frac{n_r^2 - 1}{4\pi n_l} \tag{3.23}$$

where n_r and n_l are refractive index and the Loschmidt constant that are measured and tabulated for a variety of species (Cox et al. 2002).

3.1.4 Governing radiative transfer equations

In the limit of plane-parallel two-stream approximation, the photon flux is assumed to be propagating in two discrete up and down directions (Liou 2002):

$$F(\lambda, z) = \downarrow F(\lambda, z) + \uparrow F(\lambda, z) \tag{3.24}$$

The intensity of the scattered radiation due to molecular diffusion is proportional to $1+\cos^2\phi$, where ϕ is the scattering angle. Thus, the scattered radiation is more pronounced along the direction of the stellar radiation. Therefore, it is possible to simplify the calculations of the scattered light by considering all scattering occurring in the direction of the stellar radiation. Following this approximation, Isaksen et al. (1977), Luther (1980), and Dvortsov et al. (1992) proposed two schools of fast method to estimate these fluxes under a diffusive condition: one is through successive scattering methods or the other one is by matrix inversion techniques. We use the former method (successive iteration) due to its simplicity in implementation and computational speed. In order to obtain the first solution of the radiative transfer equations (i.e. order-zero), we can simply set the downward flux at the top of the atmosphere to the stellar flux at TOA.

$$\downarrow F^0(\lambda, TOA) = F_{star}(\lambda) \tag{3.25}$$

and for the rest of the atmosphere, the photon flux attenuates according to Beer-Lambert law:

$$\downarrow F^0(\lambda, z_j) = \downarrow F^0(\lambda, z_{j+1}) e^{-\tau(\lambda, z_j, \theta)} \tag{3.26}$$

where $\tau(z_j)$ is the opacity between level z_j and z_{j+1}. Likewise, the order-zero upward flux can be calculated from bottom, and written as:

$$\uparrow F^0(\lambda, z_j) = \uparrow F^0(\lambda, z_{j-1}) e^{-\tau(\lambda, z_{j-1}, \theta)} \tag{3.27}$$

At the presence of a surface or a cloud deck at the bottom layer, z_0, boundary condition for the order zero upward flux can be calculate as below:

$$\uparrow F^0(\lambda, z_0) = a(\lambda) \downarrow F^0(\lambda, z_0) \tag{3.28}$$

where $a(\lambda)$ is the wavelength dependent albedo at the bottom layer, i.e. the reflected radiation from the bottom. As a result, for a planet with zero albedo, the order zero upward flux of all layers becomes zero.

$$\uparrow F^0(\lambda, z_j) = 0 \tag{3.29}$$

For the first iteration, we use Equations 3.26 and 3.27 as the basis and include the scattered photons from order zero. Hence, all higher order calculations (iterations) of upward and downward fluxes can then be expressed by fluxes of lower orders. This additional term for an altitude of z_j can be written as:

$$F^i_{add}(\lambda, z_j) = \left(1 - e^{-\tau_{sct}(\lambda, z_j, \theta)}\right) \left(\uparrow F^{i-1}(\lambda, z_j) + \downarrow F^{i-1}(\lambda, z_{j+1})\right) \tag{3.30}$$

where τ_{sct} is the optical depth due to scattering only. Half of this additional flux broadcasts downward and the other half upward. Putting all together, for i^{th}-iteration we can use following equations to calculation the photon fluxes:

$$\begin{aligned} \downarrow F^i(\lambda, z_j) = \Bigg\{ & \downarrow F^i(\lambda, z_{j+1}) + \\ & 0.5 \left(1 - e^{-\tau_{sct}(\lambda, z_j, \theta)}\right) \left(\uparrow F^{i-1}(\lambda, z_j) + \downarrow F^{i-1}(\lambda, z_{j+1})\right) \Bigg\} e^{-\tau(\lambda, z_j, \theta)} \end{aligned} \tag{3.31}$$

$$\begin{aligned} \uparrow F^i(\lambda, z_j) = \Bigg\{ & \uparrow F^i(\lambda, z_{j-1}) + \\ & 0.5 \left(1 - e^{-\tau_{sct}(\lambda, z_{j-1}, \theta)}\right) \left(\uparrow F^{i-1}(\lambda, z_{j-1}) + \downarrow F^{i-1}(\lambda, z_j)\right) \Bigg\} e^{-\tau(\lambda, z_{j-1}, \theta)} \end{aligned} \tag{3.32}$$

3.1.5 Discretization onto the model grid

In general, there is no analytical solution for the continuity equation, Equation 3.2, in its general form. The solutions can be approximated by numerical methods and in order to apply these methods, the equation must be discretized. We use the first-order upwind scheme (Wendt 2008) to discretize the equation. In continue is the continuity equation in its discretized form:

$$\frac{\partial f_i^j}{\partial t} = \frac{P_i^j}{n_T} - f_i^j L_i^j - \frac{(r^{j+1/2})^2 \Phi_i^{j+1/2} - (r^{j-1/2})^2 \Phi_i^{j-1/2}}{n^j (r^j)^2 (z^{j+1/2} - z^{j-1/2})}, \tag{3.33}$$

where i and j denote species and altitude layer indices, respectively. j+1/2 and j-1/2 refer to the upper and lower boundaries of j^{th} layer. All variables at the boundaries (except $\Phi^{j\pm1/2}$) are approximated as the arithmetic mean of their values at the sandwiching layers; e.g.:

$$n^{j\pm1/2} \approx (n^{j\pm1} + n^{j})/2 \tag{3.34}$$

The transport terms ($\Phi^{j\pm1/2}$) can then be approximated as:

$$\begin{aligned}\Phi^{j\pm1/2} \approx -K_{zz}^{j\pm1/2} n^{j\pm1/2} \left.\frac{\partial f_i}{\partial z}\right|_{j\pm1/2} - \\ D_i^{j\pm1/2} n^{j\pm1/2} \left\{ \left.\frac{\partial f_i}{\partial z}\right|_{j\pm1/2} + \left\{ \frac{f_i^{j\pm1/2}}{H_i^{j\pm1/2}} - \frac{f_i^{j\pm1/2}}{H_0^{j\pm1/2}} + \frac{\alpha_i}{T^{j\pm1/2}} \left.\frac{dT}{dz}\right|_{j\pm1/2} f_i^{j\pm1/2} \right\} \right\},\end{aligned} \tag{3.35}$$

where the derivatives can be approximated according to their values at the neighbouring layers as follow:

$$\left.\frac{\partial f_i}{\partial z}\right|_{j\pm1/2} \approx \frac{f_i^{j\pm1} - f_i^{j}}{z^{j\pm1} - z^{j}}, \left.\frac{dT}{\partial z}\right|_{j\pm1/2} \approx \frac{T^{j\pm1} - T^{j}}{z^{j\pm1} - z^{j}} \tag{3.36}$$

In the next section we provide an overview of our choice of numerical solver and chemical networks and in Section 3.3, we present the results of verification of our model under different conditions such as thermochemical equilibrium or by including molecular and eddy diffusion, photochemistry, condensation, and setting up atmospheric influxes and different boundary conditions.

3.2 Numerical solver and added physics

3.2.1 Chemical solvers

The challenge of most chemical kinetic models is to find an efficient method to solve the system of ordinary differential equations (ODEs), which are stiff and sparse in nature. Diversity of physical and computational complexities in the simulation of planetary atmospheres results in different degrees of stiffness, and hence complicates the choice of a fast and yet accurate sparse-stiff ODE solver. We have examined two well-established ODE solver packages from the ODEPACK collection, namely DLSODE (Double precision Livermore Solver for Ordinary Differential Equations) and

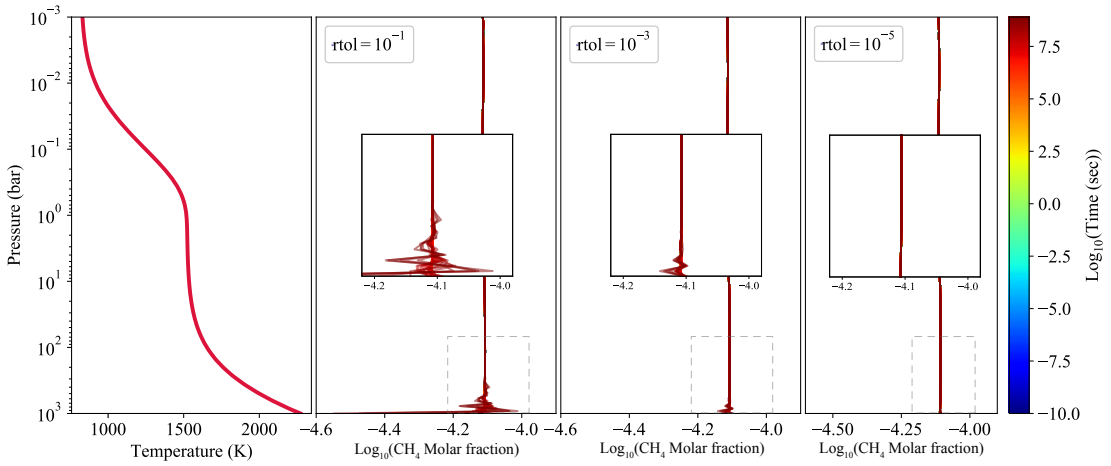

Figure 3.1: Numerical instability due to the choice of relative tolerance, rtol, in the numerical solver. Poor numerical convergence occurs at high temperature-pressure regions of the atmosphere, unless a proper rtol value is chosen. **Left)** Temperature profile of a typical Hot Jupiter with T_{eff}=1500 K. **Rest of panels)** show the time evolution of CH_4 vertical abundance. Initial abundances are calculated by Gibbs free minimization and are expected to remain the same throughout the simulation. Three simulations are the same, except their choice of rtol. Simulations with rtol= 10^{-1} and 10^{-3} show non-negligible numerical instabilities, whereas rtol= 10^{-5} results in an adequately accurate abundance estimation.

DVODPK (Double precision Variable-coefficient method for Ordinary Differential equations using Preconditioned Krylov method) (Hindmarsh 1983).

The DLSODE solver is based on the older GEAR and GEARB packages, and has the same numerical core. In GEAR, the error is controlled only by one scalar relative error tolerance, called EPS. In DLSODE, on the other hand, the user can set both relative and absolute error tolerances, rtol and atol, which optionally can be scalar or vector. The choice of these error tolerances are usually a compromise between the accuracy and speed of the simulation, i.e. a smaller error tolerance makes the solutions more accurate, but at the same time it increases the computational time, because the solver requires more iterations to achieve the specified tolerance. Our extensive examination of rtol and atol indicates that the computational time scales with rtol exponentially, but the choice of atol has no significant effect on the computational time. Therefore, we choose a very small atol, 10^{-99}, as the default atol value for our simulations.

A choice of rtol= 10^{-1}, 10^{-2} or 10^{-3} can be used for a rapid verification of the

system's behavior, but we recommend rtol= 10^{-5} to insure numerical stability when the production and loss terms are large, but of the same order, i.e. the system is at or close to ∼steady state, see Figure 3.1. In this figure we present a worst case scenario where the atmosphere is initialized at its equilibrium state and is forced to remain at that condition by using chemical kinetic calculations. This is not the usual setup and planetary models normally include at least one disequilibrium process such as diffusion. The numerical instability at rtol= 10^{-1} and 10^{-3} are shown in Figure 3.1 are for CH_4 abundance profiles but almost all other species behave similarly. Diffusion usually relaxes the limit on rtol for achieving the numerical stability and introduces a damping effect. In addition, stronger diffusion forces the system to reach the steady state faster; leading to less propagated numerical errors in the steady state solution of the system. Hence, a lower rtol can be selected when stronger diffusion mechanism are in play.

It is also possible to specify the tolerances as vectors; i.e. assigning each species its own relative and absolute tolerances. This treatment could be used, for instance, on a reactant that is completely depleted in at least one vertical layer. In this chapter, we use scalar values for rtol and atol with the values of 10^{-5} and 10^{-99}, respectively.

DVODPK employs iterative methods to solve linear algebraic systems. It is based on orthogonal projection techniques, which approximate a solution of the linear system from a Krylov subspace. This technique is more advanced and more efficient in comparison with DLSODE's method (Nejad 2005), however, its usage requires decomposition and initialization of the Jacobian matrix. This is not a trivial task and our investigations revealed that this technique requires adaptation of the Jacobian decomposition for every new simulation. Moreover, DVODPK's performance changes significantly with the physical conditions considered in the model, such as inclusion of condensation, ablation, outgassing, etc.

On top of all is DVODPK's inefficiency under planetary atmosphere conditions. Figure 3.2 illustrates the DVODPK's running time for a suite of 0D simulations over a broad range of densities and temperatures. We found DVODPK is less efficient to solve ODEs at higher density and temperature conditions, and hence is not suitable

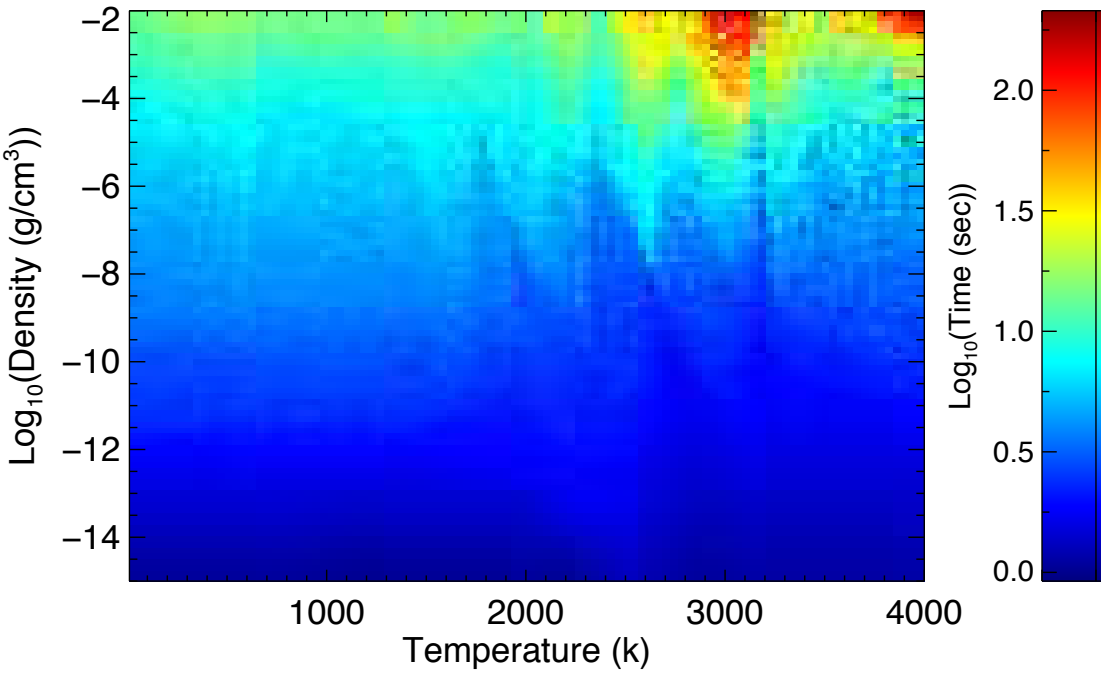

Figure 3.2: DVODPK's running time for a suite of 0D simulations over a broad range of densities and temperatures. The solution of the system of ODEs by DVODPK appears to be less efficient at higher density and temperature conditions.

for the application to planetary atmosphere kinetic simulations. Therefore we use DLSODE from the ODEPACK library as our default solver.

3.2.2 Chemical networks

Answering the question of which set of reactions, i.e. chemical network, must be used in a chemical kinetic model is arguably the most important question that should be addressed before setting up a model. One could establish a chemical network from the scratch by doing a standard literature search for the thermodynamic polynomial coefficients, reaction rate constants, UV cross sections, and branching ratios, or alternatively employ the commonly used networks in the field. Here we took the latter approach as the establishment of a new network is beyond the scope of this study. Currently, nine chemical networks are available in `ChemKM`: Moses's Hot Jupiter network (Moses et al. 2011), Venot's 2012 network (Venot et al. 2012), Hebrard's Titan network (Hébrard et al. 2012), Hebrard's C_3H_p network (Hébrard et al. 2013), Venot's full network (Venot et al. 2015), Vulcan H-C-O

Chemical Network	Elements	Species	Reactions	Reference
Moses Hot Jupiters	H-C-O-N	90	800	Moses et al. 2011
Venot 2012	H-C-O-N	103	963	Venot et al. 2012
Hébrard 2012	H-C-O-N	135	788	Hébrard et al. 2012
Hébrard 2013	H-C-O-N	90	941	Hébrard et al. 2013
Venot 2015	H-C-O-N	238	2011	Venot et al. 2015
VULCAN H-C-O	H-C-O	29	143	Tsai et al. 2017
Moses Ice-giants	H-C-O	69	385	Moses et al. 2018
Venot reduced	H-C-O-N	29	181	Venot et al. 2019
Pearce HCN	H-C-N	11	42	Pearce et al. 2019

Table 3.1: General characteristics of chemical networks implemented in `ChemKM`. He and Ar are excluded from the list of species. The reverse reactions calculated by using the thermodynamic principle of microscopic reversibility are not included.

network (Tsai et al. 2017), Moses's ice-giants network (Moses et al. 2018), Venot's reduced network (Venot et al. 2019), and Pearce's HCN network (Pearce et al. 2019), which differ in the complexity, size (number of species and reactions), type of chemistry (reversible/irreversible, H-C-O species, H-C-O-N species, HCN network), and the temperature range over which the chemical schemes are valid, see Table 3.1.

`ChemKM` is able to handle a variety of reaction types including KIDA's standard formulations[2] (e.g. Modified Arrhenius reactions, third body assisted reactions with Troe (Troe 1983; Gilbert et al. 1983), and SRI (Stewart et al. 1989; Kee et al. 1989) falloff functions) as well as Vuitton (Vuitton et al. 2011) and Jasper (Jasper et al. 2007) formulations. Therefore `ChemKM` can easily accept new networks as the input of models.

3.2.3 Condensation and rainout

Observations of planets suggest the presence of clouds nearly in all classes of planets with substantial atmosphere. For instance, Venus is fully covered by a thick cloud layer, containing mostly H_2SO_4 particles (e.g., Molaverdikhani et al. 2012). On Earth, water clouds produce a patchy scenery, covering about 70% of the surface with optical depth of larger than 0.1 (e.g., Stubenrauch et al. 2013). Despite its

[2] http://kida.obs.u-bordeaux1.fr

tenuous atmosphere, conditions on Mars allow for the formation of what is mostly believed to be high-altitude CO_2 clouds (e.g., Clancy & Sandor 1998).

Outer planets in the solar system have even colder atmospheres, resulting in more efficient cloud-forming environments. Observations and simulations support the formation of NH_3, NH_4SH, and H_2O Jovian clouds above 10 bar. Their altitude and thickness, however, could vary both spatially and temporally (Pater et al. 2016). Clouds with similar compositions are expected to form on Saturn; owing to their similarities in temperature structure and bulk composition. However, there are some subtle differences that result in vertically more extended clouds and higher amount of gas above the cloud-bases on Saturn (West et al. 2009; Atreya et al. 1999). Saturn and Neptune observations also show evidence of CH_4 and H_2S clouds in addition to NH_3, NH_4SH, and H_2O clouds, due to their colder environments (Irwin et al. 2018, 2019b).

Although not a planet anymore, Pluto, as seen by the New Horizon spacecraft, is covered by layers of hazes (Gladstone et al. 2016; West 2017), likely due to condensation of hydrocarbons and nitriles such as C_2H_2, C_2H_4, C_2H_6, and HCN (Gao et al. 2017). We also have to mention Titan, since it has a unique and substantial atmosphere, with hydrocarbon and nitrile cloud types. This includes HCN, HC_3N, CH_4, C_2H_2, and C_2H_6 coated particles (Lavvas et al. 2011).

Clouds on gaseous planets beyond the solar system have also been observed. Sing et al. (2016) studied the transmission spectra of 10 Hot Jupiters and concluded that there is very likely a continuum of exoplanetary atmospheres; covered by haze and clouds with a variety of compositions. For instance, a nearly flat transmission spectrum of GJ 1214b (a sub-Neptune planet with an equilibrium temperature of 580 K) is consistent with a planet which is fully covered by clouds; most likely composed of ZnS and KCl (Kreidberg et al. 2014a). Hotter Class-II gaseous exoplanets[3] with a temperature range of ∼1000 K to ∼1650 K could have Na_2S, MnS, Fe, Al−oxides, or silicate clouds such as Mg_2SiO_3 and Mg_2SiO_4 clouds. Even Ultra-Hot Jupiters ($T \gtrsim 2500$ K) are expected to have cloud formation on

[3]See Chapter 2 or (Molaverdikhani et al. 2019b) for the classification scheme.

their nightside (Helling et al. 2019a; Keating & Cowan 2018), which could be dragged toward the dusk terminator of the planet and potentially contribute in the transmission spectra and transit depth of these planets (e.g. Helling in perp.). For a recent review on exoplanet cloud formation see Helling (2019a).

All these studies suggest the importance of condensation and particle formation in planetary atmosphere models. However, including even a simplified microphysiscs model, such as atmospheric models by Rossow (1978), in a chemical kinetic model demands high computational resources mostly because of the shorter timescales that condensation and evaporation operate on relative to the vapor transport or gas-phase chemistry timescales (Moses 2014). Hence a simpler approach is usually taken.

Dobrijevic et al. (2010) assumed condensation of species when their abundances reach their saturation level. After hitting this condition, they did not solve the continuity equation of that species at the given altitude; resulting in numerical stability and high computational efficiency of the scheme. A consequence of this approach is that the abundance of the condensed species follows its saturation curve perfectly. But condensation processes could occur at different saturation levels. Capillary condensation is an example, which through this mechanism the vapor condensation occurs below the saturation vapor pressure (Stokes & Evans 1997).

Moses et al. (2000a,b) treated the condensed phase of a species as a separate species that is produced by condensation and lost by evaporation through the following reactions:

$$\mathrm{species\,(g)} + \mathrm{dust} \longrightarrow \mathrm{species\,(s)} \tag{3.37}$$

$$\mathrm{species\,(s)} + \mathrm{V} \longrightarrow \mathrm{species\,(g)} \tag{3.38}$$

where “dust” represents the condensation nuclei (CN) and must be provided, “V” represents a dummy molecule and its number density assumed to be 1 cm^{-3} at all atmospheric levels, and the subscripts (g) and (s) refer to the gas and condensed phases, respectively. This scheme assumes the pre-existence of CN in the atmosphere; allowing the condensation of materials on these sites. They estimated

the rate of these reactions by assuming steady-state diffusion-limited condensation and followed Seinfeld (1986) rate estimations.

We follow a similar approach to account for the condensation, but with slightly different rate estimations adapted from Seinfeld & Pandis (2012) as follow:

$$J_c = 4\pi R_p D_g (c_\infty - c_s) \tag{3.39}$$

where J_c is the total flow of the species toward the particle (moles $\sec^{-1}$), R_p is the particle's radius, D_g is the diffusivity of the species in the atmosphere, c_∞ is the concentration of the species far from the particle, and c_s is its vapor-phase concentration at the particle surface. It is evident that when $c_\infty > c_s$ then the species flows toward the particle and if $c_\infty < c_s$ it moves away from it. c_s can be estimated from the vapour pressure of species at any given temperature (vapour pressure data of more than 1700 substances are provided in Haynes (2016) and being updated regularly). To consider the condensation in `ChemKM`, the user is only required to provide a list of desired species to condense. The code then internally handles the addition of "dummy" reactions and condensed phase of species.

Gravitational acceleration leads to the settlement of condensed particles, i.e. rainout, which tends to remove the condensed materials from the atmosphere. Hence, not including the rainout could cause some discrepancies between the observations and models. Two well-known cases are the detection of H_2S gas on Jupiter (Niemann et al. 1998) and the presence of gaseous alkalies in cool brown dwarf and exoplanet atmospheres (Marley et al. 2002; Morley et al. 2012; Line et al. 2017; Zalesky et al. 2019). On Jupiter, Fe could deplete all sulphur content from the upper atmosphere through condensation of FeS; leaving no sulphur to form H_2S. Adding a Fe-rainout mechanism, however, could deplete all Fe from those regions, hence allowing H_2S to form. Similarly, on brown dwarfs and exoplanets, retaining the silicates at high altitudes can eventually lead to the formation of alkali feldspars; resulting in the depletion of alkalies from the upper atmosphere. Including silicate-rainout processes could prevent such an outcome by removing the silicates from those regions (e.g., Mollière et al. 2015). As an option in `ChemKM`, this effect can be included by removing

the condensates as soon as they condense. A more sophisticated rainout scheme is under development to take into account a proper estimation of the drag force upon the particles and approximation of the settling velocity.

3.2.4 Ablation and escape

Ablation of micro-meteoroids during atmospheric entry is thought to be a potential source of volatile gases (such as H_2O, CO, CO_2, and SO_2) that cannot be maintained at the upper atmosphere of planets otherwise. These species could change the chemistry and dynamics of the upper layers. For instance, photolysis of the ablated water produces hydroxyl radicals (OH) (Moses & Poppe 2017), which can react with many other species and cause new reaction pathways and products. Although the details of such processes (even on Earth) is not fully understood (e.g., Hawkes et al. 2008), usually an ablation rate for each species can be estimated based on the observations of the upper atmosphere of planets through a retrieval procedure (Moses 1992; Hörst et al. 2008; Moses & Poppe 2017).

Atmospheric escape is another process in action at the outermost layers of planetary atmospheres. Several atmospheric escape mechanisms have been identified so far; most of which are non-thermal processes, such as pickup by stellar-wind, bulk escape through magnetic flux ropes, or sputtering (e.g., Hunten 1982). While these processes could be the dominant escape mechanisms on colder planets (e.g., Brain et al. 2015; Jakosky et al. 2015), hydrodynamic escape (as one of the thermal processes) is believed to be, at least, as important as non-thermal mechanisms for hot exoplanets (e.g., Salz et al. 2016). Including all these processes into a chemical kinetic model would be a major task and computationally expensive. Thus, a simplified approach (e.g., Moses et al. 2018; Dobrijevic et al. 2014; Hébrard et al. 2013) could be useful. In this approximation, an escape rate is provided for each species at the top of the atmosphere (TOA) and species are removed from the uppermost layer by this rate.

Although gaseous planets have no solid surface, a virtual boundary can be defined as well. For the adequately hot planets, the bottom layer can be selected

at a high pressure, where the atmosphere remains at thermochemical equilibrium. However, for cold gaseous planets, their upper troposphere, where a cold-trap is formed, is usually selected to set a boundary layer condition for the chemical models as the bottom layer in the kinetic models is usually not at the thermochemical equilibrium and the local atmosphere is likely prone to the disequilibrium processes. This setting provides more flexibility at the bottom layer of chemical models. For instance, it can be used to estimate the vertical CH_4 vapor flux that makes it past the tropopause cold trap of Uranus and Neptune (e.g., Moses et al. 2018).

These processes can be included by setting the flux rate of species at the top of the atmosphere. Similarly, outgassing and deposition can be included by setting the flux rate of species at the bottom boundary layer in `ChemKM`.

3.2.5 Cosmic rays and scattered Ly-alpha by LIPM

Galactic and solar cosmic rays (GCRs) are the main source of ionization at altitudes below 55–60 km on Earth (Velinov 1968; Bazilevskaya 2000); shaping Earth's stratosphere and thermosphere. GCRs are also the main driving factor of Titan's photochemistry at pressures between 1 and 50 mbar. Particularly GCR-cascade dissociates N_2, a crucial process to synthesis nitrogen organics such as HCN (e.g., Capone et al. 1983). GCRs have shown to be important on Neptune's (e.g., Selesnick & Stone 1991; Lellouch et al. 1994; Aplin & Harrison 2016), Titan's (e.g., Molina-Cuberos et al. 1999; Yung et al. 1984), and likely exoplanets' (e.g., Helling et al. 2011; Rimmer & Helling 2013; Scheucher et al. 2018) upper atmospheres, too. A list of GCR reactions along with their rate profiles can be provided to the current version of `ChemKM` for the inclusion of GCRs. A new GCR module is under development to self-consistently calculate the GCR rates.

Isotropic source of stellar background UV radiation and solar Lyman-α photons that are scattered from atomic hydrogen in the local interplanetary medium (LIPM) are important dissociation/ionization sources at weakly irradiated environments (e.g., Strobel et al. 1991; Moses 1991; Bishop et al. 1998), such as polar regions and nightside of closely orbiting planets or the entire atmosphere of planets orbiting

at large distances from their host stars. A wavelength dependent flux of these irradiation sources can be provided to `ChemKM` to be included in the model.

3.2.6 Initialization

Once all desired physics in the model are set up, one should provide the initial conditions for the temperature-pressure (TP) and abundance profiles. The current version of `ChemKM` only considers the TP structure statically; i.e. the TP structure does not change as abundances evolve with time. Abundances can be initialized with two options: 1) by providing the elemental abundances or 2) by providing the molar fraction of any desired species at t_0=0.

As a first step, it is possible to calculate the thermochemical equilibrium abundances of species through Gibbs free minimization. We use a slightly modified version of petitCODE's easy_chem module to perform this (Mollière et al. 2017). Alternatively, the thermochemical equilibrium can be achieved through kinetic calculations. The first approach is usually more suitable, unless the temporal evolution of a system to its thermochemical equilibrium state is as of interest.

Finally, depending on what physical processes are considered in the model, other inputs are also required; for instance the vertical mixing coefficient profile for the eddy diffusion or the influx rates.

3.3 Model verification

3.3.1 Numerical integrator

We start the verification of the code by showing how the DLSODE numerical integrator performs. Figure 3.3 shows the numerical and analytical solutions of the following system of ODEs:

$$\begin{aligned} \frac{dy_1}{dt} &= -y_2 \\ \frac{dy_2}{dt} &= y_1 \end{aligned} \tag{3.40}$$

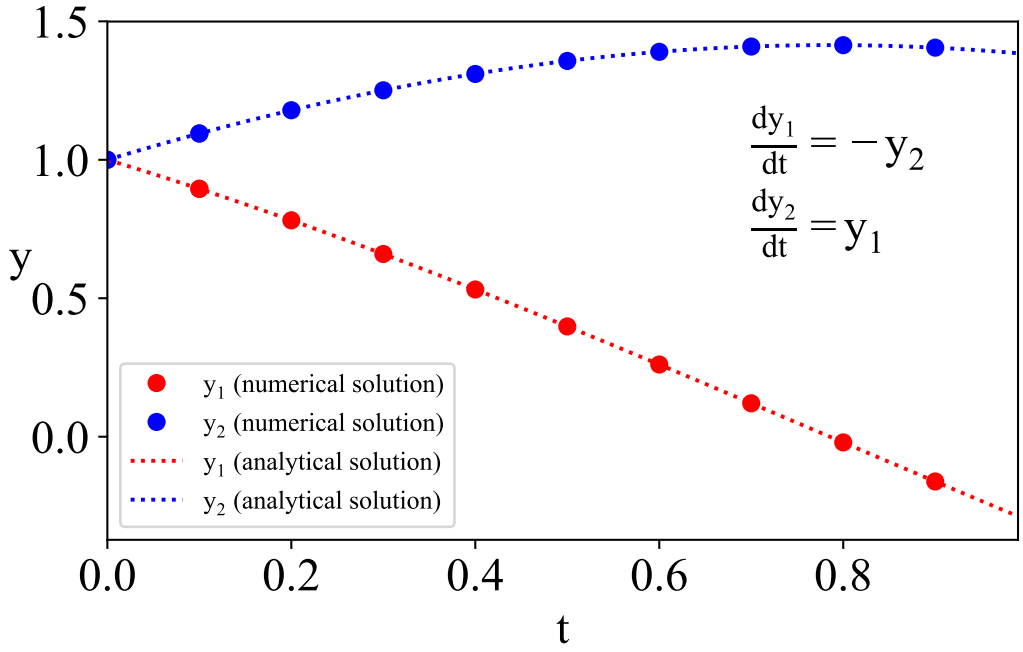

Figure 3.3: Numerical integrator's performance for a simple case. The results are compared with the analytical solution of the system. They agree within the numerical errors.

where y_i is the abundance of species i at any given time, t. Abundance variation of each species depends on one another, hence the system is coupled. The analytical solution of this simple system is as follow, assuming $y_1(0) = y_2(0) = 1.0$:

$$\begin{aligned} y_1 &= Cos(t) - Sin(t) \\ y_2 &= Cos(t) + Sin(t) \end{aligned} \tag{3.41}$$

The results of analytical and numerical solutions are in agreement, hence the numerical performance is assured within the numerical errors.

3.3.2 Thermochemical equilibrium

Because of the relatively high temperatures at the photosphere of most of known giant exoplanets, simulations of their atmospheric chemistry usually require the consideration of reversible reactions in the model. One issue that have been addressed by previous studies as well (e.g. Moses et al. (2011); Venot et al. (2012);

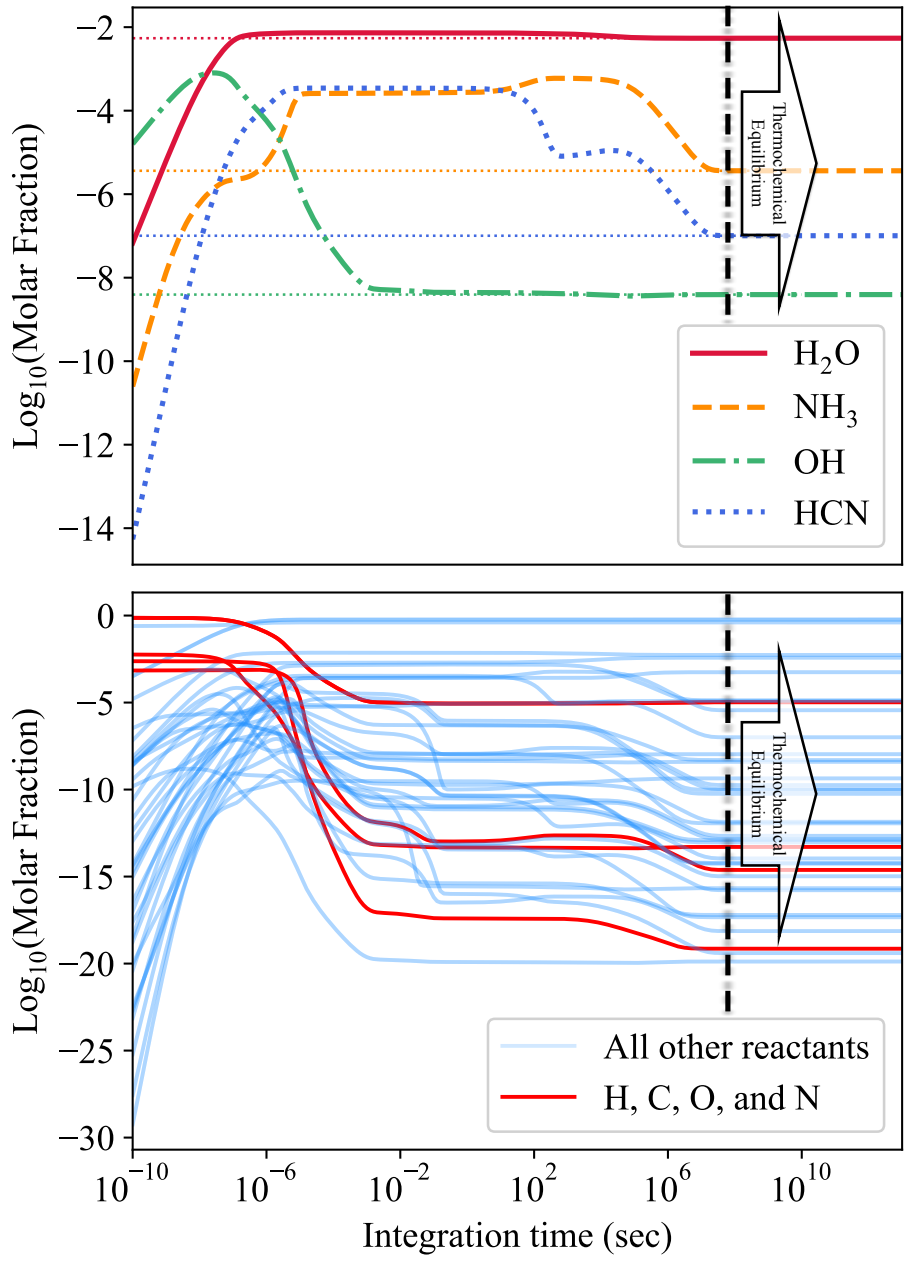

Figure 3.4: Consistency of the thermodynamic equilibrium composition (dotted straight lines) and `ChemKM`'s kinetic steady state solutions in a reversible system of reactants in a 0D model setup with T=1560 K and P=10 bar. The result of the thermochemically reversed model is shown as a function of integration time for different species. **Top)** Evolution of H_2O (solid red), NH_3 (dashed orange), OH (dashed-dotted green), and HCN (dotted blue), until they reach their thermochemical equilibrium abundances. **Bottom)** Evolution of H_2, He, H, CO, H_2O, CH_4, N_2, NH_3, CO_2, HCN, C_2H_2, O_2, O(^{3}P), O(^{1}D), C, N(^{4}S), N(^{2}D), OH, CH_3, $^3CH_2$, $^1CH_2$, CH, NH_2, NH, H_2CO, HCO, CN, C_2H, NO, HNO, NCO, HNCO, HOCN, HCNO, C_2H_3, C_2H_4, C_2H_5, and C_2H_6 abundances. Atomic abundances (red lines) deplete as molecules (blue lines) are being produced under this condition.

Drummond et al. (2016)) is the unavailability of rate coefficients for most reverse reactions. A common workaround is to calculate these rates as the ratio between the forward rate constant and the equilibrium constant. The equilibrium constant, therefore, can be calculated by using NASA thermodynamic polynomial coefficients (McBride et al. 2002). Inclusion or exclusion of reverse reactions in `ChemKM` is optional, but if it is chosen to be included then it follows the above described method to calculate the reverse rate coefficients.

Taking this approach ensures the consistency of kinetics and thermodynamics steady state solutions. Figure 3.4 shows this consistency and compares the results of a simple 0D model at T=1560 K and P=10 bar for a kinetic chemical model with reversible reactions (curves) and thermodynamic equilibrium calculations (straight thin dotted lines). The kinetic model reaches the thermodynamic equilibrium after 10^7 sec with molar fractions practically being identical. Initial atomic abundances (red lines) deplete as molecules (blue lines) are being produced. Obviously, the chemical evolution of reactants depends on the choice of chemical network. For this test, and all other verification tests in this section, we employ the Venot et al. (2012) kinetic network as a verified and benchmarked chemical network.

Figure 3.5 provides a similar comparison for a 1D model. Neither our 0D nor the 1D model includes mixing or photolyses for these two tests. The temporal evolution of abundances are color-coded by time where green to red shows the progress in time from 10^{-10} sec to 1.6×10^{18} sec (beyond the age of universe). We show a chemically important atom, N(^{4}S), one oxygen−bearing major opacity molecule, H_2O, and one expectedly abundant carbon−bearing molecule at high temperatures, HCN, as examples. It is evident that the abundances at kinetically steady state (dark red) are in agreement with their thermodynamic equilibrium values (gray lines) when the local temperature is adequately high (usually above 1000 K). The N(^{4}S) and HCN abundances at pressures between 10^{-2} and 10^{-8} bar have not fully reached their thermochemical equilibrium and require longer integration times. This shows that the calculation of thermochemical equilibrium is better performed through Gibbs free energy minimization.

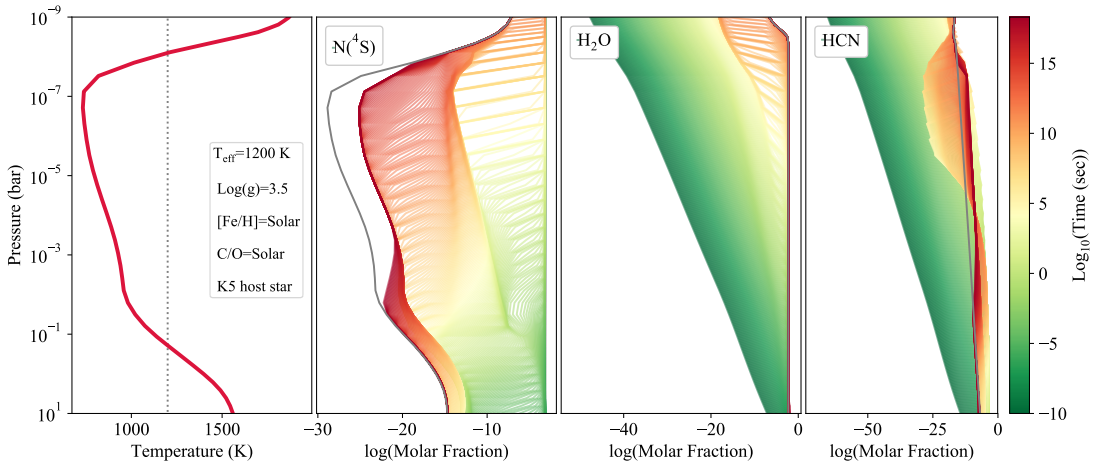

Figure 3.5: Similar to Figure 3.4 but with a 1D model; without the inclusion of vertical mixing or photolyses. **left)** Temperature profile of an irradiated exoplanet with T_{eff}=1200 K, log(g)=3.5, with solar metallicity and C/O ratio, orbiting around a K5 star. **Rest of panels)** from left to right: The temporal evolution of N(^{4}S), H_2O, and HCN abundances, color-coded by time, where green to red shows the progress in time from 10^{-10} sec to more than the age of universe, 1.6×10^{18} sec. The thermochemically reversed model (colored lines) is in agreement with the thermochemical equilibrium calculations (gray lines) at adequately high temperatures ($\geq$1000 K). However, abundances at pressures between 10^{-2} and 10^{-8} bar ($<$1000 K) have not fully reached their thermochemical equilibrium yet and demand longer integration times.

As already mentioned, the "kinetically thermochemical equilibrium" mode, i.e. solving the system of ODEs without diffusion or photolyses, can be used as a pre-processing step to initialize the model with thermochemical equilibrium abundances. However, `ChemKM` has the option to quickly calculate abundances at thermochemical equilibrium by using Gibbs free energy minimization. Figure 3.1 shows an example of such a setup, where the model is initialized by using Gibbs free energy minimization and *all* abundances remain the same in the kinetic calculations due to the lack of additional physics such as diffusion or photolyses, hence verifying the validity of our reversible setup to reach or keep the same composition as in thermochemical equilibrium. See Section 3.2.6 for a description of initialization options in ChemKM.

3.3.3 Molecular and eddy diffusion

Transport-induced quenching is one of the main kinetic-related disequilibrium processes in planetary atmospheres. Both molecular and eddy diffusion could play pivotal roles to drive away the atmospheric composition from their thermochemical

equilibrium. If the chemical kinetic timescales are larger than the transport timescales, the mole fraction of a parcel of gas can become quenched in the atmosphere. This usually happens when the temperature and pressure are low enough that the kinetic reactions cannot rapidly occur in both directions; allowing the diffusion processes to drive the system away from its thermochemical equilibrium state.

Figure 3.6 gives an example for such a system with a 1D atmosphere evolving from its thermochemical equilibrium state. We use the same setup as our 1D example presented in the previous section (Figure 3.5), but initialize the composition with their thermochemical equilibrium values. We include a vertically constant eddy diffusion (K_{zz}=10^4 cm^2s^{-1}) in the model. We choose this relatively low K_{zz} to demonstrate its significance even in the case of a hot atmosphere (e.g. in this case T_{eff}=1200 K). No photolyses is included in this setup to only present the effect of diffusion. The abundances reach to a new steady state known as the "diffusion equilibrium" (e.g. Lettau 1951). A cross-section of Figure 3.6 at 10^{-10} bar is shown in Figure 3.7 to graphically illustrate the evolution of abundances until they reach the diffusion equilibrium at TOA. Continuing the integration until 10^{20} sec did not change this new steady state within numerical errors; hence we conclude that this state is a real diffusion equilibrium.

The quenching levels of of O(^{1}D), N(^{4}S),NO, CH_4, CO_2, CO, see Figure 3.6, are in agreement with the general estimations of quenching levels in Venot et al. (2018). The quenching level of each constituent, however, depends on its chemical kinetics timescales, ranging from 1 to 10^{-3} bar in this example.

A commonly used definition of the "quenching point" (a.k.a. quenching pressure or quenching level) is that the composition of all species remain constant above that level, that is the abundances remain the same as their abundances of their quenching point (e.g. Moses 2014). This assumption has been also used to mimic a parameterization of disequilibrium processes, usually in the retrieval models as a trade-off to gain more speed (e.g. Madhusudhan & Seager 2011). However, a constant abundance profile is rarely the case in realistic planetary atmospheres and atmospheric constituent abundances could show significant deviations from

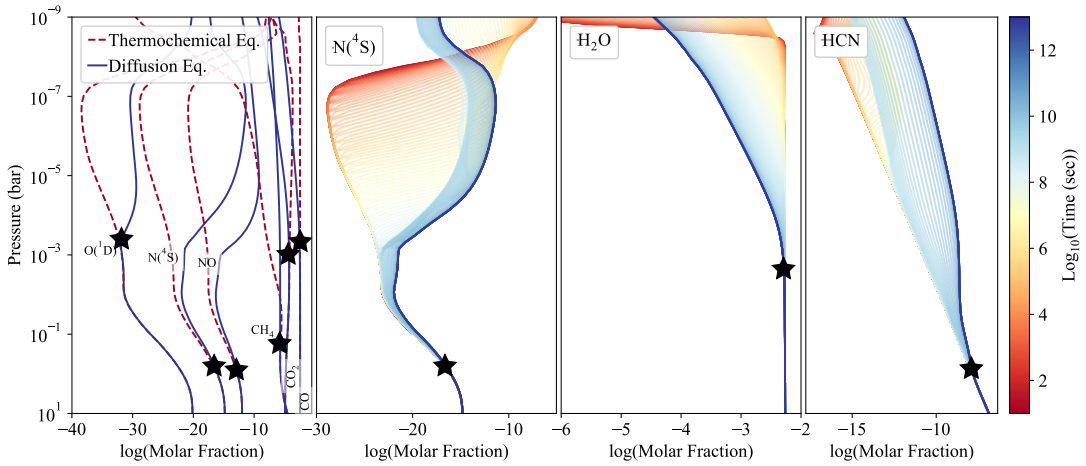

Figure 3.6: Time evolution of our 1D model presented in Figure 3.5 from its thermochemical equilibrium state to diffusion equilibrium, by introducing molecular diffusion and a vertically constant eddy diffusion (K_{zz}=10^4 cm^2s^{-1}). **Left panel)** Thermochemical equilibrium (dashed red lines) and diffusion equilibrium of $O(^1D)$, $N(^4S)$,NO, CH_4, CO_2, CO (solid blue lines). **Rest of panels)** Temporal evolution of $N(^4S)$, H_2O, and HCN abundances in detail. They are color-coded by time, where blue to red shows the progress in time from 10^1 sec to 10^{13} sec. The quenching points are shown by the stars.

their quenched abundances. Prominent processes at mbar level, such as molecular diffusion or photolysis, could drive the abundance profiles away from an idealized constant profile. A non-isothermal TP structure, for example a hot thermosphere with local heating at TOA (as it is the case in the current example, see the TP structure in Figure 3.5), can result in a variation of chemical timescales at different altitudes and might trigger the system to move in and out of thermochemical equilibrium. Including the vertical diffusion causes mixing of these abundances at different pressures; potentially keeping them away from a constant profile. For instance, dissociation of H_2O at TOA due to a hot upper thermosphere depletes its abundances at higher pressures through vertical mixing, see e.g. Figure 3.6.

In addition, such sharp temperature gradient could also enhance the molecular diffusion (see Equation 3.3), resulting in more deviation from a constant abundance profile. The left panel of Figure 3.6 represents such examples, where abundances do not remain constant above their quenching points (black stars) both due to molecular diffusion and thermal−dissociation. More discussion will follow in Section 4.2.3. As a rule of thumb, a constant quenched abundance profile is likely to be valid

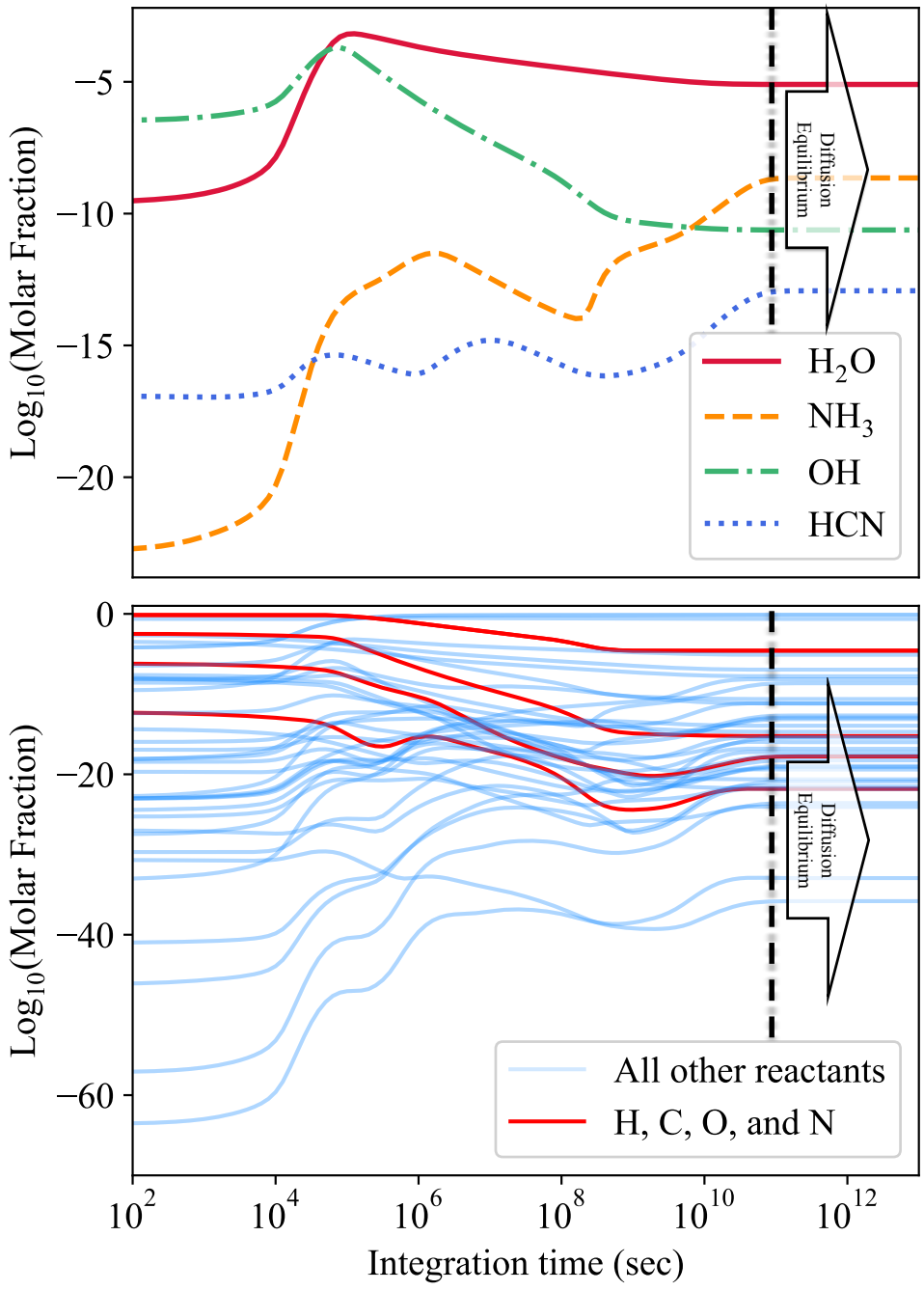

Figure 3.7: A cross-section of Figure 3.6 at 10^{-10} bar to illustrate the "diffusion-equilibrium" at the top of the atmosphere after 10^{11} sec.

when the chemical kinetics timescale is much shorter than the timescale of all other processes at all pressures above the quenching point.

3.3.4 Photochemistry

Photochemistry is another prominent disequilibrium process in planetary atmospheres. We examine the same case as in the previous section, but include photochemistry instead of diffusion. We use an updated version of Hébrard et al. (2012) photolysis reactions (originally adapted from the MPI-Mainz UV/VIS Spectral Atlas Keller-Rudek et al. (2013)) and a stellar flux similar to the average solar flux over an entire solar cycle from Thuillier et al. (2004) as the radiation flux at TOA. We initialize abundances with their thermochemical equilibrium values, identical to the previous section initialization.

Figure 3.8 shows the effect of photolysis on this model. The photochemical timescales are typically shorter than diffusion processes and hence the photolysis should be the dominant mechanism at TOA. Each species responds to the irradiation differently, depending on its shielding and UV cross-section. Some have excess production through photolysis reactions, e.g. $N(^4S)$ in this model, some face considerable destruction by this process, e.g. H_2O, and some could have a combination of those depending on the altitude, e.g. HCN.

After some time, the system reaches a new steady state, the "photochemical equilibrium", balancing between reversible reactions and photodissociation. The required integration time to achieve photochemical equilibrium at all vertical levels strongly depends on the atmospheric temperature structure; with hotter atmospheres tending to reach the photochemical equilibrium faster. This is evident in Figure 3.8, where reaching the photochemical equilibrium at around 10^{-3} bar requires integration times larger than the age of the universe.

Absorption cross-sections, the quantum yields, and the actinic flux[4] at a given altitude determine the photodissociation rate of a photo-reactant. Figure 3.9 shows

[4] "The quantity of light available to molecules at a particular point in the atmosphere and which, on absorption, drives photochemical processes in the atmosphere." See Calvert (1990) for more details.

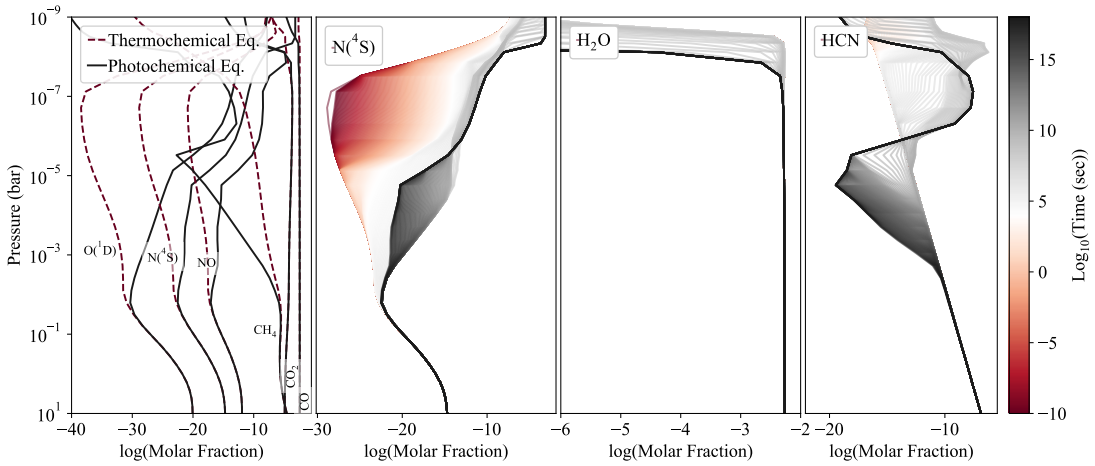

Figure 3.8: Temporal evolution of the 1D model presented in Figure 3.5 but evolving from its thermochemical equilibrium to photochemical equilibrium by introducing photolysis into the model. No diffusion is included in the model to purely present the effect of photolysis. The temporal evolution of abundances are color-coded by time, where red to black shows the progress in time from 10^{-10} sec to beyond the age of universe, 10^{18} sec. Abundances around 10^{-3} bar have not fully reached their photochemical equilibrium yet and require longer integration times.

the irradiation at TOA and the actinic flux at different pressures. The stellar flux quickly vanishes at wavelengths shorter than 220 nm due to strong UV absorption cross-section of photo-reactants at those wavelengths. The rest of the stellar flux is also affected by Rayleigh scattering in this model.

3.3.5 Condensation

To demonstrate `ChemKM`'s ability to capture condensation, we model an atmosphere with a temperature structure similar to that of Neptune. This "cold" case creates a suitable environment to examine this process, although `ChemKM` is capable of including the condensation for hot planets as well. No diffusion or photolysis is included in this model. We also employ the Venot (2012) kinetic network with no reverse reaction. First, we consider a nearly water-saturated atmosphere. This nearly water-saturated atmosphere would allow the condensation to begin at pressures below the intersection of Neptune's TP structure and H_2O's condensation curve. We initialize the model identical to the Moses et al. (2018) Neptune model, except for He and H_2O abundances, and assume an initial atmospheric composition of

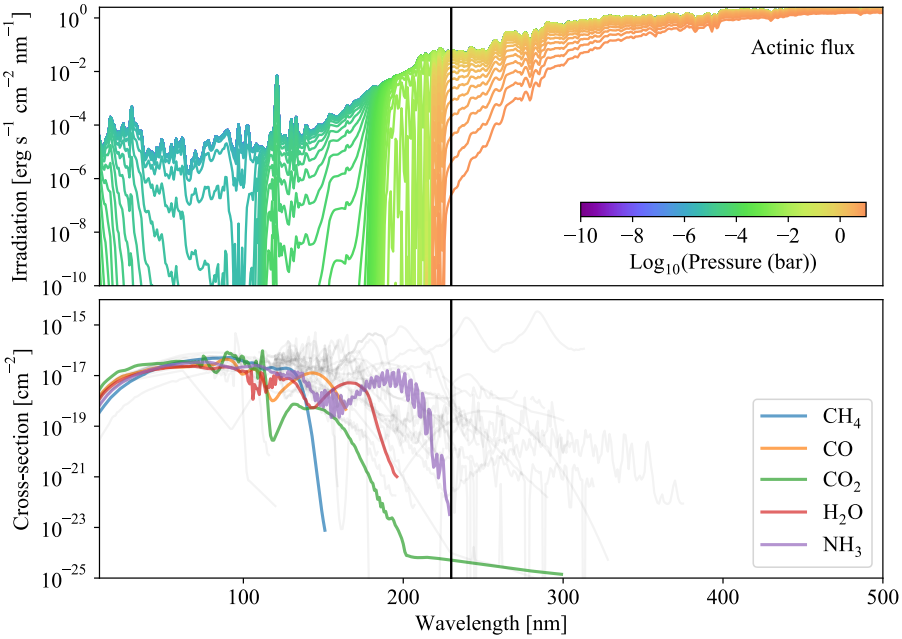

Figure 3.9: Top) Local stellar intensity (actinic flux) in logarithmic scale. Lower pressures are color-coded by cooler colors. **Bottom)** UV absorption cross-section of species in `ChemKM` (gray). Some of the species with usually major opacity contributions are shown in color.

80.8% H_2O, 19% He, 1.2×10^{-3} CH_4 and 8×10^{-8} CO. The particle size is also assumed to be 0.15 μm and fixed, following the Moses et al. (2018) assumption. Figure 3.10 shows the production of H_2O[s] (water ice) under these circumstances, with the expected condensation rates discussed in Section 3.2.3.

In reality, water condensation in the atmosphere of Neptune occurs at higher pressures (≈0.01-1 bar) due to water undersaturation. However, the temperature increases again at the regions deeper than 1 bar, causing the water to remain in the gas phase and making the ≈0.01-1 bar region a tropopause “cold-trap". This is shown for water condensation in Figure 3.11. The initial abundances for this model are 80.8% H_2, 19% He, and the rest is CH_4 and CO with molar fraction of 1.2×10^{-3} and 8×10^{-8} respectively, identical to the initial conditions in Moses et al. (2018). We allow for the condensation of H_2O, NO, N_2, O_2, C, HCN, CH_4, CO, CO_2, C_2H_2, C_2H_4, and C_2H_6 for demonstration purposes. Condensation of C_2H_2 and C are shown in Figure 3.11 as examples. In this setup, carbon condenses at all altitudes. However,

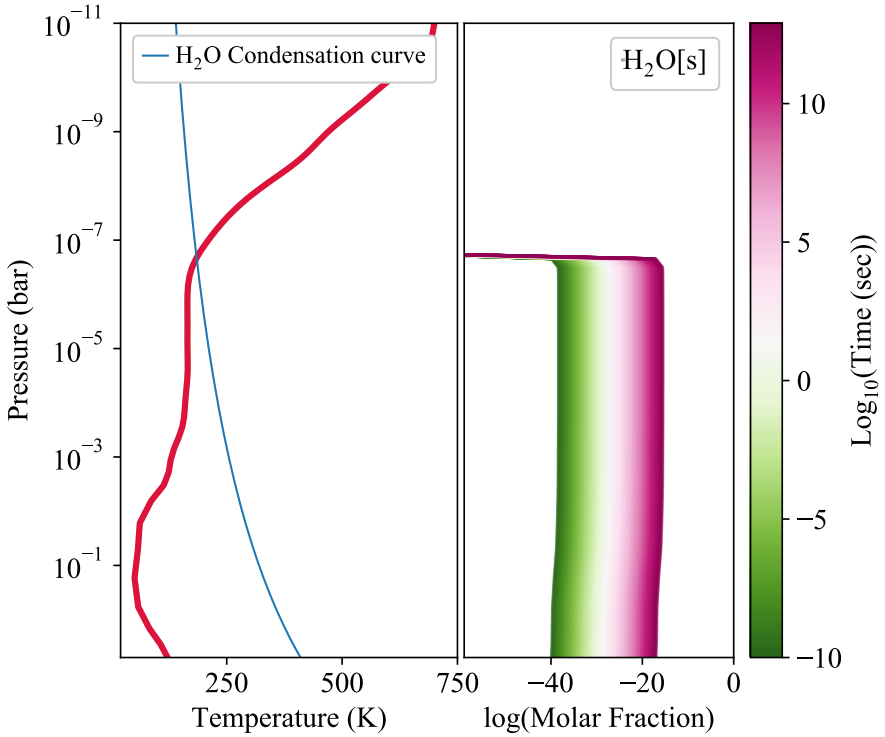

Figure 3.10: Water condensation in a nearly water-saturated Neptune-like planet, i.e. the temperature profile is similar to that of Neptune, but the initial composition is set to 80.8% H_2O, 19% He, and the rest is CH_4 and CO with molar fraction of 1.2×10^{-3} and 8×10^{-8} respectively. Water condensation occurs (right panel) below the intersection of the TP profile (left panel red line) and H_2O's condensation curve (left panel blue line).

most Neptune photochemical models do not allow carbon to condensate. This is to maintain a higher production rate of hydrocarbons, such as C_2H_2 and C_2H_6.

3.3.6 Influxes and boundary conditions

Ablation, atmospheric escape, and GCR can be included in `ChemKM` by setting the influx or production rate of reagents. To demonstrate these capabilities, we use the same Neptune model and initialization as the previous section. We include molecular and eddy diffusion as well as photolysis in this case.

First, we only include an influx of H_2O equal to 2×10^5 molecules $cm^{-2}s^{-1}$ (as discussed in the Moses et al. 2018) to examine how abundances would change. We initialize the atmospheric composition by its "photo-diffusion equilibrium"[5]. We use the same K_{zz} and irradiation spectrum as in the Moses et al. (2018) Neptune model.

[5]The steady state after the inclusion of photochemistry and diffusion in the model

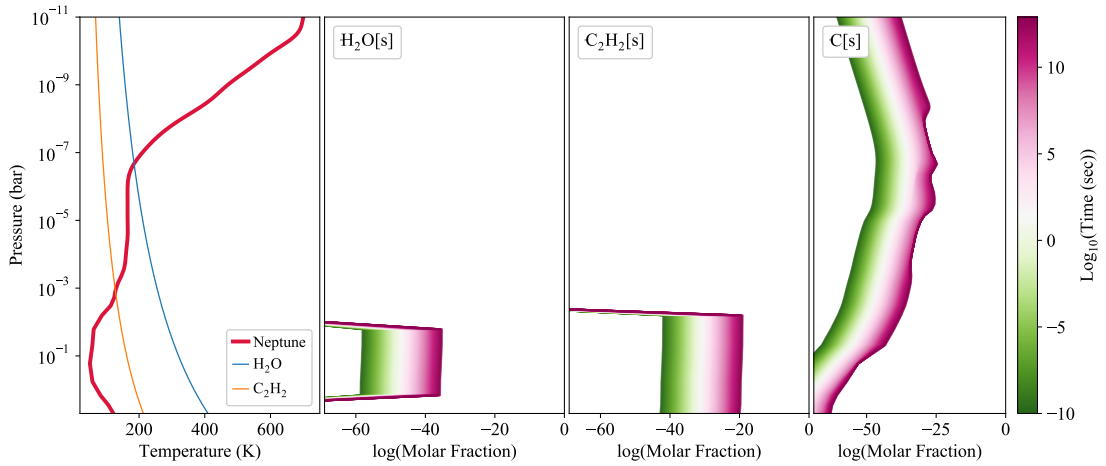

Figure 3.11: Condensation and cold-trap on Neptune. **Left)** Neptune's temperature structure (red line) and condensation curves of H_2O (blue line) and C_2H_2 (orange line). **Rest of panels)** Temporal evolution of condensate production, and formation of a cold-trap roughly between 1 and 0.01 bar.

Any deviation from this state will be caused by the imposed influx. Figure 3.12 shows the time evolution of H_2O, CO, $O(^1D)$ and C_2H_2 abundances. As one might expect, H_2O, CO, and $O(^1D)$ abundances increase, but C_2H_2 remains almost the same, due to the lack of free radical carbon. Diffusion plays a pivotal role and transports the deposited material at TOA to the deeper parts of the atmosphere. In this model, the abundance variations caused by H_2O influx at 10^{-11} bar typically require 10^5-10^7 sec (weeks to months) to reach 10^{-7} bar, where the highest altitude measurements of hydrocarbon mixing ratios have taken place (e.g. Moses et al. 2018). This time scale would be very different if the required oxygen to explain the observations were supplied by a large cometary impact (e.g. Lellouch et al. 2005; Luszcz-Cook & de Pater 2013; Moses et al. 2018). These possibilities can be addressed by JWST measurements of Neptune's composition (e.g. Roman et al. 2018; Fletcher et al. 2018) or a dedicated mission to ice-giants (e.g. Hofstdater et al. 2017).

In the next case study, we run the same model but include an influx of 2×10^8 molecules $cm^{-2}s^{-1}$ CO (see Moses et al. 2018, for the motivation) in addition to H_2O. Under these circumstances, excessive production of free carbon radicals and therefore additional carbon-bearing compounds can be expected. However, individual species at different altitudes might respond to these free radicals differently.

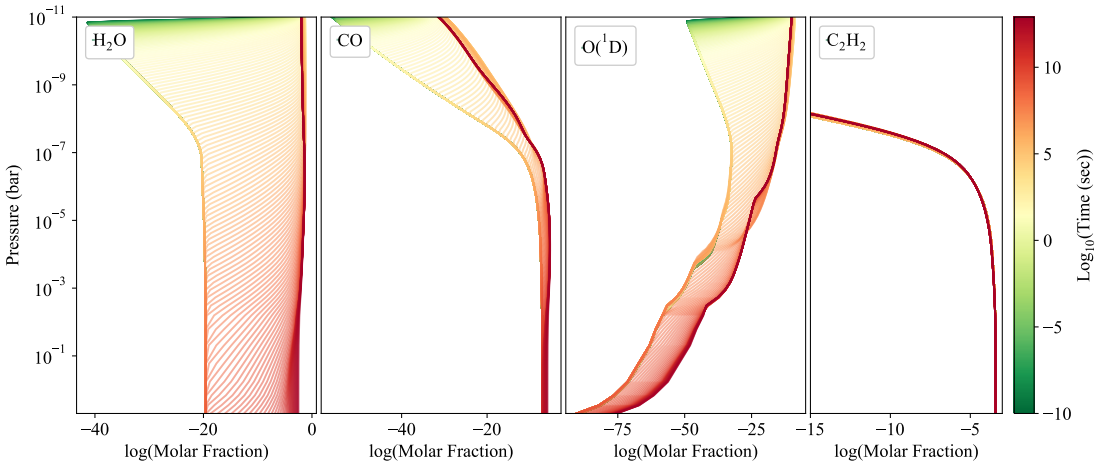

Figure 3.12: Abundance variations due to 2×10^5 molecules $cm^{-2}s^{-1}$ water influx at TOA. The model has a temperature structure similar to the Neptune model presented in Figure 3.11, but we initialize the atmospheric composition by its "photo-diffusion equilibrium"; to study the abundance deviations only due to the water-influx.

Photolysis of incoming H_2O and CO results in the production of free radical H, C, and O; hence an increase in the abundance of their elements is expected (e.g. see the variation of $O(^1D)$ abundances in Figure 3.13), unless there are sink terms with higher loss rates. As expected, the production of CO and C_2H_2 are enhanced early in the simulation, however, at later times ($t \gtrsim 10^6$ sec), C_2H_2 abundances seem to be restored to their initial values. This is, of course, not a universal trend and an examination of C_2H_2 abundance reveals its depletion at pressures between 0.1 and 10^{-7} bar. Although CO photodissociation enhances C_2H_2 production by offering additional free carbons, it also shields it at longer timescales and returns the C_2H_2 abundances at TOA to their initial values. This extra shielding also causes the depletion of C_2H_2 at mid-pressures and depletion of H_2O and $O(^1D)$ abundances at TOA.

Similar to these models, boundaries with fixed molar fractions and vertical profile of influxes of reagents (i.e. production rates) can be easily included in `ChemKM`'s modeling setup. In the case of GCRs, `ChemKM` includes a separated module to take into account the effect of Galactic/solar cosmic rays. Vertical profiles of production rates of each species with their branching and yields for each GCR reaction can be provided in the current version of the code (similar to the setup of photolysis module).

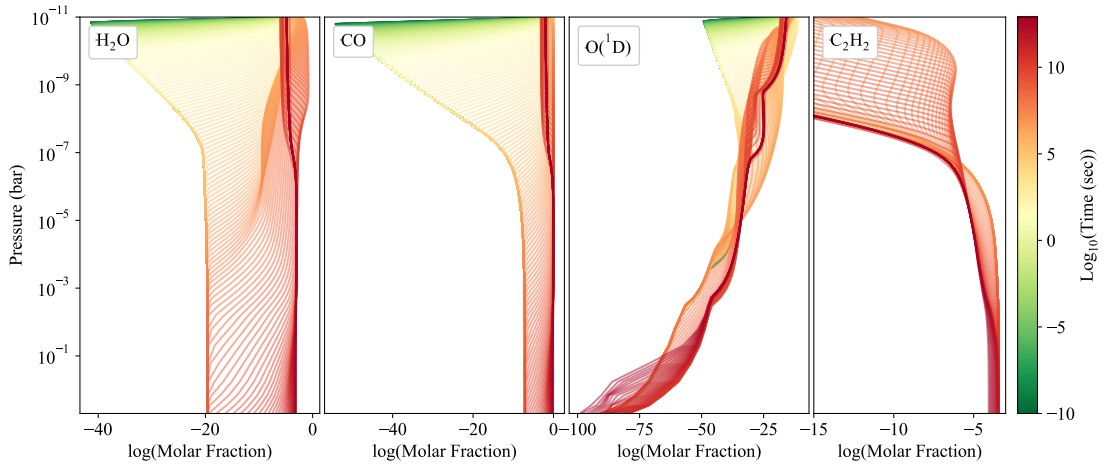

Figure 3.13: Similar to Figure 3.12 but additionally 2×10^8 molecules $cm^{-2}s^{-1}$ CO influx is included.

3.3.7 Solar system observations

An ultimate verification of atmospheric models could be a comparison between their results and atmospheric measurements. We selected Saturn and Neptune and our case studies for the verification of `ChemKM` with their observations.

We follow Moses et al. (2018) to setup and initialize Uranus and Neptune models in `ChemKM`, but following Dobrijevic et al. (2010) does not change the results significantly. To provide an example of setup parameters in these models, here we briefly mention the set in the model of Neptune's atmosphere. The vertical grid expands from 10 to 10^{-11} bar with 100 vertical levels. The temperature profile is adapted from Moses et al. (2005) and the chemical network is adapted from Hébrard et al. (2013). The abundance of CH_4, He, and CO are fixed at the lower boundary with these corresponding values: 1.2×10^{-3}, 0.19, and 8×10^{-8}. At the top of the atmosphere, H_2O, CO, CO_2, and H assumed to have influx, with these values: 2×10^5, 2×10^8, 2.3×10^4, and 10^7 in (the unit of molecule·$cm^{-2}s^{-1}$), respectively. An average solar activity is assumed and LIMP and K_{zz} are adapted as prescribed in Moses et al. (2018).

Figures 3.14 and 3.15 compare the calculated abundances of some hydrocarbons (such as CH_4, C_2H_2, and C_2H_6) with the observation of these atmospheric constituents on these ice-giants. In general, the photochemical produces abundances

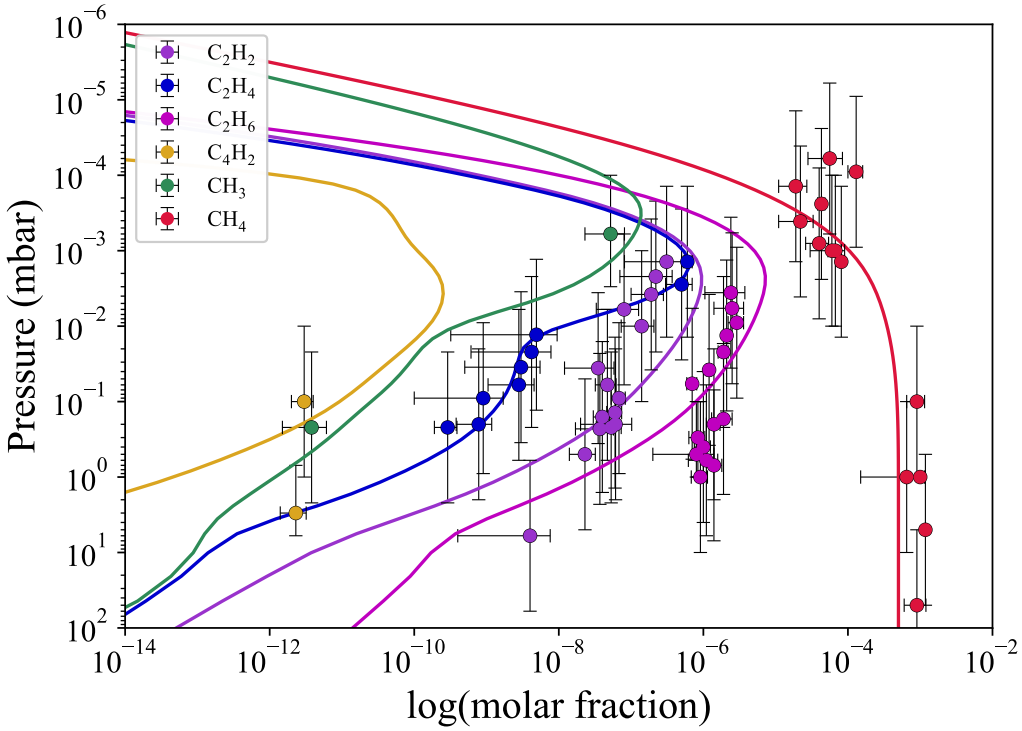

Figure 3.14: Comparison of `ChemKM` model and atmospheric measurements of Neptune. The model is setup according to the model of Neptune atmosphere by Moses et al. (2018). Calculated abundances of CH_4, CH_3, C_2H_2, C_2H_4, C_2H_6, and C_4H_2 are consistent with the observation of these atmospheric constituents on Neptune.

consistent with the observations. In the next chapter we present an example of a photochemical model of a hot exoplanet, HD 189733b, to introduce our large-scale parameter-space study of the effect of disequilibrium processes on exoplanets.

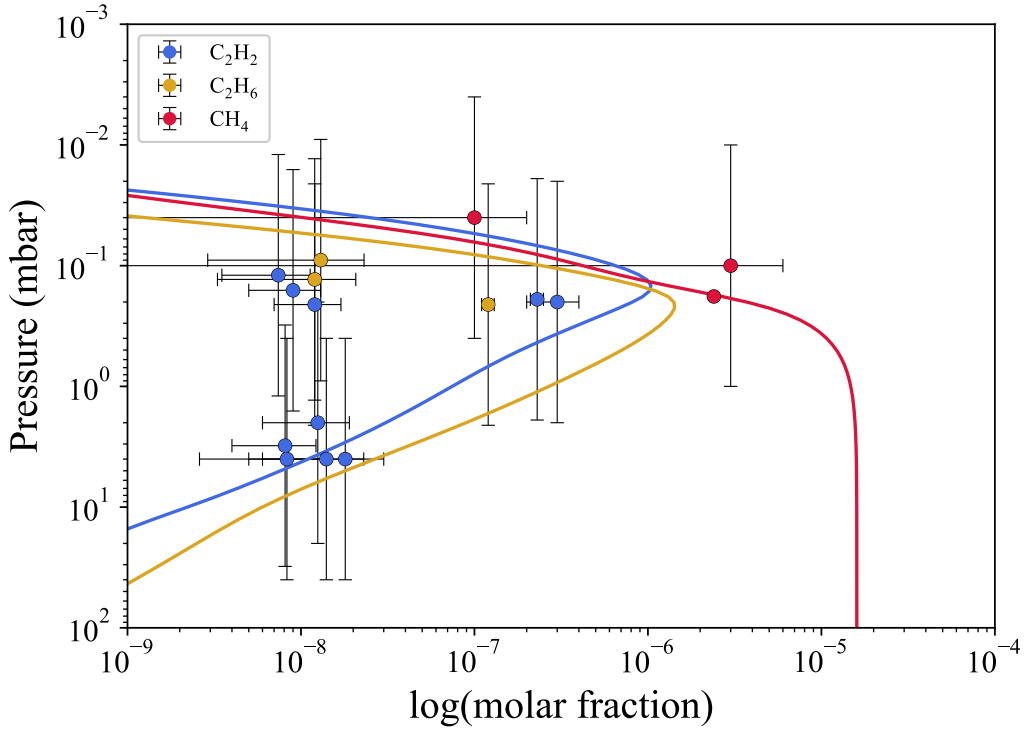

Figure 3.15: Comparison of `ChemKM` model and atmospheric measurements of Uranus. The model is setup according to the model of Uranus atmosphere by Moses et al. (2018). Calculated abundances of CH_4, C_2H_2, and C_2H_6 are consistent with the observation of these atmospheric constituents on Uranus.

"Values are like fingerprints. Nobody's are the same, but you leave 'em all over everything you do."

— Elvis Presley.

4

Fingerprints of Disequilibrium Chemistry

Contents

4.1 Introduction

[1]The atmospheric composition of solar system planets is not at their thermochemical equilibrium state, mostly due to the irradiation by the Sun and mixing through atmospheric transport and turbulence. These effects are so pronounced that even the earliest atmospheric models of these objects include disequilibrium chemistry (e.g. review articles on the early modern models of Venus (Noll & McElroy 1972),

[1]This chapter was published as a refereed article "From cold to hot irradiated gaseous exoplanets: Fingerprints of chemical disequilibrium in atmospheric spectra", Molaverdikhani et al. (2019a), for which I am the lead author and has been adapted for this thesis.

Earth (Lou 1973), Mars (Noll & McElroy 1974), Jupiter (Danielson 1968), Saturn (Divine 1972), Titan (Divine 1974), Uranus, and Neptune (Encrenaz 1974)).

With the discovery of Hot Jupiters (Mayor & Queloz 1995), however, the assumption of thermochemical equilibrium resurfaced as a first-order estimation of their atmospheric properties thanks to their high temperatures (e.g. Burrows & Sharp 1999; Lodders & Fegley 2002; Fortney et al. 2005). But further studies suggested that the non-thermal processes could potentially alter their chemical composition at the photospheric levels; predominantly because of the intense UV irradiation and strong atmospheric mixing (e.g. Seager et al. 2005a; Madhusudhan & Seager 2009; Stevenson et al. 2010; Moses et al. 2011; Agúndez et al. 2012; Venot et al. 2012; Hu et al. 2012, 2013; Hébrard et al. 2013; Hu & Seager 2014; Miguel et al. 2014; Zahnle & Marley 2014; Drummond et al. 2016; Tsai et al. 2017; Wang et al. 2017; Blumenthal et al. 2018; Zhang & Showman 2018a; Changeat et al. 2019) or other processes such as lightning (Helling 2019b) and cosmic rays (Rimmer & Helling 2013).

Madhusudhan & Seager (2011) performed an extensive retrieval analysis of the GJ 436b spectrum observed by Stevenson et al. (2010) and concluded that the methane abundance paucity cannot be explained by thermoequilibrium chemistry. While the lack of a robust methane detection in the spectra of irradiated gaseous planets (e.g. Brogi et al. 2016, 2018; Pino et al. 2018; Alonso-Floriano et al. 2019) could be an indication of disequilibrium chemistry, there is no large-scale systematic investigation of how disequilibrium processes change the abundance of methane (or any other major opacity compound) at photospheric pressures ($\sim$1 bar to $\sim$1 μbar), and how this manifests itself in the atmospheric spectra. Zahnle & Marley (2014) and Miguel & Kaltenegger (2014) both perform such studies however over a limited parameter space. The complexity of photochemical models makes the large-scale simulations computationally expensive, and thus such investigations require code optimization. In addition, the models must be flexible and generic enough to perform efficiently over a range of atmospheric conditions and compositions.

We introduce a new chemical kinetic model (`ChemKM`), which is both fast and generic. We employ `ChemKM` to perform an extensive parameter study over a

broad range of atmospheric conditions. In total, we calculate 84,672 full-network chemical kinetic models with more than 100 reactants and 1000 reactions, to study how the variation of major opacity sources (e.g. H_2O, CH_4, CO, and CO_2) due to disequilibrium chemistry affect the spectra. We also present a case study of HD 189733b, a well-studied exoplanet, for benchmarking.

In what follows, we describe our chemical kinetic model and the parameter space that we have explored. In Section 4.2.1, we present the results of our case study for HD 189733b and benchmark it against the model developed by Venot (2012). In the rest of Section 4.2, we present the results of our parametric study and check the validity of our proposed classification scheme for irradiated planetary spectra (see Molaverdikhani et al. (2019b) for more details on the classification under cloud-free equilibrium chemistry conditions). In Section 4.2.3, we report the dependency of quenching point on atmospheric parameters, and in Section 4.2.4 we investigate the detectability of disequilibrium processes by JWST. Finally, in Section 4.2.5 we discuss Spitzer transmission and emission color diagrams variation from thermochemical equilibrium models due to the vertical mixing, and its observability. We summarize and conclude our results and findings in Section 4.3.

4.1.1 The temperature structures for the parametric study

In Section 4.2, we study a broad range of parameter space, based on a large grid of cloud-free atmospheric models. We use the self-consistently calculated temperature-abundances profiles as the input of our chemical kinetic model (`ChemKM`) to calculate the effect of vertical mixing on the chemical composition of the atmospheres. The input profiles were calculated by the petitCODE (Mollière et al. 2015, 2017). We then use petitRADTRANS to calculate the spectra of atmospheres at chemical disequilibrium to investigate how the quenching point changes with atmospheric parameters, and whether the classification scheme proposed in (Molaverdikhani et al. 2019b) would still hold after introducing vertical mixing. Here we briefly review the properties of the grid and the range of investigated parameters.

In the first chapter of this series (Molaverdikhani et al. 2019b) we calculated a large grid of 28,224 self-consistent cloud-free atmospheric models using the petitCODE. The petitCODE is able to calculate planetary atmospheric temperature profiles, chemical abundances, and emergent and transmission spectra and it assumes radiative-convective and thermochemical equilibrium in a 1D setup. The stellar effective temperature, stellar radius, planetary effective temperature or distance, planetary internal temperature, planetary radius, planetary mass or alternatively its surface gravity and irradiation treatment must be provided.

We considered five factors as the free parameters in our petitCODE grid models: planetary effective temperature (T_{eff}), surface gravity (log(g)), metallicity ([Fe/H]), carbon-to-oxygen ratio (C/O) and spectral type of the host star. The lower limit of T_{eff} was set to 400 K to avoid non-negligible contributions of the interior temperature (all models have T_{int} = 200 K) into the atmospheric properties, and the upper limit was chosen to be 2600 K to avoid highly irradiated regions where the heat redistribution becomes inefficient and the planetary average irradiation treatment might become invalid. The surface gravity spans from 2.0 to 5.0 to broadly cover possible surface gravity values. Metallicity ranges from -1.0 to 2.0 with an increment of 0.5. The stellar spectral types were chosen to be M5, K5, G5 and F5. For C/O we selected irregular parameter steps ranging from 0.25 to 1.25 with smaller steps around unity to capture possible transitions from water- to methane- dominated atmospheres as predicted by Madhusudhan (2012), reported by Mollière et al. (2015), and discussed in detail in Molaverdikhani et al. (2019b). We then add K_{zz} as a new dimension to be explored; more discussion and results in Section 4.2. Planetary spectra are calculated with petitRADTRANS (Mollière et al. 2019).

4.2 Results

4.2.1 Case study: HD 189733b

HD 189733b is one of the most studied exoplanets so far (e.g. Moses et al. 2011) and hence represent a proper case for benchmarking. Moses et al. (2011) provided the thermal structure and the K_{zz} profile for this planet, which has been used by several

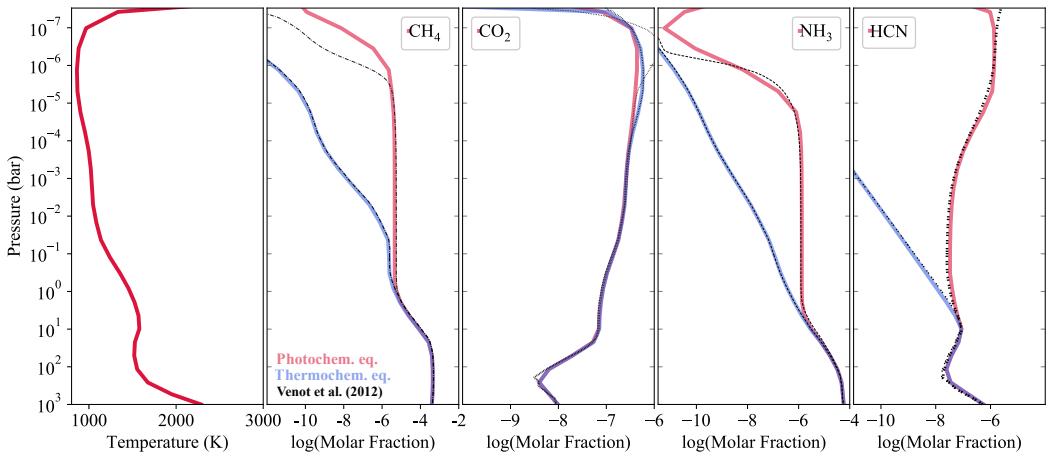

Figure 4.1: HD 189733b photochemical model comparison. **Left)** The temperature structure. **Rest of panels)** `ChemKM`'s calculated abundances of CH_4, CO_2, NH_3, HCN, and H at thermochemical equilibrium (solid blue lines) and photo-diffusion equilibrium (solid red lines), compared with the results of Venot et al. (2012) (black lines). The results are in good agreement except at and above the μbar regime, where photolysis reactions and molecular diffusion are the dominant processes. Hence a careful implementation of these processes is necessary if TOA abundances are desired.

studies to perform benchmark calculations (e.g. Venot et al. 2012; Moses 2014; Drummond et al. 2016; Tsai et al. 2017). Thus we use the same set of inputs to compare the outcome of our HD 189733b model with previously published results.

To set up the model, we use Venot et al. (2012)'s full kinetic network and an updated version of Hébrard et al. (2012)'s UV absorption cross-sections and branching yields. For UV irradiation at TOA, both Moses et al. (2011) and Venot et al. (2012) used ϵ Eridani as a proxy of HD 189733 due to their similarities in spectral type, age, and metallicity. Lack of high quality data at shorter wavelengths led them to use only a portion of ϵ Eridani's spectrum (Moses et al. (2011) used ϵ Eridani's data in the range of 115 nm to 283 nm and Venot et al. (2012) uses data between 90 nm and 330 nm). They combined other datasets and models to extend the spectrum. We use the most recent measurements of ϵ Eridani as a full and coherent spectrum from X-ray to optical to take a more consistent approach. The data were obtained from the MUSCLES database (France et al. 2016). We initialize the atmospheric composition at its thermochemical equilibrium state and let the model reach its steady state after an integration time of 10^9 sec.

Venot et al. (2012) and Moses (2014) reported the importance of kinetic network and its effect on the quenching level and quenching abundances. Since we opted for the usage of Venot et al. (2012)'s network, we compare our results with their findings. Our thermochemical equilibrium abundances (blue lines in Figure 4.1) are almost identical to the Venot et al. (2012)'s results. Similarly, our disequilibrium abundances (red lines in Figure 4.1) are almost identical, except in the μbar regime. By using the same stellar flux as Venot et al. (2012) and finding no significant abundance variation, we rule out the role of stellar flux as a cause of discrepancies at high altitudes. Therefore, these subtle differences between HD 189733b photochemical models are likely caused by different molecular diffusion implementation and different photolysis reactions. As briefly mentioned in Chapter 3, this might have significant consequences in the interpretation of high-resolution spectra.

4.2.2 Methane depletion in GJ 436b

We discussed that while the atmospheric composition of deeper regions of gaseous planets tend to remain at thermochemical equilibrium, their photospheres are usually prone to disequilibrium processes. This effect may have its fingerprint on the planets' atmospheric spectra, but its detection is not a trivial task with the current observational facilities.

In a well-known case, Stevenson et al. (2010) reported CH_4 depletion inferred from the thermal emission of the GJ 436b dayside (a Class-I planet with T$\sim$700 K). Several studies suggested that this CH_4 deficiency, relative to its thermochemical equilibrium predictions, could be explained by disequilibrium processes such as diffusion and polymerization of CH_4 (see e.g. Stevenson et al. 2010; Madhusudhan & Seager 2011; Line et al. 2011). Madhusudhan & Seager (2011) performed a detailed retrieval analysis of the spectrum and concluded that the atmosphere maintains a possible high metallicity (10$\times$ solar) and a vertical mixing with $K_{zz}\approx10^6$-10^7 (cm^2 s^{-1}). They constrained these values by assuming a suite of parametric TP structures. Under thermochemical equilibrium conditions, such temperature profiles could result in a monotonically decreasing CH_4 abundance at the upper portion of the atmosphere.

If the mixing timescale is much shorter than the kinetic timescales at those pressures, then the vertical mixing could "transport" these deeper/lower abundances and bring them to the upper levels. Hence a CH_4 deficiency at TOA could occur under these conditions. Such abundance variation could change the measured flux by *Spitzer* IRAC instrument in particular the 3.6 μm channel (Stevenson et al. 2010).

To illustrate how such an abundance deficiency occurs, we setup a simple model by selecting a parametric TP structure from Madhusudhan & Seager (2011), Figure 4.2 (a). Here, we do not intend to perform a retrieval to reproduce the Madhusudhan & Seager (2011)'s results, but rather it is a demonstration of abundance variation at TOA due to imposing the vertical mixing. We assume 500 K and 1500 K for the temperature of upper and deeper regions respectively, with solar metallicity and C/O ratio for the bulk composition of the atmosphere. With this setup, methane's thermochemical equilibrium abundance at TOA is around 4.6×10^{-4}. By increasing the vertical mixing, the atmosphere quenches at deeper levels, see Figure 4.2 (b). The CH_4 abundance at TOA decreases as K_{zz} increases, as long as quenching occurs at pressures smaller than $\sim$1 bar. Any K_{zz} higher than 10^5 cm^2 s^{-1}, however, mixes the deeper levels where CH_4 has higher abundances; causing to an enhancement of CH_4 abundance at TOA. Figure 4.2 (c) illustrates the variation of CH_4 at TOA, due to the change of vertical mixing, and a minimum CH_4 abundance in the case of $K_{zz}=10^5$ cm^2 s^{-1}. Here we only showed the results of CH_4 abundance, however, almost all reagents respond to the variation of vertical diffusion; although differently. Their collective variation could affect the transmission spectrum of the planet as can be seen in Figure 4.2 (d).

This non-linear atmospheric response is likely to be more pronounced for hotter planets, e.g. Class-II, where the abundance of methane and water (as two of the major opacity sources in the planetary atmospheres) are more sensitive to the variation of C/O ratio at their photospheres due to partial evaporation of condensates.

We expand these results by conducting an extensive survey on the effect of vertical mixing in the spectra of our self-consistently calculated cloud-free grid

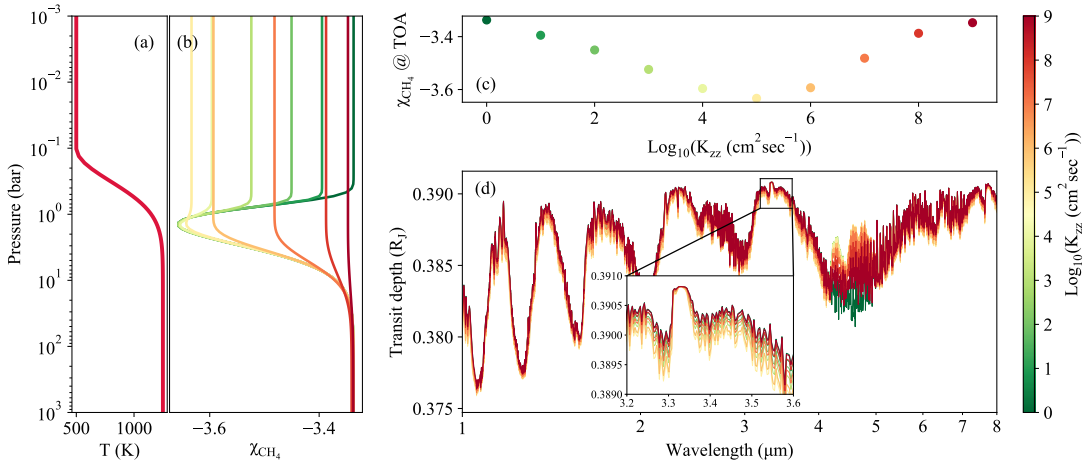

Figure 4.2: Effect of vertical mixing on CH_4 abundances at the top of the atmosphere. **(a)** A simple parametric GJ 436b−like TP structure, adapted from Madhusudhan & Seager (2011). **(b)** CH_4 abundance profiles caused by different K_{zz} values. Stronger mixing causes a deeper quenching level, but does not guarantee a monotonic abundance variation. **(c)** CH_4 abundance at TOA as a function of K_{zz} in this particular case. **(d)** Variation of the transmission spectrum as a function of K_{zz}. In this example, variation of CH_4 abundance at TOA appears as a slight shift in the transmission spectrum. The CO_2 and CO spectral features, between 4−5 μm, varies as well; resulting in higher CO_2 and CO molar fractions at TOA when the mixing is in action.

of models (see Section 4.1.1 and (Molaverdikhani et al. 2019b)). By using these TP structures as `ChemKM`'s input and assuming three values for K_{zz} (10^6, 10^9, and 10^{12} cm^2 s^{-1}) we calculate the atmospheric abundances of these planets at their diffusion equilibrium. The grid of models and their emission and transmission spectra will be publicly available.[2] As the first step, we determine the dependency of quenching levels to the atmospheric parameters.

4.2.3 Parametric study: Quenching levels

The atmospheric diffusion not always results in a constant "quenched abundance" above the "quenching level" (see, e.g., Figure 3.6, and Section 3.3.3 for an overview). Therefore, this definition of quenching level (and consequently constant quenched abundance) is not general. Here we propose a parameter, the Coefficient of variation (CV), for a quantitative definition of quenching levels based on the deviation of abundances from their thermochemical equilibrium values at each pressure level.

[2] www.mpia.de/homes/karan

This parameter is a standardized measure of dispersion of a quantity and has been used in other fields, e.g. in the clinical research (Schiff et al. 2014), to estimate deviation of particular quantities from its mean value. In this work, we introduce this parameter as a mean to quantitatively estimate the quenching levels. In the chemical kinetic simulations, this parameter can be calculated as the ratio of the temporal standard deviation of abundances, s, to the mean value of abundances for a given species at any given pressure level. In our simulations, we use exponential time steps to calculate abundances, hence a better parameter would be the geometric Coefficient of variation (gCV) of abundances. This can be calculated as follows:

$$\mathrm{gCV} = \sqrt{\mathrm{e}^{s_{\ln}^2} - 1}, \tag{4.1}$$

where $s_{\ln}$ is the sample standard deviation of abundances after a natural log transformation and can be estimated as $s_{\ln} = s\ln(10)$. Stronger variation of abundance at any given altitude results in a higher gCV. We find that gCV_i =0.05 represents the onset of disequilibrium chemistry of species i very well, hence $\mathrm{gCV}_i \geq$0.05 can be used to mark the regions at which abundances have deviated from their thermochemical equilibrium values significantly. An example is given in Figure 4.3 based on the results of our diffusion verification model (presented in Figure 3.6), where water remains in thermochemical equilibrium when $\mathrm{gCV}_{\mathrm{H_2O}}$<0.05 (below the red dash-dotted line at ∼0.5 mbar) and is driven away from it when $\mathrm{gCV}_{\mathrm{H_2O}}\geq$0.05 (above ∼0.5 mbar). The bottom panel in Figure 4.3 shows the temporal evolution of abundances at different pressures. At the times longer than $t > 10^{11}$ sec, abundances reach to steady state at all pressures.

We present the results based on the "quench point from each species", gCV_i. An alternative method would be to calculate all the timescales relevant for a species at any given pressure. While the alternative method is mathematically correct, our method provides a much simpler picture of the quenching levels based on the actual abundance variation due to the kinetics. Another advantage of our method is that there is no need to trace all the reactions and timescales when calculating the abundances, and the quenching can easily be calculated once the simulations are

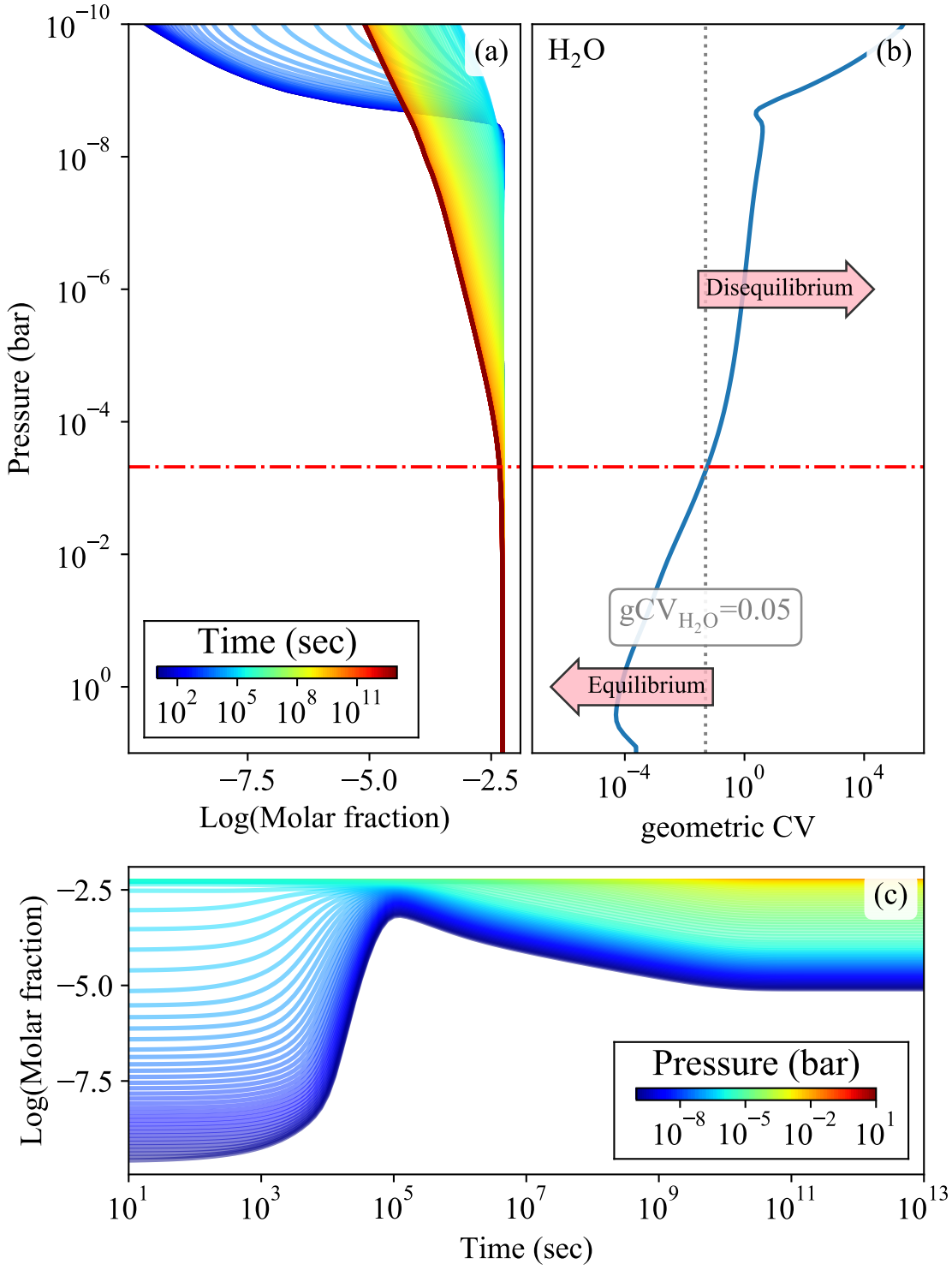

Figure 4.3: A quantitative definition of disequilibrium. We use the results of our diffusion verification model (presented in Figure 3.6) as an example. **(a)** Temporal variation of H_2O abundance from thermochemical equilibrium (blue) to diffusion equilibrium (red). **(b)** Water remains in thermochemical equilibrium when $gCV_{H_2O}<0.05$ (below the red dash-dotted line at ∼0.5 mbar) and is driven away from the thermochemical equilibrium when $gCV_{H_2O}\geq0.05$ (above ∼0.5 mbar). The red dash-dotted line marks the quenching point. **(c)** Temporal evolution of water abundances at different pressures. Invariant abundances at $t > 10^{11}$ sec insures diffusion equilibrium.

over. The gCV can be also used in a broader sense to study any abundance deviation from any initial condition as a standard mathematical method for such analysis.

By using this new metric we investigate the quenching levels in our grid of models. Figure 4.4 (a) shows the density plot of quenching levels of all species in our K_{zz}=10^{12} cm^2 s^{-1} models. In general, P_{quench} decreases to lower pressures as temperature increases, but its variation at any given temperature is large. For instance, models with T_{eff}=2600 K have shown quenching at all pressures ranging from 100 to 10^{-8}bar in these simulations. But, if we calculate the average P_{quench} along T_{eff} (solid black line) the result is similar to the Venot et al. (2018) results of P_{quench} for K_{zz}=10^{12} cm^2 s^{-1}, dashed line in Figure 4.4 (a).

We find that for a given mixing strength, quenching levels strongly depend on the effective temperature of the planet, but it also depends on the complexity of abundance profiles. For instance, in most cases if a species is the dominant species, then its abundance profile tends to be almost constant. This constant shape of the profiles leads to an underestimation of their P_{quench} (their abundance does not change very much by mixing since it is constant already, therefore gCV_i remains small at higher pressures and a lower P_{quench} will be determined). This "constant profiles" region is marked by a dotted line in Figure 4.4.

The role of T_{eff} (and K_{zz}) on the determination of P_{quench} is rather obvious by following the chemical versus mixing timescale argument; e.g. see Section 3.3.3. However, relating atmospheric parameters to the complexity of abundance profiles is not trivial. Nevertheless, we find that all atmospheric parameters that we have investigated (i.e. T_{eff}, log(g), [Fe/H], and C/O) affect the complexity of abundance profiles up to some degree. The averaged value of [Fe/H], log(g), and C/O (calculated in each 2D histogram bin represented in the panel (a) of Figure 4.4) are shown in Figure 4.4 panels (b), (c), and (d) respectively, to present a graphical demonstration of these dependencies. While Venot et al. (2018) also explored the effect of C/O ratio on the quenching levels, they only found negligible variation. This is mainly due to their narrower parameter-space coverage and their methodology for the determination of the quenching levels as an integrated quantity over the main species.

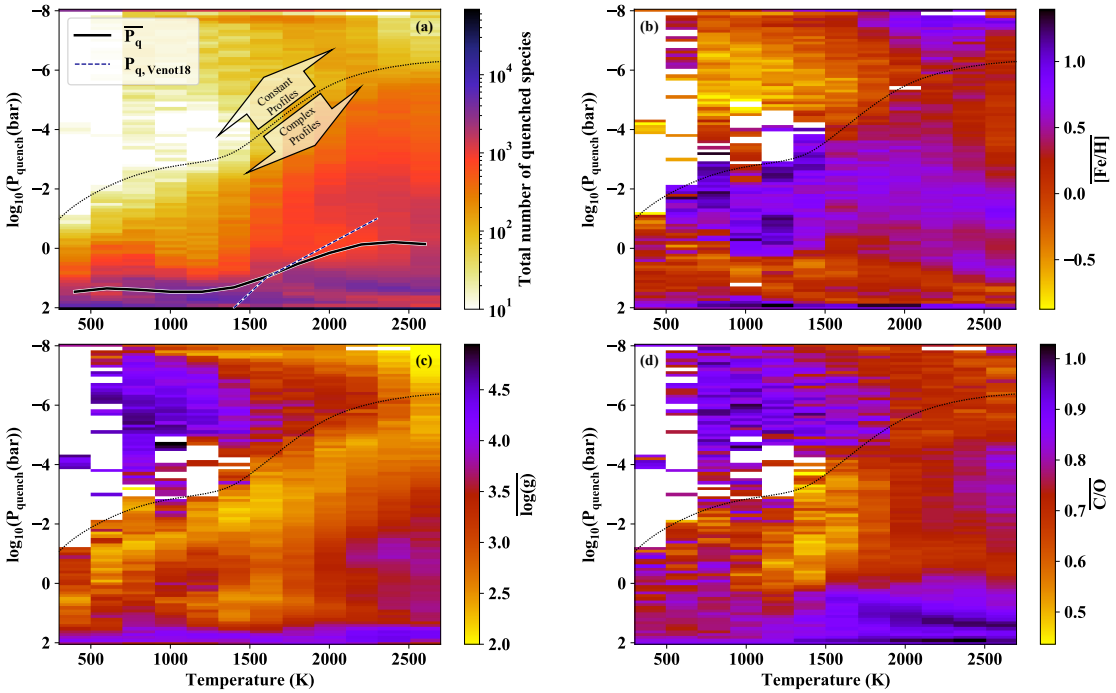

Figure 4.4: A quantitative determination of quenching levels in our grid of chemical kinetic models for $K_{zz}=10^{12}$ cm^2 s^{-1} cases. **(a)** Density plot of quenching levels of all species. In general, P_{quench} decreases to lower pressures as temperature increases, but its variation at any given temperature is large. However, the average P_{quench} (solid black line) is similar to the Venot et al. (2018) results of P_{quench} for $K_{zz}=10^{12}$ cm^2 s^{-1}, dashed line. Constant abundance profiles of abundant species cause estimation of P_{quench} at lower pressures (above dotted line). **(b,c,d)** Maps of average [Fe/H], log(g), and C/O to graphically demonstrate P_{quench} degree of dependence to these parameters.

We will use gCV_i to present an empirical equation for P_{quench}([Fe/H],log(g),C/O) in a follow-up work.

4.2.4 Observability of the disequilibrium chemistry with JWST

One of the key upcoming missions to address the diversity and characterization of exoplanetary atmospheres is JWST. Naturally, the first question would be: "Is there any sweet-spot in the parameter-space to detect the effect of disequilibrium chemistry in the planetary spectra by JWST?". In order to investigate this, we take a simple approach by subtracting the transmission spectra of each atmospheric model at thermochemical equilibrium and disequilibrium chemistry. The wavelength range spans 0.8 μm to 20 μm, covering most of the JWST's wavelength range. The shorter

wavelengths, i.e. 0.6 μm to 0.8 μm, would be likely influenced by the Rayleigh scattering and wavelengths longer than 20 μm do not show significant molecular features; hence excluded from this analysis. We then find the maximum spectral deviation for each model due to the disequilibrium.

We should, however, note that using the measured radius at one wavelength is not adequate for a robust detection of disequilibrium fingerprint on the spectra due to the reference pressure degeneracy. Therefore, this analysis should be taken only as a first step toward a spectrum-sensitivity analysis and not a retrieval-degeneracy analysis.

Figure 4.5 shows an example of the transmission spectra for a Jupiter-sized planet around a G5-type star, with solar metallicity, C/O$\sim$0.5, and a surface gravity of 3.5 under two conditions: the thermochemical equilibrium and diffusion equilibrium. The diffusion equilibrium model is shown for K_{zz}=10^{12} cm^2 s^{-1}. In this example, the maximum difference between the spectra of the two models, ΔTD, occurs at the CH_4 feature at $\sim$3.3 μm. The difference is about 150 ppm in this model; see the bottom panel of the same figure. While this CH_4 spectral feature is one of the most prominent features to detect the fingerprints of disequilibrium chemistry, other spectral features from CH_4, H_2O, CO_2, or CO could be also used as the disequilibrium tracing features. To produce Figure 4.6, we analyzed where in a spectrum the ΔTD was maximal for all spectra in the grid and calculated the occurrence at different wavelengths. By finding these occurrence rates we determine which wavelengths are likely to have the highest sensitivity to the vertical mixing. We identify five spectral regions with the highest occurrence rates at $\sim$1 μm (CH_4, H_2O, or CO), $\sim$3.3 μm (mostly CH_4), $\sim$4.5 μm (CO_2 or CO), $\sim$12 μm (CH_4), and $\sim$15 μm (CH_4). Hence, investigation of these wavelengths could provide a higher chance of the detection of disequilibrium spectral signature.

Blumenthal et al. (2018) performed a case study comparing the synthetic emission spectra of HD 189733b, WASP-80b, and GJ 436b. They found that the most significant differences in the emission spectra of these planets within the wavelength rage of 4 to 5 μm are due to CO_2 and CO disequilibrium processes. Although

our predictions are based on the synthetic transmission spectra, their results are consistent with our findings for the mentioned wavelength range; see Figure 4.6.

By averaging the maximum ΔTD over the free parameters domain, i.e. T_{eff}, log(g), [Fe/H], C/O ratio, and the spectral type of the star (or alternatively its surface temperature, i.e. T_{star}), we identify the parameter-space at which the transmission spectra are highly sensitive to the vertical mixing. The results are shown in Figure 4.7. The T_{eff}-log(g) panel, at the top-left, suggests a strong dependency of disequilibrium detectability on the surface gravity of the planet. While this is not surprising, this panel shows a higher probability of disequilibrium detection at T_{eff} between 1000 and 2000 K. This region coincides with the Class-II and Class-III planets, where the evaporation of condensates plays a crucial role in the photospheric chemistry of planets. In fact, all T_{eff}-dependent results in the left column support this finding. Moreover, the T_{eff}-C/O panel reveals an interesting trend: as T_{eff} increases, a higher chance of disequilibrium detectability occurs at higher C/O ratios. More precisely, there is a region around C/O∼0.95 with a higher probability of disequilibirum detection. This coincides with the minimum-IR opacity/inversion temperature profiles (see e.g. Mollière et al. 2015). It appears that such atmospheric condition makes the chemistry to be more easily driven away from its thermochemical equilibrium state. Therefore, this feedback could make the inversion due the minimum-IR opacity, chemically and radiatively unstable. A further self-consistent disequilibirum chemistry calculation must be performed in order to quantitatively assess the significance of this feedback on the inversion.

The T_{star}-dependent panels, bottom row in Figure 4.7, illustrate a higher probability of disequilibrium detection when the host stars are colder. This is solely due to the fact that colder stars are associated with smaller radius; hence a larger transit depth for a given planetary radius. The T_{star}-log(g) panel also suggests that the detection of disequilibrium for a Jupiter-sized planet with high surface gravity maybe only possible for M-dwarfs.

A higher metallicity and C/O ratio results in a higher concentration of carbon-bearing species; in particular CH_4, CO_2, and CO. Hence, a higher detectability

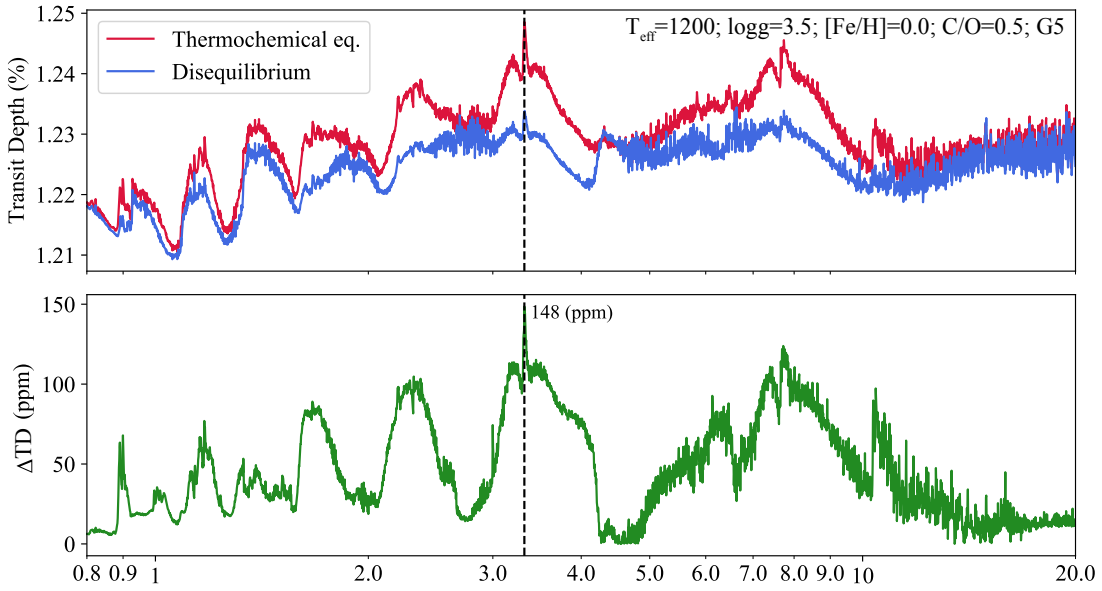

Figure 4.5: Variation of transmission spectrum due to disequilibrium chemistry for a Jupiter-sized planet orbiting a G5-type star with solar metallicity, C/O∼0.5, and surface gravity of 3.5. **Top)** Methane abundance decreases as a result of added vertical mixing with $K_{zz}=10^{12}$ cm^2 s^{-1} (blue) with respect to the thermochemical equilibrium state (red). **Bottom)** The difference between the two spectra indicates that the CH_4 feature at 3.3 μm has the maximum variation within JWST's wavelength coverage.

of disequilibrium is expected at these conditions. This is shown in the [Fe/H]-C/O panel, where the region of interest (with dark-blue colors) is associated with super-solar metallicities and super-solar C/O ratios.

In summary, we find that the detectability of disequilibrium could be maximized by focusing on the targets with T_{eff} between 1000 and 1800 K, orbiting around M-dwarfs, having low surface gravity but high metallicity and a C/O ratio value around unity.

4.2.5 Classification and Color-diagram

In the first chapter in this series (Molaverdikhani et al. 2019b), we proposed a new classification scheme for irradiated gaseous planets based on a grid of cloud-free self-consistent models with four classes. Class-I includes planets colder than 600−1100 K. Class-II planets are hotter than Class-I ranging from 600−1000 K to about 1650 K. The boundary between Class-I and II changes with log(g), metallicity, and stellar

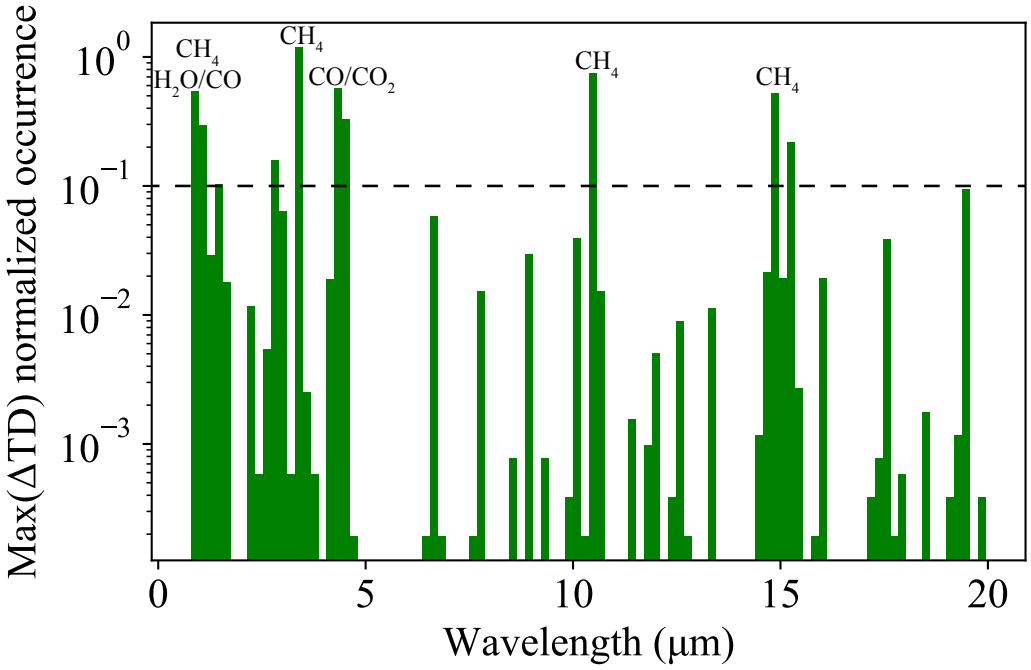

Figure 4.6: Occurrence rate of maximum variation in the transmission spectra, max(ΔTD), within JWST's wavelength range. Five wavelength regions show the highest occurrences, namely ∼1 μm (CH_4, H_2O, or CO), ∼3.3 μm (mostly CH_4), ∼4.5 μm (CO_2 or CO), ∼10.5 μm (CH_4), and ∼15 μm (CH_4).

type of the host star. Class-III planets have a temperature between 1650 K and 2200 K, and Class-IV planets are hotter than 2200 K. Here we employ the results of our grid of disequilibrium chemistry models to study the effect of vertical mixing on the atmospheric spectra and hence our proposed classification scheme.

As discussed in Chapter 2, carbon-to-oxygen ratio affects the composition of hot planetary atmospheres in a way that water is expected to be more prominent at lower C/O ratios and methane, CO, or HCN to be the dominant chemical products at higher C/O ratios. The spectral decomposition technique provides the necessary tool to find the transition C/O ratio, i.e. the C/O ratio at which the atmospheric spectra changes from a water- to methane-dominated spectrum. By employing this technique, we estimate the transition C/O ratios for our grid of disequilibrium chemistry models, see Figure 4.8, for $K_{zz}=10^{12}$ cm^2 s^{-1} models.

In general, but not always, vertical mixing on Class-II and III planets cause the

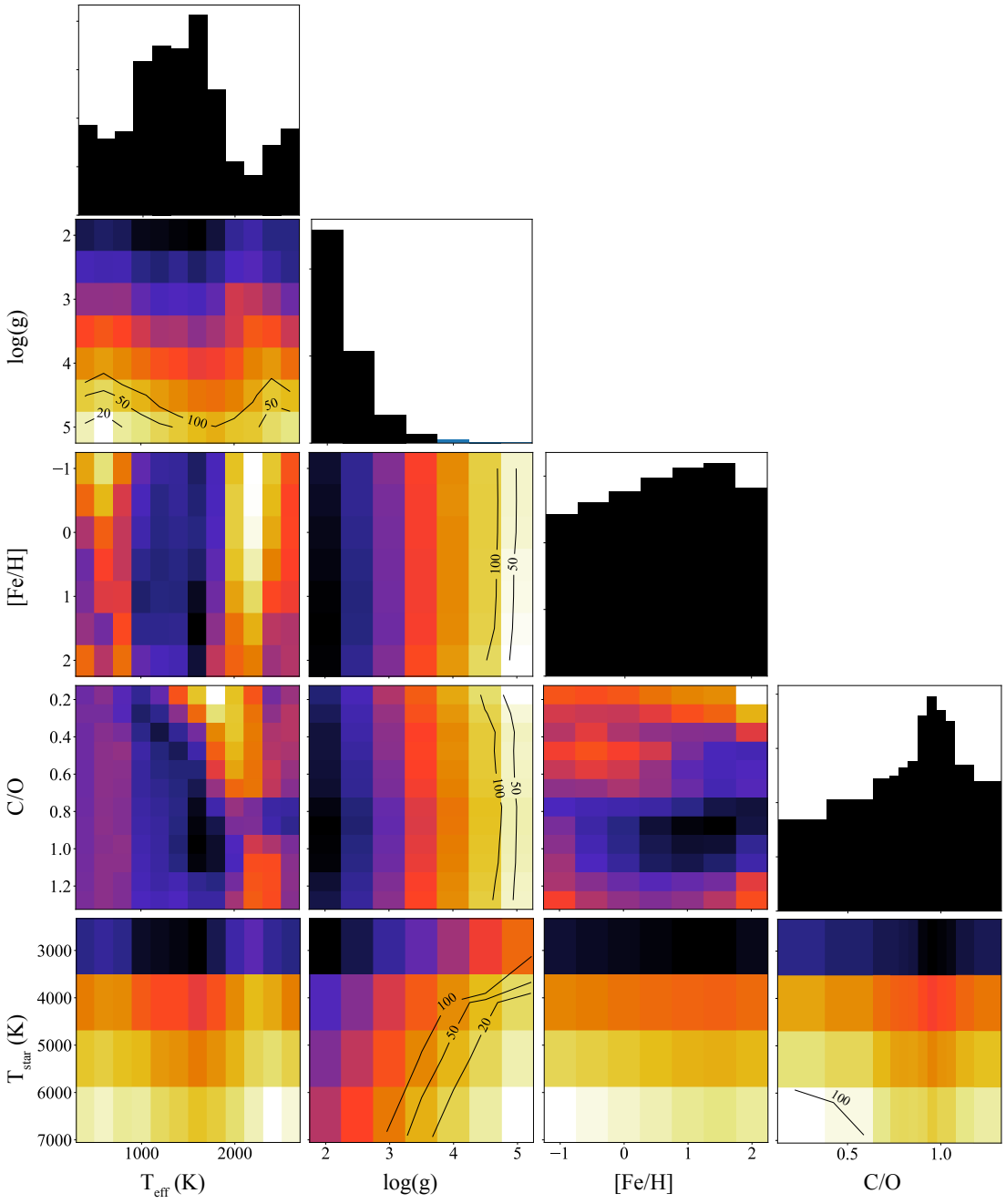

Figure 4.7: The average maximum variation in the transmission spectra, max(ΔTD), due to the disequilibrium for a Jupiter-size planet. Dark-blue represents the parameter-space with the highest max(ΔTD). Colormaps are scaled for each panel to show the patterns in more detail. Regions with 20, 50, and 100 ppm levels are shown with counters; 20 and 50 ppm represent the noise levels for NIRISS SOSS and MIRI LRS, respectively (Greene et al. 2016). Panels without the counters have max(ΔTD) higher than 100 ppm. The marginal panels (1D black histograms at the top) represent ΔTD of individual atmospheric parameters.

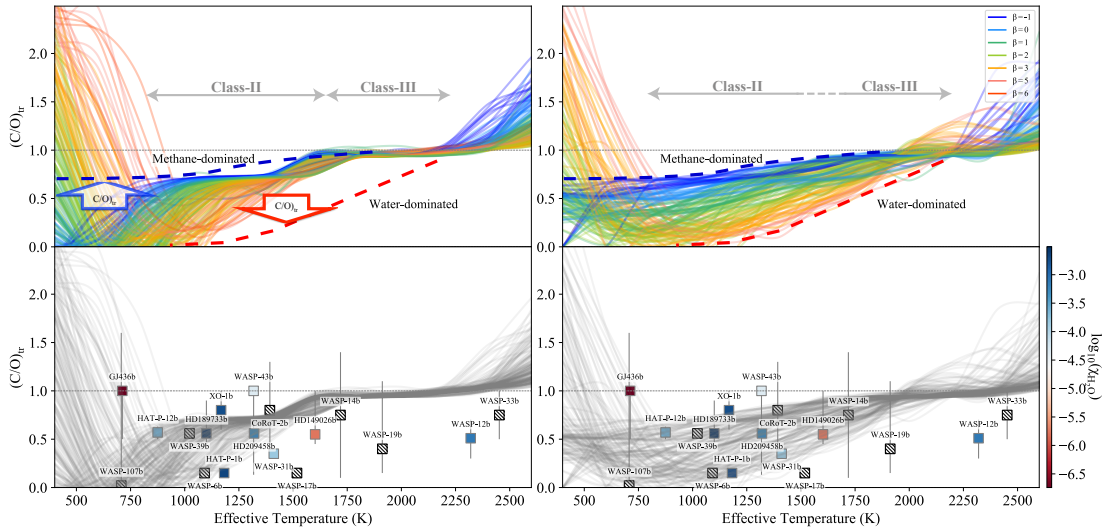

Figure 4.8: The effect of vertical mixing on the transition C/O ratios. **Upper left)** Transition C/O ratios of thermochemically equilibrium models presented in Molaverdikhani et al. (2019b). The transmission spectra above the transition lines are expected to be CH_4-dominated and below them to be H_2O-dominated. Different colors represent the transition C/O ratio at different β factors. **Bottom left)** The location of exoplanets on the thermochemical equilibrium map with estimated T_{eff} and C/O. **Upper right)** Transition C/O ratios of chemical kinetic models. **Bottom right)** The location of exoplanets with estimated C/O ratio, on the chemical kinetic map. The lines in the bottom panel are gray to increase the visibility of colors for the water content of the observed planets.

transition C/O ratios to decrease for atmospheres with high β. The β factor is a linear combination of surface gravity and metallicity. Higher β values represent deeper photospheres, i.e. at higher pressures. See (Molaverdikhani et al. 2019b) for a detailed discussion on the β factor. This is mostly caused by the higher amount of CH_4 at the photospheric level, when β is higher. Its effect is different for atmospheres with low β and vertical mixing increases the transition C/O ratios. These are shown by blue (for low β models) and red (for high β models) vectors on Figure 4.8 left panel.

The only difference between Class-II and Class-III planets is that in Class-II the atmosphere still contains some oxygen-bearing condensates, but in Class-III planets all those condensates are evaporated. This causes the transition C/O ratios in Class-III to become independent of atmospheric conditions and remain at a constant value of ~0.9. Vertical mixing removes this difference and merges Class-II with III

to one extended class; covering the whole range of ∼900 K to ∼2000 K in one class.

In Class-I planets, both H_2O and CH_4 are usually the dominant species and have relatively less vertically variant profiles. Hence, their abundance variation at TOA is less sensitive to the vertical mixing. Class-IV planets with C/O<1.0 are mostly deficient of CH_4 due to their hot temperatures. Hence their transition C/O ratio remains higher than unity at all time and are usually insensitive to the vertical mixing. However, some Class-IV planets, T_{eff}>2000 K, with very high β, > 5, show an increase in their transition C/O ratio due to lower CH_4 abundances at high pressures. Consequently, our proposed four classes of planets based on our grid of cloud-free models can change to a three classification scheme of planets assuming strong vertical mixing in their atmospheres.

Regardless of the naming of these classes, there exists a "Methane Valley" in both thermochemical equilibrium and vertical mixing cases (see Figure 4.8). The Methane Valley is a region between 800 and 1500 K, where methane is expected to cause the dominant spectral features in the transmission spectra of planets. Hence, a greater chance of CH_4 detection is expected for the planets within this region. The first robust CH_4 detection on an irradiated planet was indeed reported for HD 102195b (Guilluy et al. 2019). This is a Class-II planet with T_{eq}∼963 K, within the Methane Valley and consistent with our prediction.

We also calculate the transmission and emission color-maps, using Spitzer IRAC channel 1 and 2, similar to what we presented in Chapter 2. We note small changes seen in the IRAC emission maps, when going from thermochemical equilibrium to disequilibrium chemistry. Vertical mixing is expected to play a strong role in the atmospheres of cool (T < 1000 K), self-luminous atmospheres with low (planet-like) log(g) (see, e.g., Zahnle & Marley 2014). In such atmospheres the abundances of the cooler upper atmospheric layers is overruled by the abundances mixed up from hot layers at higher pressures, which leads to a significant increase in CO abundance, at the expense of CH_4. A similar effect appears to occur for a few hundred atmospheres in our grid of +28,000 models, which start to fill in the region with $(F_{3.6}\text{-}F_{4.5})/F_{4.5} >$ -0.5. This happens for the models with effective temperatures

below ∼900 K and with very small C/O ratios (<0.25) only (blue points in the low C/O regime in Figure 4.9). Considering what has been predicted for self-luminous atmospheres, this is unexpected. A likely reason for this difference is that the atmospheric temperature profiles of irradiated planets are more isothermal than those of self-luminous ones, such that the deeper (higher pressure) regions from which material is mixed up is cooler, and hence richer in CH_4[3].

The color maps do not show any other statistically meaningful differences, see Figure 4.9, and the two main populations (i.e. CH_4-driven and CO/CO_2-driven populations) remain almost invariant. Our results indicate that deviations from the Spitzer equilibrium chemistry color map presented here are most likely due to effects different than the disequilibrium processes studied in our work, with clouds being a strong contender, the effect of which we will study in the next chapter. If disequilibrium should be the culprit for such deviations, it would point to very small C/O ratios (< 0.25).

4.3 Conclusion

In this chapter, we introduced our newly developed Chemical Kinetic Model (`ChemKM`). The code includes a variety of atmospheric processes including photolysis, molecular and eddy diffusion, and condensation and rainout. Other processes, such as atmospheric ablation and escape can also be included. It is also possible to include galactic and solar cosmic rays (GCRs) and scattered UV sources by LIPM in the models.

After verification of individual processes in `ChemKM`, we compared our results to the Venot (2012) model for HD 189733b. The calculated abundances were consistent between the models except at the μbar regime, where the molecular diffusion and photochemistry are the dominant processes. As a conclusion, we recommend careful consideration of these processes when abundances at TOA have to be calculated.

[3] CO to CH_4 conversion is favored at cool, high pressure conditions; see e.g. Lodders & Fegley (2006); Marley et al. (2002); Hubeny (2017); Noll et al. (2000); Skemer et al. (2012); Saumon et al. (2003).

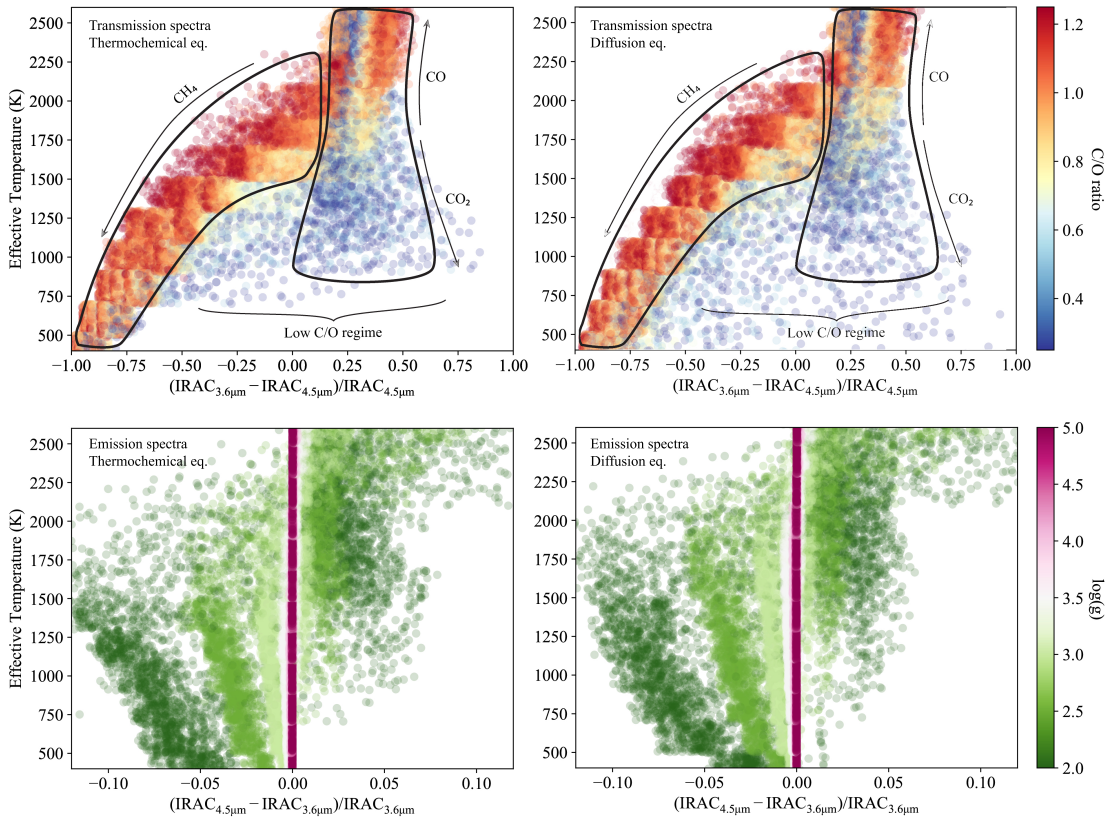

Figure 4.9: Synthetic Spitzer IRAC color–temperature diagrams for cloud-free atmospheres under thermochemical equilibrium (**left panels**) and diffusion equilibrium (**right panels**) conditions. **Top panels** Color diagram based on emission spectroscopy, i.e., IRAC data describes the secondary eclipse depth at λ (μm). **Bottom panels** Same for the transmission technique, i.e., IRAC data describes the transit depth at λ (μm). No significant difference can been seen between thermochemical and diffusion equilibrium models, except for Class-I planets with very low C/O ratios.

We used our grid of disequilibrium chemistry atmospheres with six free parameters, planetary effective temperature (T_{eff}), surface gravity (log(g)), metallicity ([Fe/H]), carbon-to-oxygen ratio (C/O), spectral type of the host star, and vertical mixing (K_{zz}=10^6, 10^9, and 10^{12} cm^2 s^{-1}), to determine the quenching levels. We propose a new metric, the geometric Coefficient of variation (gCV) of abundances, for a quantitative measure of quenching. We find P_{quench} varies significantly under our self-consistent static TP structure setup. We find that all atmospheric parameters ([Fe/H], log(g), and C/O) affect P_{quench} by changing the atmospheric composition.

To explore the detectability of disequilibrium spectral fingerprints due to the molecular and eddy diffusion by JWST, we recommend focusing on the targets

with T_{eff} between 1000 and 1800 K, orbiting around M-dwarfs, having low surface gravity but high metallicity and high C/O (see Section 4.2.4).

We also find that the "Methane Valley" remains largely unchanged by the inclusion of vertical mixing. This is a region between 800 and 1500 K, where a greater chance of CH_4 detection is expected. Indeed, the first robust CH_4 detection on an irradiated planet was within this region (Guilluy et al. 2019); supporting our prediction from Molaverdikhani et al. (2019b). We argued in Chapter 2 that the detection of CH_4 or the lack of such detection, could hint at the prevalence of cloud formation or disequilibrium chemistry. Here we find that disequilibrium unlikely to change this picture significantly. Thus, characterization of planetary atmospheres within this parameter space is expected to provide a diagnostic tool to identify cloud formation condition.

Our further analysis showed that the two main populations in the Spitzer IRAC's emission color-maps remain largely unchanged, when including mixing. Although we note some differences between the two maps for the models with effective temperatures below ~900 K and with very small C/O ratios (<0.25), see Figure 4.9. Therefore any deviation of observational points from these color-maps is likely to be due to the presence of clouds and not disequilibrium chemistry, but the effect of mixing for cold planets with very low C/O ratios could be significant.

Clouds can potentially change the TP structure, composition, and ultimately the spectra of planetary atmospheres. In the next chapter we investigate how cloud formation affect the atmospheric spectra and what types of planets are most affected by this process.

Clouds come floating into my life, no longer to carry rain or usher storm, but to add color to my sunset sky.

— Rabindranath Tagore.

5 The Role of Clouds

Contents

5.1 Introduction

After discovery of the first exoplanet in 1990's (Wolszczan & Frail 1992) and a fast growing number of discoveries since then[1], there have been many attempts to observe and characterize their atmospheres (for some recent reviews see e.g. Sing 2018; Fortney 2018; Helling 2019a; Madhusudhan 2019). Water and methane have been the focus of many investigations due to their relevance to the origin of life

[1] https://exoplanets.nasa.gov

and habitability, as well as their major roles to shape the structure of planetary atmospheres (e.g. Sudarsky et al. 2000; Ackerman & Marley 2001; Swain et al. 2008, 2009a; Benneke & Seager 2013; Birkby et al. 2013; Agúndez et al. 2014b; Fraine et al. 2014; Hu 2014; Kreidberg et al. 2014b, 2015; Sing et al. 2016; Airapetian et al. 2016; Evans et al. 2016; Brogi et al. 2018; Kreidberg et al. 2018b; Tsiaras et al. 2018; Alonso-Floriano et al. 2019; Arcangeli et al. 2018; Badhan et al. 2019; Benneke et al. 2019; Chachan et al. 2019; Dencs & Regály 2019; Irwin et al. 2019a; Kirk et al. 2019; Sánchez-López et al. 2019; Smith et al. 2019). Abundances retrieved for these species can be also used as a tracer of carbon-to-oxygen ratio (C/O) and metallicity of these atmospheres; hence potentially linking the formation scenarios with the observations (e.g. Raymond et al. 2004; Bethell & Bergin 2009; Henning & Semenov 2013; O'Brien et al. 2014; Mordasini et al. 2016; Cridland et al. 2019). Water's spectral signature is everywhere, but despite many efforts, there has been only one robust detection of methane on exoplanets, and only through high-resolution spectroscopy (Guilluy et al. 2019).

In contrast, methane has been observed on most planets in the solar system. In Earth's atmosphere, living organisms primarily produce it (e.g. Schoell 1988; Catling et al. 2001). On gaseous planets, it is believed to be due to abiogenic processes (e.g. Guillot 1999; Glasby 2006; Guillot 2019). On Mars, its origin is yet to be known (e.g. Krasnopolsky et al. 2004; Atreya et al. 2007). Abiogenic processes have remained to be tested to explain possible presence of methane on early Mars (e.g. Kite et al. 2019) and methane and oxygen abundances measured by the Curiosity rover over several Martian years (e.g. Trainer et al. 2020). These recent measurements have been examined several times to dilute the possibility of human errors. But, how well we understand CH_4 chemistry to rule out an abiogenic origin on the present Mars? While further in-situ measurements, laboratory studies, and model development are crucial to address this question (e.g. Hu et al. 2016), exploring the validity of CH_4 chemistry over a broad range of chemical environments on exoplanets opens a new path. Consequently, consistency of observations and

simulations of CH_4 on highly irradiated exoplanets might provide a framework on CH_4 chemistry to be further adapted to study the chemistry of temperate planets.

To investigate the origin of apparent paucity of methane on the majority of observed exoatmospheres, we isolated the effect of atmospheric processes by applying a hierarchical modelling approach. In Molaverdikhani et al. (2019b), we present the results of our extensive thermochemical cloud-free self-consistent simulations with more than 28,000 models. We propose a new classification scheme for irradiated gaseous planets based on their dominant chemistry at their photospheric levels. We focus on planets with an effective temperature between 400 K and 2600 K. The classification is consist of four classes. Class-I planets (with an effective temperature more than 400 K and less than 600-1100 K) are expected to show strong methane and water features in their transmission spectra, *if* cloud-free and at thermochemical equilibrium. Class-II planets are hotter than Class-I (T_{eff} < 1650 K). Their transmission spectra is largely sensitive to the atmospheric C/O ratio, effective temperature, and β-factor (a linear combination of metallicity and surface gravity, β=log(g)-1.7×[Fe/H], which provides an indication of the photospheric pressure level). Low C/O ratios usually result in water-dominated spectra and high C/O ratios lead to methane-dominated spectra. C/O ratios at which this transition occurs are referred to as the transition C/O ratios, C/O_{tr}. Class-III planets are hotter than Class-II and free of condensates. Such lack of condensates makes the transition C/O ratios insensitive to the β-factor and temperature, and remains around a value of 0.94. Class-IV planets demands higher C/O ratios to present CH_4 features in their transmission spectra. This is mainly due to their hotter photosphere and the formation of HCN and CO, as the main sinks of carbon instead of CH_4. We also find a parameter-space (800 K < T_{eff}<1500 K and C/O ratio above a certain threshold value) with a higher chance of methane detection; the Methane Valley. HD 102195b resides in this parameter-space, which supports our prediction. Comparing the rest of observed planets with these results suggests either these planets have extremely low C/O ratios or other atmospheric processes are in play.

In Molaverdikhani et al. (2019a) we describe a Chemical Kinetic Model, ChemKM, that we implemented to investigate the importance of kinetics in the planetary atmospheres. The results of more than 112,000 chemical kinetic models with full chemical network indicates strong vertical mixing could homogenize vertical abundance of methane; causing quenched abundances. A quenched abundance may result in methane depletion or methane enhancement, depending on its vertical distribution. An example of such case is shown in Molaverdikhani et al. (2019a) Figure 2. Nevertheless, strong vertical mixing makes the boundary between class-II and III planets less profound, but the Methane Valley persists to take place at similar parameter-space. Rarity of methane observations brings us to the next step to explore yet another fundamental process in the atmosphere of planets: clouds.

All planets in the solar system with a substantial atmosphere possess clouds. Their composition and vertical distribution, however, varies from one planet to another, Figure 1.1. This includes, temperatures ranging from 50 to 350 K at around 1 bar and clouds composed of CH_4, H_2S, NH_3, NH_3SH, H_2O, H_2SO_4, etc. Regardless of the temperature structure or the composition of these planets, their visible cloud deck appear to be located at around 1 bar, which makes it a convenient reference pressure in the solar system community (e.g. Seiff et al. 1998; Guillot 1999).

Exoplanets seem to follow a similar story. Observations of exoplanets in their near-infrared spectra revealed lower amplitude of water signatures in comparison to the expected amplitudes from cloud-free simulations (e.g. Sing et al. 2016; Tsiaras et al. 2018; Pinhas et al. 2019). Water depletion in the protoplanetary disks at the planet's formation location has been debated as a cause of this lower amplitude (e.g. Seager et al. 2005b; Madhusudhan et al. 2014a,b; Sing et al. 2016). An alternative explanation is perhaps the presence of haze and clouds. Their physical properties (such as particles' shape, size distribution and chemical composition) affect their optical properties (e.g. Heng & Demory 2013), and their gray or semi-gray opacity in the optical and NIR could obscure atomic and molecular features in this wavelength range. These physical properties depend on the atmospheric structure and dynamics (e.g. Morley et al. 2012), and in turn, their radiative feedback could change the

temperature structure of the atmosphere and the atmospheric scale height (e.g. Morley et al. 2012), which also influences the atmospheric composition (e.g. Helling 2019a; Poser et al. 2019). Consequently, our proposed classification and the Methane Valley might be affected by the formation of clouds in the atmosphere of irradiated exoplanets and might explain the observed paucity of methane.

In what follows, we describe the method and our grid of self-consistent cloudy models in Section 5.2. In Section 5.3, we present the results of $(C/O)_{tr}$ ratios and how our classification and the Methane Valley are affected by clouds. In Section 5.4, we construct synthetic Spitzer transmission and emission color-diagrams and discuss the consistency of our results with observations. We summarize and conclude our results and findings in Section 5.5.

5.2 Methods

In order to investigate the influence of clouds on the atmospheric properties, we have synthesized a population of 37,800 1D self-consistent cloudy planetary atmospheres by using *petitCODE* (Mollière et al. 2015, 2017). The model assumes radiative-convective and thermochemical equilibrium and iteratively solves for the atmospheric composition and thermal structure. The code can be used to also calculate the emission and transmission spectra. The chemical inputs of the code are a list of atomic species and a list of reaction products that are the same as the chemical inputs described in Molaverdikhani et al. (2019b)[2].

In addition to the gas opacity species (CH_4, H_2O, CO_2, HCN, CO, H_2, H_2S, NH_3, OH, C_2H_2, PH_3, Na, K, TiO, and VO) considered in our grid of cloud-free models, cloud opacity species are also provided, which includes Mg_2SiO_4, Fe, KCl and

[2]As a reminder they are the lists of atomic species (H, He, C, N, O, Na, Mg, Al, Si, P, S, Cl, K, Ca, Ti, V, Fe, and Ni) with their mass fractions and reaction products (H, H_2, He, O, C, N, Mg, Si, Fe, S, Al, Ca, Na, Ni, P, K, Ti, CO, OH, SH, N_2, O_2, SiO, TiO, SiS, H_2O, C_2, CH, CN, CS, SiC, NH, SiH, NO, SN, SiN, SO, S_2, C_2H, HCN, C_2H_2, CH_4, AlH, AlOH, Al_2O, CaOH, MgH, MgOH, PH_3, CO_2, TiO_2, Si_2C, SiO_2, FeO, NH_2, NH_3, CH_2, CH_3, H_2S, VO, VO_2, NaCl, KCl, e^-, H^+, H^-, Na^+, K^+, PH_2, P_2, PS, PO, P_4O_6, PH, V, VO(c), VO(L), $MgSiO_3$(c), Mg_2SiO_4(c), SiC(c), Fe(c), Al_2O_3(c), Na_2S(c), KCl(c), Fe(L), Mg_2SiO_4(L), SiC(L), $MgSiO_3$(L), H_2O(L), H_2O(c), TiO(c), TiO(L), $MgAl_2O_4$(c), FeO(c), Fe_2O_3(c), Fe_2SiO_4(c), TiO_2(c), TiO_2(L), H_3PO_4(c) and H_3PO_4(L))

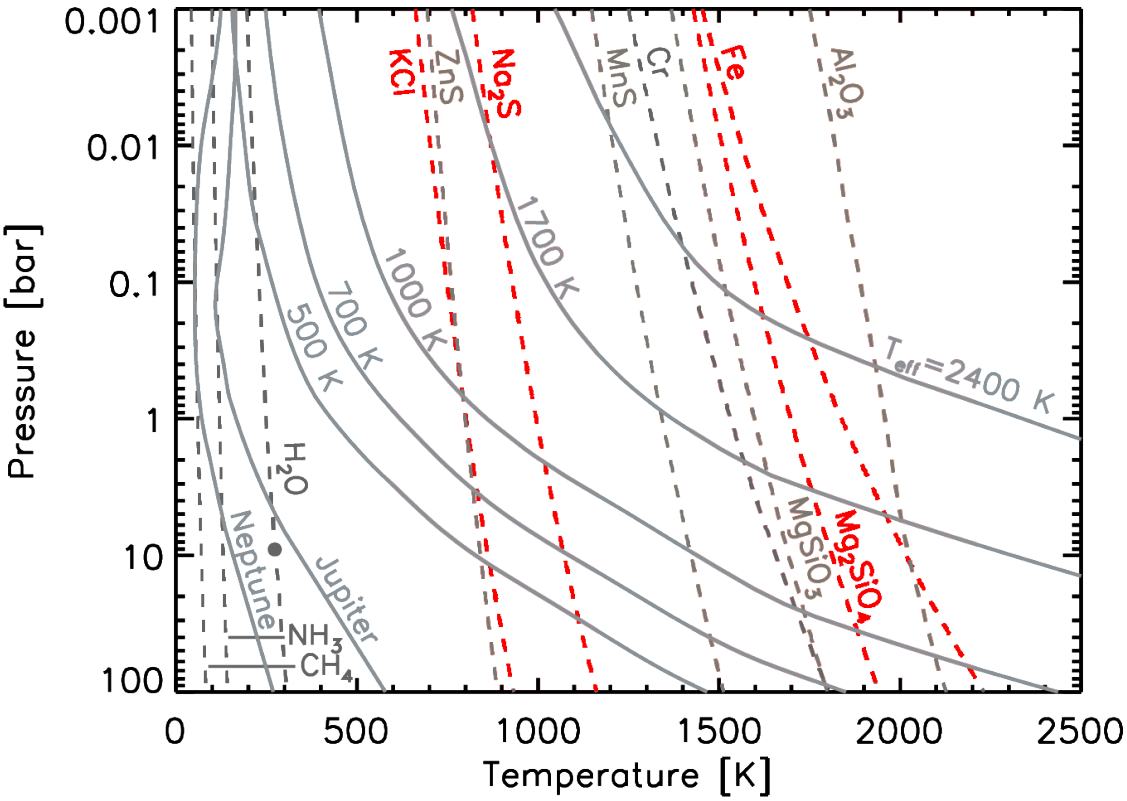

Figure 5.1: Temperature profiles of the planets in solar system and some synthesized TPs for cloud-free exoplanets (solid lines). Condensation curves for variety of chemical substances (dashed lines). The opacities of Mg_2SiO_4, Fe, KCl and Na_2S are considered in our cloudy grid (red dashed lines), which could affect the temperature profile and vertical composition of the planetary atmospheres. Adapted from Marley & Robinson (2015)

Na_2S. Figure 5.1 shows the condensation curves over a broad range of temperatures encountered in the atmosphere of planets and marks the condensation curves of these four condensates as they cross the temperature structure of cloud-free planets. Inclusion of these cloud opacities is expected to introduce a radiative feedback, hence affecting the atmospheric thermal structure and composition. H_2–H_2 and H_2–He collision-induced absorption (CIA) is also included in the model.

There are two options to treat clouds in petitCODE. One option is to follow the method introduced by Ackerman & Marley (2001), for which the following equation must be solved:

$$-K_{zz}\frac{\partial q_t}{\partial z} - f_{sed} w_* q_c = 0 \tag{5.1}$$

where K_{zz} is the vertical eddy diffusion coefficient and w_* is the convective velocity scale. The product of f_{sed} and w_* represents an effective sedimentation velocity for

the condensate. Therefore, f_{sed} (the settling or sedimentation factor) can be regarded as the ratio of the mass-weighted droplet sedimentation velocity to w_*. q_c and q_t are the condensate mass fraction and the total mass fraction of the cloud species. The treatment of vertical mixing is described in Appendix A3 of Mollière et al. (2017).

The second option for the treatment of clouds is assuming a constant size for the cloud particles and set the maximum cloud mass fraction (see Mollière et al. 2017). We choose the first approach, which is more physically driven. When interpreting the results of our simulations, it should be noted that there is no rainout of condensates in petitCODE. Hence, an overestimation of cloud opacities might be introduced in the case of colder planets. This is discussed in more detail in Sections 5.2.1 and 5.5. In continue, we describe the properties of the grid of cloudy models.

5.2.1 Grid properties

We consider the effective temperature (T_{eff}), surface gravity (log(g)), metallicity ([Fe/H]), carbon-to-oxygen-ratio (C/O), stellar type, and the settling factor (f_{sed}) as the free parameters of this grid of models. These parameters and their values are discussed below.

Effective temperature (T_{eff})

For the cloud-free (Molaverdikhani et al. 2019b) and disequilibrium (Molaverdikhani et al. 2019a) grids, we set the interior temperature at 200 K to be consistent with the Fortney (2005) and Mollière et al. (2015) simulations. In the cloudy grid (this work) we assume the same interior temperature, consistent with the previous grids.

In both previous grids (cloud-free and disequilibrium), the range of temperature was selected to span from relatively cold planets, 400 K, to ultra hot planets, 2600 K. Therefore, the best choice of temperature range for the cloudy grid would be using the same range. However, as shown in Figure 5.1, none of the considered cloud opacities (Mg_2SiO_4, Fe, KCl and Na_2S) would result in cloud formation at temperatures above 2400 K under a 1D setup. Thus, we limit the upper effective temperature of the planets to 2400 K. At the other end of the temperature range,

due to the lack of rain-out implementation in the petitCODE, colder planets would suffer from the over abundance of cloud opacities if all the cloud opacities remain the same for all planets. Again, as shown in Figure 5.1, at temperatures below 800 K, all planets are expected to be covered by all four considered cloud types (Mg_2SiO_4, Fe, KCl and Na_2S) in 1D setup. Therefore, any planet with an effective temperature colder than 800 K would result in a spectrum void of atomic and molecular features. Hence, less information regarding the composition of atmosphere at the photospheric level can be interpreted from the planetary spectra of these planets. Therefore, we limit the lowest effective temperature to 800 K. We choose an increment of 200 K to be consistent with the previous grids.

Surface gravity (log(g))

In the previous grids, surface gravity in the models spans over a very wide range of possibilities, from 2.0 to 5.0. But planets with a surface gravity of 2.0 or 5.0 are very exceptional (see Figure 1 in Molaverdikhani et al. 2019b). Since the computational time of cloudy models is at least one order of magnitude longer than that of cloud-free models (usually a few hours for a cloud-free model and a few days for a cloudy model), we opt for excluding the rarely observable parameter-space from the cloudy grid. We thus explore this parameter from 2.5 to 4.5 with increment of 0.5; similar increment to that of previous grids.

Metallicity ([Fe/H])

In the previous grids, we chose to explore a wide range of metallicities from sub-solar, [Fe/H]=-1.0, to super-solar [Fe/H]=2.0 with increment of 0.5. We choose the same setup for the range and increment of metallicity in the cloudy grid.

Carbon-to-oxygen-ratio (C/O)

As discussed in the introduction, one major goal of performing the cloudy grid is to find the transition C/O ratios; i.e. a boundary in the parameter space where the planetary atmosphere transitions from a water-dominated to water-dominated one as C/O ratio increases. For this reason, in our cloud-free and disequilibrium

grids, we selected irregular parameter steps spanning from 0.25 to 1.25 with smaller steps around unity: C/O=[0.25, 0.5, 0.7, 0.75, 0.80, 0.85, 0.90, 0.95, 1.0, 1.05, 1.10, 1.25]. These smaller steps around unity were in order to capture the traditionally believed boundary at around the unity. However, we showed that this transition could occur at any C/O (Molaverdikhani et al. 2019b,a). Hence a finer step-size at unity is no longer needed. As a result we choose to vary the C/O from 0.2 to 1.2 with an increment of 0.2 everywhere.

Stellar type

We choose the same stellar types in the cloudy grid as the previous grids, i.e. M5, K5, G5 and F5, in order to cover a wide range of stellar types.

Settling factor (f_{sed})

As noted before, we use the cloud implementation in the petitCODE that is introduced by (Ackerman & Marley 2001). The product $f_{sed}w_*$ represents an average sedimentation velocity for the condensate, which cause an offset to the turbulent mixing. In the case of no sedimentation velocity (with f_{sed}=0), condensates remain "frozen-in" and move with the gas particles; i.e. following the same velocity. As f_{sed} increases, and so the sedimentation velocity, larger cloud particles, lower cloud mass fraction and larger settled clouds (i.e. less extended) are expected.

Estimated and assumed values of f_{sed} depend on a variety of parameters such as the cloud type and the atmospheric environment. But to provide an order of magnitude value and as a rule of thumb it can vary between 0.01 and 10; but often it retains a value less than 1.0 (Lunine et al. 1989) (Ackerman & Marley 2001; Mollière et al. 2017). Therefore, we investigate the effect of the sedimentation factor from $10^{-1.5}$ ($\sim$0.03) to $10^{0.5}$ ($\sim$3) with a logarithmic increment of $10^{0.5}$. It is worth mentioning that f_{sed} and K_{zz} are degenerate and should be considered when interpreting the results.

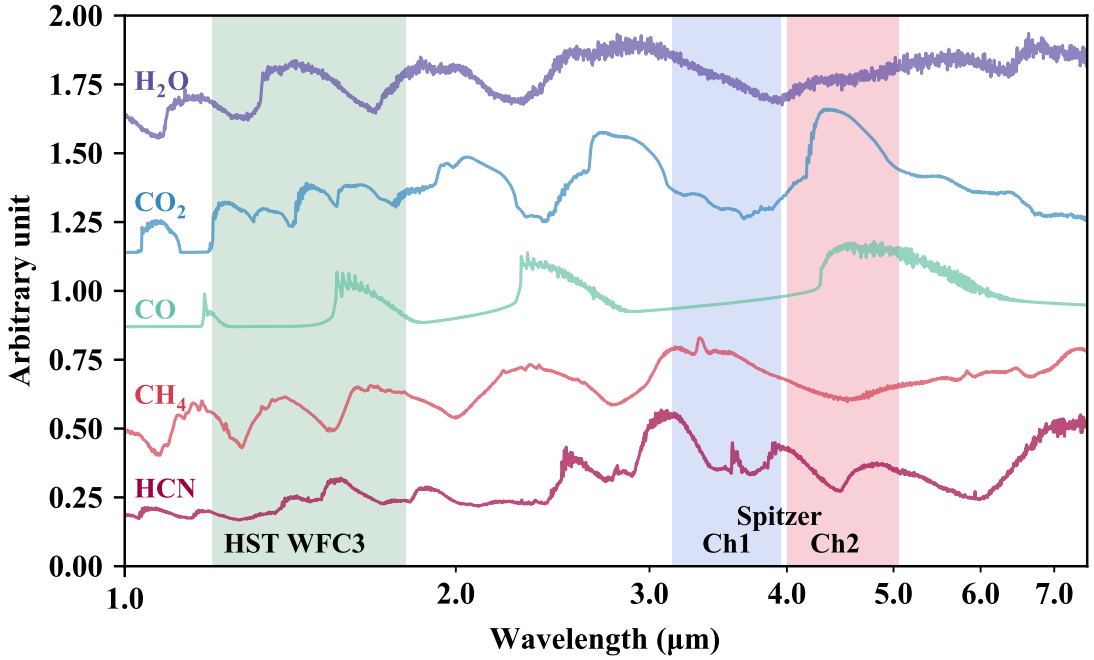

Figure 5.2: Templates of major opacity sources used in the spectral decomposition technique, see Section 5.2.2. The wavelength coverage of HST-WFC3 and Spitzer-IRAC's channel 1 and 2 are shown for reference.

5.2.2 Spectral Decomposition

In order to quantitatively estimate the transition C/O ratios, the contribution of each atmospheric constituent in the spectra should be estimated. To perform this, we follow the same as in (Molaverdikhani et al. 2019b), using the spectral decomposition technique. Constructed templates of transmission spectra of individual species, assuming an isothermal TP with T=1600 K, are shown for some major opacity sources in Figure 5.2. We find the best linear combination of these templates that fits to the model the best. The best fitted coefficients are then the contribution coefficients of the species. By definition, the ratio of contribution coefficient of methane to water, c_{CH_4}/c_{H_2O}, is unity at any transition C/O ratio. For a methane-dominated spectrum $c_{CH_4}/c_{H_2O} > 1$ and for a water-dominated spectrum it is $c_{CH_4}/c_{H_2O} < 1$.

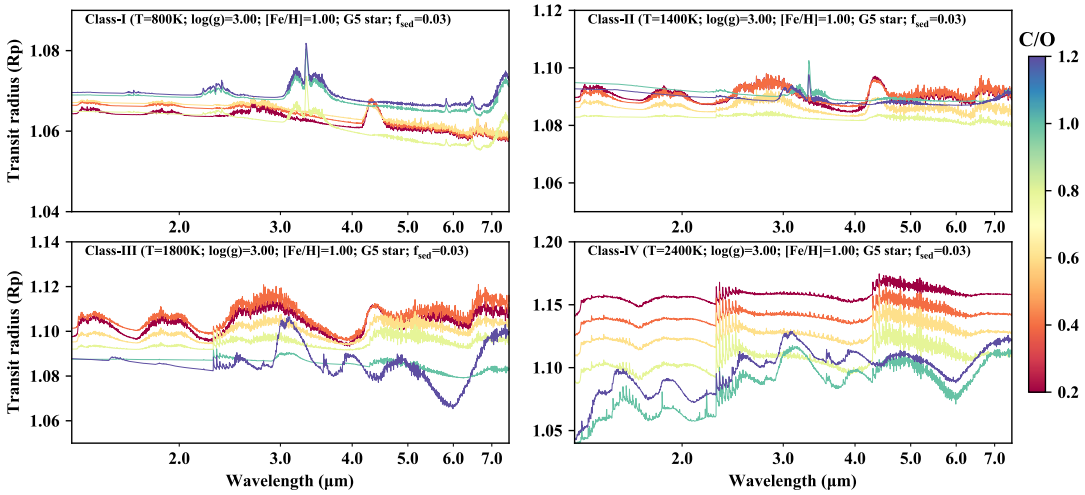

Figure 5.3: Examples of transmission spectra of self-consistent cloudy models at f_{sed} ∼0.03. Carbon-rich class-I and class-II planets show spectral signatures of CH_4 but in hotter classes (III and IV) CH_4 is replaced with CO and HCN in comparison to the cloud-free atmospheres.

5.3 Classification scheme and the Methane Valley

5.3.1 The role of clouds

Complexity of clouds' radiative feedback in self-consistent calculations makes studying their effects in an automated way a challenge. We therefore begin our investigation by exploring these effects through the analysis of several examples. We then generalize our findings by using an automated and quantitative approach in Section 5.3.3.

Figure 5.3 illustrates how the transmission spectrum of cloudy models changes with carbon-to-oxygen ratio in four classes of planets. We assume log(g)=3.0, [Fe/H]=1.0, G5 star, and f_{sed} ∼0.03 for these models. This surface gravity and metallicity are chosen to be representative of atmospheric compositions of sub-Jovian gaseous planets in the solar system[3].

Comparing these spectra with the cloud-free spectra (e.g. see Figure 4 in Molaverdikhani et al. 2019b) reveals several striking differences. Due to low settling

[3]Saturn, Uranus and Neptune, all have a surface gravity of around 3.0 with super-solar metallicities.

factor in these examples, clouds remain high in the atmosphere (at low pressures) and prevent molecular features to appear in full. Unsurprisingly, colder planets are influenced by the cloud opacities the most. This is evident in the transmission spectra of Class-I planets, as the coldest planets in our grid of models. Low C/O ratios (redder colors) are expected to result in the presence of both methane and water in the transmission spectra, assuming cloud-free atmospheres. In cloudy models, however, methane is vanished at low C/O ratios. The level of clouds' continuum in these examples suggests that methane is depleted at lower C/O ratios rather than being obscured by clouds.

To examine this, abundances of methane at low C/O ratio environment are compared between self-consistent cloudy models and self-consistent cloud-free models in Figure 5.4. Metallicity, C/O ratio, and stellar type are assumed to be 1.0, 0.25 and G5, respectively. For the cloudy models the results of C/O=0.2 and C/O=0.4 are linearly combined to estimate the abundance profiles at C/O=0.25. These models show that for Class-I planets, at most altitudes methane abundances are diminished at the presence of clouds. Although there are some regions with more CH_4 production. These local depletion and production of methane are due to local atmospheric heating and cooling as show in Figure 5.5. This mechanism is also consistent with the observation of depleted methane on self-luminous objects (Barman et al. 2011; Currie et al. 2011; Marley et al. 2012). The excess heating releases the sequestered oxygen from the condensates partially, to accelerate the formation of water instead of methane. This excess H_2O manifests itself in the transmission spectra of cold planets with low C/O ratios, see e.g. Figure 5.3. The following reaction is a possible chemical pathway for this conversion:

$$CH_4 + 2\,O_2 \longrightarrow CO_2 + 2\,H_2O\,. \tag{5.2}$$

A hotter deeper atmosphere due to clouds' radiative feedback could result in the depletion of NH_3 too. This is consistent with the observations of GJ 3470 b, a warm sub-Neptune (Benneke et al. 2019). Therefore, an atmosphere depleted of CH_4 and NH_3 could be an indication of heating at deeper regions by a thick

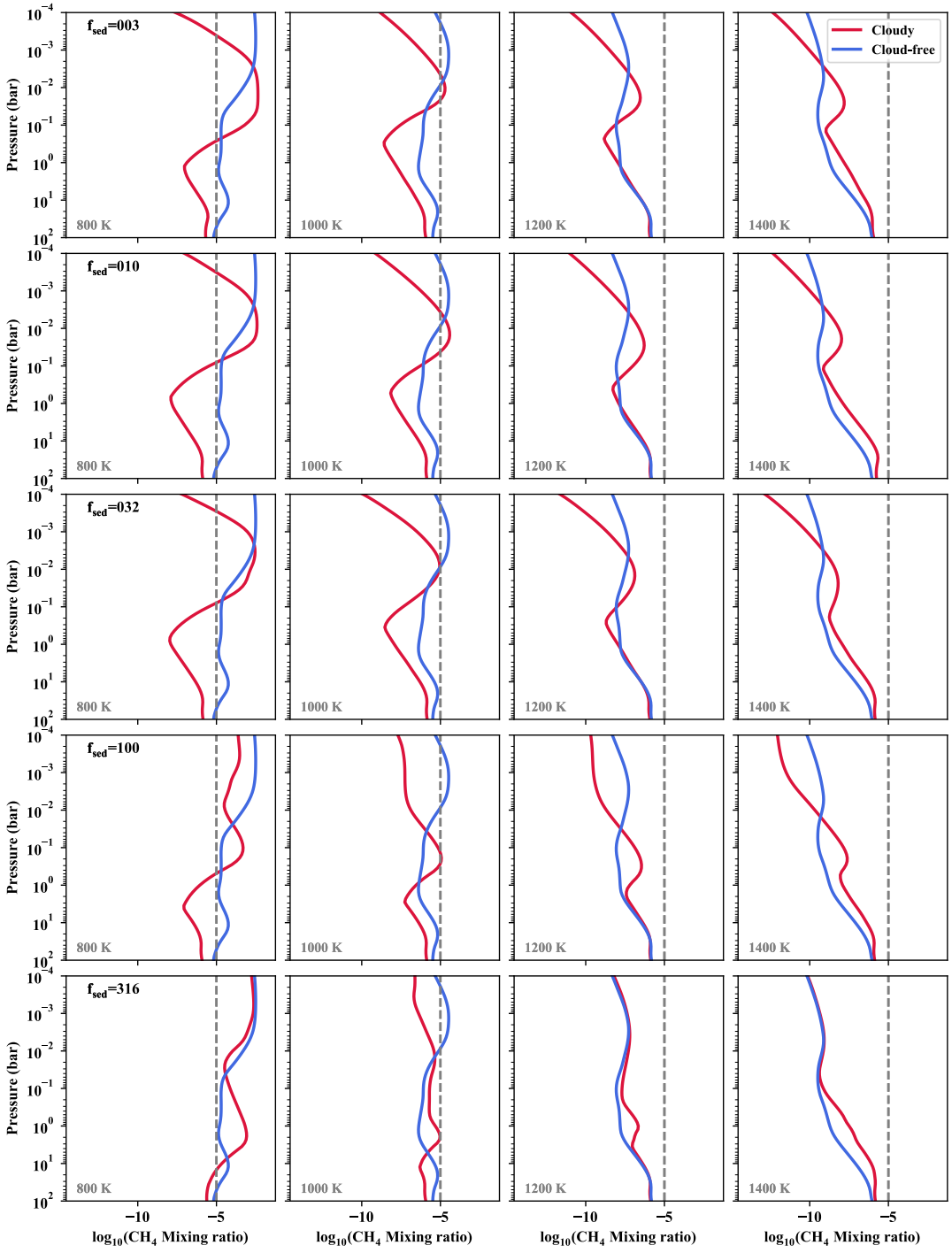

Figure 5.4: Comparing methane abundances at low C/O ratio environment, in self-consistent cloudy models and in self-consistent cloud-free models. In all examples, metallicity, C/O ratio, and stellar type are assumed to be the same, and are [Fe/H]=1.0, C/O=0.25, and G5. Methane abundances are lower at most altitudes and in most cases, although there are some regions with more CH_4 production due to local atmospheric cooling. Hotter planets, in general, produce much less methane as expected; the vertical dashed line marks a reference at 10^{-5} mixing ratio for reference. Abundances are shown for different values of sedimentation factor, f_{sed}.

layer of silicate, alkali feldspars or other non-soot clouds rather than depletion by photochemical processes. Constraining the composition of clouds could aid to link the observable parts to the deeper levels and address which process is in act.

Figure 5.5 shows the corresponding temperature structures of Figure 5.4 models, where the temperature profiles appear to be relatively hotter for all models with temperatures relevant to the formation of CH_4, e.g. $T_{eff} < 1200$ K. At hotter temperatures, where clouds are thinning, the deeper parts of the atmosphere could be cooled down by the presence of clouds, e.g. models with $T_{eff} = 1400$ K. Nevertheless, clouds' feedbacks are found to be highly non-linear throughout the entire parameter-space. The effects of different values of sedimentation factor, as shown in Figures 5.4 and 5.5, will be discussed later.

Getting back to the Class-I planets in Figure 5.3, even the strongest water features between 2.5 to 3.5 μm have been heavily muted. CO_2, on the other hand, has an appreciable fingerprint between 4.0 to 5.0 μm due to weaker other opacities (such as water's and clouds') at these wavelengths and excess production through Reaction 5.2. At higher C/O ratios (bluer colors) CH_4 comes into sight; although it is significantly muted by clouds. The most prominent spectral signature of methane at 3.3 μm seems to be persisting and a good target-wavelength for the future observations of possible carbon-rich but cloudy planets, such as GJ 1214b-like or GJ 436b-like planets (e.g. Kawashima et al. 2019).

The onset of evaporation of condensates in our models is, by definition (Molaverdikhani et al. 2019b), the boundary between Class-I and Class-II planets. This partial evaporation of condensates at hotter temperatures diminishes the contribution of clouds in the opacity budget. Thus, molecular features are expected to be more pronounced with respect to Class-I cloudy planets. While at lower C/O ratios water features follow this prediction and become more pronounced, methane signal at higher C/O ratios seems to be even more muted than in Class-I; e.g. compare the weak methane feature between 2.0 and 3.0 μm in these two classes. This is yet another hint for the depletion of methane at the photospheric levels, rather than obscuration by clouds.

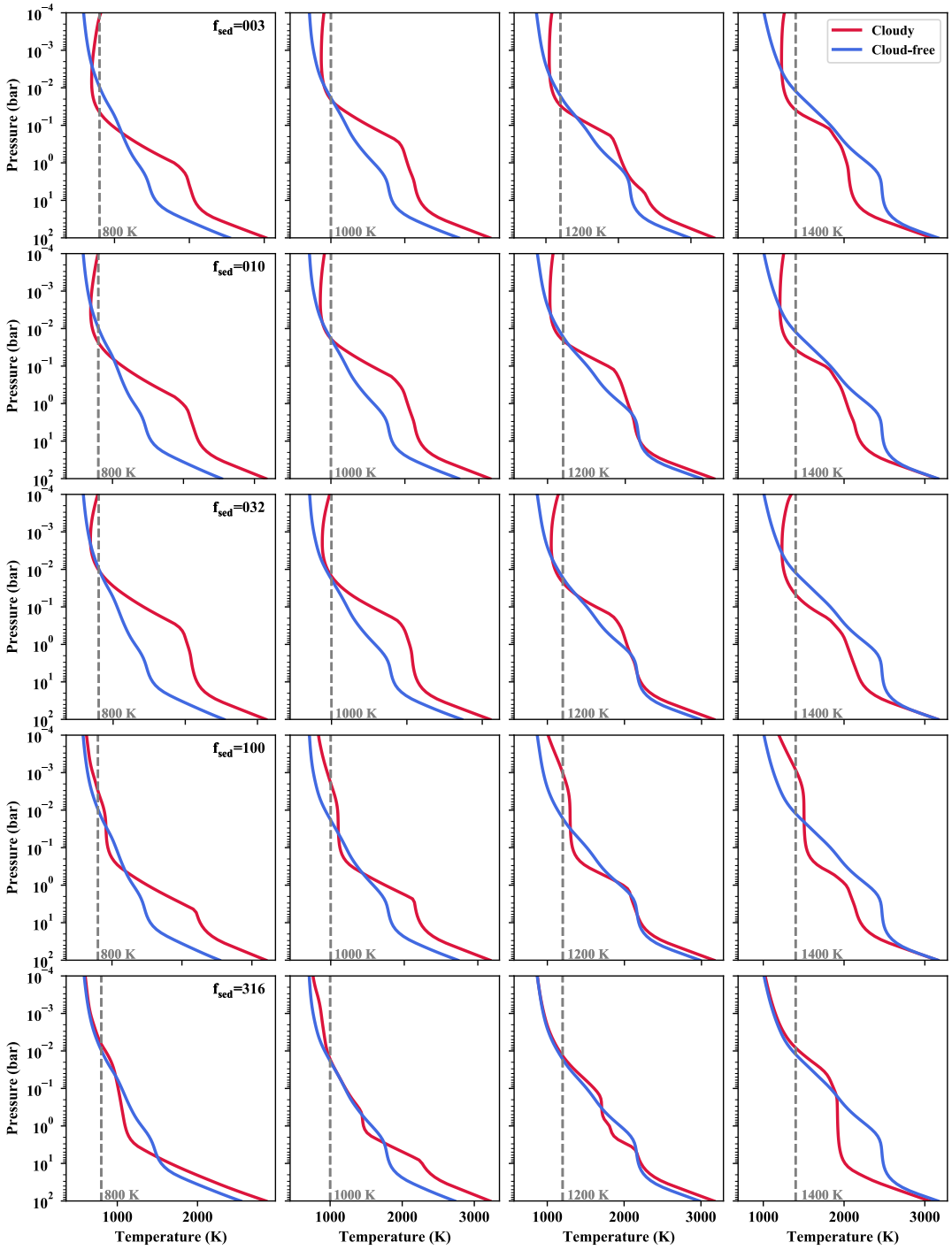

Figure 5.5: Corresponding temperature structures to Figure 5.4 models; Metallicity, C/O ratio, and stellar type are assumed to be the same, and are [Fe/H]=1.0, C/O=0.25, and G5. Atmospheric temperatures are relatively hotter for all planets with temperatures relevant to the formation of CH_4, e.g. $T_{\rm eff} < 1200$ K, although clouds' feedbacks are highly non-linear. Temperature profiles are shown for different values of sedimentation factor, f_{sed}.

Class-III planets, with effective temperatures between 1650 K and 2200 K, show a similar pattern: more pronounced water features at low C/O ratios and no sign of methane at higher C/O ratios. At these temperatures, KCl and Na_2S are completely evaporated but Mg_2SiO_4 and Fe are partially in their solid phase. Partial evaporation of condensates (including the ones that are not considered as the cloud opacities) releases excess oxygen and aid water production. These diminished cloud opacities and enhanced water production explain stronger water features at low C/O ratios of Class-III planets. This additionally produced water at deeper levels makes the atmospheric cooling to be more efficient, which is consistent with the cooled regions of hotter planets shown in Figure 5.5.

On the other hand, higher C/O ratios result in lower water abundances. Therefore, cloud continuum becomes the dominant opacity source at higher C/O ratios in Class-III. This is the minimum opacity condition in cloudy atmospheres. This trend continues until the introduction of other carbon-bearing sources at C/O ratios above the transition C/O ratio. In this example, i.e. Class-III planets in Figure 5.3, CO and HCN become the dominant carbon-bearing species at high C/O ratios and methane's presence is obscured by these species in a non-gray way. Noll et al. (2000) reported a similar mechanism on L Dwarfs for which methane can be obscured by other opacities such as clouds, molecular hydrogen continuum or line opacities. The replacement of CH_4 with CO and HCN in comparison with the cloud-free spectra (e.g. see Figure 4 in Molaverdikhani et al. 2019b), and lower cloud opacity contributions support the methane depletion as the main cause of methane's paucity on hot exoplanets.

When the settling factor is extremely low, clouds remain at very low pressures and contribute significantly in the restructuring of atmosphere. Thus the remaining methane features could be also muted; see the void of methane feature at 3.3 μm for high C/O ratio Class-III spectra, e.g., in Figure 5.3 (see also Figures 5.13, 5.14 and 5.15 in the Appendix, to compare cases with other sedimentation factors). But occasionally and under specific circumstances the 3.3 μm feature emerges debilitated in the models with low settling factors; see e.g. Figure 5.7.

Transmission spectra of Class IV planets, Figure 5.3, are conspicuously different from that of Class-III. In particular, H_2O and CO_2 are replaced by CO at low C/O ratios and there is no sign of cloud continuum even at higher C/O ratios. Methane remains depleted because these temperatures, $T_{eff} > 2200$ K, make inauspicious environment for methane production.

Figure 5.6 illustrates the main CH_4-CO conversion pathway for the similar models in Figures 5.4 and 5.5; except C/O ratio is selected to be 0.5 (instead of 0.25) to achieve higher chemical contribution of methane in the composition of atmosphere for illustration purposes. These conversions can be understood by following this reaction:

$$CH_4 + H_2O \underset{\lesssim 1000K}{\overset{\gtrsim 1000K}{\rightleftharpoons}} 3\,H_2 + CO \tag{5.3}$$

At deeper regions, where atmosphere becomes hotter due to the presence of thick clouds, methane depletes and CO captures the freed carbon. This continues at lower pressures, but CO_2 also also contributes and becomes CO. These all hint for a prominence of CO features in the transmission spectra of irradiated planets.

Mid to late T dwarfs are also expected to have methane-rich atmospheres, if assuming chemical equilibrium state for them. However, observations of CO with relatively high mixing ratios suggested that their atmospheric compositions are likely out of equilibrium (Noll & McElroy 1974; Saumon et al. 2000, 2006; Geballe et al. 2009; Barman et al. 2011). This interpretation is plausible if abundance enhancement at larger pressures is monotonic. If not, then vertical mixing could lead to depleted, enhanced, or invariant CH_4 abundances, depending on the shape of the abundance profile and the strength of atmospheric mixing (e.g. Molaverdikhani et al. 2019a). Therefore, an alternative explanation could be the presence of clouds where higher temperatures at high pressure result in the formation of CO and methane depletion without a need for a strong vertical quenching. A combination of both processes to explain the observed CO on the mid to late T dwarfs seems to be more plausible.

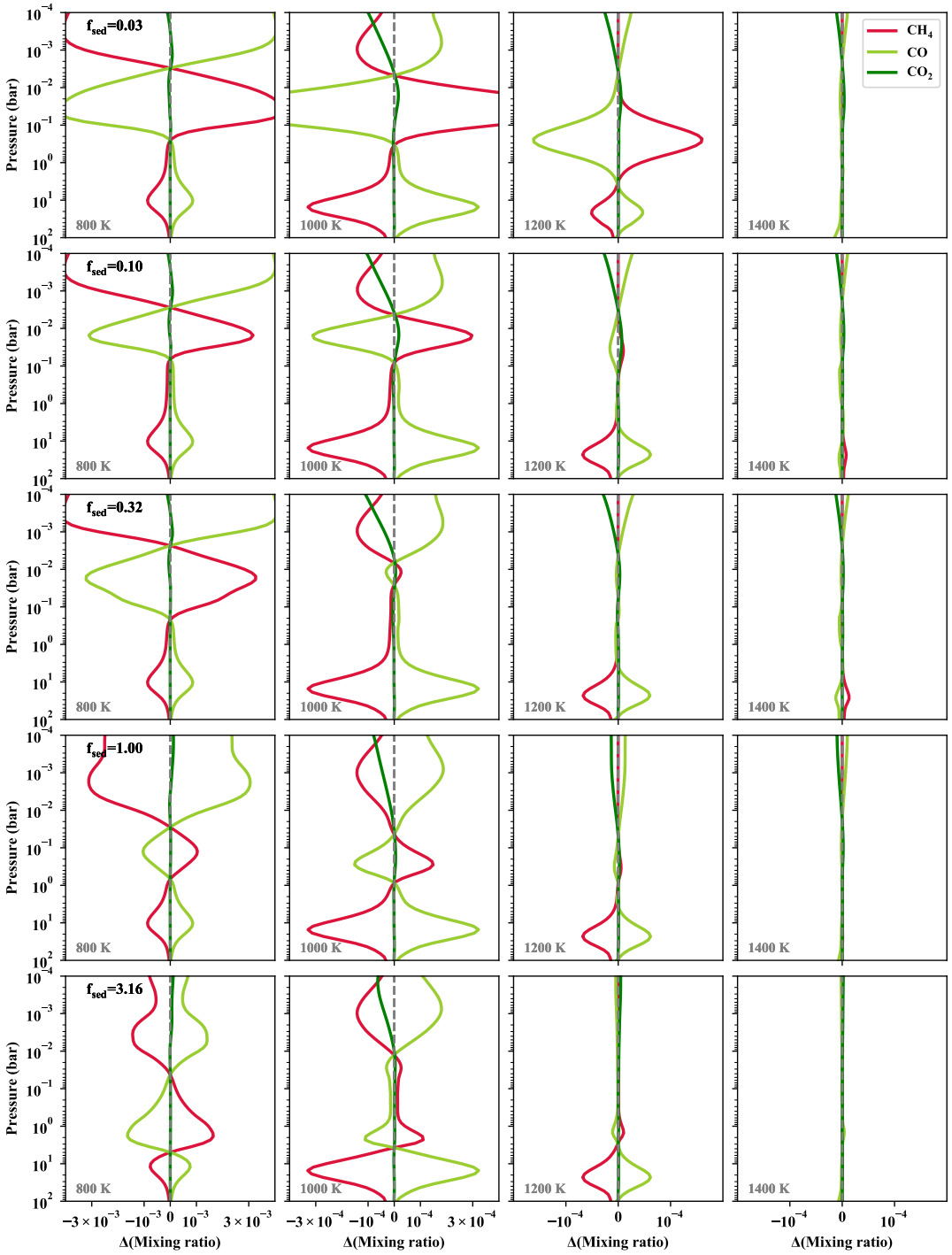

Figure 5.6: Abundance difference between cloudy and cloud-free models for CH_4, CO and CO_2. Models are the same as in Figure 5.4 and 5.5, except C/O ratio is selected to be 0.5 for higher chemical contribution of methane in the composition of atmosphere, for illustration purposes. Vertical dashed lines show zero abundance variation between the two models. Carbon in CH_4 is mostly deposited in CO at the hotter regions of colder planets. On hotter planets, CH_4 plays a negligible role in the carbon chemistry; unless the C/O ratio is very high (not shown here).

5.3.2 The role of sedimentation factor, f_{sed}

Figure 5.5 presents the temperature structure of Class-I and II cloudy models (red lines) at different sedimentation factors, ranging from 0.03 to just above 3. In general, a higher f_{sed} results in the cloud vertical expansion to be narrower and remain at deeper levels (e.g. Ackerman & Marley 2001). This makes the effect of clouds at lower pressures less significant. Consistency of cloud-free and cloudy temperature structures at low pressures (<10 mbar) for the cases with high sedimentation factor, e.g. f_{sed}=3.16, supports this statement. Simultaneously, temperature differences at deeper parts of the atmospheres also decrease at high f_{sed} values. Thus, cloudy models with very high f_{sed} are expected to resemble cloud-free models in general. The highest sedimentation factor in our grid of model is 3.16 and Figure 5.7 illustrates corresponding transmission spectra to this value. The rest of model parameters are the same as in Figure 5.3. The contribution of cloud opacities is barely noticeable in these spectra (Figure 5.7 with f_{sed}=3.16). Class-I and II spectra indeed resemble the spectra of cloud-free models. Methane is the prominent feature in Class-I at all C/O ratios. CO_2 spectral feature at 4.5 μm can be seen as well for this class. Methane in Class-II planets appear in C/O ratios above the transition C/O ratio but not at low C/O ratios. HCN have a persisting appearance in Class-III and IV planets; hinting for a chemical fingerprint of clouds even at high f_{sed} values.

However, as noted, the radiative response to the cloud opacity is highly non-linear and clouds' feedback depends on a variety of parameters, including the sedimentation factor. The response of temperature structure to the variation of f_{sed} is shown in Figures 5.5 for a set of models. Looking at the examples with an effective temperature of 800 K, an increase in f_{sed} from 0.03 to 0.32 heats up the atmosphere in some regions but cools elsewhere. For instance, three atmospheric regions are notable in these particular cases: above a few mbar, below a few hundred mbar, and pressures levels in between. This translates to the depletion of methane at some levels but not the others, Figure 5.6. These regions, however, are not

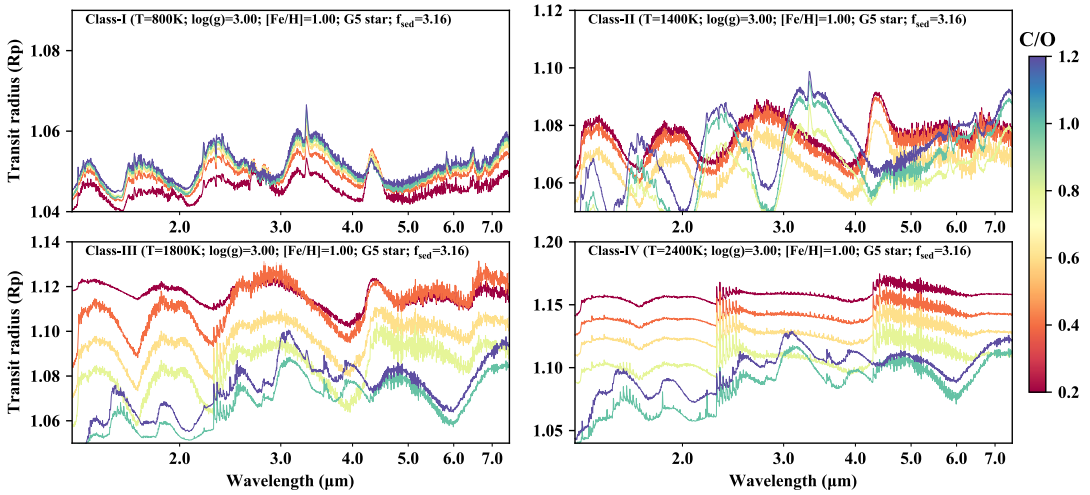

Figure 5.7: Examples of transmission spectra of self-consistent cloudy models at f_{sed} =3.16. High sedimentation factor removes the clouds from the low pressure regime; hence spectra appear similar to their cloud-free counterparts to some degree.

universal and vary strongly with atmospheric parameters. See, for example, how the temperature profiles varies in hotter cases in Figures 5.5.

Other atmospheric parameters, such as the surface gravity and metallicity, affect the atmospheric response to the variation of sedimentation factor as well. For instance, Figures 5.8 and 5.9 have a lower metalicity ([Fe/H]=-1.0) in comparison to the examples given in Figures 5.3 and 5.7 ([Fe/H]=1.0). A striking difference is the presence of methane. Even the hottest cases, T_{eff}=2400 K, show the contribution of methane in their spectra between 3.0 and 4.0 μm. Lower metalicity results in higher cooling efficiency of atmosphere at the photospheric levels. Such environment is favorable for the production of methane; consistent with the presence of methane in Figures 5.8 and 5.9 (see also Figures 5.16, 5.17 and 5.18 in the Appendix, to compare cases with other sedimentation factors).

5.3.3 Estimation of Transition C/O Ratios and the Methane Valley

Our results indicate that clouds can drastically limit the parameter-space at which methane is expected to be present in the transmission spectra of exoplanets. The transition C/O ratios at which methane features become the dominant spectral features are estimated by using the spectral decomposition technique. Figure 5.10

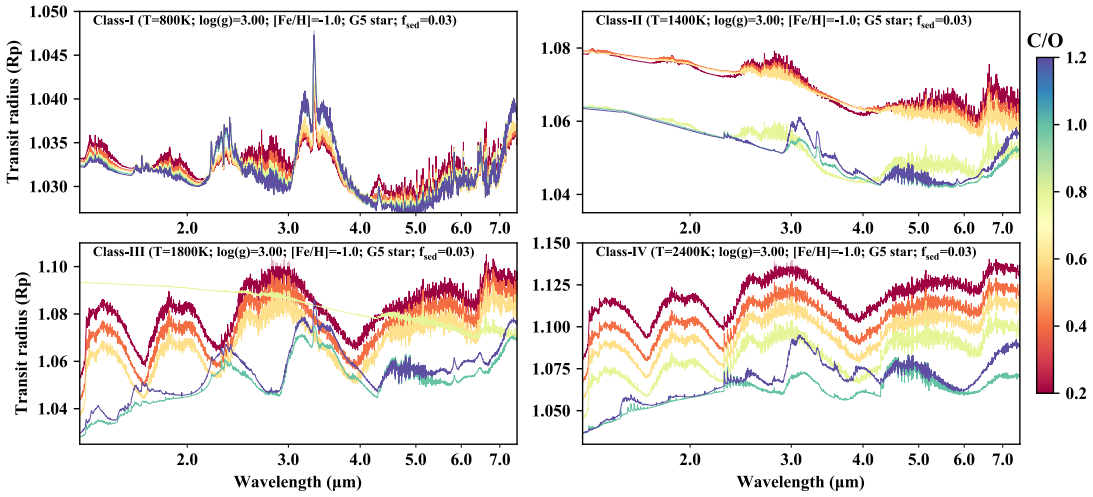

Figure 5.8: = -1.0]Examples of transmission spectra of self-consistent cloudy models at f_{sed} ∼0.03 and [Fe/H]=-1.0. Due to lower β-factor, and hence the placement of the photosphere at lower pressures, CH_4 is more efficiently produced with respect to HCN.

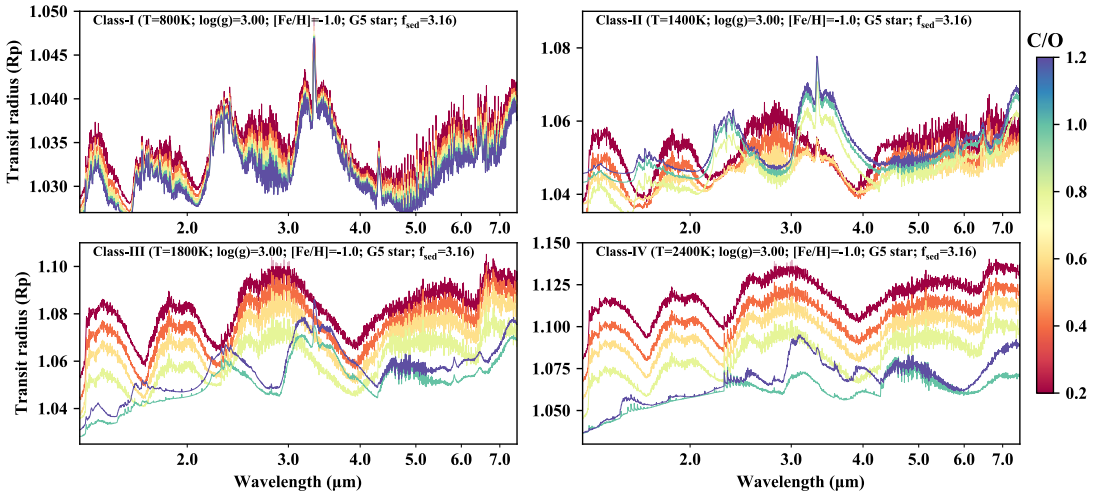

Figure 5.9: = -1.0.]Examples of transmission spectra of self-consistent cloudy models at f_{sed} ∼3.0 and [Fe/H]=-1.0.

shows the corresponding parameter-space separated for different sedimentation factors. The transition C/O ratios are color-coded by the β-factor. β-factors of Jupiter ($\sim$2.6), Saturn ($\sim$1.3), and Uranus ($\sim$-0.5) are also marked for comparison.

We start by interpreting the results of f_{sed}=3.16 models (lowest panel in Figure 5.10). Models below 1650 K (mostly Class-II, but also Class-I) show transition C/O ratios significantly less than unity. Under these conditions, the Methane Valley is a persisting domain above C/O$\sim$0.7 where methane features are expected to be present in the planetary spectra regardless of their metallicity or surface gravity. $(C/O)_{tr}$ ratio increases by temperature due to partial evaporation of condensates and the release of sequestered oxygen. At any given temperature in this regime, a lower metallicity favors cooling the photosphere (e.g. Mollière et al. 2015). This increases the amount of methane at the photospheric levels, which in turn lowers the $(C/O)_{tr}$ ratios at higher β-factors. Above 1650 K, $(C/O)_{tr}$ ratios remain around the unity for models with higher β-factors. The lower β-factors ($\lesssim$2.0), however, have terminated ends on their $(C/O)_{tr}$ ratios (circles at the right-end of $(C/O)_{tr}$ ratio lines). This represents the lack of methane in the transmission spectra of all hotter models with the same β-factor. This due to the methane depletion and obscuration by other opacity sources as discussed. While the termination of $(C/O)_{tr}$ ratios at lower β-factors limits the Methane Valley to colder planets, the results of models with f_{sed}=3.16 resemble the results of cloud-free atmospheres in general, as expected (See Section 4 in Molaverdikhani et al. 2019b).

Models with f_{sed}=1.0 start to differentiate from the cloud-free models and the Methane Valley shrinks for low β-factor models. Under these conditions, the observation of methane on planets with similar β-factor to that of Saturn (and Uranus/Neptune) would be limited to temperatures below 1400 K (and <1200 K). The Methane Valley does not change much for planets with Jovian-like β-factors as its β-factor is not very low.

At lower sedimentation factors, f_{sed} <1.0, the Methane Valley would vanish for planets with Uranus- or Neptune-like β-factors. We should recall that one of the main assumptions in our grid of cloudy models is the presence of four cloud

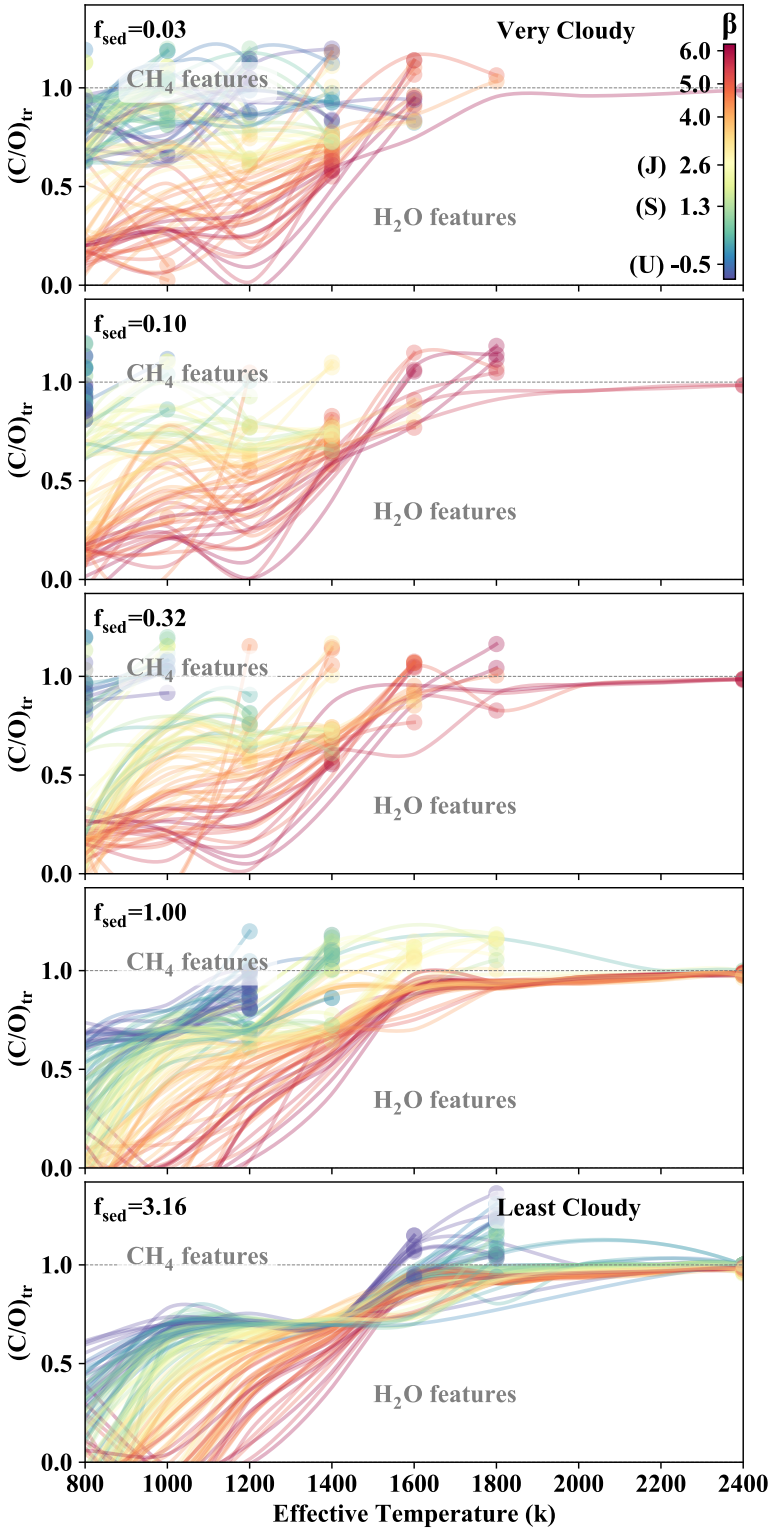

Figure 5.10: Transition carbon-to-oxygen ratios, $(C/O)_{tr}$, for different sedimentation factors, f_{sed}. The higher sedimentation factor is the deeper clouds would settle; making them less pronounced in the transmission spectra. See Section 5.3.3 for a discussion.

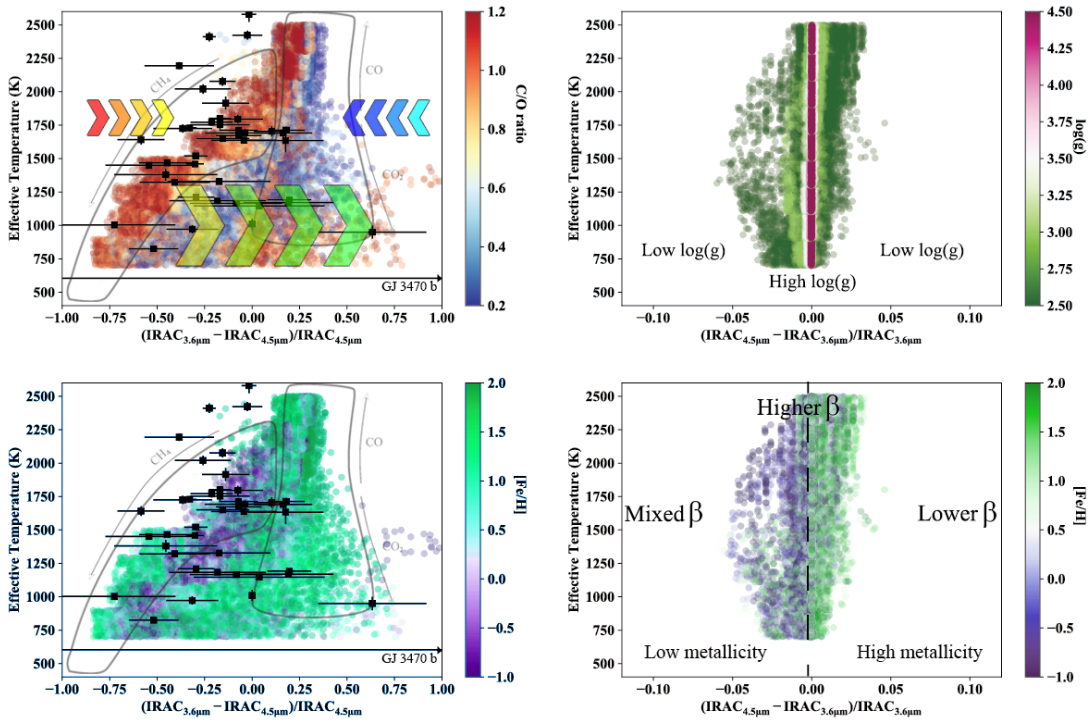

Figure 5.11: Spitzer's synthetic color-diagrams of cloudy irradiated planets in emission (left panels) and transmission (right panels). Emission diagram is compared with the observations (black squares). Cloud-free CH_4 and CO/CO_2 populations are shown by gray lines for reference. The shape of these populations in cloudy models have shifted: Hotter models are less scattered due to methane depletion and HCN production, and colder planets (with effective temperature less than ∼1200 K) are skewed toward right, where a higher contribution from IRAC channel 1 at 3.6μm influences the color. The cloudy transmission diagram remains similar to its cloud-free analogue. See Section 5.4 for details.

opacities (KCl, Na_2S, Mg_2SiO_4 and Fe), and only these four. The lack of rain-out in these simulations could result in an over-estimation of cloud opacities at colder regimes. Inclusion of rain-out may remove some of the condensates from the photosphere to make room for the reappearance of methane in the transmission spectra of these planets. Nevertheless, our systematic survey provides a framework to investigate the effect of rain-out on the observability of methane (and other species) on exoplanets in the future.

5.4 Spitzer's Color-diagrams

We construct synthetic Spitzer IRAC color-diagrams by extracting the normalized "colors" of our cloudy grid of atmospheric models. These colors are based on IRAC's photometric channels 1 and 2, which are centered at 3.6 and 4.5 μm, respectively, and for the transmission diagrams are calculated as below:

$$color = (IRAC_{3.6\mu m} - IRAC_{4.5\mu m})/IRAC_{4.5\mu m} \tag{5.4}$$

and it is the other way around for the emission diagrams:

$$color = (IRAC_{4.5\mu m} - IRAC_{3.6\mu m})/IRAC_{3.6\mu m} \tag{5.5}$$

Channel 1 (3.6 μm) is mostly suitable to study CH_4/H_2O spectral features and channel 2 (4.5 μm) is more sensitive to CO/CO_2 features. HCN contributes in both channels similarly, with slightly higher contribution in channel 1. Clouds are expected to change the color of planets significantly (e.g. Parmentier et al. 2016). They could have either gray or non-gray contributions in these channels, depending on their properties, such as their particle size distribution. Therefore, the presence of populations on the color-diagram could reveal dominant processes at the photosphere of planetary atmospheres from a statistical point of view.

Figure 5.11 shows the constructed color-diagram of the cloudy atmospheres, both in emission (left panels) and transmission (right panels). In the emission diagrams, two main populations from cloud-free simulations are shown by gray lines: CH_4 (left) and CO/CO_2 (right) dominated populations. The overall shape of the cloudy populations remain similar to that of cloud-free and disequilibrium atmospheres (Molaverdikhani et al. 2019a) with some subtle differences. Paucity of methane at hotter planets and its replacement with HCN (mostly in models with temperatures above 1500 K) pushes the originally populated regions with methane-dominated cloud-free atmospheres to the right (shown by red to yellow arrows from left to right). This is because HCN contributes more evenly in IRAC channels than CH_4; see Figure 5.2. On the other hand, obscuration of CO by HCN results in a color-shift of the hot population with low C/O toward zero from the right-side of the map

(blue arrows from right to left). In addition to the contribution of HCN instead of CO and CH_4, gray/semi-gray cloud opacities also cause less contrast between the two channels, which makes the models to populate color values around zero.

In the cloud-free models, the population of colder planets (particularly for $\lesssim$1200 K) are mostly bounded to the CH_4-population (gray area at the left with significantly negative color values). Only limited number of these planets with low C/O ratios show higher color values than that of CH_4-population. This is mainly because of the persisting presence of CH_4 in cold cloud-free models. As shown by Molaverdikhani et al. (2019a), introducing disequilibrium processes does not change this picture, but in this work we show that clouds affect this population remarkably. In the cloudy models, the population is skewed toward right, where a higher contribution from IRAC channel 1 at 3.6μm influences the color (yellow to green arrows from left to right). The reason is the presence of clouds; through methane depletion and more importantly obscuration of molecular features. In addition, high-metallicity planets favor the formation of CO_2, which in turn skews the population to bluer colors even more. Studying this population could therefore help determining the presence of clouds on exoplanets as their colors at these wavelengths would differ from their cloud-free counterparts considerably.

GJ 3470 b is a sub-Neptune with an equilibrium temperature around 600 K; solid line in the emission maps marks its location. Benneke et al. (2019) performed photometric measurements of the thermal emission of this planet with IRAC channel 1 (F_p/F_*=115$\pm$27) and 2 (F_p/F_*=3$\pm$22). They argued that the high contrast in these two channels and a very low flux in channel 2 is in contrast with solar abundance models and a low methane abundance is in favor. They also noted that photochemistry at upper layers cannot explain this contrast and possible explanations are 1) substantial interior heating, 2) photochemical destruction of CH_4 at deeper levels, or 3) a low C/O ratio as a result of the planet formation process.

Molaverdikhani et al. (2019a) showed a low C/O ratio could indeed explain the emission color of some of the low temperature cloud-free planets that are skewed to the right of the map. However, that alone would be insufficient to explain

the observations of GJ 3470 b. While our cloudy grid is not extended to 600 K, it is apparent that at temperatures lower than 800 K the contribution from the clouds would continue to skew the emission map to the right. Therefore, the role of clouds could be a more likely explanation for the photometric observation of GJ 3470 b as opposed of a lower C/O (unless its atmospheric C/O ratio is extremely low). We should, however, note that an internal heat could be still a plausible explanation which requires further investigations.

Figure 5.11 lower-left panel shows the same emission color-diagram but color-coded by metallicity instead of C/O ratio. The scattered population of colder planets ($\lesssim$1200 K) seems to be associated with higher metallicities in general. This is consistent with the depletion of CH_4 at higher metallicities as also summarized in Figure 5.10. As noted, higher metallicity is also in favor of a higher CO_2/H_2O, which enhances the shift toward more positive colors. It is worth noting that such "hidden metallicity" cannot be estimated directly from the free or cloud-free self-consistent retrievals as they do not consider any physicochemical feedback from the clouds during the forward model calculations. Consequently, an obscured spectrum by clouds could be interpreted as a low-metallicity atmosphere through these approaches.

Transmission color-map (Figure 5.11 right panels) does not change significantly from that of cloud-free and disequilibrium; i.e. planets with lower surface gravity would have a more disperse colors and high log(g) would make the spectral features less pronounced and clustered around zero. Note that the grid of cloudy models is extended from log(g) of 2.5 to 4.5; hence a less scattered models are noticeable relative to the previous models with a log(g) of 2.0 to 5.0. As a final remark on the transmission map is that, in general, planets with higher metallicities tend to populate the right side of the map and otherwise for the low metallicity atmospheres. Therefore, a combination of low metallicity and low surface gravity (i.e. low β-factor) could potentially explain some of the observations at the far-right region of the transmission map; e.g. HAT-P-18 b and WASP-107 b as reported by Baxter et al. (2018).

5.5 Conclusion

We calculated a grid of 37,800 cloudy atmospheric models and investigated the role of clouds in the classification of planets based on their transmission spectra. Our quantitative analysis confirms that our proposed classification scheme holds true in the case of cloudy atmospheres, in principal. However, alteration of this classification by the presence of clouds is noticeable. For instance, high-metallicity and low sedimentation factor could affect the the dominant chemical processes at the photospheric levels and change the transmission spectra remarkably.

For a given atmosphere, the significance of methane's spectral signature can change in two ways: by changing its abundance or by obscuration due to the presence of other opacities (whether in gas- or solid-phase). We found that in all carbon-poor cold cloudy planets (< 1200 K) the transmission spectra are void of methane. This is in contrast with our findings based on cloud-free models where methane appears in all cold planets' spectra regardless of their C/O ratio. We linked the heating of the photosphere to this depletion of methane that is caused by optically thick layers of clouds in the models. The heating is more efficient when metallicity is high. Such heating also release the sequestered oxygen from the condensates; making the transmission spectra of cold carbon-poor exoplanets water-dominated.

We predict that an observation consequence of such photospheric heating is simultaneous depletion of NH_3 and CH_4 from the photosphere. Photochemical reactions could also deplete these species. However, determination of clouds' composition could distinct between photochemically formed soot haze and silicate, alkali feldspars or any other non-soot clouds.

Oxygen release from the condensates at hotter planets increases the abundance of water. This and the fact that clouds are optically thinner at these temperatures, lead to a more efficient cooling condition. Thus the photosphere of these planets becomes cooler than their cloud-free counterparts. This cooling, however, does not results in significant methane production as the temperatures are still much higher than suitable temperatures for CH_4 formation. HCN and CO, on the other hand, form efficiently both on hotter planets and colder planets with heated photospheres.

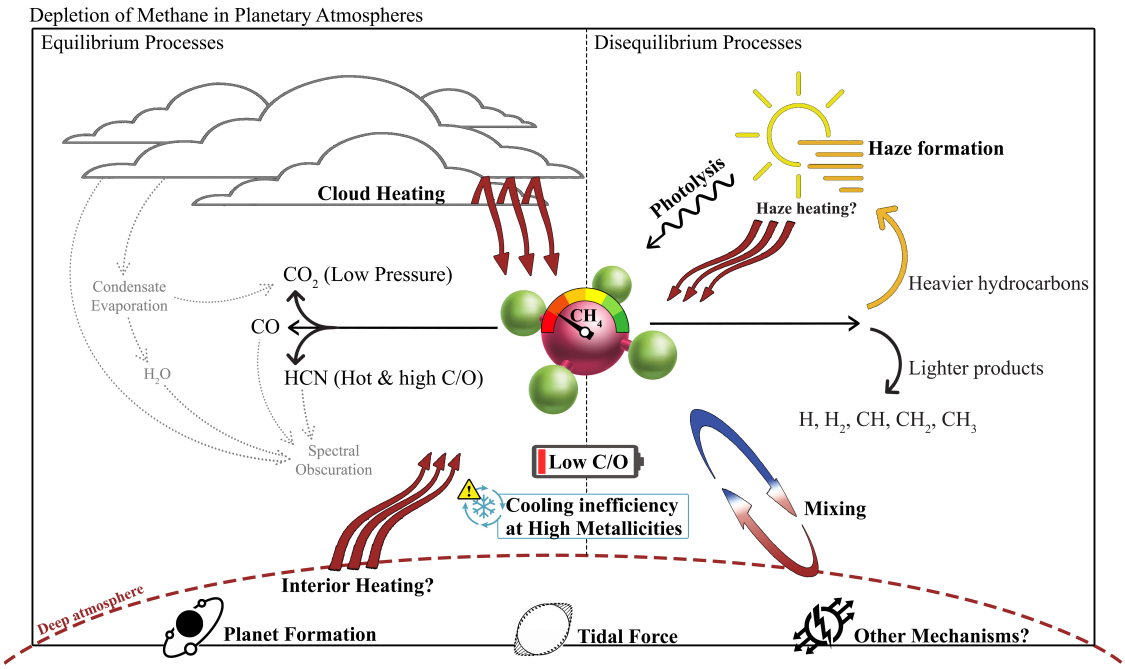

Figure 5.12: A summary of major atmospheric processes that cause methane depletion.

Hence HCN features are expected to be more prominent in the atmosphere of carbon-rich atmospheres, and in particular on high-metallicity planets. The detection of HCN is observationally favorable as its spectral features contrast H_2O in the range of 3-5μm (e.g. MacDonald & Madhusudhan 2017). A lack of CH_4 and the presence of HCN may be another indication of cloud formation in the atmosphere of exoplanets.

In general, the detection of methane on exoplanets with β-factors similar to Jupiter's and Saturn's is more likely than planets with β-factors similar to Uranus's and Neptune's. In addition, higher sedimentation factors remove the clouds from the photospheres more efficiently. Thus atmospheric properties resemble cloud-free atmospheres. In contrast, lower f_{sed} forms extended clouds that heat the photosphere more, deplete methane and mute its remaining signatures from the transmission spectra. Under these suppressed conditions, observation of methane at NIR bands is a challenging task. We therefore propose observing its fundamental band at 3.3 μm as has been also proposed by others (e.g. Noll et al. 2000; Kawashima et al. 2019). Nevertheless, low metallicity planets, e.g. HAT-P-11b (Chachan et al. 2019), are in favour of methane detection for the future observations. A summary of major atmospheric processes that cause methane depletion are illustrated in Figure 5.12.

We also investigated the shape of populations in the emission and transmission color-diagrams due to the cloud formation. At higher temperatures the populations tend to cluster around lower contrast values relative to the cloud-free and disequilibrium emission maps. We found that this is mainly due to the conversion of CH_4 and CO into HCN. Since HCN has more even contribution in the IRAC channels, the scattered population of hot planets becomes more clustered. At low temperatures, however, the colors are more dispersed and skewed toward right, where the depletion of methane and higher CO_2 contributions in high-metallicity planets makes the normalized color to become more positive (bluer in a non-normalized sense). This scattered population of cold planets can be used to characterize the formation of clouds on exoplanets through multi-color photometry using facilities that are more accessible than spectrographs.

Due to the lack of a rainout mechanism in the current version of petitCODE, an overestimation of opacity contribution from the cloud might occur, especially at lower temperatures. Thus the results presented in this chapter must be considered as an upper limit of how much clouds can influence the spectra of planetary atmospheres in a 1D setup. Planets are 3D objects and the geometry of planets could play a role in the atmospheric properties of planets as we discuss in the next chapter.

5.6 Appendix) Additional Figures

Figures 5.13, 5.14, 5.15, 5.16, 5.17 and 5.18 are shown as the examples of how sedimentation factor affects the transmission spectra of exoplanets at different metallicities and for different classes of planets.

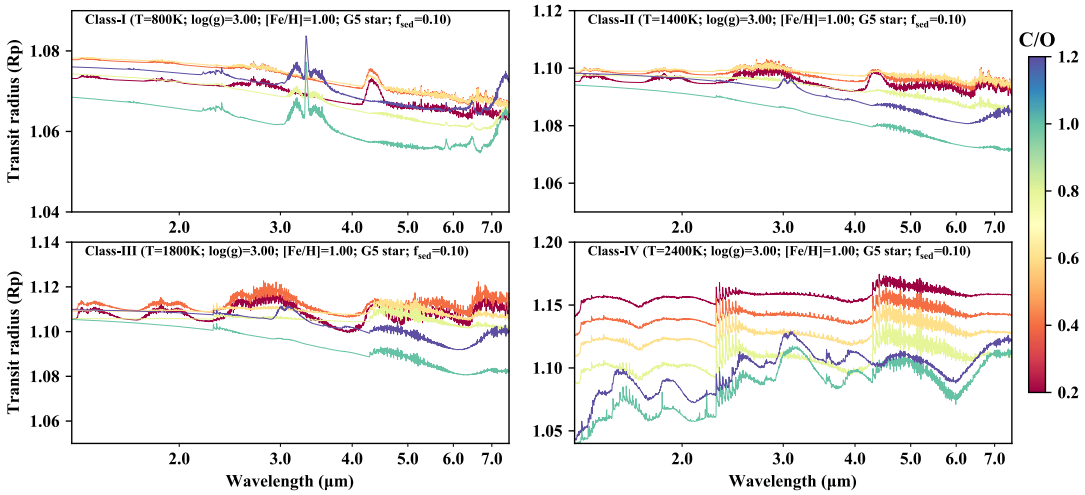

Figure 5.13: Examples of transmission spectra of self-consistent cloudy models at f_{sed} ∼0.1.

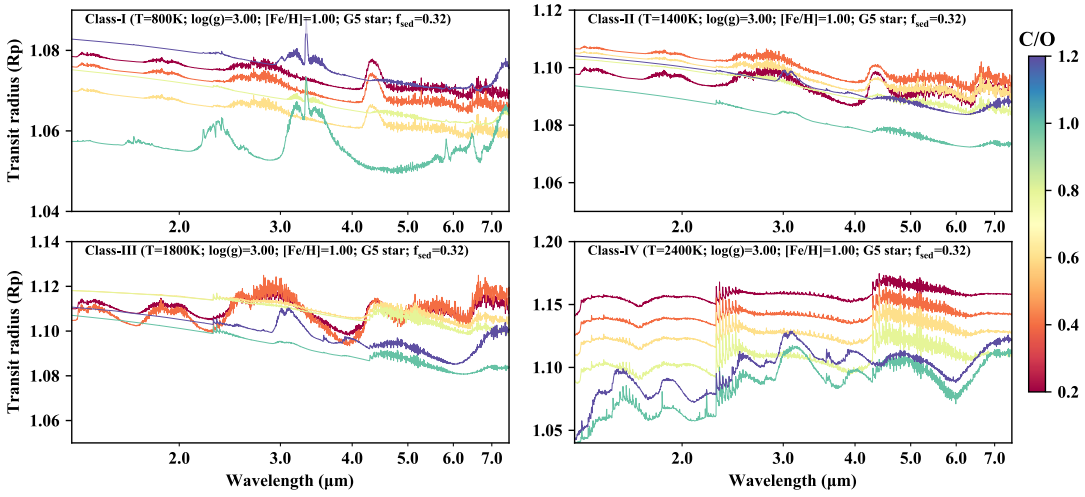

Figure 5.14: Examples of transmission spectra of self-consistent cloudy models at f_{sed} ∼0.3.

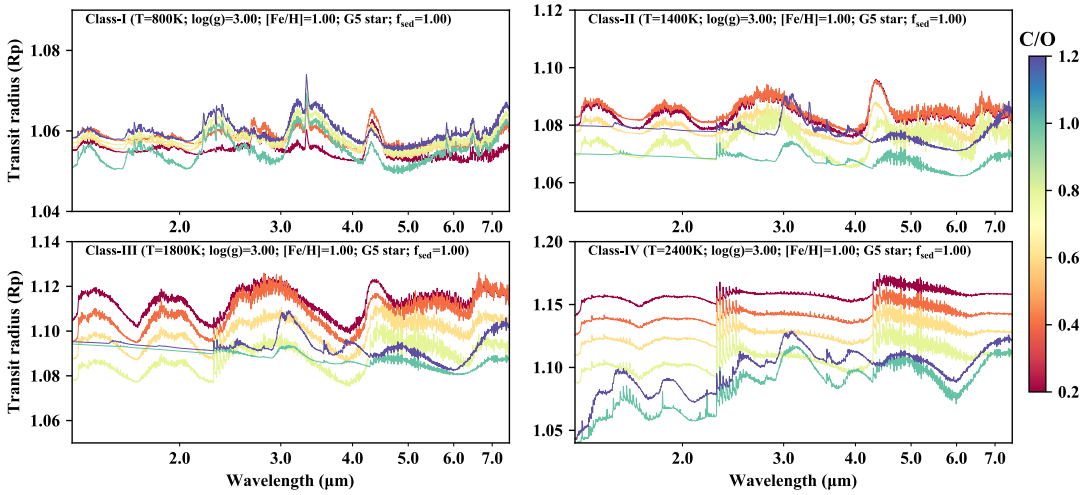

Figure 5.15: Examples of transmission spectra of self-consistent cloudy models at f_{sed} ∼1.0.

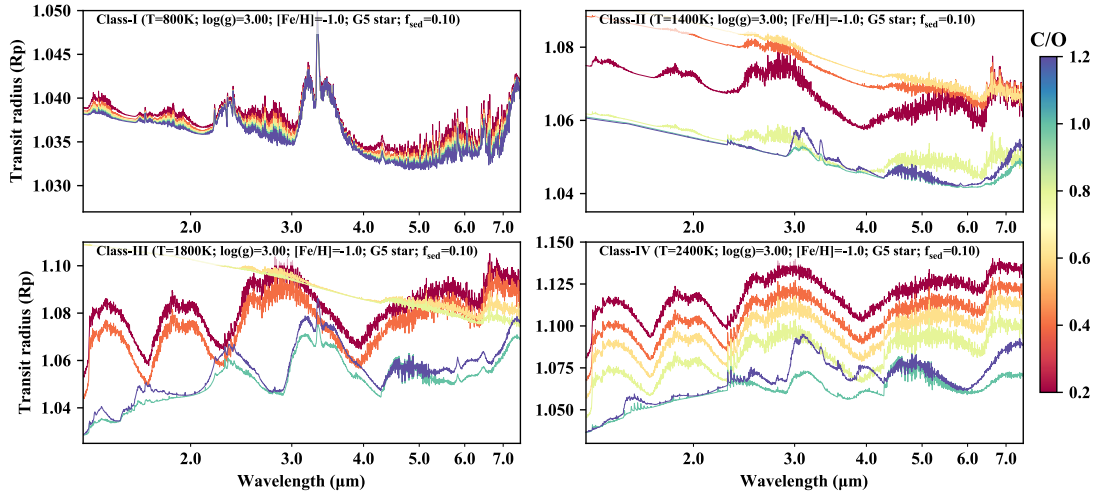

Figure 5.16: = -1.0]Examples of transmission spectra of self-consistent cloudy models at f_{sed} ∼0.1 and [Fe/H]=-1.0.

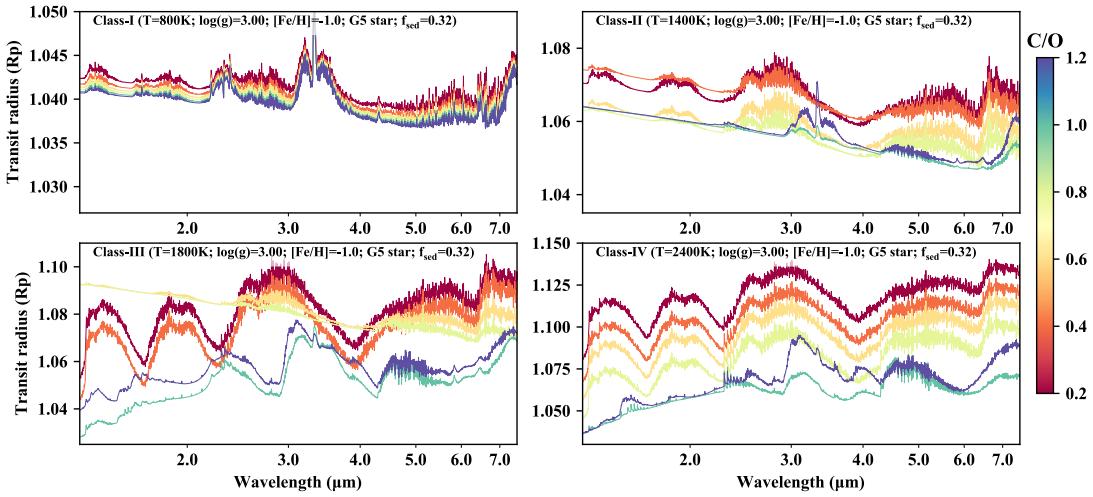

Figure 5.17: =
-1.0]Examples of transmission spectra of self-consistent cloudy models at f_{sed} ∼0.3 and [Fe/H]=-1.0.

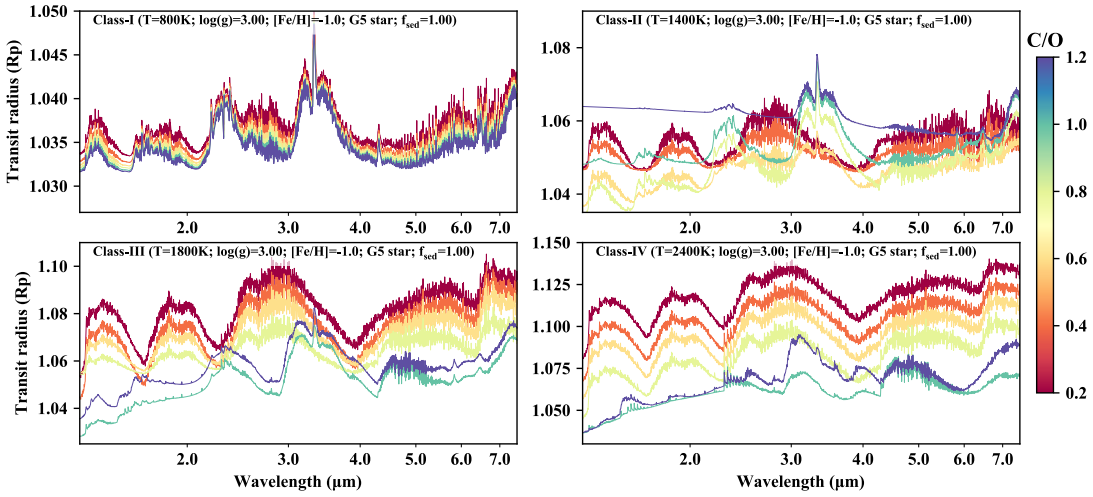

Figure 5.18: =
-1.0]Examples of transmission spectra of self-consistent cloudy models at f_{sed} ∼1.0 and [Fe/H]=-1.0.

Where there is matter, there is geometry.

— Johannes Kepler.

6

The Effect of 3D Geometry

Contents

[1]Ultra-hot Jupiters are highly irradiated, tidally locked planets with extreme

[1]This chapter is submitted for publication as a refereed article, titled "Understanding the atmospheric properties and chemical composition of the ultra-hot Jupiter HAT-P-7b: II. Mapping the effects of kinetic gas composition", for which I am the lead author and has adapted for this

day/night temperature differences (e.g. Delrez et al. 2018; Parmentier et al. 2018; Bell & Cowan 2018; Kreidberg et al. 2018a; Komacek & Tan 2018; Lothringer et al. 2018; Lothringer & Barman 2019; Molaverdikhani et al. 2019b; Tan & Komacek 2019; Arcangeli et al. 2019; Mansfield et al. 2019; Wong et al. 2019). A day/night temperature difference of $\geq$ 2000 K on, for example, WASP-18b and HAT-P-7b, results in different chemical regimes. The hot dayside atmosphere is predominately composed of H/He and largely cloud-free, while the cold nightside is composed of a H_2/He atmosphere where cloud particles can form in abundance (Helling et al. 2019b).

The extreme insolation received by ultra-hot jupiters, resulting in large atmospheric scale heights, has rendered them prime targets for spectroscopic studies. The most extreme of these planets is KELT-9b; the hottest known exoplanet with an equilibrium temperature of $\sim$ 4000 K. High-resolution HARPS-North observations of KELT-9b indicate an abundance of ions, such as Fe^+ and Ti^+, in its upper atmosphere (Hoeijmakers et al. 2018). The non-detection of atomic Ti, and less significant detection of Fe, point toward a highly ionised environment. This proliferation of ions is consistent with expectations from thermochemical equilibrium at these temperatures (Kitzmann et al. 2018). The somewhat cooler world MASCARA-2b/KELT-20b ($T_{eq} \sim 2300$ K) also shows signs of ions, namely Ca^+, and Fe^+, in addition to Na in its transmission spectrum (Casasayas-Barris et al. 2019). Successes such as these, across a wide temperature regime, demonstrate the observational accessibility of these atmospheric systems.

The progress in detecting spectral features in spectra of ultra-hot Jupiters motivates detailed theoretical modelling of their atmospheres. 1D simulations, e.g., suggest these atmospheres to be in thermochemical equilibrium at the pressures probed by low resolution spectroscopy, i.e. larger than 1 mbar (Kitzmann et al. 2018). However, hydrodynamic transport processes (advection/winds), turbulent eddies and interactions with a radiation field or charged particles (cosmic rays)

chapter.

can affect the local gas phase composition if they favour (or enable) a certain reaction path over its backward/forward reaction.

It has been shown that turbulent and molecular diffusion, photochemical processes, as well as interaction with free electrons may alter the chemical composition of planetary atmospheres from thermochemical equilibrium to a disequilibrium chemistry state (see e.g. Line et al. 2010; Moses et al. 2011; Venot 2012; Miguel & Kaltenegger 2014; Moses 2014; Rimmer & Helling 2016; Tsai et al. 2017; Helling 2019b). While previous studies have been usually conducted on colder planets, Kitzmann et al. (2018) reported that the chemical state of KELT-9b's atmosphere also deviates from thermochemical equilibrium at pressures less than 1 mbar in a 1D setup. Moreover, according to their simulations, disequilibrium processes drive some of the atomic and molecular abundances away from their chemical equilibrium states at pressures even larger than 1 mbar. For instance, assuming an inversion in the atmosphere of KELT-9b, they report a pressure of ∼0.03 bar at which or less than that H_2, H_2O, and CO_2 abundances deviate from their thermochemical equilibrium values. CO and HCN abundances also deviate from their thermochemical equilibrium values at around a similar pressure, 0.02 bar. Transmission spectroscopy is sensitive to these pressures; suggesting that disequilibrium processes might have observable fingerprints on the chemical composition of highly irradiated planets as well.

The 3D nature of planets and their resulted colder nightside could also enhance the effect of disequilibrium processes by extending the quenching level of major opacity species to larger pressures at the terminators and nightside. Consequently, 3D studies are needed to take into account local processes (such as disequilibrium chemistry) and connect the probed regions of the atmosphere to its global properties. Here, we begin to assess the nature of disequilibrium processes in ultra-hot Jupiters using full 3D modelling of the governing chemical and physical processes. The chosen target of our investigation is the ultra-hot Jupiter HAT-P-7b ($T_{eq} \sim 2100$ K). We began this exercise by studying global cloud formation, and its impact on local elemental abundances, in Helling et al. 2019b. We continue our investigation by

addressing the role of kinetic processes in altering the 3D gas-phase composition from thermochemical equilibrium expectations.

We note, however, that models linking kinetic gas-phase chemistry to dynamic atmosphere simulations are quite time-consuming. Usually, therefore, relaxation schemes are applied to omit the long computational times required to assure independence of the solution from the initial conditions, (see e.g. Cooper & Showman 2006; Drummond et al. 2018c,b; Mendonça et al. 2018). In such schemes, it is assumed that if the timescale for hydrodynamic transport processes becomes longer than the chemical timescale, then the local atmosphere will achieve chemical equilibrium (wherein both forward and backward reactions occur with a similar rate). This mostly occurs at hot and high-pressure atmospheric levels or in hydrodynamically inactive regions. The atmosphere will be driven out of thermochemical equilibrium if the hydrodynamic timescales (also called "mixing timescales") become shorter than the chemical timescales. This occurs, for example, if a cell of material is transported more rapidly than its thermodynamic state can adjust to its new surrounding (e.g. Prinn & Barshay 1977; Griffith & Yelle 1999; Saumon et al. 2006; Cooper & Showman 2006; Drummond et al. 2018b). Hence, the composition of the cell may remain that of a hotter gas as long as there is no decay reaction fast enough (e.g. N_2/NH_3, CO/CH_4). This had been demonstrated for brown dwarfs, e.g., by Saumon et al. (2000). The effect of such a dynamically-induced gas disequilibrium on phase curves has been demonstrated, e.g., in Steinrueck et al. (2019). For instance, in wavelength bands with significant methane absorption, the amplitude of phase curves can be dramatically reduced. This effect is expected to be more significant for planets on which the nightside becomes cold enough that, under equilibrium chemistry, methane becomes the dominant nightside carbon-bearing species while CO prevails on the dayside (Steinrueck et al. 2019). We, however, note that CH_4 maybe destroyed by lightning locally Bailey et al. (2014).

Transport induced chemical disequilibrium mostly occurs for gaseous species at higher-altitude atmospheric conditions. Here, it may lead to a chemical stratification as each species reacts according to its own timescale, and each species diffuses

on its own time scale, in principle. The pressure level at which this transition between thermodynamic equilibrium and kinetic disequilibrium takes place is called the *quenching point* or quenching level (Smith 1998). The determination of the quenching level varies between models which, for example, apply a constant diffusion constant for all (gas and cloud) species (Zhang et al. 2018; Zhang & Showman 2018b). We further note that quenching levels can only be studied for molecules with known kinetic forward and backward rates, and with known diffusion constants.

The relative gas number densities, i.e. mixing ratios, of the affected species at pressures lower than the pressure of the quench point (i.e. higher altitudes) are believed to remain equal to the equilibrium abundances at the quench point, or so called quenched-abundances (see e.g. Prinn & Barshay 1977; Moses et al. 2011; Venot et al. 2018). This uniform ("quenched") mixing ratio profile has been frequently used in the atmospheric retrievals as a simplified approach to increase the computational speed (see e.g. Madhusudhan & Seager 2011; Tsiaras et al. 2018; Pinhas et al. 2019). We propose a fast zeroth-order method (based on Venot et al. (2018) results) to estimate the quench levels and compare it with the gas-phase kinetic estimations.

In addition, under different circumstances and for different species, the abundance above the quenched level can deviate from a constant value in a chemical kinetic context (see e.g. Molaverdikhani et al. 2019a). If significant, this deviation might pose a problem in the retrieved abundances as shown by, e.g., Changeat et al. (2019). We discuss the validity of constant mixing ratio approximation for the case of HAT-P-7b, in Section 6.2.2.

We, therefore, aim to quantitatively assess the importance of kinetic gas-phase chemical processes that are driven by hydrodynamic motion or by photochemistry, and map them in the case of HAT-P-7b; an ultra-hot Jupiter. We describe our hierarchical modelling approach in Section 6.1 and present the results on the quenching levels for the HAT-P-7b's atmosphere in Section 6.2 where we add a critical evaluation of the "quenching level" concept. In Section 6.3 we highlight our findings on how much the abundances of H_2O, CO and CH_4 change due to

diffusion (both turbulent eddies and molecular) and photochemistry. We summarize and conclude our findings in Sections 6.4 and 6.5.

6.1 Approach

We use our modelling tools as virtual laboratories, expanding our hierarchical approach of modelling environments from Helling et al. (2019b). In that paper, we utilised 97 1D profiles extracted from the 3D GCM calculated for the cloud-free HAT-P-7b (Mansfield et al. 2018). We then applied our kinetic cloud formation model to solve for the gas phase composition under chemical equilibrium, while consistently accounting for element abundance changes due to cloud formation. The next modelling step is to use the 97 1D (T_{gas}(z), p_{gas}(z), $w(x, y, z)$)-profiles for HAT-P-7b (Fig. 1 in Helling et al. (2019b): T_{gas}(z) is the local gas temperature [K], p_{gas}(z) is the local gas pressure [bar], w(x,y,z) is the local vertical velocity component [cm s^{-1}]) to derive the diffusion coefficient K_{zz}, which assumes that all gas species have the same eddy diffusion coefficient.

In this section, we outline the two approaches we adopt to study the effect of gas-phase kinetic processes on the atmosphere of HAT-P-7b. We follow a hierarchical approach, wherein we begin in Section 6.1.1 with a simple quenching level calculation (i.e. 'zeroth-order'), before increasing the complexity in Section 6.1.2 by considering full gas-phase chemical kinetic modelling.

6.1.1 Quenching levels: a zeroth-order approximation

Modelling kinetic gas chemistry is computationally expensive. Hence, it can be instructive to explore fast, but reasonably accurate, approaches to investigate chemical quenching in 3D atmospheric models. As a zeroth-order approximation, we adapt Figure 1 of Venot et al. (2018) to find the quenching levels for each 1D trajectory in the 3D model of HAT-P-7b. In brief, Venot et al. (2018) use a series of different thermal profiles (following analytical models from Parmentier & Guillot (2014)) to determine the quenching level as a function of temperature and eddy diffusion coefficient (K_{zz}) by examining the criteria of at least one of their main

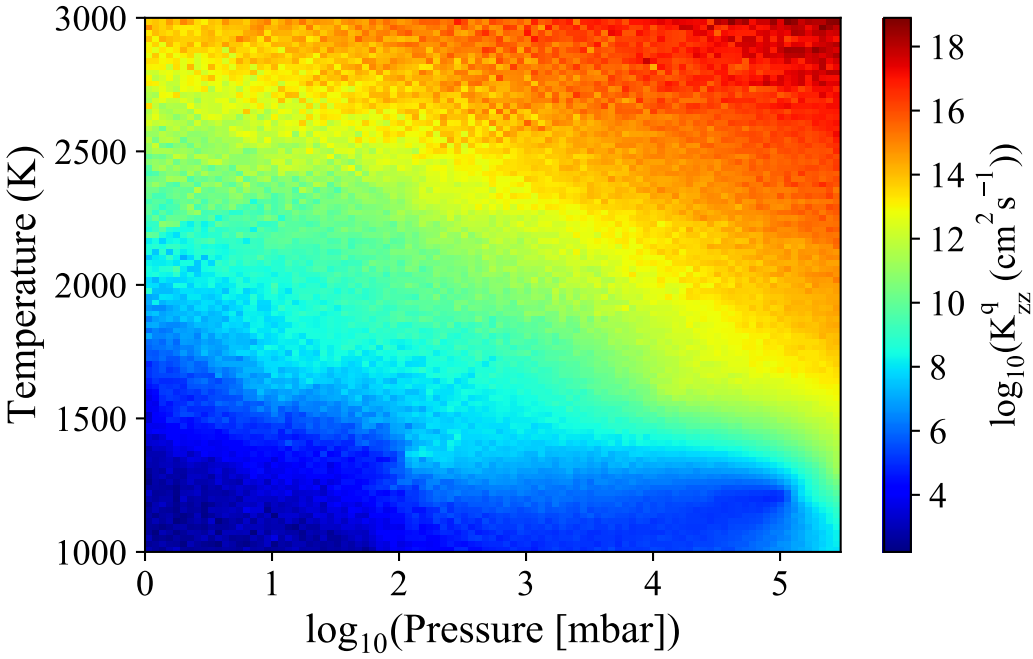

Figure 6.1: Estimation of eddy coefficient needed for quenching to happen as a function of pressure and temperature, K^q_{zz}(p,T). Venot et al. (2018) report the quenching pressures for several pairs of temperature-vertical mixing strength (in their Figure 1), and we interpolate their results to obtain a continuous K^q_{zz} function at any chosen pressure and temperature. See Sec. 6.1.1 for more details.

species (i.e. H_2, H, H_2O, CH_4, CO, CO_2, N_2, NH_3, HCN, CH_3, and OH) deviating from its thermochemical equilibrium abundance.

Given the monotonic nature of these functions (the quenching pressure as a function of temperature and K_{zz}), their inverse functions can be easily constructed, i.e. eddy diffusion coefficients at the quenching points (K^q_{zz}) as a function of pressure and temperature. We linearly interpolate/extrapolate these K^q_{zz} values (using radial basis functions) in the range of 1000 K$<T_{gas}<$3000 K and 1 mbar$<P_{gas}<10^6$ mbar; see Fig. 6.1. Comparing K^q_{zz} with the derived eddy diffusion coefficient at any given pressure and temperature from the GCM's 1D trajectories provides an estimate for whether that atmospheric level is quenched or not (i.e. if $K_{zz}(P,T) > K^q_{zz}(P,T)$, it is quenched).

In 1D kinetic models, the eddy diffusion coefficient (K_{zz}) is usually estimated by multiplying the vertical wind speed (w) by the relevant vertical length scale,

e.g. scale height (H) (see e.g. Lewis et al. 2010; Moses et al. 2011). However, Parmentier et al. (2013) derived K_{zz} values from passive tracers in their GCM and found that these values were about two orders of magnitude lower than the traditional approach. Therefore, we approximate the mixing strength as follows:

$$K_{zz} = |w| \cdot H \times 10^{-2}. \tag{6.1}$$

where H, the atmospheric scale height, is given by H=RT/μg at any pressure level (R is the universal gas constant, $T_{\rm gas}$ is the gas temperature, μ is the mean molar mass – defined as the mass of the atmosphere at each level divided by the amount of substance in that level, and g is the gravitational acceleration). The average eddy diffusion coefficient at pressures larger than 1 bar shows a somewhat linear relation with pressure as $\log(K_{zz}) = 5.5 - 1.7\log(P_{gas})$; Fig. 6.2. Above this region, the eddy diffusion coefficient is less variable on average; revolving around values of 2×10^{7}cm^{2}s^{-2} and 2×10^{6}cm^{2}s^{-2} on the dayside and nightside, respectively. The stronger K_{zz} on the dayside, along with the cooler atmosphere on the nightside, hint towards the existence of a region between the day and night with a minimum quenching pressure. This is discussed in the results section (Sec. 6.2.1). Note that by taking this approach, small scale and local variations of K_{zz} might be introduced in comparison to the case of a smoothed parametrized K_{zz} approach. Therefore, small scale variations of abundances are possibly not very realistic and the results should be taken for their order-of-magnitude significance.

Although this approach is quite simple, it provides a reasonable overall picture about where we should expect chemical quenching to occur. Nevertheless, a more sophisticated approach should be considered in order to quantitatively assess the importance of disequilibrium processes on Ultra-hot Jupiters. For this, we turn now to chemical kinetic modelling.

6.1.2 Chemical kinetic modelling

As discussed in Section 3, chemical network is essential to quantitatively trace the chemical abundances resulting from interactions between major and minor species

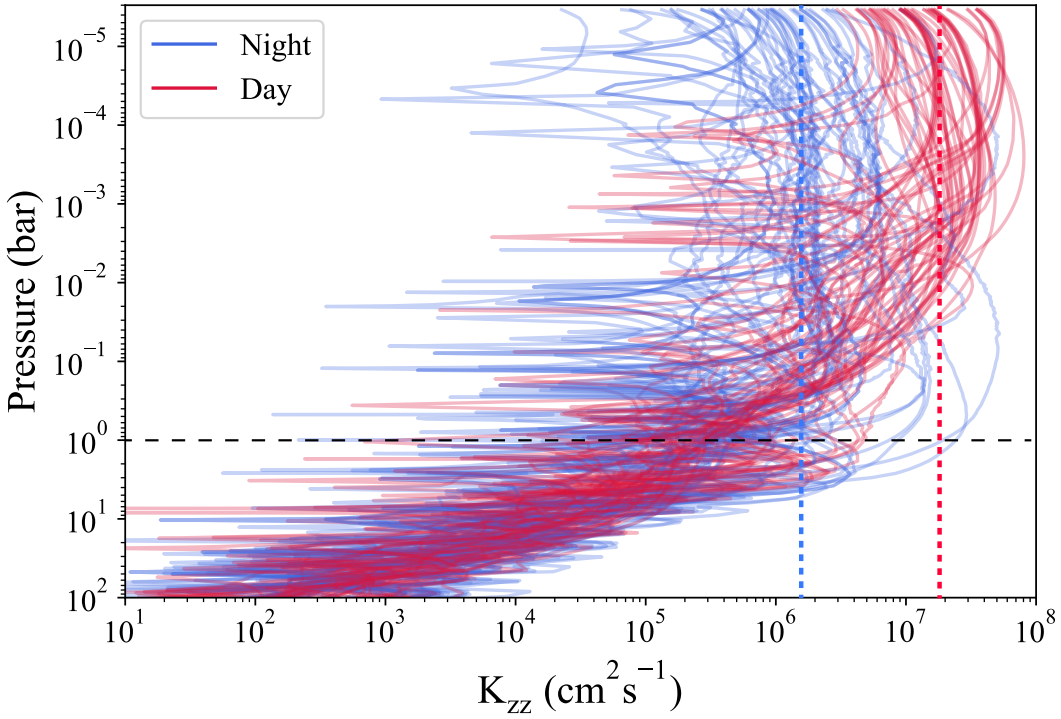

Figure 6.2: Calculated eddy diffusion coefficient (K_{zz}) profiles using Equation 6.1. The average eddy diffusion coefficient at pressure larger than 1 bar roughly follows a simple relation as log(K_{zz})=5.5-1.7log(P). Above this pressure and on the dayside, K_{zz} has an average values around $2\times10^{7} cm^2 s^{-2}$ (vertical red dashed line), while it is weaker by about one order of magnitude on the nightside (vertical blue dashed line).

at different pressures and temperatures. For this, we use `ChemKM`, a photochemical kinetic model (Molaverdikhani et al. 2019a) to perform a detailed study of gas-phase chemical kinetics and quenching levels on HAT-P-7b for CNOH-binding species. `ChemKM` is a modular package that calculates the vertical distribution and temporal evolution of atmospheric constituents in 1D. As discussed in Chapter 3, it employs the ODEPACK library (Hindmarsh 1983) and solves the coupled mass-continuity equations as a function of pressure for each species:

$$\frac{\partial n_i}{\partial t} + \frac{\partial \Phi_i}{\partial z} = P_i - n_i L_i, \tag{6.2}$$

where n_i is the number density (cm^{-3}), Φ_i is the vertical flux (cm^{-2} s^{-1}), P_i is the production rate (cm^{-3} s^{-1}), t is time, z is the vertical distance from the center of planet, and L_i is the chemical loss rate (s^{-1}) of species i.

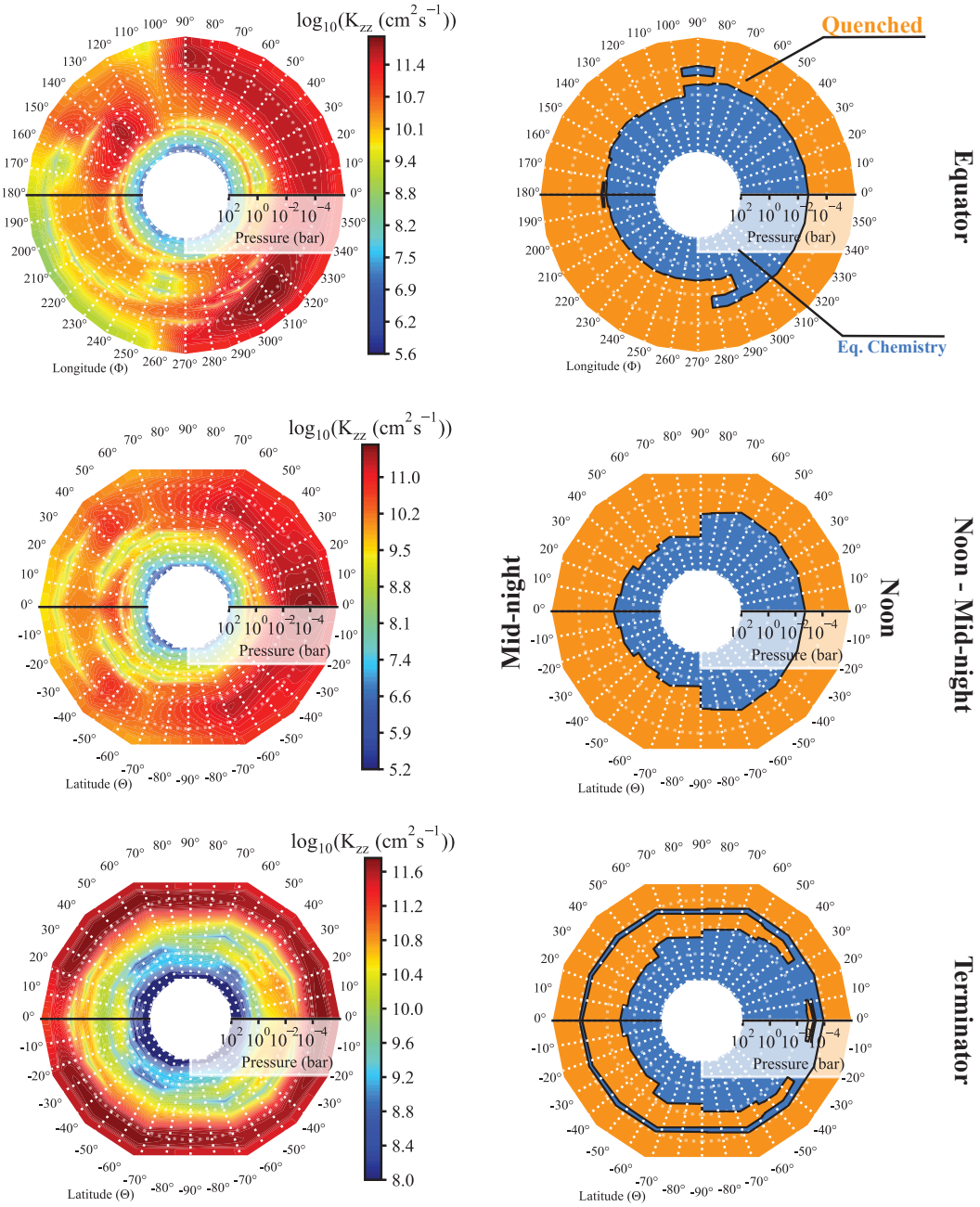

Figure 6.3: Left) Calculated K_{zz} using Equation 6.1, and **Right)** Calculated quenching levels by following a zeroth order approach. In the blue regions the atmosphere is in thermochemical equilibrium while orange highlights the regions that are expected to be affected by disequilibrium processes and at least one major species deviates from its thermochemical equilibrium abundance.

Photochemical processes by UV and X-rays, photodissociation by galactic cosmic rays, flux attenuation due to Rayleigh scattering, condensation, ablation, outgassing, molecular diffusion and eddy mixing could all driven the chemical composition of

atmosphere out of thermochemical equilibrium. However, here we only explore the effects of diffusion/mixing and photochemical processes by UV and X-ray as the other processes are poorly known for the exoplanets.

In order to solve Eq. 6.2, we adopt a reduced version of the Venot (2012) network that accounts for most of the dominant species expected at HAT-P-7b's atmospheric conditions. This contains 38 species (namely, H_2, He, H, CO, H_2O, CH_4, N_2, NH_3, CO_2, HCN, C_2H_2, O_2, O(3P), O(1D), C, N(4S), N(2D), OH, CH_3, $^3CH_2$, $^1CH_2$, CH, NH_2, NH, H_2CO, HCO, CN, C_2H, NO, HNO, NCO, HNCO, HOCN, HCNO, C_2H_3, C_2H_4, C_2H_5, and C_2H_6), corresponding to 611 kinetic reactions. The UV absorption cross-sections and branching yields were adapted from an updated version of the Hébrard et al. (2012) network, which includes 29 photo-reactions for the species in our reduced network. The photo-species are H_2O, CO_2, H_2CO, OH, CO, H_2, CH_4, CH_3, C_2H_2, C_2H_3, C_2H_4, C_2H_6, N_2, HCN, NH_3, NO, HCO.

The irradiation field was determined by interpolating between Phoenix stellar atmosphere models (Hauschildt et al. 1999; Husser et al. 2013), assuming the following stellar parameters: $T_* = 6441$ K, $\log(g) = 4.02$ cm s^{-2}, and [Fe/H]=0.15 (Torres et al. 2012). While some UV observations by HST/STIS/COS are available for similar stars, such as HD 27808 (e.g. Bowyer et al. 1994), we use the Phoenix models to take a coherent approach. This means no data stitching is required in order to construct the host star's flux between 1 nm to 300 nm (the wavelengths at which the irradiation becomes relevant to the photolysis of atmospheric constituents). In addition, the dayside of the planet is very hot and, hence, likely to be insensitive to the photochemistry (see Sections 6.2.3 for details). Therefore, small differences in the UV portion of the constructed stellar spectra using different methods (i.e. data stitching or Phoenix model) is not expected to cause a noticeable change in the results, and the Phoenix model provides an adequately accurate estimation of HAT-P-7's spectrum.

Following our hierarchical modelling approach, we use the gas-phase chemical equilibrium results from Helling et al. (2019b) as the input values. We then compute the thermochemical abundances of species considered in our kinetic network to

calculate the initial abundances for the kinetic gas-phase modelling in this chapter, as discussed in Sect. 6.1.2. The results from Helling et al. (2019b) include the effect of cloud formation on the element abundances through depletion and/or enrichment (see Sect 2.1. in Helling et al. (2019b)). We use the same 1D atmospheric temperature-pressure profiles (Figs. 1 and 3 in Helling et al. (2019b)). We present and discuss the results of our kinetic gas-chemical models in Section 6.2.2.

In order to solve the continuity equation, Eq. 6.2, we follow Hu et al. (2012) (Eq. 2) and express the vertical transport flux of species i (Φ_i) as follow:

$$\Phi_i = -K_{zz} n \frac{\partial f_i}{\partial z} - D_i n \left(\frac{\partial f_i}{\partial z} + \frac{f_i}{H_i} - \frac{f_i}{H_0} + \frac{\alpha_i}{T} \frac{dT}{dz} f_i \right) \tag{6.3}$$

where K_{zz} is approximated using Eq. 6.1, n is the total number density, H_0 is the mean scale height of the atmosphere, H is the molecular scale height, $T_{\rm gas}$ is the gas temperature, f_i is mixing ratio, D_i is molecular diffusion coefficient, and α_i is the thermal diffusion factor of species i. A detail description of how we approximate the molecular diffusion coefficients is provided in Section 3.1.2.

As pointed out, the gas phase number density profiles of the 38 CHNO-bearing species, as result the kinetic cloud formation presented in Helling et al. (2019b), are used as input values for our chemical kinetic gas-phase calculations. These input molecular abundances already account for elemental depletion or enrichment by cloud formation processes. However, we note here that the comparison with our gas-chemistry results from Helling et al. (2019b) bears a conceptional problem, namely the definition of an interface.

Defining the interface: A challenge for hierarchical models may be to define an interface that is unambiguous and practical at the same time. The comparison between results from an equilibrium gas-phase code with a kinetic rate network gas-phase code is challenged by the kinetic model only treating a limited number of gaseous species. In this paper, the interface is therefore defined by the number densities, $n_{\rm x}/n_{\rm tot}$ [cm^{-3}], of those species that can be considered by the kinetic code (H_2, He, H, CO, H_2O, CH_4, N_2, NH_3, CO_2, HCN, C_2H_2, O_2, O(3P), O(1D), C,

N(4S), N(2D), OH, CH_3, $^3CH_2$, $^1CH_2$, CH, NH_2, NH, H_2CO, HCO, CN, C_2H, NO, HNO, NCO, HNCO, HOCN, HCNO, C_2H_3, C_2H_4, C_2H_5, and C_2H_6). Hence, the ***input*** (interface) values for all quenching approaches (Sect. 6.1.1-6.1.2) considered here are set by the results from our thermochemical equilibrium calculation in Helling et al. (2019b). The ***initial*** abundances in our kinetic model are then computed by calculating the new thermochemical equilibrium abundances of these 38 species, given these input values. Any significant deviation from these initial abundances is considered as an indication of the fingerprints of disequilibrium processes, as discussed in Sect. 6.2.2.

This choice of interface, however, results in lower element abundances of C, N and O if they are derived based on the above listed 38 species only (rather than from the full list of species used in Helling et al. (2019b)). If the element abundances were kept consistent between the two modelling steps, we would have inconsistencies in the initial molecular number densities compared to the values derived in Helling et al. (2019b).

We also note that our 1D approach neglects horizontal transport, which could alter the exact location of the quenching and abundances (e.g., Agúndez et al. 2014a; Drummond et al. 2018c; Mendonça et al. 2018). This limitation is discussed in Section 6.4.

6.2 Quenching levels

6.2.1 Results of zeroth-order approximation

The quenching levels by the zeroth-order approximation are determined by following the criteria of at least one of Venot et al. (2018) model's main species (i.e. H_2, H, H_2O, CH_4, CO, CO_2, N_2, NH_3, HCN, CH_3, and OH) deviating away from its thermochemical equilibrium abundance. Therefore, this approximation does not associate the quenching levels to any specific species, unlike the kinetic approach.

Figure 6.3 top panels reproduce the transection maps of K_{zz} and the quenched regions at the equator. Despite weaker vertical mixing at the night-side, quenching levels are deeper ($p_q^{\rm night}$ ≈10-100 mbar) relative to the dayside ($p_q^{\rm day}$ ≈1-10 mbar) due

to the much hotter atmospheric environment by about 2000 K on the dayside. This is more evident in the noon-midnight maps, i.e. Fig. 6.3 middle-panels. No significant latitudinal quench point variation is noticeable at the noon-midnight plane; resulting in a sudden change in the quenching levels from the dayside (∼1 mbar) to the night-side(∼100 mbar) over the pole. The transition, however, is more gradual between the evening and morning terminators, see Fig. 6.3 bottom-panels.

The value of the quenching pressure depends on the mixing efficiency (K_{zz}) and temperature. Komacek et al. (2019) found that in general K_{zz} increases with temperature in the mbar regime. As both of these quantities decrease at higher zenith angles (i.e. toward the nightside), there should be a region where the quenching pressure is at its minimum values (i.e. quenching point occurs at its maximum altitude) for the affected species by the diffusion. This is evident in Figure 6.4 where the quenching levels have a maximum altitude at the evening (hotter) terminator according to our zeroth-order approximation. Hence, thermochemical equilibrium assumption is the most relevant at the evening terminator. This may partially support the applicability of this assumption for the transmission spectroscopy of ultra hot Jupiters. Further analysis will be performed in a forthcoming work to investigate this in more details.

As shown in both Fig. 6.3 and 6.4, deeper regions usually remain in chemical equilibrium, however, there might be some detached regions at the lower pressures which do not satisfy the Venot et al. (2018) quenching criteria. For instance, the blue ring in the terminator transection map, Fig. 6.3 bottom-right panel, where the chemistry departs from the quenched profiles and returns toward the equilibrium profiles at some pressures. This is mostly due to a combination of temperature inversion and lower vertical velocity. Nevertheless, if only one quenching level at each 1D trajectory is desired, then the deepest level at which the quenching occurs can be selected as the quenching point.

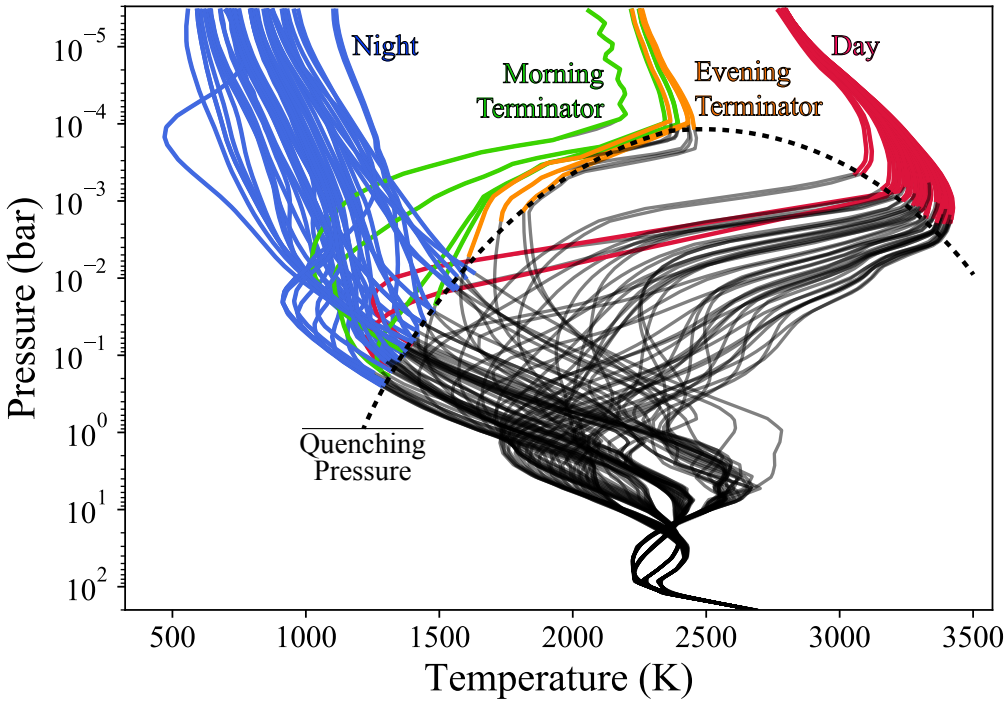

Figure 6.4: Variation of quenching pressure with the zenith angle, using the zeroth-order approximation (Sec. 6.2.1). Temperature profiles of all trajectories are color-coded above the quenching pressures. Red, orange, green, and blue represent temperature profiles at day, evening terminator, morning terminator, and nightside respectively. Minimum quenching pressure occurs at the evening terminator; where the atmosphere contributes significantly in the transmission spectra. Hence, the effects of disequilibrium chemistry is expected to be less pronounced in the transmission spectra.

6.2.2 Results of Chemical kinetic modelling

Temporal variation of H_2O, CO_2, and CH_4 vertical abundances at the equator and longitude ϕ=225° are shown in Fig. 6.5 (a, d, g) to demonstrate how disequilibrium processes change the composition of the upper atmosphere (see Section 6.1.2 for a description of the chemical kinetic model). The temporal evolution of the molecular abundances of H_2O, CO and CH_4 are color-coded by time where blue to red shows the progress in time from thermochemical equilibrium to their disequilibrium steady-states. All three molecular abundances depart from thermochemical equilibrium values at lower pressures and at some point remain constant up to the top of the atmosphere. By following the Moses (2014) definition of quenching level, CH_4

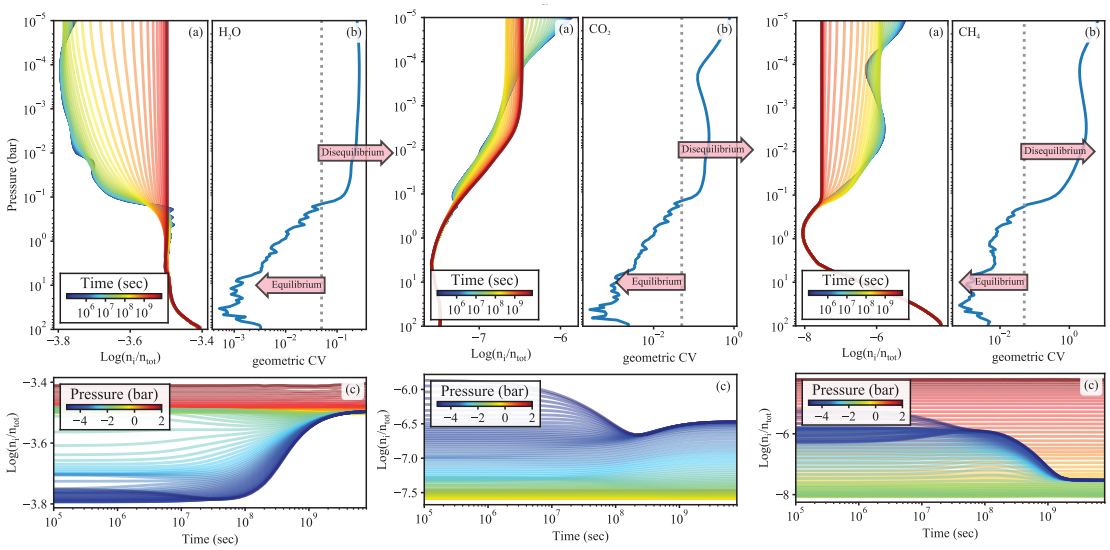

Figure 6.5: (a, d, g) Temporal variation of H_2O, CO_2, and CH_4 vertical abundances at the equator and longitude=225°, i.e. night-side. (b, e, h) Geometric Coefficient of Variation (gCV) of abundances; a higher value represents a stronger variation of abundance at any given pressure level. A choice of gCV=0.05 seems to reasonably separate the chemical equilibrium and disequilibrium regions (dashed gray vertical lines). (c, f, i) The quenching timescales. An invariant abundance profile at the longer times ensures a new steady-state. See Section 6.2.2 for more details. We note that the quenching level cannot be associated with one particular pressure for all species, but usually spans more than 1 order of magnitude in pressure.

quenches at around 0.1 bar for this particular trajectory (Fig. 6.5 (g)).

The quenching level of H_2O, however, can not be estimated easily and at the first glance could be somewhere between 0.3 and 30 bar. Its thermochemical equilibrium abundance is almost constant through this region and hence diffusion does not significantly change its abundance below 0.3 bar. Fig. 6.5 (d) shows yet another complication with the quenching level determination. In this case, CO_2 departs from its thermochemical equilibrium value at around 0.3 bar, while it does not reach a constant value until around 3 mbar. This usually occurs when the chemical and mixing timescales are comparable in that region. Examining abundance variation of all species at all trajectories reveals that in many cases the abundances do not reach a constant value at lower pressures and thus no quenching level (and consequently no "quenched-abundance") can be defined. Now, the question is, *what should be reported as the quenching levels?*

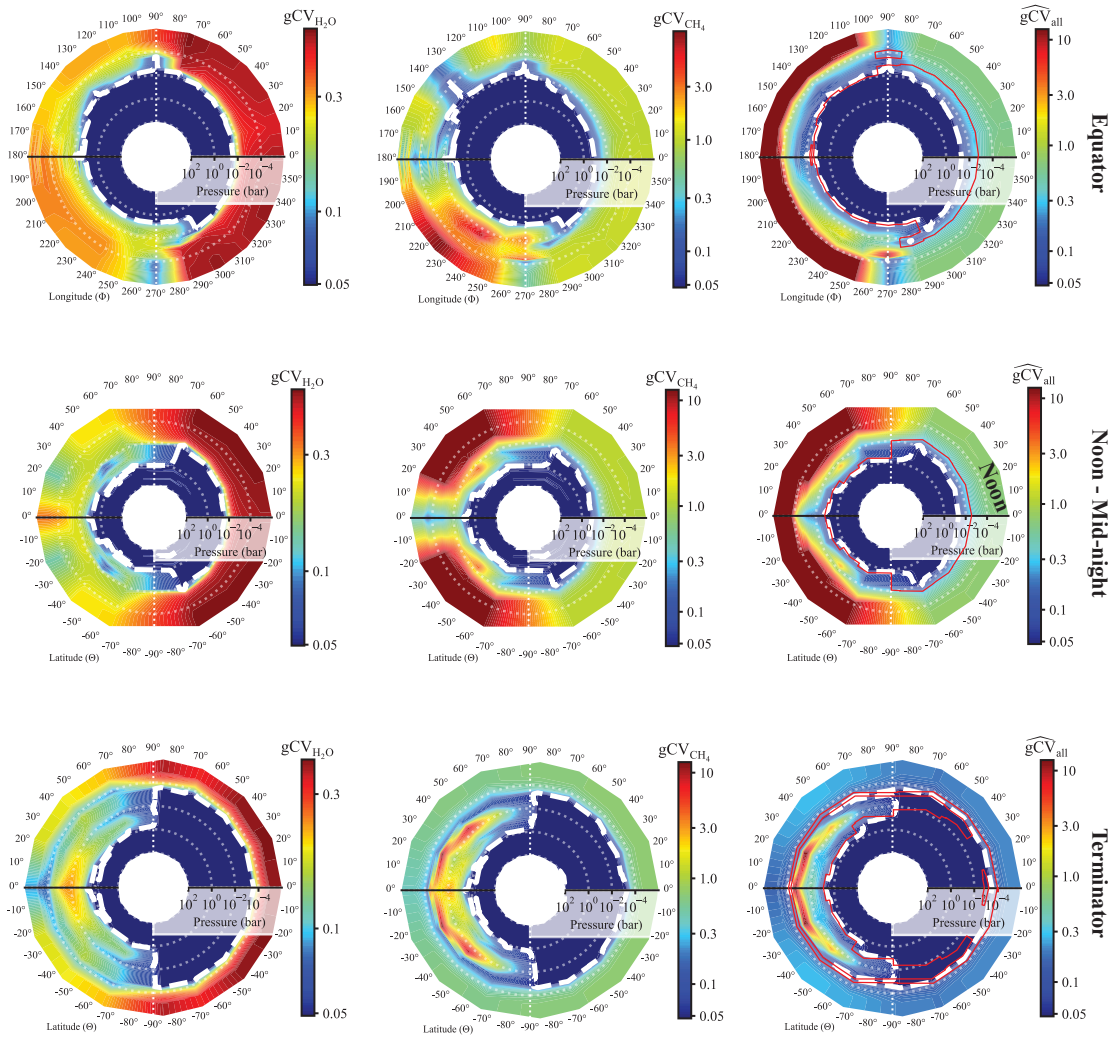

Figure 6.6: Estimation of quenching levels using the chemical kinetic modeling (Section 6.2.2). Top panels) Transection maps of the geometric Coefficient of Variance (gCV) of H_2O, CH_4, and all species abundances at the equator (Latitude=0°). We choose gCV=0.05 to separate the chemical equilibrium and disequilibrium regions (dashed white lines). This boundary is in good agreement with the zeroth-order approximation results (red solid lines in the right panels; Fig. 6.19). Middle panels) Similar to the top panels but at the noon-midnight plane (Longitude=0° or 180°). Bottom panels) Similar to the top panels but at the terminator (Longitude=90° and 270°). $\widehat{\text{gCV}}_{\text{all}}$ map suggests a morning-evening asymmetry where the dawn-side abundances have been driven more significantly out of thermochemical equilibrium and at deeper pressure levels.

We follow Molaverdikhani et al. (2019a) in suggesting the use of the 'Coefficient of Variation (CV)' to estimate the deviation from chemical equilibrium. This quantity can be calculated as the ratio of the standard deviation of a given species' abundance, s, to its temporal mean abundance at any given pressure level. CV is a relative and dimensionless measure of dispersion and hence independent of

the absolute value of the mixing ratios. For each 1D trajectory we can therefore calculate a 1D CV profile. Since in our kinetic model the time step for the numerical integration is exponential, we use the geometric Coefficient of Variation (gCV) of abundances for this purpose, calculated as follows (Schiff et al. 2014):

$$\mathrm{gCV} = \sqrt{\mathrm{e}^{s_{\ln}^2} - 1}, \tag{6.4}$$

where $s_{\ln}$ is the scaled natural log of the standard deviation of abundances and can be estimated as $s_{\ln} = s\ln(10)$. Fig. 6.5 (b, e, h) show the calculated gCV profiles of H_2O, CO_2, and CH_4, respectively, for latitude θ=0° longitude ϕ=225° trajectory as an example. A higher gCV value represents a stronger variation of abundance at any given pressure level. A choice of gCV=0.05 seems to reasonably separate the chemical equilibrium and disequilibrium regions. The geometric mean of gCV for all species, $\widehat{\mathrm{gCV}}_{\mathrm{all}}$, can be also used to determine the quenching level of the atmosphere:

$$\widehat{\mathrm{gCV}}_{\mathrm{all}} = \left(\prod_{i=1}^{n} \mathrm{gCV}_{\mathrm{i}}\right)^{\frac{1}{n}}. \tag{6.5}$$

The gCV can be thought of as a measure of normalised abundance deviation from its mean value and within a given time period. Therefore, the chosen time interval during which the abundances are considered should start at a time at which the atmosphere is at the thermochemical equilibrium and end after reaching a new steady state, such as diffusion equilibrium.

Transection gCV-maps of H_2O, CH_4, and for all species are shown in Fig. 6.6. Interestingly, the zeroth-order approximation results (red solid lines in Fig. 6.6 right-panels) are in good agreement with our kinetic modeling results, although it generally underestimates the depth of quenching on the dayside. An improved zeroth-order approximation can be foreseen as a fast method to estimate the quenching levels in parameterized atmospheric simulations.

The gCV values can be also used to compare the effectiveness of disequilibrium processes on different atmospheric constituents. For instance, H_2O has been driven away from thermochemical equilibrium less effectively than CH_4 given $\mathrm{gCV}_{\mathrm{H_2O}} < \mathrm{gCV}_{\mathrm{CH_4}}$, Fig. 6.6; left and middle panels. $\widehat{\mathrm{gCV}}_{\mathrm{all}}$ values also hint that

most of the species have been driven out of thermochemical equilibrium more effectively than these three species on the night-side at the equatorial plane.

The noon-midnight gCV-maps (Fig. 6.6 middle-panels) support shallower quenching levels on the dayside and a slight latitudinal dependency on the night-side. The anti-substellar point (Lat=0°, Lon=180°) appears to behave slightly different relative to its neighbouring trajectories, mostly due to stronger vertical velocity (w) at that region.

The deepest quenching levels occur at the polar regions, where the temperature is lower and the mixing is relatively strong. The $\widehat{\mathrm{gCV}}_{\mathrm{all}}$ map suggests a morning-evening asymmetry where the morning-side abundances have been driven more significantly out of thermochemical equilibrium and at deeper pressure levels. This asymmetry can potentially shape the transmission spectra of the two limbs differently. Observational consequences of chemical disequilibrium will be discussed in a forthcoming work.

6.2.3 The effect of photochemistry on the quenching levels

Photochemistry is another disequilibrium process. The main source of photolysis on highly irradiated planets is the irradiation from the host star. Other sources (such as cosmic rays, GCR, stellar background UV radiation, or solar Lyman-α photons that are scattered from atomic hydrogen in the local interplanetary medium, LIPM) could be also important on weakly irradiated planets, and can be neglected in the case of HAT-P-7b. But how much does the photochemistry affect the quenching levels on a highly irradiated planet?

Figure 6.7 compares the latitudinal quenching levels, $\widehat{\mathrm{gCV}}_{\mathrm{all}}$, with and without considering the photochemistry. The bottom panel shows the differences and suggests that the photochemistry plays a negligible role. This is not surprising since the photochemistry mostly affects the mbar regime and higher altitudes (see e.g. Molaverdikhani et al. (2019a) and references therein) and HAT-P-7b's dayside quenching points are located at deeper levels. The two exceptions are the evening terminator and a portion of the morning terminator where the quenching pressures

can be lower than mbar, as discussed in Section 6.2.1. However, at these regions the zenith angle is 90°; hence irradiation is ignored in our 1D kinetic calculations. The nightside also does not change since GCR and LIPM are not included.

6.2.4 The effect of mixing strength on the quenching levels

As discussed in Section 6.1.1, we decreased K_{zz} values by two orders of magnitude, Eq. 6.1, to follow Parmentier et al. (2013) conclusion. Using the traditional mixing strength approximation, i.e. without decreasing K_{zz} by a factor of 0.01, would then result in different quenching levels. Figure 6.8 compares the two cases and as one might expect the difference is non-negligible.

The resulted quenching levels from the traditional approach, K_{zz}=w·H, are usually deeper than the modified one, K_{zz}=w·$H\times$ 10^{-2}. The differences are on the order of 20%-40% on the dayside and 40%-80% on the nightside. The quenching levels at the terminator trajectories, however, show stronger variations as high as several orders of magnitude.

6.3 Disequilibrium abundances due to Diffusion and Photochemistry

6.3.1 CO and CH_4 abundance at equatorial and terminator regions

In Fig. 6.9 and 6.10, we present the differences of the CO and CH_4 abundance of the kinetic model and the equilibrium condition in the equatorial (left) and terminator (right) regions. The initial conditions (top row) is set to the equilibrium results from Helling et al. (2019b) where the element depletion due to cloud formation affects the gas-phase abundances in the cloud-forming regions of the atmosphere.

The carbon monoxide abundance (Fig. 6.9) on HAT-P-7b is only marginally affected by quenching as a result of vertical transport as the kinetic modelling results vary by less than a factor of two compared to the number densities in chemical equilibrium for both equatorial and terminator regions.

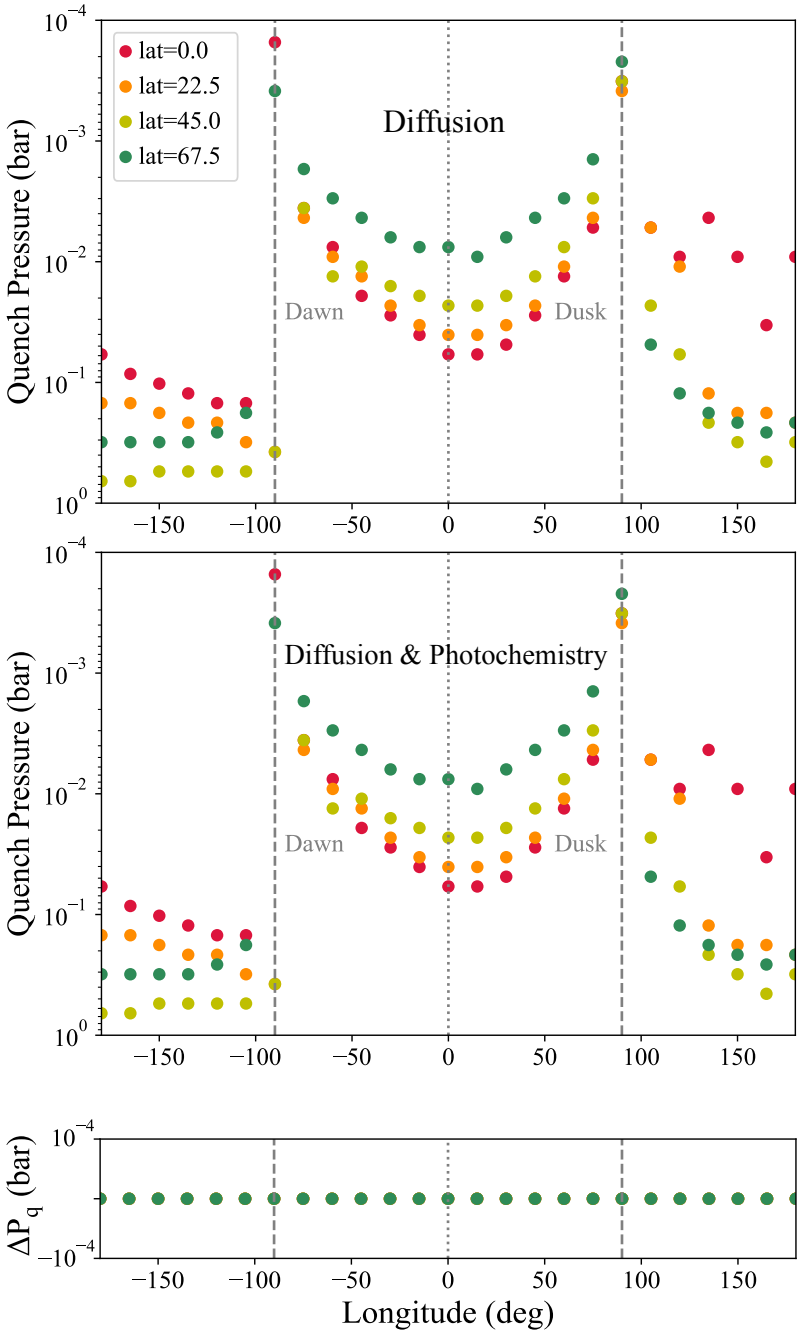

Figure 6.7: Top) Latitude and longitude dependency of quenching pressures, calculated from kinetic simulations by only including diffusion. The quenching criterion is discussed in Section 6.2.2 **Middle)** Similar to the top panel but photochemistry is also considered. **Bottom)** The difference between the quenching pressures of models with only diffusion and models including both diffusion and photochemistry. No difference is noticeable; suggesting photochemistry does not play a significant role in the quenching levels of HAT-P-7b.

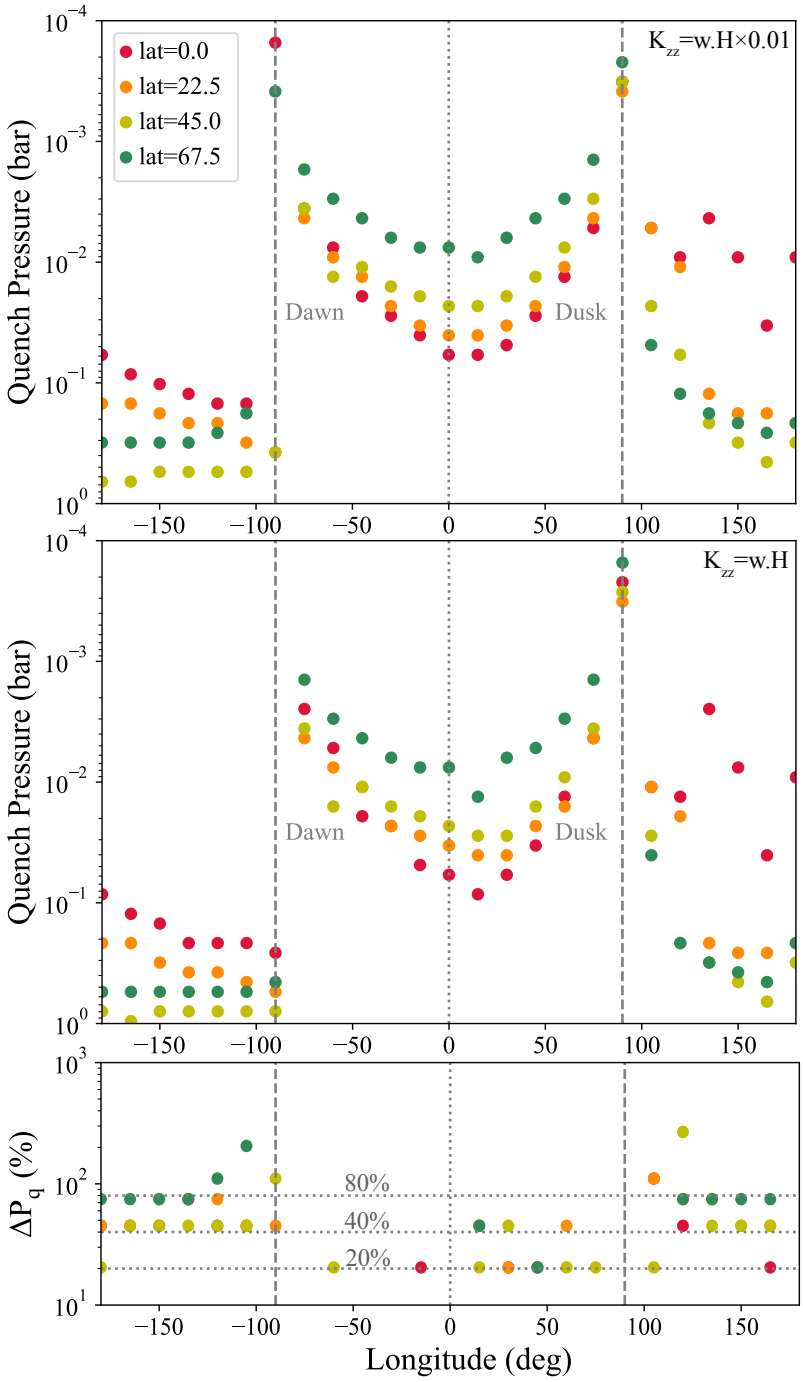

Figure 6.8: Top) Latitude and longitude dependency of quenching pressures, calculated using K_{zz}=w$\cdot H\times$ 10^{-2}. **Middle)** Similar to the top panel but using $K_{zz} = w \cdot H$, i.e. traditional approach. **Bottom)** The difference between the quenching pressures of the approaches. The atmosphere is being quenched at deeper levels, usually 20%-40% on the dayside and 40%-80% on the nightside. Some terminator trajectories, however, show several orders of magnitude change in their quenching levels, deepening from the mbar to 1 bar pressures.

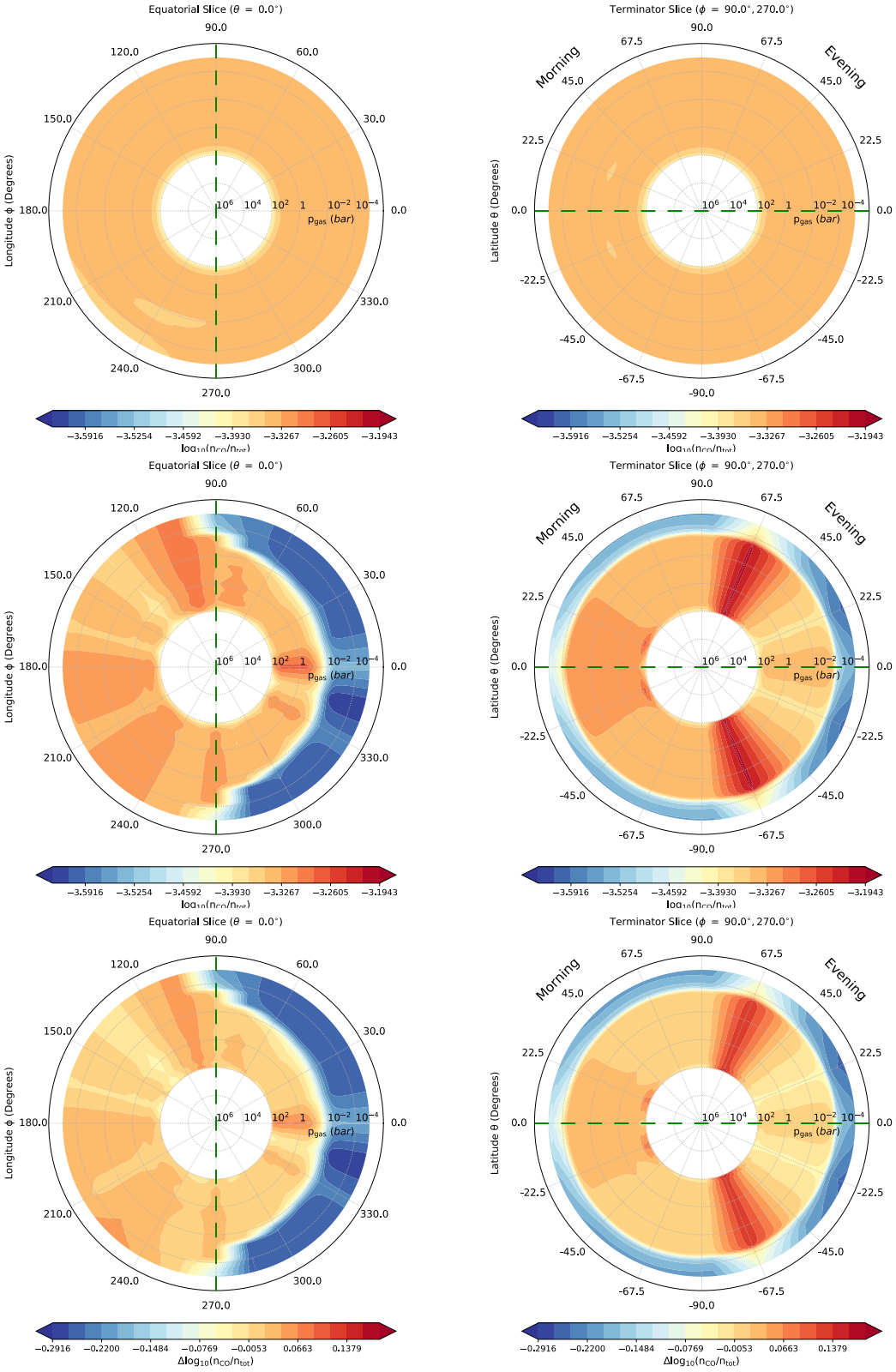

Figure 6.9: Carbon monoxide (CO): **Left column:** equatorial slices ($\theta = 0°$), **Right column:** terminator slices; **Top:** initial condition, $\log(n_{\rm CO}^{\rm init}/n_{\rm tot})$; **Middle:** final result from kinetic simulation, $\log(n_{\rm CO}^{\rm final}/n_{\rm tot})$ **Bottom:** difference, $\log(n_{\rm CO}^{\rm init}/n_{\rm tot} - n_{\rm CO}^{\rm final}/n_{\rm tot}$ between the initial (equilibrium) values and the kinetic results.

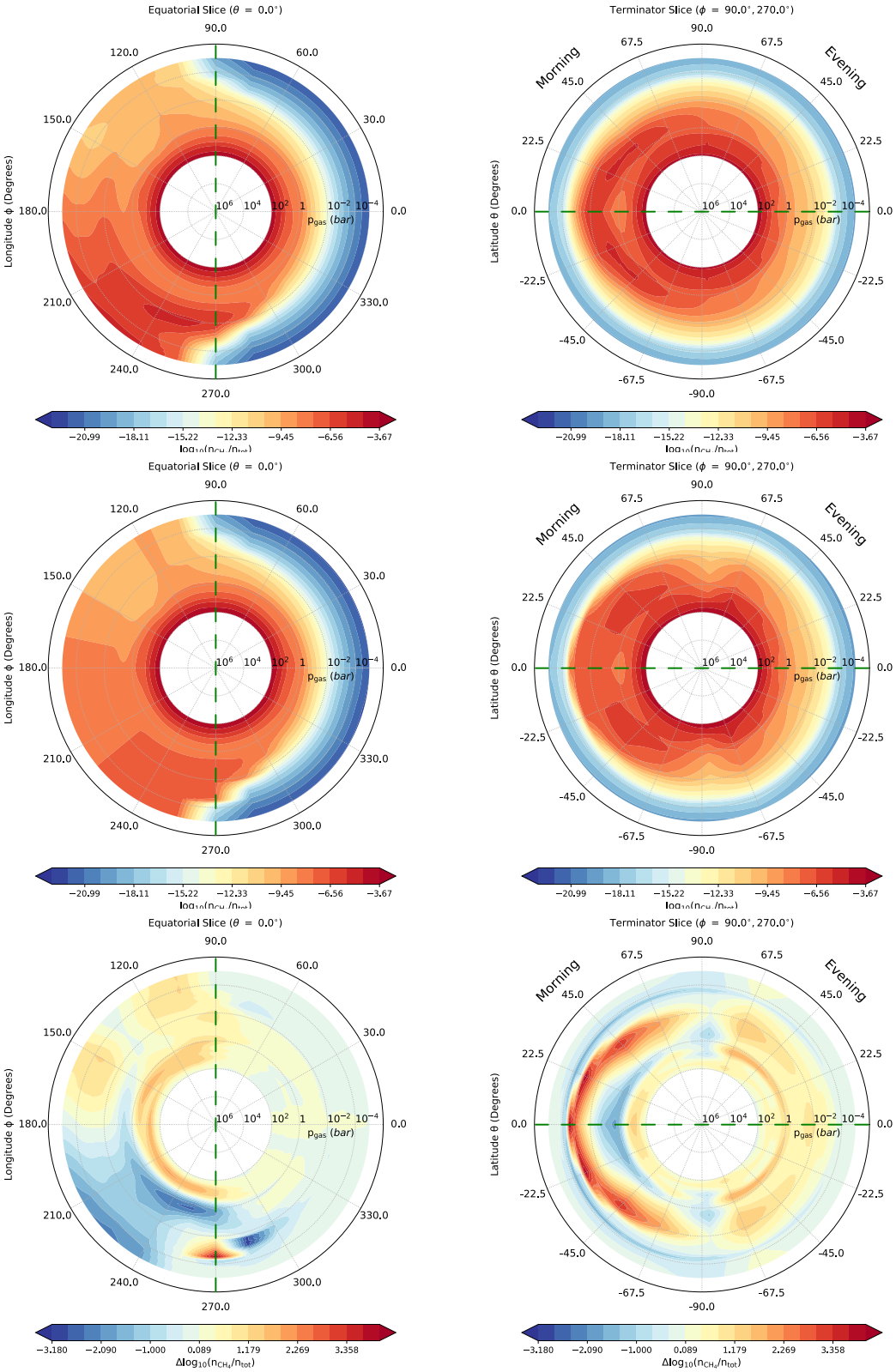

Figure 6.10: Methane (CH_4): **Left column:** equatorial slices ($\theta = 0°$), **Right column:** terminator slices; **Top:** initial condition, $\log(n^{\text{init}}_{CH_4}/n_{\text{tot}})$; **Middle:** final result from kinetic simulation, $\log(n^{\text{final}}_{CH_4}/n_{\text{tot}})$ **Bottom:** difference, $\log(n^{\text{final}}_{CH_4}/n_{\text{init}})$ between the initial (equilibrium) values and the kinetic results.

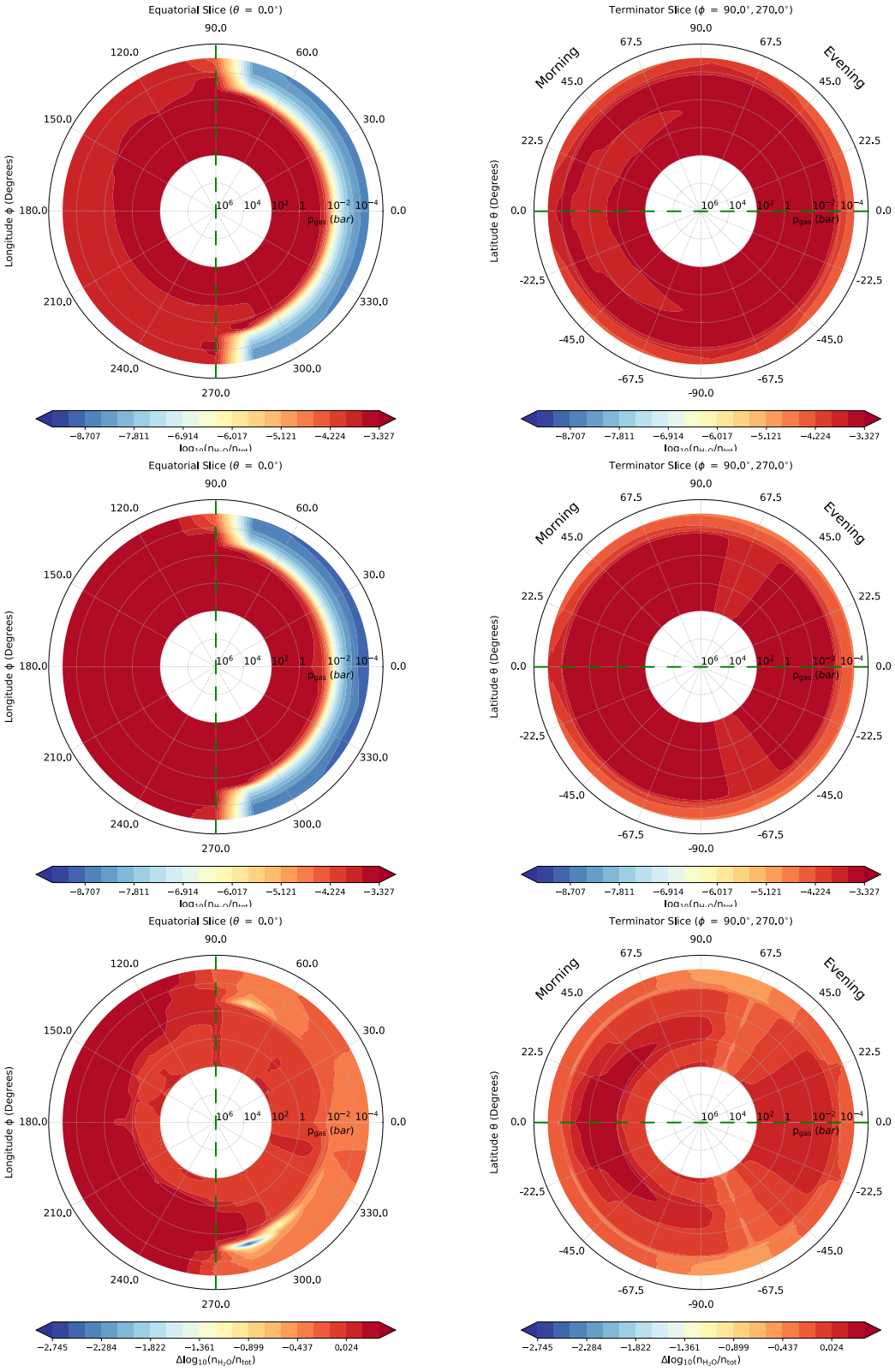

Figure 6.11: Water (H_2O): **Left column:** equatorial slices ($\theta = 0°$), **Right column:** terminator slices; **Top:** initial condition, $\log(n^{\text{init}}_{H_2O}/n_{\text{tot}})$; **Middle:** final result from kinetic simulation, $\log(n^{\text{final}}_{H_2O}/n_{\text{tot}})$ **Bottom:** difference, $\log(n^{\text{final}}_{H_2O}/n_{\text{init}})$ between the initial (equilibrium) values and the kinetic results.

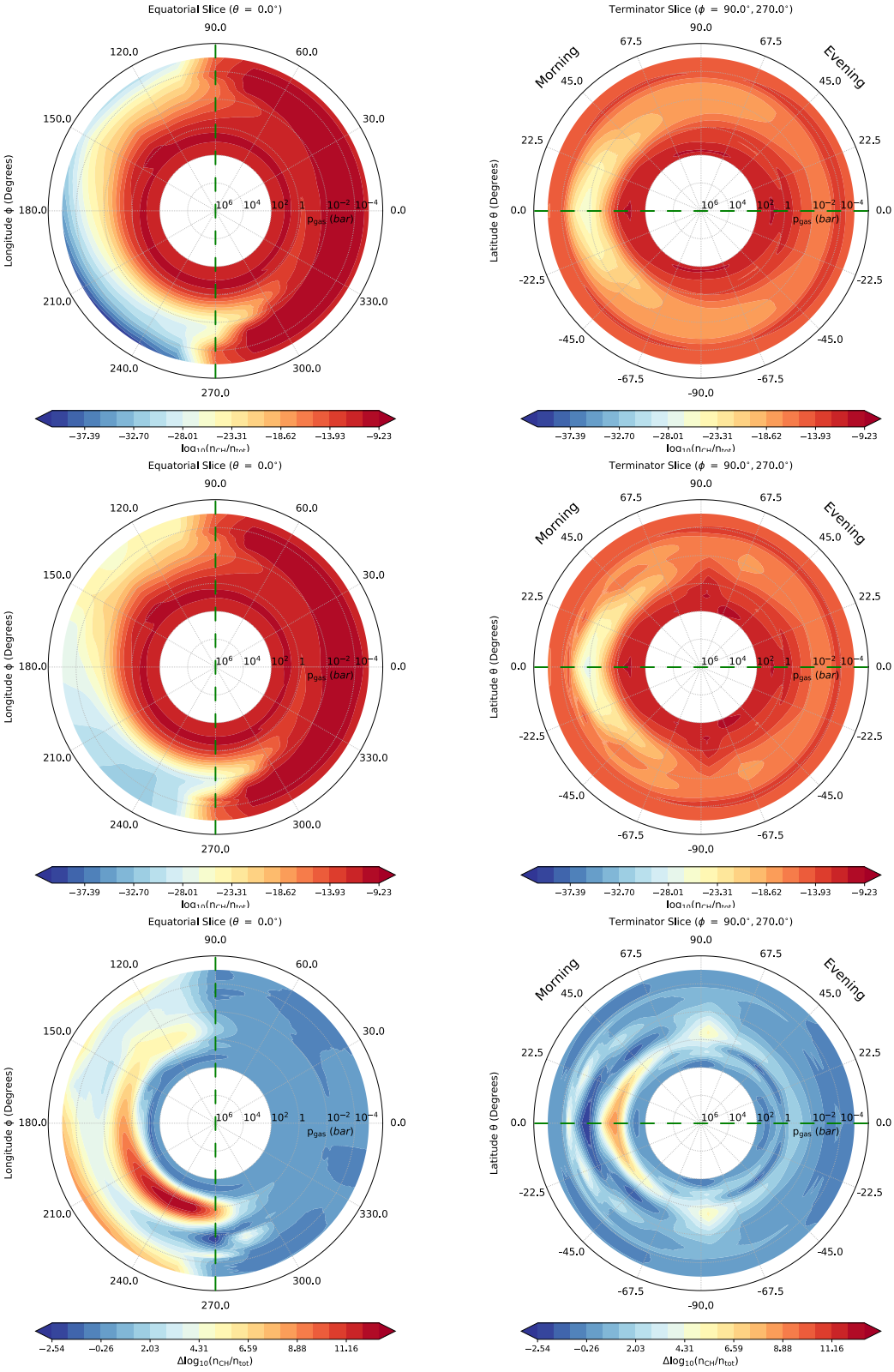

Figure 6.12: Methylidyne (carbyne) (CH): **Left column:** equatorial slices ($\theta = 0°$), **Right column:** terminator slices; **Top:** initial condition, $\log(n_{\rm CH}^{\rm init}/n_{\rm tot})$; **Middle:** final result from kinetic simulation, $\log(n_{\rm CH}^{\rm final}/n_{\rm tot})$ **Bottom:** difference, $\log(n_{\rm CH}^{\rm final}/n_{\rm init})$ between the initial (equilibrium) values and the kinetic results.

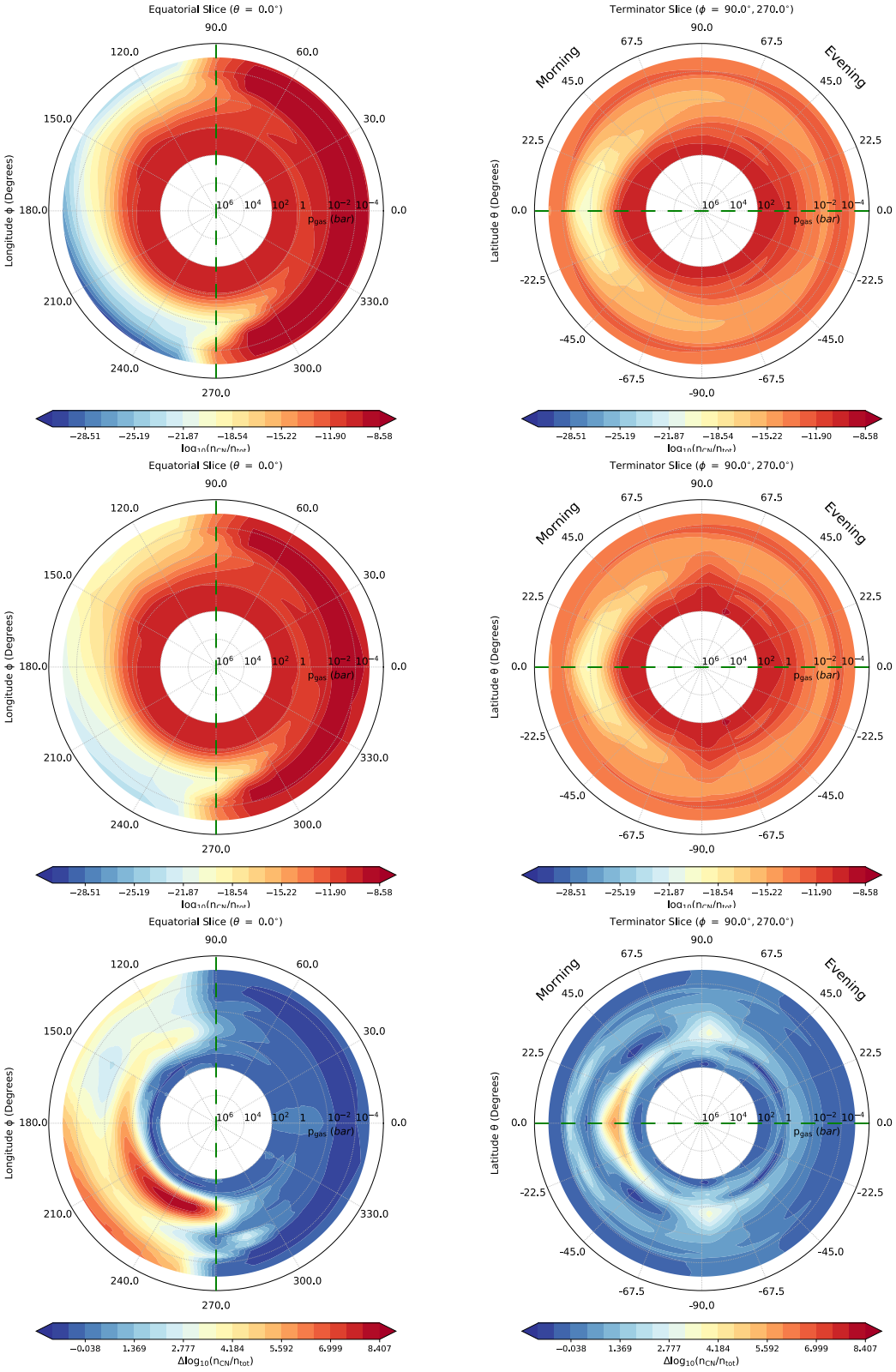

Figure 6.13: Cyanide (CN): **Left column:** equatorial slices (θ =0°), **Right column:** terminator slices; **Top:** initial condition, $\log(n_{\rm CN}^{\rm init}/n_{\rm tot})$; **Middle:** final result from kinetic simulation, $\log(n_{\rm CN}^{\rm final}/n_{\rm tot})$ **Bottom:** difference, $\log(n_{\rm CN}^{\rm final}/n_{\rm init})$ between the initial (equilibrium) values and the kinetic results.

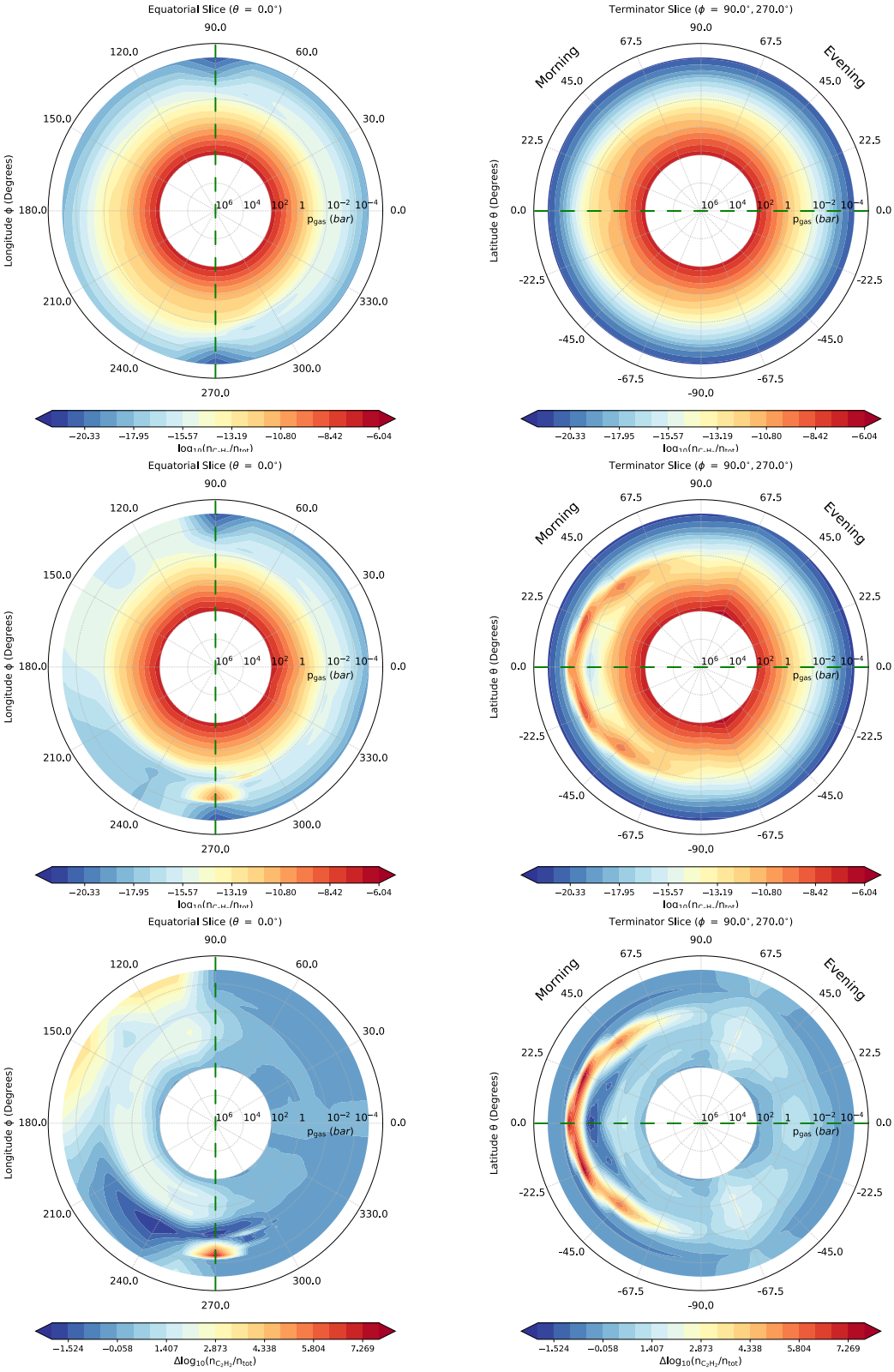

Figure 6.14: Acetylene (C_2H_2): **Left column:** equatorial slices ($\theta = 0°$), **Right column:** terminator slices; **Top:** initial condition, $\log(n^{\rm init}_{\rm C2H2}/n_{\rm tot})$; **Middle:** final result from kinetic simulation, $\log(n^{\rm final}_{\rm C2H2}/n_{\rm tot})$ **Bottom:** difference, $\log(n^{\rm final}_{\rm C2H2}/n_{\rm init})$ between the initial (equilibrium) values and the kinetic results.

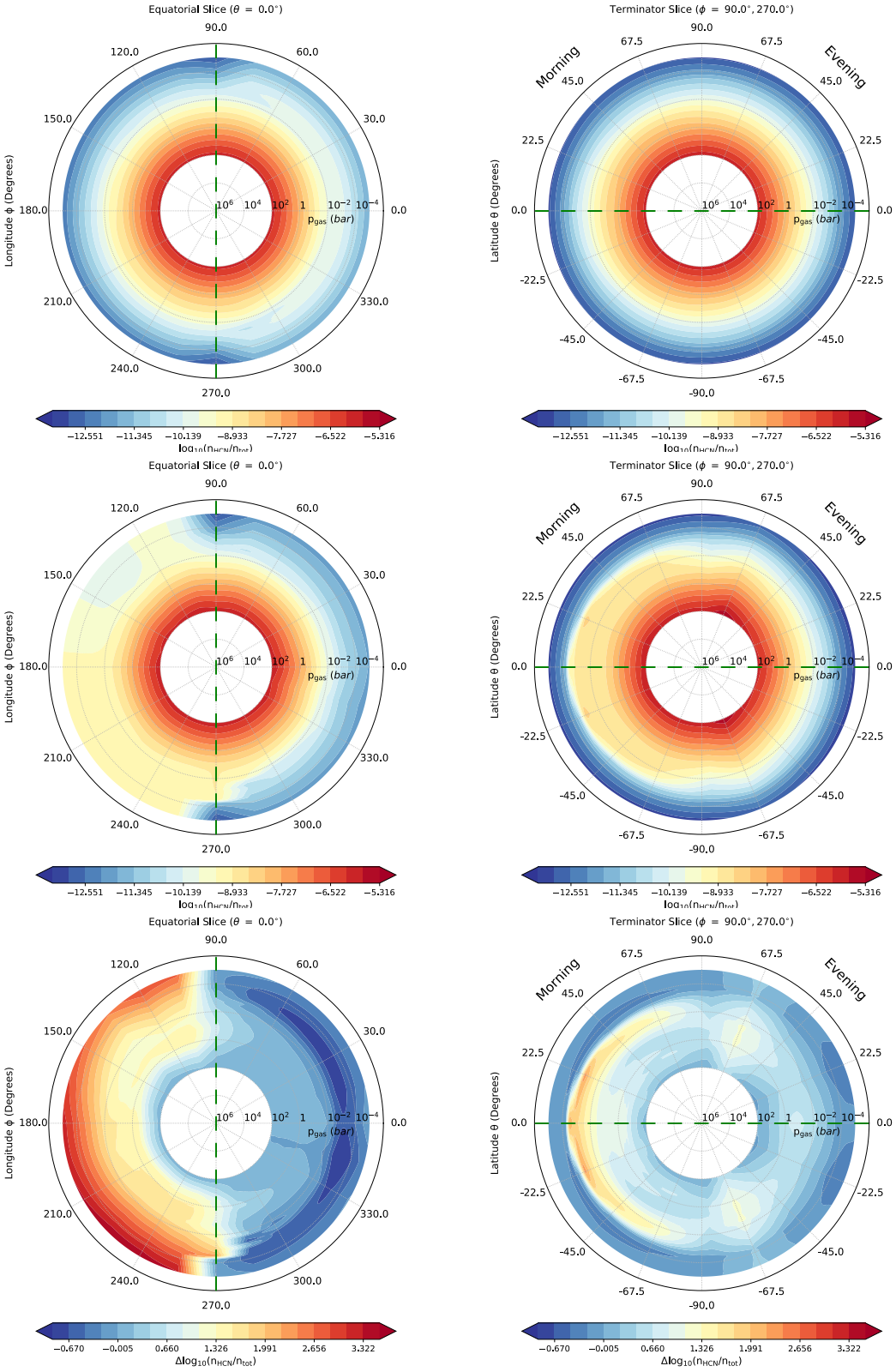

Figure 6.15: Hydrogen cyanide (HCN): **Left column:** equatorial slices ($\theta = 0°$), **Right column:** terminator slices; **Top:** initial condition, $\log(n^{\text{init}}_{\text{HCN}}/n_{\text{tot}})$; **Middle:** final result from kinetic simulation, $\log(n^{\text{final}}_{\text{HCN}}/n_{\text{tot}})$ **Bottom:** difference, $\log(n^{\text{final}}_{\text{HCN}}/n_{\text{init}})$ between the initial (equilibrium) values and the kinetic results.

On the other hand, the methane abundance (Fig. 6.10) in the kinetic model shows a stronger deviation from the equilibrium results at ∼10 mbar level. The strong vertical mixing causes the lower-than-equilibrium methane number density for P<1 bar at around longitude $\phi = 240°$ by about -3 dex and enhancement in methane number density at $p_{\rm gas}$ >1 bar by more than 1 dex. At the morning terminator, there is a strong local methane enhancement in between 1-10 mbar level. We interpret that this methane enhancement is related to the thermal inversion at ∼10 mbar level (see Fig. 6.4 and Fig. 6.19 in the appendix). The vertical mixing homogenizes the relatively methane-rich layer of the cooler region at $p_{\rm gas}$ >10 mbar with the hotter region at $p_{\rm gas}$ <10 mbar. As a result, the vertical mixing leads to a local enhancement in methane's number density between 1-10 mbar level relative to that of equilibrium result.

6.3.2 H_2O abundance at equatorial and terminator regions

Similarly we show the effects on H_2O abundance (Fig 6.11), as with carbon monoxide the abundance is relatively unchanged, continuing to display an asymmetry between the dayside and nightside. However, some subtle variations are notable. While abundances at pressures larger than 1 bar mostly stay constant at all longitudes around the equator, abundances at higher altitudes on the nightside increase slightly. On the dayside, the abundance difference between equilibrium and kinetic chemistry is almost invariant at pressures larger than 100 mbar and at higher altitudes it decreases by about -0.5 dex on average.

The terminator also shows only small variations. Albeit a prominent change being the shifting of relatively low abundance regions from around 0.01 bar between $\phi\pm$ 67.5 degrees latitude at the morning side to two vertical columns at the same latitudes on the evening side. The most significant change of a factor of nearly three orders of magnitude decrease occurs just on the dayside of the morning terminator ($\theta \sim 285$ degrees longitude) at 1-10 mbar, this is likely linked to the thermal inversion there as was the case for methane.

We should note that the abundance variation results due to disequilibrium are consistent with the interpretations based on gCV calculations, as discussed in Section 6.2.2 for the two cases of H_2O and CH_4. Therefore, gCV can be used both for the determination of quenching pressures and as a quantitative measure of the efficiency of disequilibrium processes on the atmospheric constituents.

6.3.3 CH, C_2H_2, CN, HCN abundance at equatorial and terminator regions

Here we show how the abundances of small carbon molecules CH (methylidyne, Fig. 6.12) and CN (cyanide, Fig. 6.13) may be affected by vertical transport processes compared to the chemical equilibrium results in Helling et al. (2019b). We note, however, that the atmosphere is globally oxygen-rich, hence, oxygen-binding molecules will dominate the atmosphere's chemical composition. It is, however, worthwhile to consider carbon-molecules that can be of relevance for the formation of biomolecules (like CH_4, C_2H_2 and HCN) and their precursors in order to identify possible tendencies in the unexplored parameter ranges that exoplanet provide. HCN is furthermore suggested as spectral tracer for lightning events in planetary atmospheres. Knowing its background abundance may help to disentangle such lightning traces (Hodosán et al. 2018; Helling 2019b).

CN and CH are precursor for more complex molecules as well; such as C_2H_2 (Fig. 6.14) and HCN (Fig. 6.15). CH, CN, C_2H_2 and HCN are molecules which typically appear in spectra of carbon-rich stars (Eriksson et al. 1984; Helling et al. 1996) and which therefore maybe considered as potential tracers for carbon-enriched planetary environments (e.g., Hron et al. 1998; Uttenthaler et al. 2016; Hamren et al. 2016).

Firstly, CH and CN show a clear day/night asymmetry with both being more abundant on the dayside and in the warmer atmospheric regions. This day/night asymmetry is unaffected by quenching as it is driven by the local day/night temperature difference instead of hydrodynamic motions. The CH abundance has decreased on the nightside compared to the thermochemical equilibrium results.

Differences are generally small but amount to orders of magnitudes in localised areas in the equatorial plane as much as 12 dex. Differences remain negligible in the low-pressure terminator regions ($p_{\rm gas} < 1$bar).

C_2H_2 is very low abundant and kinetic chemistry only affects its abundances in localised areas in the terminator regions at $p_{\rm gas} \approx 10^{-2}$bar. HCN is somewhat more abundant than C_2H_2, but disequilibrium effects introduce a day/night asymmetry for HCN. As a result, the nightside HCN abundance has increased by 3 orders of magnitude compared to the chemical equilibrium results. The absolute number densities, however, remain small compared to CO and H_2O, for example. This asymmetry is also visible in the terminator regions where the morning terminators show a higher HCN abundance. The terminator regions (right column) is again only locally affected by the kinetic gas chemistry, mainly at the nightside at $p_{\rm gas} \approx 10^{-2}$ bar. In general, we note that all molecules in the form of C_nH_m are affected by disequilibrium processes on the nightside, where heavier C_nH_m molecules are affected the most.

The result in this section emphasis our finding from the previous sections: Quenching of the gas phase chemistry does take place for some of the molecules but the actual deviation needs to be considered with care as large deviations can be local phenomena only.

6.3.4 The atmospheric C/O in HAT-P-7b

The carbon-to-oxygen ratio (C/O) became one of the parameters that was hoped to be useful to characterise an exoplanet's formation and/or evolution. C/O from $\ll 1$ to $\gg 1$ has served as one of the stellar parameters which allowed the link to stellar evolution and the spectral changes have widely been studied (Gustafsson et al. 2008; Eck et al. 2017).

C/O can not be straight forwardly linked to planetary evolutionary states nor to planet formation easily if clouds form (Helling et al. 2014). We note that other mineral ratios (like Mg/O, Mg/Si etc.) will be similarly unsuitable as a direct link to planet formation unless cloud formation and related chemical processes are simulated

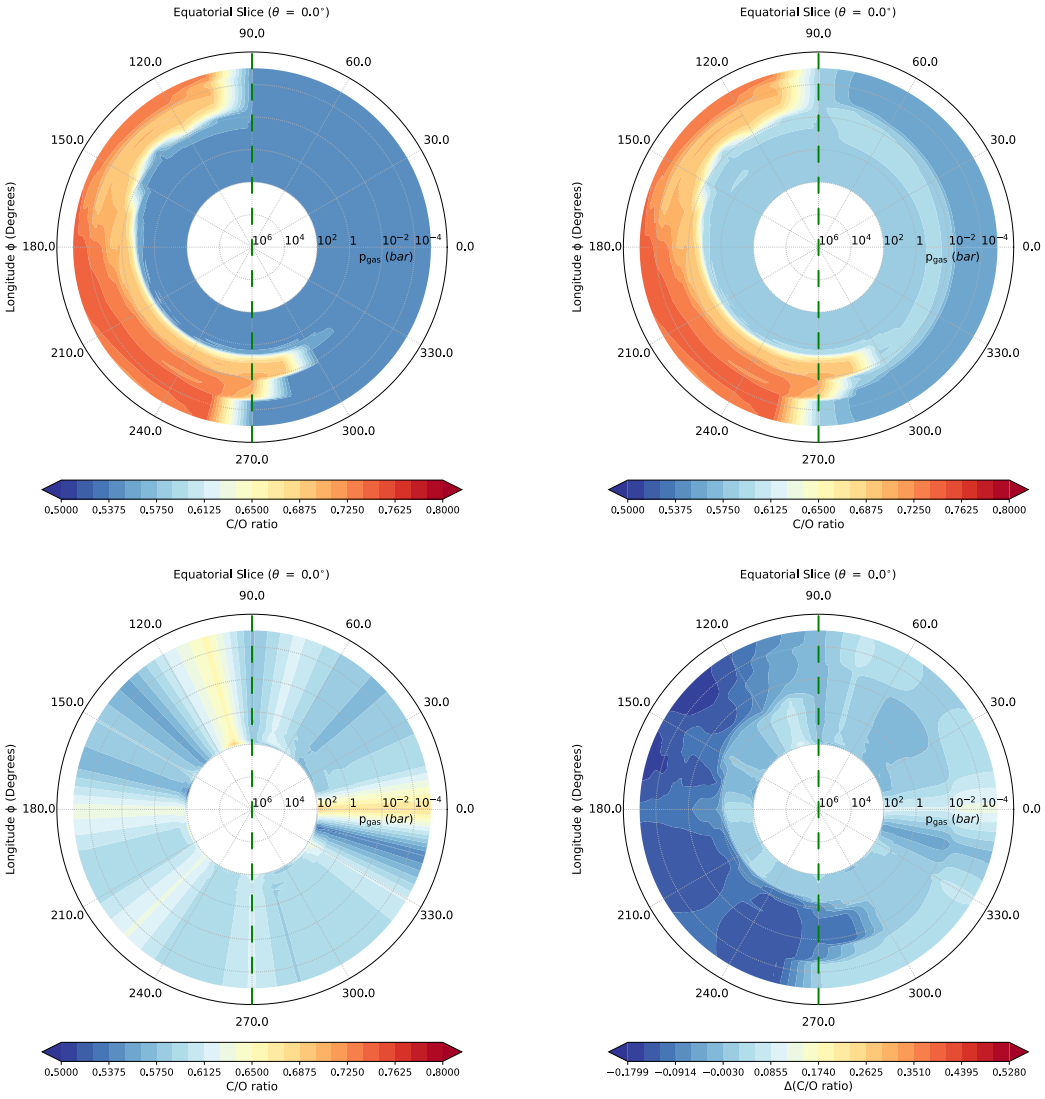

Figure 6.16: The carbon-to-oxygen ratio (C/O): **top left:** C/O after cloud formation as in Helling et al. (2019b) according to ϵ_C/ϵ_O, **top right:** C/O for initial condition of gas-kinetic calculations (from CH, CO, CO_2, C_2H_2, ...),, **bottom left:** C/O at the end of gas-kinetic calculations (t=10^{12} sec) **bottom right:** C/O change between initial condition (top right) and final gas-kinetic solution (bottom left).

simultaneously (see e.g. Fig. 4 in Helling 2019a). The only known way to determine such mineral ratios is due to high-resolution spectroscopy of polluted white dwarfs. No carbon-rich planetary debris has been found so far (Wilson et al. 2016).

C/O measures the overabundance of carbon compared to oxygen. C/O can change by changing the carbon abundance or the oxygen abundance. The main contribution to changes of C/O in our simulations comes from the change in oxygen abundance due to consumption in cloud particles..

Our cloud formation simulations for HAT-P-7b start from solar element abundances with C/O=0.54, i.e. more oxygen than carbon element abundance. The resulting C/O for the cloud-forming atmosphere of HAT-P-7b linked to the equilibrium gas-phase code GGChem is reproduced in Fig. 6.16 (top left) for the equatorial slice ($\theta = 0°$): The cloud forming nightside reaches C/O$\approx$ 0.78 and the cloud free parts of the dayside remain at the undepleted, solar value as expected. The oxygen and carbon element abundances that result from our kinetic gas simulations are shown in Fig. 6.16 (bottom left).

We compare in how far the undepleted, solar C/O ratio is reflected in the initial conditions for the gas-kinetic analysis conducted in this chapter. Then, we study how C/O may have been affected by chemical gas-kinetic processes. We present our results in the form of slice plots through the equatorial plane in Fig. 6.16. The corresponding terminator slices can be found in the appendix (Fig. 6.20).

The C/O ratio used as initial condition for the kinetic modelling (top right in Fig. 6.16) is smaller than the C/O derived in Helling et al. (2019b) (top left in Fig. 6.16). The reason is that such rate networks consider less molecules than, e.g., our gas-phase equilibrium calculations with GGChem, and hence, C/O is derived from only the C and O binding molecules considered in the gas-kinetic network simulation (see list in Sect. 6.1.2). The input abundances for these molecules were set to those resulting from our cloud formation calculations in Helling et al. (2019b), as discussed in Set. 6.1.2.

The gas kinetic C/O ratios appear to be relatively homogenised toward a value slightly higher than its solar value. This is expected as the global initial C/O ratio

in the gas phase was higher than the solar value due to the depletion of oxygen by cloud formation. The largest differences between $(C/O)_{eq}$ and $(C/O)_{kin}$ appear for p_{gas} <1 bar on the nightside and to some extend on the morning terminator. All other regions show negligible deviations between $(C/O)_{eq}$ and $(C/O)_{kin}$ in the equatorial plane. This homogenisation of C/O ratio removes the morning-evening C/O asymmetry due to the cloud formation only (reported in Paper I). This suggests a C/O asymmetry may be less pronounced in the ultra-hot jupiters, however, an observed global enhancement of C/O ratio could be still an indication of cloud formation on a hot exoplanet.

6.3.5 Observability of disequilibrium chemistry in HAT-P-7b's atmosphere

Having examined how molecular abundances are modified by accounting for chemical kinetics, we now turn to the prospect of observing the influence of disequilibrium chemistry. There are many ways in which disequilibrium chemistry can manifest in an exoplanet spectrum. The clearest diagnostic would be the appearance of absorption features caused by a molecule expected to be undetectable for equilibrium chemical abundances. For example, signatures of NH_3 and HCN can become detectable in hot Jupiter transmission spectra if disequilibrium mechanisms enhance their abundances to $\gtrsim 1\%$ that of H_2O (MacDonald & Madhusudhan 2017). However, such a dramatic change requires molecular abundances to alter at the order-of-magnitude level. Alternatively, for smaller deviations from chemical equilibrium, one may examine whether the shape of a molecule's absorption features, or the relative strengths of features due to different molecules, are altered by chemical kinetics.

We quantitatively asses the influence of disequilibrium chemistry on spectral observations of HAT-P-7b using a similar approach to Helling et al. (2019b). Specifically, we compute the pressure at which the vertically integrated optical depth due to a chemical species, x, reaches unity (i.e. $p(\tau_x(\lambda) = 1)$). This provides a useful indication of the contributions of different molecules to spectra of HAT-P-7b (see the forthcoming work for a full radiative transfer calculation). We first consider which of

the molecules included in our chemical model are likely to be spectrally accessible to observations. We then examine differences due to chemical kinetics, quantified by the % difference in $p(\tau_x(\lambda) = 1)$ between the initial and final atmospheric abundances.

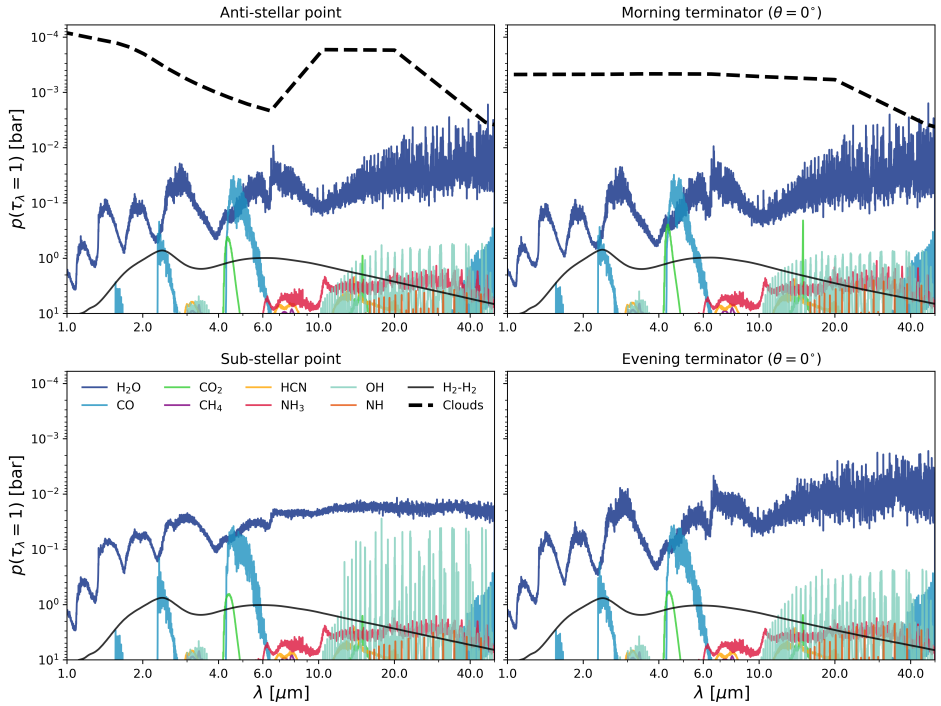

Figure 6.17: Prominent sources of molecular opacity under disequilibrium chemistry. The atmospheric pressure at which the vertical wavelength-dependent optical depth of species x reaches unity, $p(\tau_x(\lambda) = 1)$, is shown across the infrared. Several molecules included in both the kinetic model and the opacity database which do not reach $\tau_x(\lambda) = 1$ by the 10 bar level (e.g. C_2H_2) are omitted. See Helling et al. (2019b) (Fig. 20) for opacity contributions due to species not included in the kinetic model (e.g. heavy-metal oxides, atoms, etc.). All opacities are plotted at a spectral resolution of $R = 1000$. Four equatorial regions are considered: (i) the anti-stellar point, (ii) the morning terminator, (iii) the sub-stellar point, and (iv) the evening terminator. For comparison, the $\tau(\lambda) = 1$ surface due to clouds from Helling et al. (2019b) is overlaid. Source: Ryan MacDonald

Figure 6.17 shows the $p(\tau_x(\lambda) = 1)$ surfaces for prominent molecules at the end of the kinetic calculation. Here we focus on infrared wavelengths, as the opacity at visible wavelengths will contain large contributions from atomic and heavy-element molecules not included in the present kinetic chemistry model (see Helling et al. (2019b), Fig. 20, for their influence in chemical equilibrium). Three molecules are

potentially observable at near-infrared wavelengths: H_2O, CO, and CO_2 (ordered by prominence). The importance of these molecules holds in all four of the plotted atmospheric regions, though their relative influence does vary (e.g. CO and CO_2 opacity is more prominent, compared to H_2O, at the morning terminator than the evening). At the sub-stellar point, OH also becomes an important opacity source for wavelengths longer than > 10 μm (opening the possibility of its detection via mid-infrared dayside emission spectroscopy, such as with JWST's MIRI MRS mode – see Beichman et al. (2014)). While H^- is reported to be an important opacity source on the highly irradiated exoplanets (see e.g. Arcangeli et al. 2018), we found that its contribution is likely to be significant only on the dayside of HAT-P-7b and at the wavelengths longer than 15 μm; suggesting no significant impact of this compound on the transmission spectra of this planet.

It is important to note that molecular opacity at the anti-stellar point and morning terminator are likely to be obscured by clouds (see Helling et al. (2019b)). This overall picture is essentially the same as Helling et al. (2019b), indicating that relaxing chemical equilibrium does not alter the prediction for which molecules are expected to be most prominent in spectra of HAT-P-7b.

However, as we have seen, chemical kinetics plays an important role in shaping the vertical abundance profiles of various molecules. For example, Figure 6.5 demonstrates nightside quenching of the H_2O abundance in the upper atmosphere for pressures $\lesssim 10^{-1}$ bar. Given that H_2O is the most prominent molecular opacity source at infrared wavelengths, any such abundance changes at atmospheric pressures accessible to transmission and emission spectra are potentially observable. We examine the importance of disequilibrium abundance changes by computing the % difference between the initial (equilibrium) and final (kinetic) $p(\tau_x(\lambda) = 1)$ surfaces for the molecules anticipated to be most prominent in spectra of HAT-P-7b. The results are shown in Figure 6.18.

Disequilibrium chemistry tends to manifest by enhancing the prominence of molecular absorption features. The differences are most pronounced at the anti-stellar point and morning terminator, where the $p(\tau_x(\lambda) = 1)$ surfaces occur up

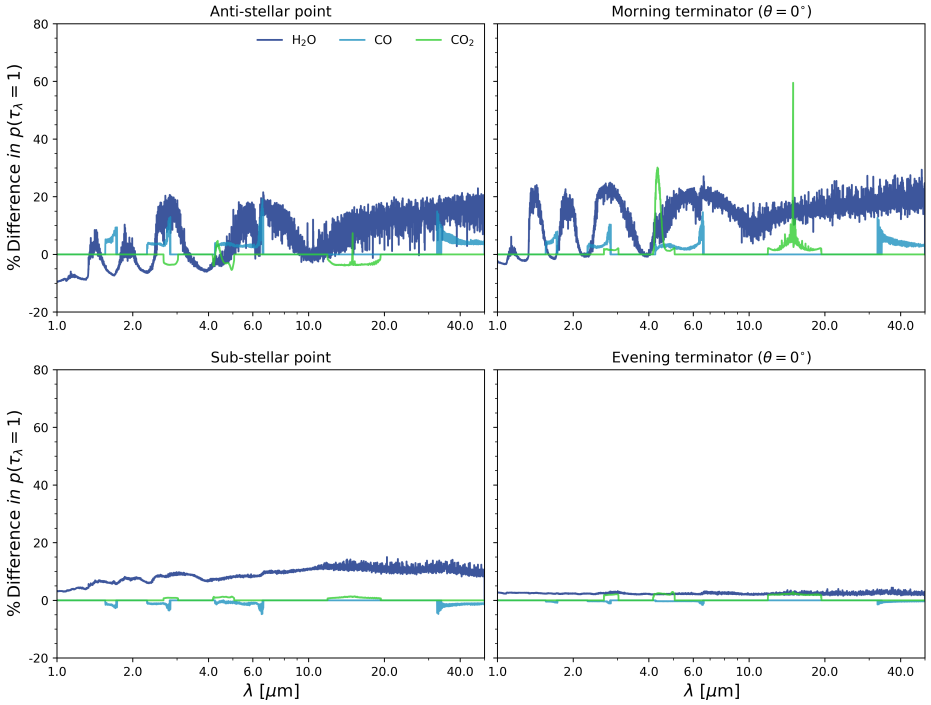

Figure 6.18: Differences to the opacity contribution of observable molecular species due to disequilibrium chemical kinetics. The difference metric, $(p(\tau_x(\lambda) = 1)_{\text{Initial}} - p(\tau_x(\lambda) = 1)_{\text{Kinetic}})/p(\tau_x(\lambda) = 1)_{\text{Initial}}$, is defined such that a positive difference implies stronger absorption after accounting for disequilibrium chemistry (i.e. $p(\tau_x(\lambda) = 1)$ occurs higher in the atmosphere). Only H_2O, CO, and CO_2 are plotted, as these molecules offer the greatest detection prospect in the near-infrared (see Figure 6.17). All opacities are plotted at a spectral resolution of $R = 1000$. Four equatorial regions are considered: (i) the anti-stellar point, (ii) the morning terminator, (iii) the sub-stellar point, and (iv) the evening terminator. Source: Ryan MacDonald

to 20% higher in the atmosphere for H_2O (and up to 60% higher for CO_2) in the centre of absorption features (e.g. 3 μm) and up to 10% lower in absorption minima (e.g. 1.7 μm). This disequilibrium-induced contrast in the pressures where the atmosphere becomes optically thick between wavelengths where molecules strongly and weakly absorb would result in 'stretched' spectral absorption features. On the other hand, at the sub-stellar point and evening terminator the $p(\tau_x(\lambda) = 1)$ surface for H_2O increases in altitude for all wavelengths, which would result in stronger, but relatively unstretched, absorption features. We thus see that, in principle, disequilibrium chemistry can transform the shape of molecular absorption features

in different ways for different atmospheric regions. Although the anti-stellar point tends to be inaccessible to observations (due to its low thermal emission), these differing vertical opacity distributions between the morning terminator (observed in transmission) and the sub-stellar point (observed in emission) could be one avenue to probe disequilibrium chemistry in ultra-hot Jupiters. A second avenue is inter-terminator differences observed in transmission spectra, due to the morning terminator experiencing enhancements in H_2O, CO, and CO_2 absorption whilst the evening terminator sees only minor changes. Ultimately, whether or not these disequilibrium-induced opacity differences will be observable depends crucially on the presence of clouds in HAT-P-7b's atmosphere. If the morning terminator is dominated by cloud opacity (as predicted in Helling et al. (2019b)), it will be difficult to observationally probe disequilibrium chemistry in this region. Dayside emission spectra may have easier time detecting H_2O features due to its enhanced abundance, but observing this alone would be difficult to uniquely attribute to disequilibrium chemistry (as opposed to, say, a higher atmospheric O/H ratio but in chemical equilibrium). We therefore conclude that observationally detecting signatures of disequilibrium chemistry in HAT-P-7b's atmospheres will be challenging. A quantitative assessment of the detectability of disequilibrium signature on HAT-P-7b will be present in a forthcoming work (MacDonald et. al. In perp.).

6.4 Discussion

Material properties: rate and diffusion coefficients. Gas-kinetic rate networks solve diffusion equations, one for each molecular species (e.g. Eq. 22 in Rimmer & Helling (2016)). Each equation requires material constants in the form of a rate, an eddy diffusion coefficient, and a molecular diffusion coefficient. In principle, they all can be measured through lab experiments, except, measuring them for many reactions/reactants is an overwhelming task. We assume that the rate values are reasonably well known (or have been benchmarked) and do not investigate the propagation of uncertainties in the rate coefficients into our results. The eddy diffusion is assumed to be the same for all species. The molecular diffusion of species

are calculated following the Lennard-Jones Theory (see Section 3.1.2 for a detailed description). This is a critical point for larger molecules in low-pressure regions where the molecular diffusion becomes more efficient than the turbulent eddy diffusion.

Network size: Gas-kinetic simulations are limited by the number of reactions included. The more focused a network is, i.e. reduced network, the faster it will be and the most complete it can be with respect to the relevant reactions for the species involved. The ultimate form of such reduced network manifests itself in the chemical timescale relaxation scheme where only one rate limiting reaction is considered. The focus of such simulation is usually on a chemical inversion between two chemical compounds only. This is the most frequently used technique to couple 3D GCM simulations with chemical disequilibrium processes.

As shown by, e.g., Drummond et al. (2018c) a consistent coupling of dynamics, radiative transfer, and chemistry demand more computational power and may result in uncovered physics by the relaxation scheme. For instance, an outcome of such full coupling leads to the wind-driven chemistry that in turn has a significant impact on thermal and dynamical structure of the cool atmospheres, such as HD 189773b. The effect of full network coupling, however, reported to be less significant in the case hotter atmospheres such as HD 209458b. Is this also the case for the ultra-hot Jupiters or not is a matter of question that requires a full coupling of chemistry and GCM.

Limitations of 1D kinetics models: One important limitation of our approach is that our chemical kinetic model is one-dimensional. Thus, horizontal mixing is neglected. Horizontal mixing can homogenize abundances longitudinally and/or latitudinally and lead to horizontal quenching. Recent studies coupling a simplified chemical relaxation scheme to 3D general circulation models of hot Jupiters have found that horizontal mixing dominates over vertical mixing (Agúndez et al. 2014a; Mendonça et al. 2018) or that abundances are determined by a combination of vertical and horizontal mixing (Drummond et al. 2018c,b).

However, all of these studies focused on hot Jupiters with equilibrium temperatures < 1500 K and it is not clear to what extend those results apply to ultra-hot Jupiters. Komacek et al. (2017) demonstrate that with increasing equilibrium temperature, day- to night flow becomes more important compared to the equatorial jet and vertical velocities increase. As a consequence, the efficiency of vertical mixing is believed to increase by more than an order of magnitude between T_{eq} =1500 K and T_{eq} =2200 K (Komacek et al. 2019). On the other hand, vertical velocities are set by the horizontal ones through the mass conservation. Therefore, in principle, stronger vertical velocities should result in stronger horizontal ones. Future studies applying GCMs including simplified chemical schemes (similar to the above-mentioned studies) to a wider range of planets will help clarify this aspect. In the long term, coupling a full chemical network to a GCM will hopefully become possible.

A related, but different limitation is that vertical mixing in kinetic models is parametrized as an eddy diffusion coefficient. Zhang et al. (2018); Zhang & Showman (2018b) demonstrate that this approximation is not always valid—the interaction of chemical species with the three-dimensional circulation can produce situations in which they do not behave diffusively. Furthermore, they find that species with different chemical lifetimes can have different eddy diffusivities, an effect that commonly has not been taken into account in the kinetic models.

We therefore stress that even though we use a state-of-the-art modelling approach, our results are meant to provide a first exploration of the extent to which disequilibrium chemistry plays a role on HAT-P-7b. Our results provide an estimate of the importance of disequilibrium abundances and in which regions of the atmosphere deviations from equilibrium chemistry can be expected. The derived disequilibrium abundances should, however, not be taken as exact.

Photochemical hazes: While the formation of photochemical hazes is poorly understood, it is typically assumed (e.g. Rimmer et al. 2013; Gao et al. 2017; Hörst et al. 2018; Edgington et al. 2018; He et al. 2018; West 2018; Kawashima & Ikoma 2018; Helling 2019a; Berry et al. 2019; Krasnopolsky 2020) that the

formation of hydrocarbon-based hazes starts with the photolysis of "haze precursor" molecules such as CH_4, C_2H_2, HCN and C_6H_6. Except for the C_6H_6, all of these species are included in our reaction network and all necessary reactions for these molecules are included in the model. The abundances of these species can thus give a rough sense of the importance of photochemical hazes. Using a combination of a kinetics model and an aerosol microphysics model, Lavvas & Koskinen (2017) found that hazes can be efficiently formed on the relatively cool hot Jupiter, such as HD 189733b. On the hotter HD 209458b, photochemical hazes did not form efficiently enough to affect the predicted transit spectra. Comparing the dayside abundances of CH_4, C_2H_2 and HCN from our kinetic model, we find that the abundances of each of these haze precursor molecules are either comparable to or significantly lower than the abundances in the HD 209458b simulation. We thus conclude that photochemical hazes are even less important for HAT-P-7b. Furthermore, temperatures exceeding 2700(Rimmer et al. 2013).

6.5 Conclusions

In this chapter we investigated the importance of chemical disequilibrium (namely vertical mixing and photochemistry) on an ultra-hot Jupiter, HAT-P-7b, as an example of this class of planets.

We employed two approaches to investigate the quenching levels: a zeroth-order approximation based on Venot et al. (2018) work and full kinetic modeling. While both approaches usually agree with each other, the zeroth-order approximation underestimates the quenching levels at high temperatures by about one order of magnitude.

By performing the chemical kinetic simulations for 38 molecules, we find that the disequilibrium is a local phenomena and affects the nightside and the morning terminator the most for specific molecules like H, H_2O, CH_4, CO_2, HCN, and all C_nH_m molecules; heavier C_nH_m molecules are more affected by disequilibrium processes. For those molecules, the variation of abundances on the dayside is also noticeable but the evening terminator is the least affected region by disequilibrium

processes. This may partially explain the observed transmission spectra of ultra-hot Jupiters to be consistent with thermochemical equilibrium state.

We find that the CO abundance is affected by vertical mixing only marginally, whereas the abundance of other major opacity species such as CH_4, H_2O, and also HCN are influenced by these processes. Photochemistry has almost no effect on the abundance of species considered in this study.

Thanks to the locality characteristic of disequilibrium processes, we propose four avenues to look for the effect of these processes on ultra-hot Jupiters. All four methods are based on comparative retrieval, where local atmospheric properties are retrieved and compared. We, however, caution that clouds will have to be taken into account for any interpretation. In the first method we suggest to investigate vertical opacity distributions between the morning terminator (in transmission) and the sub-stellar point (in emission). The second method is to look for differences observed in transmission spectra between the morning and evening terminators. And the third method is to measure C/O ratio at the two terminators and look for a lack of asymmetry (C/O ratio could deviate by 0.2 between the two limbs if only cloud formation is considered). A similar C/O ratio at the two terminators could indicate that the disequilibrium processes are in action. An enhancement of global observed C/O ratio (by about 0.05 in the case of HAT-P-7b) could also be an indication of cloud formation on this planet. Given the challenging nature of these methods, probably the best chance to observe the effect of clouds and disequilibrium chemistry with the current facilities is using precise phase curves. Through such precision photometry, a longitudinal chemical map of the planet could be constructed as reported by Tan & Komacek (2019); Arcangeli et al. (2019); Mansfield et al. (2019); Wong et al. (2019). Finally, it is worth mentioning that the 3D atmospheric structure of HAT-p-7b and possible geometric expansion of the dayside over the nightside, as described by Caldas et al. (2019), could make the retrieval of these parameters even more challenging. We investigate and discuss the observability of HAT-P-7b's atmosphere and the effects of disequilibrium on it in details in a forthcoming work.

6.6 Supplemental Figures

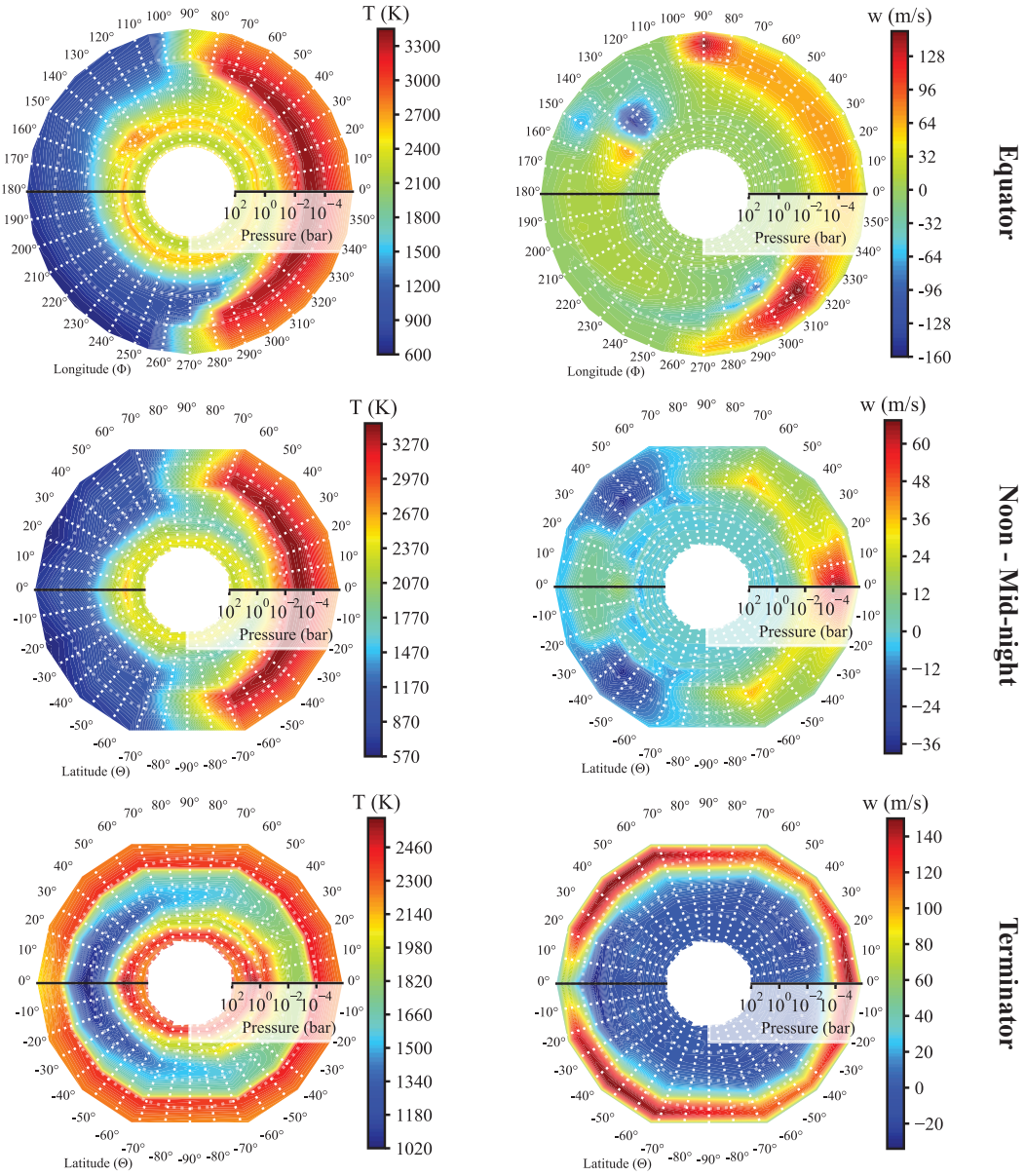

Figure 6.19: Transection maps of temperature (T) and vertical velocities (w) obtained from the GCM solution.

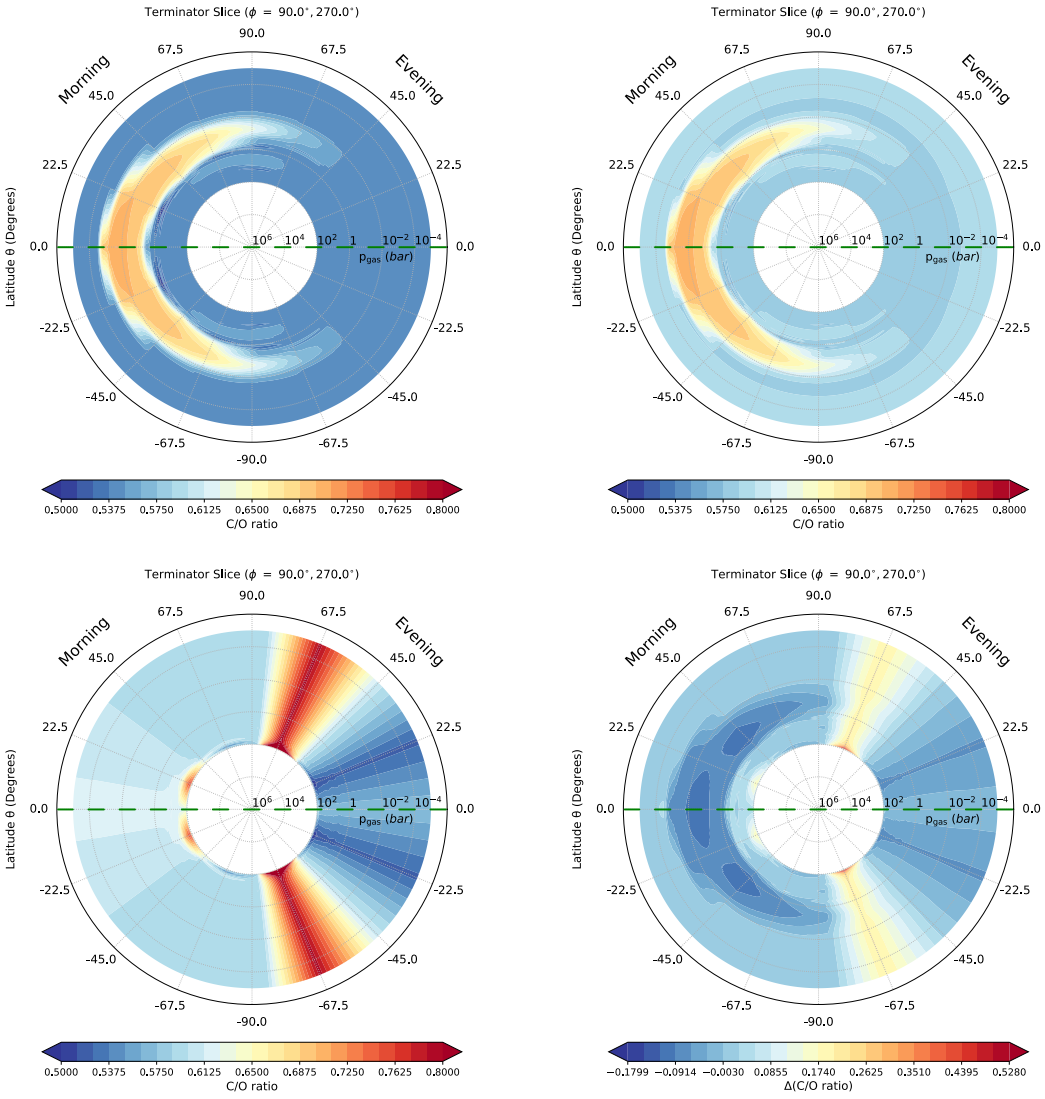

Figure 6.20: The carbon-to-oxygen ratio (C/O) in terminator slices representation: **top left:** C/O after cloud formation as in Helling et al. (2019b) according to ϵ_C/ϵ_O, **top right:** C/O for initial condition of gas-kinetic calculations (from CH, CO, CO_2, $C_2H_2, ...$),, **bottom left:** C/O at end of gas-kinetic calculation (t=300yrs), **bottom right:** C/O change between initial condition (top right) and final gas-kinetic solution (bottom left). See appendix Fig. 6.16 for terminator slice representation.

Sometimes a change of perspective is all it takes to see the light.

— Dan Brown

7 Conclusion & Perspective

Contents

After the discovery of the first exoplanet in 1990's and a fast growing number of discoveries since then, there have been many attempts to observe and characterize their atmospheres. In particular, water and methane have been the focus of many investigations due to their relevance to the origin of life and habitability, as well as their major roles to shape the structure of planetary atmospheres. Abundances retrieved for these species can be also used as a tracer of carbon-to-oxygen ratio (C/O) and metallicity of these atmospheres; hence potentially linking the formation scenarios with the observations. Water's spectral signature is everywhere, but despite many efforts, there has been only one robust detection of methane and only recently. The question is,

"***where is methane?***".

In this thesis we have investigated the role of physicochemical processes in the atmosphere of planets over a wide range of parameter-space. Within the systematic studies published in the literature there has not been a consistent hierarchical investigation of atmospheric physicochemical processes and how they change the atmospheric spectra. This thesis addresses this shortcoming and attempts to connect the sparse observations of exoplanetary atmospheres with a series of large-scale consistent grid of atmospheric models. In this chapter we summarize our results and conclusions and discuss future steps and goals.

7.1 Conclusion

7.1.1 Classification and the Methane Valley

One of the findings in the study of exoplanetary atmospheres is the abundance of water and lack of methane in their transmission spectra. Baed on the thermochemical equilibrium 0D calculations, literature have suggested that the boundary at which a water-dominated atmosphere transitions to a methane-dominated atmosphere depends mostly on the carbon-to-oxygen ratio (C/O) of an atmosphere; expecting this transition to occur around C/O$\sim$1. By using a new technique, "**Spectral Decomposition**", we quantitatively calculated the transition C/O ratios of a large self-consistent grid of cloud-free atmospheric models in chemical equilibrium. We used the latest version of *petitCODE* to perform these calculations.

A broad range of parameter-space is covered in this grid of models; including 400 K<$T_{\rm eff}$<2600 K, 2.0<log(g)<5.0, -1.0<[Fe/H]<2.0, 0.25<C/O<1.25, and stellar types from M to F. We found that the transition C/O could occur at any C/O and not only around unity; depending on many parameters such as effective temperature, surface gravity, metallicity and spectral type of the host star. We found that there are four classes are atmospheric chemistry at the photospheric level of planets and proposed a "**four-class**" classification scheme for irradiated planets in this temperature range.

We reported a parameter space ("**Methane Valley**") where methane always remains the cause of dominant spectral features. Planets belonging to this region

have an effective temperature between 800 and 1500 K and should have a C/O ratio above a certain C/O threshold value. A greater chance of CH_4 detection is expected in the methane valley; making it a potential parameter-space for the future observations focusing on methane. The lack of methane features in the transmission spectra of methane valley planets provides a diagnostic tool to identify the prevalence of cloud formation and non-equilibrium chemistry, which we discuss in the next part. As another diagnostic tool, we constructed synthetic Spitzer IRAC color-diagrams showing two distinguishable populations of planets dominated by CH_4 and CO_2/CO features in their emission spectra.

7.1.2 Disequilibrium chemical processes

However, almost all planetary atmospheres are affected by disequilibrium chemical processes. Thus, the role of these processes on the atmospheric properties was investigated as the next step. We implemented a Chemical Kinetic Model (**`ChemKM`**) to perform such study. We showed that the results of our photochemical models are in good agreement with previously published results (e.g. the case of HD 189733b) and observed abundances (e.g. the case of Uranus and Neptune). While benchmark HD 189733b results, we found that the results could be inconsistent at μbar regime, where molecular diffusion and photochemistry are the dominant processes; demanding a careful consideration of these processes when abundances at the top of the atmosphere are as of interest.

We proposed a new metric, **gCV, geometric coefficient of variation**, for a quantitative measure of quenching levels in the planetary atmospheres. By employing this metric, we found the dependency of the quenching pressure with all atmospheric parameters such as the effective temperature, [Fe/H], log(g), and C/O ratio.

In addition, we found that after including the vertical mixing in the atmospheric models, the Methane Valley still exists. Just a few months after the publication of our prediction, the first robust CH_4 detection on an irradiated planet was announced on HD 102195b. This planet is located within the methane valley and supports our prediction for the existence of such region.

We also proposed a sweet-spot to study the **detectability of disequilibrium spectral fingerprints by JWST**. Atmospheric transmission spectra of planets with T_{eff} between 1000 and 1800 K, orbiting around M-dwarfs, having low surface gravity but high metallicity and a C/O ratio value around unity are susceptible to the vertical mixing the most.

Finally, by constructing Spitzer color-maps based on our disequilibrium grid of models, we found that the main two color-populations (reported in the thermo-chemical equilibrium grid of models) are largely insensitive to the vertical mixing. Consequently, deviation of the observational points from these populations are likely to be an indication of cloud formation on these planets, which is discussed in the next part. In addition, our disequilibrium color-maps show that some cold planets (T_{eff}<900 K) with very low C/O ratios (<0.25) also show significant deviations; making these planets interesting cases for further investigation. GJ 3470 b could be an example of such candidate that has been recently observed by Spitzer.

7.1.3 Clouds

Since most of the exoplanet atmospheres appear cloudy when studied in transmission, we included the radiative feedback of the condensates in the petitCODE to self-consistently calculate the temperature profiles and the composition of atmospheres.

We calculated a large grid of cloudy atmosphere models to investigated the role of clouds in our proposed classification of irradiated gaseous planets and also on the Spitzer color-diagrams. We found that the radiative feedback of the clouds make the lower atmosphere hotter, which in turn cause **methane depletion**. On the other hand, this additional heat results in an abundant of CO and HCN under similar conditions. Therefore, the transmission spectra of hot and carbon-rich atmospheres are predicted to contain **CO and HCN spectral features**. We also proposed to interpret the presence of CO/HCN and lack of CH_4 in the transmission spectra as an indication of cloud formation. Cloud can change the shape of planetary populations in the Spitzer significantly. Hotter planets tend to show less contrast between the two IRAC channels (mainly due to the production of HCN) and

colder planets show a higher dispersion relative to the cloud-free color-diagrams (mainly due to the removal of CH_4 from their atmosphere, production of CO_2 and addition of clouds as ∼gray opacity to both channels). We discussed how cloud formation could explain the observed GJ 3470 b photometric measurements in addition to a possible low C/O ratio.

All the large-scale simulations are performed in 1D, but planets are 3D objects. This simplification is inevitable as the simulation of these three grids of 1D atmospheric models (i.e. cloud-free thermochemical equilibrium, cloud-free disequilibrium, and cloudy thermochemical equilibrium grids) took about three years. Thus, for an investigation of the role of 3D geometry of planets in the properties of atmospheres we chose a case study instead of a parameter-space and systematic study.

7.1.4 Planets are 3D!

We selected an ultra-hot Jupiter (UHJ), HAT-P-7b, to investigate the effect of geometry on the atmospheric properties. UHJs are the hottest known planets. Therefore, by finding any substantial change in the atmospheric composition of HAT-P-7b, the role of planetary geometry in the composition of any planetary atmospheres should not be neglected.

We applied a hierarchical modelling approach utilising 97 1D atmospheric profiles from a 3D General Circulation Model (GCM) of HAT-P-7b. For each atmospheric 1D profile, we evaluated our kinetic cloud formation model consistently with the local gas-phase composition in chemical equilibrium. This served as input to study the quenching of dominating CHNO-binding molecules. We then evaluated quenching results from a zeroth-order approximation in comparison to a kinetic gas-phase approach.

We found that the zeroth-order approach of estimating quenching points agrees well with the full gas-kinetic modeling results. However, it underestimates the quenching levels by about one order of magnitude at high temperatures. Chemical disequilibrium has the greatest effect on the nightside and morning abundance of species such as H, H_2O, CH_4, CO_2, HCN, and all C_nH_m molecules; heavier C_nH_m

molecules are more affected by disequilibrium processes. CO abundance, however, is affected only marginally. While dayside abundances also notably changed, those around the evening terminator of HAT-P-7b are the least affected by disequilibrium processes. The latter finding may partially explain the consistency of observed transmission spectra of UHJs with atmospheres in thermochemical equilibrium.

Photochemistry only negligibly affects molecular abundances and quenching levels. In general, the quenching points of HAT-P-7b's atmosphere are at much lower pressures in comparison to the cooler hot jupiters. We proposed four avenues to look for the effect of disequilibrium processes on UHJs: **(1)** investigating vertical opacity distributions between the morning terminator (in transmission) and the sub-stellar point (in emission) at relevant wavelengths; **(2)** using transmission spectra to look for gradients in observed abundances between the morning and evening terminators; **(3)** measuring the C/O ratio at the two terminators and looking for a lack of asymmetry due to compositional homogenisation of complex molecules; similar C/O ratios at the two terminators could indicate disequilibrium processes are in action but an enhancement of the globally-averaged observed C/O ratio could still be an indication of cloud formation on these planets; and **(4)** high-precision observation of phase curves at different wavelengths are likely to provide the global view needed to distinguish disequilibrium processes on UHJs. It remains a challenge to completely disentangle this from the chemical effects of clouds and that of a primordial non-solar abundance, which demands further investigations.

7.2 Future work

The next steps of the presented work presented include applying the existing models on new cases and further development of the models used in these simulations.

In this work, we briefly reported the results of a few case studies as a verification of the models. The models, however, can be used in a retrieval context as well. For instance, photochemical abundances and other atmospheric properties of planets in the solar system and exoplanets can be retrieved. Currently several such studies

are undergo (such as a study of Titan's atmosphere), which shows the potential of our photochemical model for the future applications.

In addition, there are several avenues which can be taken for further development of the models that were used in this work. As noted, due to the lack of a rainout mechanism in the current version of petitCODE, an overestimation of opacity contribution from the cloud might occur, especially at lower temperatures. Thus the implementation of rainout in petitCODE could be one of the first steps toward a better implementation of physics in our simulations.

Another expansion of the models could be an addition of a second dimension into the models. In particular, the current version of `ChemKM` is unable to consider horizontal mixing. But as discussed, this mixing could be as important as the vertical mixing; potentially changing the results of our photochemical models. Therefore, an expansion of `ChemKM` to 2D to include the effect of horizontal mixing could be a further step in this direction.

Finally, including the radiative feedback of species and condensates in the photochemical model would make the model to be self-consistent in this regard. This implementation, as well as the previously mentioned steps, would be pivotal steps to improve the study of the planetary atmospheres in a systematic way and at large-scale.

Bibliography

Ackerman, A. S. & Marley, M. S. 2001, The Astrophysical Journal, 556, 872

Agúndez, M., Parmentier, V., Venot, O., Hersant, F., & Selsis, F. 2014a, Astronomy & Astrophysics, 564, A73

Agúndez, M., Venot, O., Iro, N., et al. 2012, Astronomy & Astrophysics, 548, A73

Agúndez, M., Venot, O., Selsis, F., & Iro, N. 2014b, The Astrophysical Journal, 781, 68

Airapetian, V. S., Glocer, A., Gronoff, G., Hébrard, E., & Danchi, W. 2016, Nature Geoscience, 9, 452

Allen, L. E., Calvet, N., D'Alessio, P., et al. 2004, The Astrophysical Journal Supplement Series, 154, 363

Allen, M., Yung, Y. L., & Waters, J. W. 1981, Journal of Geophysical Research: Space Physics, 86, 3617

Alonso-Floriano, F. J., Sánchez-López, A., Snellen, I. a. G., et al. 2019, Astronomy & Astrophysics, 621, A74

Anderson, D. R., Cameron, A. C., Delrez, L., et al. 2017, Astronomy & Astrophysics, 604, A110

Angerhausen, D., DeLarme, E., & Morse, J. A. 2015, Publications of the Astronomical Society of the Pacific, 127, 1113

Apai, D., Radigan, J., Buenzli, E., et al. 2013, The Astrophysical Journal, 768, 121

Aplin, K. L. & Harrison, R. G. 2016, Nature Communications, 7, 11976

Arcangeli, J., Desert, J.-M., Parmentier, V., et al. 2019, arXiv:1904.02069 [astro-ph], arXiv: 1904.02069

Arcangeli, J., Désert, J.-M., Line, M. R., et al. 2018, The Astrophysical Journal, 855, L30

Asplund, M., Grevesse, N., Sauval, A. J., & Scott, P. 2009, Annual Review of Astronomy and Astrophysics, 47, 481

Atreya, S. K., Mahaffy, P. R., Niemann, H. B., Wong, M. H., & Owen, T. C. 2003, Planetary and Space Science, 51, 105

Atreya, S. K., Mahaffy, P. R., & Wong, A.-S. 2007, Planetary and Space Science, 55, 358

Atreya, S. K., Pollack, J. B., & Matthews, M. S. 1989, Origin and Evolution of Planetary and Satellite Atmospheres (University of Arizona Press)

Atreya, S. K., Wong, M. H., Owen, T. C., et al. 1999, Planetary and Space Science, 47, 1243

Badhan, M. A., Wolf, E. T., Kopparapu, R. K., et al. 2019, arXiv:1902.04086 [astro-ph], arXiv: 1902.04086

Bailey, R. L., Helling, C., Hodosán, G., Bilger, C., & Stark, C. R. 2014, The Astrophysical Journal, 784, 43

Ballard, S., Fabrycky, D., Fressin, F., et al. 2011, The Astrophysical Journal, 743, 200

Barge, P., Baglin, A., Auvergne, M., et al. 2008, Astronomy & Astrophysics, 482, L17

Barman, T. S., Macintosh, B., Konopacky, Q. M., & Marois, C. 2011, The Astrophysical Journal, 735, L39

Batalha, N. E., Mandell, A., Pontoppidan, K., et al. 2017, Publications of the Astronomical Society of the Pacific, 129, 064501

Batalha, N. E., Smith, A. J. R. W., Lewis, N. K., et al. 2018, The Astronomical Journal, 156, 158

Baudino, J.-L., Bézard, B., Boccaletti, A., et al. 2015, Astronomy & Astrophysics, 582, A83

Baudino, J.-L., Mollière, P., Venot, O., et al. 2017, The Astrophysical Journal, 850, 150

Baxter, C., Désert, J.-M., Todorov, K., et al. 2018, in Exoplanet II, Vol. 51, Cambridge, UK, 313.08

Bazilevskaya, G. 2000, Space Science Reviews, 94, 25

Beichman, C., Benneke, B., Knutson, H., et al. 2014, Publications of the Astronomical Society of the Pacific, 126, 1134

Bell, T. J. & Cowan, N. B. 2018, The Astrophysical Journal, 857, L20

Benneke, B., Knutson, H. A., Lothringer, J., et al. 2019, Nature Astronomy, 3, 813

Benneke, B. & Seager, S. 2013, The Astrophysical Journal, 778, 153

Berry, J. L., Ugelow, M. S., Tolbert, M. A., & Browne, E. C. 2019, ACS Earth and Space Chemistry, 3, 202

Berta, Z. K., Charbonneau, D., Désert, J.-M., et al. 2012, The Astrophysical Journal, 747, 35

Bethell, T. & Bergin, E. 2009, Science, 326, 1675

Beuzit, J.-L., Feldt, M., Dohlen, K., et al. 2008, in Ground-based and Airborne Instrumentation for Astronomy II, Vol. 7014 (International Society for Optics and Photonics), 701418

Biller, B. A. & Bonnefoy, M. 2017, in Handbook of Exoplanets, ed. H. J. Deeg & J. A. Belmonte (Cham: Springer International Publishing), 1–28

Birkby, J. L., de Kok, R. J., Brogi, M., et al. 2013, Monthly Notices of the Royal Astronomical Society: Letters, 436, L35

Bishop, J., Atreya, S. K., Herbert, F., & Romani, P. 1990, Icarus, 88, 448

Bishop, J., Romani, P. N., & Atreya, S. K. 1998, Planetary and Space Science, 46, 1

Blumenthal, S. D., Mandell, A. M., Hébrard, E., et al. 2018, The Astrophysical Journal, 853, 138

Bonfils, X., Astudillo-Defru, N., Díaz, R., et al. 2018, Astronomy & Astrophysics, 613, A25

Bonnefoy, M., Chauvin, G., Lagrange, A.-M., et al. 2014a, Astronomy & Astrophysics, 562, A127

Bonnefoy, M., Marleau, G.-D., Galicher, R., et al. 2014b, Astronomy & Astrophysics, 567, L9

Borysow, A. & Frommhold, L. 1989, The Astrophysical Journal, 341, 549

Borysow, A., Frommhold, L., & Moraldi, M. 1989, The Astrophysical Journal, 336, 495

Bova, B. 1971, The many worlds of science fiction (E. P. Dutton), google-Books-ID: kZgiAQAAIAAJ

Bowyer, S., Lieu, R., Lampton, M., et al. 1994, The Astrophysical Journal Supplement Series, 93, 569

Brain, D. A., McFadden, J. P., Halekas, J. S., et al. 2015, Geophysical Research Letters, 9142

Brogi, M., Giacobbe, P., Guilluy, G., et al. 2018, Astronomy & Astrophysics, 615, A16

Brogi, M., Kok, R. J. d., Albrecht, S., et al. 2016, The Astrophysical Journal, 817, 106

Brogi, M., Line, M., Bean, J., Désert, J.-M., & Schwarz, H. 2017, The Astrophysical Journal, 839, L2

Brown, H. 1950, The Astrophysical Journal, 111, 641

Burgdorf, M., Orton, G., van Cleve, J., Meadows, V., & Houck, J. 2006, Icarus, 184, 634

Burke, C. J., Christiansen, J. L., Mullally, F., et al. 2015, The Astrophysical Journal, 809, 8

Burrows, A. & Sharp, C. M. 1999, The Astrophysical Journal, 512, 843

Cabannes, J. & Rocard, Y. 1929, J. Phys. Radium, 10, 52

Caldas, A., Leconte, J., Selsis, F., et al. 2019, arXiv:1901.09932 [astro-ph], arXiv: 1901.09932

Calvert, J. G. 1990, Pure and Applied Chemistry, 62, 2167

Capone, L. A., Dubach, J., Prasad, S. S., & Whitten, R. C. 1983, Icarus, 55, 73

Casasayas-Barris, N., Palle, E., Nowak, G., et al. 2017, Astronomy & Astrophysics, 608, A135

Casasayas-Barris, N., Pallé, E., Yan, F., et al. 2019, Astronomy & Astrophysics, 628, A9

Catling, D. C., Zahnle, K. J., & McKay, C. P. 2001, Science, 293, 839

Chachan, Y., Knutson, H. A., Gao, P., et al. 2019, arXiv:1910.07523 [astro-ph], arXiv: 1910.07523

Chandrasekhar, S. 1950, Radiative transfer. (Oxford University Press)

Changeat, Q., Edwards, B., Waldmann, I., & Tinetti, G. 2019, arXiv:1903.11180 [astro-ph], arXiv: 1903.11180

Charbonneau, D., Allen, L. E., Megeath, S. T., et al. 2005, The Astrophysical Journal, 626, 523

Charbonneau, D., Brown, T. M., Latham, D. W., & Mayor, M. 1999, The Astrophysical Journal Letters, 529, L45

Charpinet, S., Fontaine, G., Brassard, P., et al. 2011, Nature, 480, 496

Chilcote, J., Pueyo, L., Rosa, R. J. D., et al. 2017, The Astronomical Journal, 153, 182

Clancy, R. T. & Sandor, B. J. 1998, Geophysical Research Letters, 25, 489

Clanton, C. & Gaudi, B. S. 2014, The Astrophysical Journal, 791, 91

Clanton, C. & Gaudi, B. S. 2016, The Astrophysical Journal, 819, 125

Conrath, B., Gautier, D., Hanel, R., Lindal, G., & Marten, A. 1987, Journal of Geophysical Research: Space Physics, 92, 15003

Cooper, C. S. & Showman, A. P. 2006, The Astrophysical Journal, 649, 1048

Cowan, N. B. & Fujii, Y. 2017, in Handbook of Exoplanets, ed. H. J. Deeg & J. A. Belmonte (Cham: Springer International Publishing), 1–16

Cox, A. J., DeWeerd, A. J., & Linden, J. 2002, American Journal of Physics, 70, 620

Cridland, A. J., van Dishoeck, E. F., Alessi, M., & Pudritz, R. E. 2019, arXiv:1910.13171 [astro-ph], arXiv: 1910.13171

Cumming, A., Butler, R. P., Marcy, G. W., et al. 2008, Publications of the Astronomical Society of the Pacific, 120, 531

Currie, T., Burrows, A., Itoh, Y., et al. 2011, The Astrophysical Journal, 729, 128

Danielson, R. E. S. 1968, in Infrared Astronomy, APR. 1-2, 1966

Dawson, R. I. & Murray-Clay, R. A. 2013, The Astrophysical Journal, 767, L24

de Pater, I., Romani, P. N., & Atreya, S. K. 1991, Icarus, 91, 220

Deeg, H. J. & Alonso, R. 2018, in Handbook of Exoplanets, ed. H. J. Deeg & J. A. Belmonte (Cham: Springer International Publishing), 1–25

Delrez, L., Madhusudhan, N., Lendl, M., et al. 2018, Monthly Notices of the Royal Astronomical Society, 474, 2334

Demarcus, W. C. & Reynolds, R. T. 1963, in La Physique des Planetes, Vol. 11 (Belgique: Institut d'Astrophysique Cointe-Solessin), 51–64

Deming, D., Harrington, J., Laughlin, G., et al. 2007, The Astrophysical Journal Letters, 667, L199

Dencs, Z. & Regály, Z. 2019, arXiv:1905.11298 [astro-ph], arXiv: 1905.11298

Diamond-Lowe, H., Stevenson, K. B., Bean, J. L., Line, M. R., & Fortney, J. J. 2014, The Astrophysical Journal, 796, 66

Divine, N. 1974, Titan atmosphere models, 1973. [Saturn satellite], Tech. rep.

Divine, N. P. 1972, SEE N72-31964 22-34, p. p 1

Dobbs-Dixon, I. & Cowan, N. B. 2017, The Astrophysical Journal Letters, 851, L26

Dobrijevic, M., Cavalié, T., Hébrard, E., et al. 2010, Planetary and Space Science, 58, 1555

Dobrijevic, M., Hébrard, E., Loison, J. C., & Hickson, K. M. 2014, Icarus, 228, 324

Dressing, C. D. & Charbonneau, D. 2015, The Astrophysical Journal, 807, 45

Drummond, B., Mayne, N. J., Baraffe, I., et al. 2018a, Astronomy & Astrophysics, 612, A105

Drummond, B., Mayne, N. J., Manners, J., et al. 2018b, The Astrophysical Journal, 869, 28

Drummond, B., Mayne, N. J., Manners, J., et al. 2018c, The Astrophysical Journal, 855, L31

Drummond, B., Tremblin, P., Baraffe, I., et al. 2016, Astronomy & Astrophysics, 594, A69

Dunne, J. A. & Burgess, E. 1978, The Voyage of Mariner 10: Missions to Venus and Mercury (National Aeronautics and Space Administration), google-Books-ID: epY9AQAAMAAJ

Dvortsov, V. L., Zvenigorodsky, S. G., & Smyslaev, S. P. 1992, Journal of Geophysical Research: Atmospheres, 97, 7593

Désert, J.-M., Des Etangs, A. L., Hébrard, G., et al. 2009, The Astrophysical Journal, 699, 478

Ebbing, D. & Gammon, S. D. 2016, General Chemistry (Cengage Learning), google-Books-ID: mylTCwAAQBAJ

Eck, S. V., Neyskens, P., Jorissen, A., et al. 2017, Astronomy & Astrophysics, 601, A10

Edgington, S., Atreya, S. K., Baines, K., et al. 2018, 42nd COSPAR Scientific Assembly, 42, C3.1

Encrenaz, T., Tinetti, G., Tessenyi, M., et al. 2015, Experimental Astronomy, 40, 523

Encrenaz, T. H. 1974, Observational constraints on model atmospheres for Uranus and Neptune

Eriksson, K., Gustafsson, B., Jorgensen, U. G., & Nordlund, A. 1984, Astronomy and Astrophysics, 132, 37

Espinoza, N., Fortney, J. J., Miguel, Y., Thorngren, D., & Murray-Clay, R. 2017, The Astrophysical Journal Letters, 838, L9

Evans, T. M., Sing, D. K., Wakeford, H. R., et al. 2016, The Astrophysical Journal Letters, 822, L4

Fazio, G. G., Hora, J. L., Allen, L. E., et al. 2004, The Astrophysical Journal Supplement Series, 154, 10

Ferruit, P., Birkmann, S., Böker, T., et al. 2014, in Space Telescopes and Instrumentation 2014: Optical, Infrared, and Millimeter Wave, Vol. 9143 (International Society for Optics and Photonics), 91430A

Fischer, D. A. & Valenti, J. 2005, The Astrophysical Journal, 622, 1102

Fletcher, L., Encrenaz, T., Orton, G., Moses, J., & Rowe-Gurney, N. 2018, in , B5.4–4–18

Fortney, J. J. 2005, Monthly Notices of the Royal Astronomical Society, 364, 649

Fortney, J. J. 2018, in Astrophysics of Exoplanetary Atmospheres: 2nd Advanced School on Exoplanetary Science, ed. V. Bozza, L. Mancini, & A. Sozzetti, Astrophysics and Space Science Library (Cham: Springer International Publishing), 51–88

Fortney, J. J., Lodders, K., Marley, M. S., & Freedman, R. S. 2008, The Astrophysical Journal, 678, 1419

Fortney, J. J., Marley, M. S., Lodders, K., Saumon, D., & Freedman, R. 2005, The Astrophysical Journal Letters, 627, L69

Fortney, J. J., Saumon, D., Marley, M. S., Lodders, K., & Freedman, R. S. 2006, The Astrophysical Journal, 642, 495

Fortney, J. J., Shabram, M., Showman, A. P., et al. 2010, The Astrophysical Journal, 709, 1396

Fortney, J. J., Sudarsky, D., Hubeny, I., et al. 2003, The Astrophysical Journal, 589, 615

Fraine, J., Deming, D., Benneke, B., et al. 2014, Nature, 513, 526

France, K., Loyd, R. O. P., Youngblood, A., et al. 2016, The Astrophysical Journal, 820, 89

Gao, P., Fan, S., Wong, M. L., et al. 2017, Icarus, 287, 116

Geballe, T. R., Saumon, D., Golimowski, D. A., et al. 2009, The Astrophysical Journal, 695, 844

Giguere, M. J., Fischer, D. A., Payne, M. J., et al. 2015, The Astrophysical Journal, 799, 89

Gilbert, R. G., Luther, K., & Troe, J. 1983, Berichte der Bunsengesellschaft für physikalische Chemie, 87, 169

Gladstone, G. R., Stern, S. A., Ennico, K., et al. 2016, Science, 351, aad8866

Glasby, G. P. 2006, Resource Geology, 56, 83

Glavin, D. P., Alexander, C. M. O., Aponte, J. C., et al. 2018, in Primitive Meteorites and Asteroids, ed. N. Abreu (Elsevier), 205–271

Goethe, J. W. v. 1821, Wilhelm Meisters Wanderjahre, oder, Die Entsagenden: ein Roman (In der Cotta'schen Buchhandlung), google-Books-ID: 7tkFAAAAQAAJ

Gould, A., Udalski, A., An, D., et al. 2006, The Astrophysical Journal, 644, L37

Goyal, J. M., Mayne, N., Sing, D. K., et al. 2017, Monthly Notices of the Royal Astronomical Society, 474, 5158

Greene, T. P., Line, M. R., Montero, C., et al. 2016, The Astrophysical Journal, 817, 17

Griffith, C. A. & Yelle, R. V. 1999, The Astrophysical Journal, 519, L85

Guerlet, S., Fouchet, T., & Bézard, B. 2008, SF2A-2008, 405

Guillot, T. 1999, Planetary and Space Science, 47, 1183

Guillot, T. 2010, Astronomy & Astrophysics, 520, A27

Guillot, T. 2019, arXiv:1908.02092 [astro-ph], arXiv: 1908.02092

Guillot, T., Atreya, S., Charnoz, S., Dougherty, M. K., & Read, P. 2009, in Saturn from Cassini-Huygens, ed. M. K. Dougherty, L. W. Esposito, & S. M. Krimigis (Dordrecht: Springer Netherlands), 745–761

Guilluy, G., Sozzetti, A., Brogi, M., et al. 2019, arXiv:1904.04170 [astro-ph], arXiv: 1904.04170

Gustafsson, B., Edvardsson, B., Eriksson, K., et al. 2008, Astronomy & Astrophysics, 486, 951

Hamren, K., Beaton, R. L., Guhathakurta, P., et al. 2016, The Astrophysical Journal, 828, 15

Hasenberg, D. & Schmidt, L. D. 1987, Journal of Catalysis, 104, 441

Hauschildt, P. H., Allard, F., Ferguson, J., Baron, E., & Alexander, D. R. 1999, The Astrophysical Journal, 525, 871, arXiv: astro-ph/9907194

Hawkes, R. L., Milley, E. P., Ehrman, J. M., et al. 2008, in Advances in Meteoroid and Meteor Science, ed. J. M. Trigo-Rodríguez, F. J. M. Rietmeijer, J. Llorca, & D. Janches (New York, NY: Springer New York), 331–336

Haynes, K., Mandell, A. M., Madhusudhan, N., Deming, D., & Knutson, H. 2015, The Astrophysical Journal, 806, 146

Haynes, W. M. 2016, CRC Handbook of Chemistry and Physics, 97th edn. (CRC Press), google-Books-ID: bNDMBQAAQBAJ

He, C., Hörst, S. M., Lewis, N. K., et al. 2018, The Astronomical Journal, 156, 38

Hebb, L., Collier-Cameron, A., Loeillet, B., et al. 2009, The Astrophysical Journal, 693, 1920

Helling, C. 2008, in Extreme Solar Systems, Vol. 398, eprint: arXiv:0711.3730, 443

Helling, C. 2019a, Annual Review of Earth and Planetary Sciences, 47, null

Helling, C. 2019b, arXiv:1910.12722 [astro-ph, physics:physics], arXiv: 1910.12722

Helling, C., Gourbin, P., Woitke, P., & Parmentier, V. 2019a, arXiv:1901.08640 [astro-ph], arXiv: 1901.08640

Helling, C., Iro, N., Corrales, L., et al. 2019b, arXiv:1906.08127 [astro-ph], arXiv: 1906.08127

Helling, C., Jardine, M., & Mokler, F. 2011, The Astrophysical Journal, 737, 38

Helling, C., Jorgensen, U. G., Plez, B., & Johnson, H. R. 1996, Astronomy and Astrophysics, 315, 194

Helling, C., Woitke, P., Rimmer, P. B., et al. 2014, Life, 4, 142

Heng, K. 2018, Research Notes of the AAS, 2, 128

Heng, K. & Demory, B.-O. 2013, The Astrophysical Journal, 777, 100

Heng, K. & Lyons, J. R. 2016, The Astrophysical Journal, 817, 149

Henning, T. & Semenov, D. 2013, Chemical Reviews, 113, 9016

Hindmarsh, A. C. 1983, Scientific Computing, 1, 55

Hodosán, G., Helling, C., & Rimmer, P. B. 2018, PLANETARY RADIO EMISSIONS VIII, 345, arXiv: 1711.08053

Hoeijmakers, H. J., Ehrenreich, D., Heng, K., et al. 2018, Nature, 560, 453

Hoeijmakers, H. J., Ehrenreich, D., Kitzmann, D., et al. 2019, arXiv:1905.02096 [astro-ph], arXiv: 1905.02096

Hofstdater, m., Simon, A., Reth, K., & Elliot, J. 2017, Ice Giants Mission Planning, NASA Mission Study JPL D-100520, Solar System Exploration Directorate Jet Propulsion Laboratory

Homeier, D., Allard, F., Hauschildt, P. H., et al. 2005, in High Resolution Infrared Spectroscopy in Astronomy, ed. H. U. Käufl, R. Siebenmorgen, & A. F. M. Moorwood, ESO Astrophysics Symposia (Springer Berlin Heidelberg), 465–476

Hron, J., Loidl, R., Hoefner, S., et al. 1998, Astronomy and Astrophysics, 335, L69

Hu, R. 2014

Hu, R., Bloom, A. A., Gao, P., Miller, C. E., & Yung, Y. L. 2016, Astrobiology, 16, 539

Hu, R. & Seager, S. 2014, The Astrophysical Journal, 784, 63

Hu, R., Seager, S., & Bains, W. 2012, The Astrophysical Journal, 761, 166

Hu, R., Seager, S., & Bains, W. 2013, The Astrophysical Journal, 769, 6

Hubeny, I. 2017, Monthly Notices of the Royal Astronomical Society, 469, 841

Huitson, C. M., Sing, D. K., Vidal-Madjar, A., et al. 2012, Monthly Notices of the Royal Astronomical Society, 422, 2477

Humboldt, A. v., Paul, B. H., & Dallas, W. S. 1852, Cosmos: a sketch of a physical description of the universe (Harper), google-Books-ID: UrSHpOprOIYC

Hunten, D. M. 1982, Planetary and Space Science, 30, 773

Husser, T.-O., von Berg, S. W., Dreizler, S., et al. 2013, Astronomy & Astrophysics, 553, A6, arXiv: 1303.5632

Hébrard, E., Dobrijevic, M., Loison, J. C., Bergeat, A., & Hickson, K. M. 2012, Astronomy & Astrophysics, 541, A21

Hébrard, E., Dobrijevic, M., Loison, J. C., et al. 2013, Astronomy & Astrophysics, 552, A132

Hörst, S. M., He, C., Lewis, N. K., et al. 2018, Nature Astronomy, 2, 303

Hörst, S. M., Vuitton, V., & Yelle, R. V. 2008, Journal of Geophysical Research: Planets, 113

Irwin, P. G. J., Parmentier, V., Taylor, J., et al. 2019a, arXiv:1909.03233 [astro-ph], arXiv: 1909.03233

Irwin, P. G. J., Toledo, D., Garland, R., et al. 2018, Nature Astronomy, 2, 420

Irwin, P. G. J., Toledo, D., Garland, R., et al. 2019b, Icarus, 321, 550

Isaksen, I. S. A., Midtbo, K. H., Sunde, J., & Crutzen, P. J. 1977, Geophysica Norvegica, 31, 11

Jakosky, B. M., Grebowsky, J. M., Luhmann, J. G., & Brain, D. A. 2015, Geophysical Research Letters, 42, 8791

Jasper, A. W., Klippenstein, S. J., Harding, L. B., & Ruscic, B. 2007, The Journal of Physical Chemistry A, 111, 3932

Jensen, A. G., Redfield, S., Endl, M., et al. 2011, The Astrophysical Journal, 743, 203

Kataria, T., Showman, A. P., Fortney, J. J., et al. 2015, The Astrophysical Journal, 801, 86

Kawashima, Y., Hu, R., & Ikoma, M. 2019, arXiv:1902.10151 [astro-ph], arXiv: 1902.10151

Kawashima, Y. & Ikoma, M. 2018, The Astrophysical Journal, 853, 7

Keating, D. & Cowan, N. B. 2018, arXiv:1809.00002 [astro-ph], arXiv: 1809.00002

Kee, R. J., Rupley, F., & Miller, M. 1989, Sandia National Laboratories Report

Keller-Rudek, H., Moortgat, G. K., Sander, R., & Sörensen, R. 2013, Earth System Science Data, 5, 365

Kempton, E. M.-R., Bean, J. L., & Parmentier, V. 2017, The Astrophysical Journal Letters, 845, L20

Keppler, M., Benisty, M., Müller, A., et al. 2018, Astronomy & Astrophysics

Kerley, G. I. 2013, arXiv:1307.3094 [astro-ph], arXiv: 1307.3094

Kirk, J., Lopez-Morales, M., Wheatley, P. J., et al. 2019, arXiv:1908.02358 [astro-ph], arXiv: 1908.02358

Kite, E. S., Mischna, M. A., Gao, P., Yung, Y. L., & Turbet, M. 2019, arXiv:1709.08302 [astro-ph], arXiv: 1709.08302

Kitzmann, D., Heng, K., Rimmer, P. B., et al. 2018, The Astrophysical Journal, 863, 183

Kneer, F. 1987, in Solar and Stellar Physics, ed. E.-H. Schröter & M. Schüssler, Lecture Notes in Physics (Berlin, Heidelberg: Springer), 157–172

Knutson, H. A., Charbonneau, D., Cowan, N. B., et al. 2009, The Astrophysical Journal, 690, 822

Knutson, H. A., Lewis, N., Fortney, J. J., et al. 2012, The Astrophysical Journal, 754, 22

Komacek, T. D. & Showman, A. P. 2016, The Astrophysical Journal, 821, 16

Komacek, T. D., Showman, A. P., & Parmentier, V. 2019, The Astrophysical Journal, 881, 152

Komacek, T. D., Showman, A. P., & Tan, X. 2017, The Astrophysical Journal, 835, 198

Komacek, T. D. & Tan, X. 2018, arXiv:1805.07415 [astro-ph, physics:physics], arXiv: 1805.07415

Kotz, J. C., Treichel, P. M., Townsend, J., & Treichel, D. 2014, Chemistry & Chemical Reactivity (Cengage Learning), google-Books-ID: i1g8AwAAQBAJ

Krasnopolsky, V. A. 2020, Icarus, 335, 113374

Krasnopolsky, V. A., Maillard, J. P., & Owen, T. C. 2004, Icarus, 172, 537

Kreidberg, L. 2017, in Handbook of Exoplanets, ed. H. J. Deeg & J. A. Belmonte (Cham: Springer International Publishing), 1–23

Kreidberg, L., Bean, J. L., Désert, J.-M., et al. 2014a, Nature, 505, 69

Kreidberg, L., Bean, J. L., Désert, J.-M., et al. 2014b, The Astrophysical Journal Letters, 793, L27

Kreidberg, L., Line, M. R., Bean, J. L., et al. 2015, arXiv:1504.05586 [astro-ph], arXiv: 1504.05586

Kreidberg, L., Line, M. R., Parmentier, V., et al. 2018a, The Astronomical Journal, 156, 17

Kreidberg, L., Line, M. R., Thorngren, D., Morley, C. V., & Stevenson, K. B. 2018b, The Astrophysical Journal Letters, 858, L6

Kuchner, M. J. & Seager, S. 2005, arXiv preprint astro-ph/0504214

L'Amour, L. 1984, Lonely on the Mountain (Bantam Books), google-Books-ID: InU4oBoIdxAC

Lavvas, P., Griffith, C. A., & Yelle, R. V. 2011, Icarus, 215, 732

Lavvas, P. & Koskinen, T. 2017, The Astrophysical Journal, 847, 32

Lecavelier des Etangs, A., Pont, F., Vidal-Madjar, A., & Sing, D. 2008, Astronomy & Astrophysics, 481, L83

Lellouch, E., Bézard, B., Moses, J. I., et al. 2002, Icarus, 159, 112

Lellouch, E., Moreno, R., & Paubert, G. 2005, Astronomy & Astrophysics, 430, L37

Lellouch, E., Romani, P. N., & Rosenqvist, J. 1994, Icarus, 108, 112

Lettau, H. 1951, in Compendium of Meteorology: Prepared under the Direction of the Committee on the Compendium of Meteorology, ed. H. R. Byers, H. E. Landsberg, H. Wexler, B. Haurwitz, A. F. Spilhaus, H. C. Willett, H. G. Houghton, & T. F. Malone (Boston, MA: American Meteorological Society), 320–333

Lewis, N. K., Showman, A. P., Fortney, J. J., et al. 2010, The Astrophysical Journal, 720, 344

Line, M. R., Knutson, H., Wolf, A. S., & Yung, Y. L. 2014, The Astrophysical Journal, 783, 70

Line, M. R., Liang, M. C., & Yung, Y. L. 2010, The Astrophysical Journal, 717, 496

Line, M. R., Marley, M. S., Liu, M. C., et al. 2017, The Astrophysical Journal, 848, 83

Line, M. R., Stevenson, K. B., Bean, J., et al. 2016, The Astronomical Journal, 152, 203, arXiv: 1605.08810

Line, M. R., Vasisht, G., Chen, P., Angerhausen, D., & Yung, Y. L. 2011, The Astrophysical Journal, 738, 32

Line, M. R., Wolf, A. S., Zhang, X., et al. 2013, The Astrophysical Journal, 775, 137

Liou, K. N. 2002, An Introduction to Atmospheric Radiation (Elsevier), google-Books-ID: mQ1DiDpX34UC

Lodders, K. 2010, in Formation and Evolution of Exoplanets (John Wiley & Sons, Ltd), 157–186

Lodders, K. & Fegley, B. 2002, Icarus, 155, 393

Lodders, K. & Fegley, B. 2006, in Astrophysics Update 2, ed. J. W. Mason, Springer Praxis Books (Berlin, Heidelberg: Springer Berlin Heidelberg), 1–28

Lothringer, J. D., Barman, T., & Koskinen, T. 2018, The Astrophysical Journal, 866, 27, arXiv: 1805.00038

Lothringer, J. D. & Barman, T. S. 2019, arXiv:1903.12183 [astro-ph], arXiv: 1903.12183

Lou, G. Y. 1973, Models of earth's atmosphere (90 to 2500 km), Tech. rep.

Lunine, J. I. 1993, Annual Review of Astronomy and Astrophysics, 31, 217

Lunine, J. I., Hubbard, W. B., Burrows, A., Wang, Y.-P., & Garlow, K. 1989, The Astrophysical Journal, 338, 314

Luszcz-Cook, S. H. & de Pater, I. 2013, Icarus, 222, 379

Luther, F. M. 1980, Annual Report of Lawrence Livermore National Laboratory to the Federal Aviation Administration on the High Altitude Pollution Program - 1980., Tech. Rep. UCRL-50042-80, LAWRENCE LIVERMORE NATIONAL LAB CA

MacDonald, R. J. & Madhusudhan, N. 2017, The Astrophysical Journal, 850, L15

Macintosh, B., Graham, J. R., Barman, T., et al. 2015, Science, 350, 64

Macintosh, B., Graham, J. R., Ingraham, P., et al. 2014, Proceedings of the National Academy of Sciences, 111, 12661

Madhusudhan, N. 2012, The Astrophysical Journal, 758, 36

Madhusudhan, N. 2019, arXiv:1904.03190 [astro-ph], arXiv: 1904.03190

Madhusudhan, N., Amin, M. A., & Kennedy, G. M. 2014a, The Astrophysical Journal, 794, L12

Madhusudhan, N., Burrows, A., & Currie, T. 2011, The Astrophysical Journal, 737, 34

Madhusudhan, N., Crouzet, N., McCullough, P. R., Deming, D., & Hedges, C. 2014b, The Astrophysical Journal, 791, L9

Madhusudhan, N., Knutson, H., Fortney, J., & Barman, T. 2014c, arXiv:1402.1169 [astro-ph], arXiv: 1402.1169

Madhusudhan, N. & Seager, S. 2009, The Astrophysical Journal, 707, 24

Madhusudhan, N. & Seager, S. 2011, The Astrophysical Journal, 729, 41

Mancini, L., Giordano, M., Mollière, P., et al. 2016, Monthly Notices of the Royal Astronomical Society, 461, 1053

Mancini, L., Southworth, J., Ciceri, S., et al. 2013, Astronomy & Astrophysics, 551, A11

Mansfield, M., Bean, J. L., Line, M. R., et al. 2018, The Astronomical Journal, 156, 10

Mansfield, M., Bean, J. L., Stevenson, K. B., et al. 2019, arXiv:1910.01567 [astro-ph], arXiv: 1910.01567

Marley, M. & Robinson, T. 2015, Annual Review of Astronomy and Astrophysics, 53, 279

Marley, M. S., Saumon, D., Cushing, M., et al. 2012, The Astrophysical Journal, 754, 135

Marley, M. S., Seager, S., Saumon, D., et al. 2002, The Astrophysical Journal, 568, 335

Marshall, J. & Plumb, R. A. 2013, Theory of Planetary Atmospheres: An Introduction to Their Physics and Chemistry (Academic Press), google-Books-ID: KiTLCQAAQBAJ

Martins, J. H. C., Figueira, P., Santos, N. C., & Lovis, C. 2013, Monthly Notices of the Royal Astronomical Society, 436, 1215

Martins, J. H. C., Santos, N. C., Figueira, P., et al. 2015, Astronomy & Astrophysics, 576, A134

Mayor, M., Marmier, M., Lovis, C., et al. 2011, arXiv:1109.2497 [astro-ph], arXiv: 1109.2497

Mayor, M. & Queloz, D. 1995, Nature, 378, 355

McBride, B. J., Zehe, M. J., & Gordon, S. 2002, NASA Glenn Coefficients for Calculating Thermodynamic Properties of Individual Species, Technical Paper E-13336, NASA, National Aeronautics and Space Administration John H. Glenn Research Center at Lewis Field Cleveland, Ohio 44135-3191

Mendonça, J. M., Tsai, S.-M., Matej, M., Grimm, S. L., & Heng, K. 2018, arXiv:1808.00501 [astro-ph], arXiv: 1808.00501

Miguel, Y. & Kaltenegger, L. 2014, The Astrophysical Journal, 780, 166

Miguel, Y., Kaltenegger, L., Linsky, J. L., & Rugheimer, S. 2014, Monthly Notices of the Royal Astronomical Society, 446, 345

Miller, N. & Fortney, J. J. 2011, The Astrophysical Journal Letters, 736, L29

Miller, S., Aylward, A., & Millward, G. 2005, Space Science Reviews, 116, 319

Molaverdikhani, K. 2010, arXiv preprint arXiv:1002.4025

Molaverdikhani, K., Henning, T., & Mollière, P. 2019a, The Astrophysical Journal, 883, 194, arXiv: 1908.09847

Molaverdikhani, K., Henning, T., & Mollière, P. 2019b, The Astrophysical Journal, 873, 32

Molaverdikhani, K., McGouldrick, K., & Esposito, L. W. 2012, Icarus, 217, 648

Molaverdikhani, K. & Tabeshian, M. 2009, arXiv preprint arXiv:0911.4424

Molina-Cuberos, G. J., López-Moreno, J. J., Rodrigo, R., Lara, L. M., & O'Brien, K. 1999, Planetary and Space Science, 47, 1347

Mollière, P., Boekel, R. v., Bouwman, J., et al. 2017, Astronomy & Astrophysics, 600, A10

Mollière, P. & Snellen, I. A. G. 2018, arXiv:1809.01156 [astro-ph], arXiv: 1809.01156

Mollière, P., van Boekel, R., Dullemond, C., Henning, T., & Mordasini, C. 2015, The Astrophysical Journal, 813, 47

Mollière, P., Wardenier, J. P., van Boekel, R., et al. 2019, arXiv:1904.11504 [astro-ph], arXiv: 1904.11504

Mollière, P. M. 2017, PhD Thesis, Heidelberg University

Mordasini, C., Boekel, R. v., Mollière, P., Henning, T., & Benneke, B. 2016, The Astrophysical Journal, 832, 41

Morley, C. V., Fortney, J. J., Marley, M. S., et al. 2012, The Astrophysical Journal, 756, 172

Moses, J. I. 1991, phd, California Institute of Technology

Moses, J. I. 1992, Icarus, 99, 368

Moses, J. I. 2014, Phil. Trans. R. Soc. A, 372, 20130073

Moses, J. I., Bézard, B., Lellouch, E., et al. 2000a, Icarus, 143, 244

Moses, J. I., Fletcher, L. N., Greathouse, T. K., Orton, G. S., & Hue, V. 2018, Icarus, 307, 124

Moses, J. I., Fouchet, T., Bézard, B., et al. 2005, Journal of Geophysical Research: Planets, 110

Moses, J. I., Lellouch, E., Bézard, B., et al. 2000b, Icarus, 145, 166

Moses, J. I. & Poppe, A. R. 2017, Icarus, 297, 33

Moses, J. I., Visscher, C., Fortney, J. J., et al. 2011, The Astrophysical Journal, 737, 15

Müller, A., Keppler, M., Henning, T., et al. 2018, Astronomy & Astrophysics

National Academies of Sciences, E. 2018, Exoplanet Science Strategy (The National Academy of Sciences Engineering and Medicine)

Nejad, L. A. M. 2005, Astrophysics and Space Science, 299, 1

Neufeld, P. D., Janzen, A. R., & Aziz, R. A. 1972, The Journal of Chemical Physics, 57, 1100

Ng, K. 1974, The Journal of Chemical Physics, 61, 2680

Niemann, H. B., Atreya, S. K., Carignan, G. R., et al. 1998, Journal of Geophysical Research: Planets, 103, 22831

Noll, K. S., Geballe, T. R., Leggett, S. K., & Marley, M. S. 2000, The Astrophysical Journal, 541, L75

Noll, R. & McElroy, M. 1972, Models of Venus atmosphere (1972), Tech. rep.

Noll, R. & McElroy, M. 1974, Models of Mars' atmosphere (1974), Tech. rep.

Nortmann, L., Pallé, E., Salz, M., et al. 2018, Science, 362, 1388

Nugroho, S. K., Kawahara, H., Masuda, K., et al. 2017, The Astronomical Journal, 154, 221

Nymeyer, S., Harrington, J., Hardy, R. A., et al. 2011, The Astrophysical Journal, 742, 35

Oklopčić, A., Silva, M., Montero-Camacho, P., & Hirata, C. M. 2019, arXiv:1910.02504 [astro-ph], arXiv: 1910.02504

Olson, G. L., Auer, L. H., & Buchler, J. R. 1986, Journal of Quantitative Spectroscopy and Radiative Transfer, 35, 431

Oppenheimer, B. R., Baranec, C., Beichman, C., et al. 2013, The Astrophysical Journal, 768, 24

Orton, G. S., Moses, J. I., Fletcher, L. N., et al. 2014, Icarus, 243, 471

Owen, J. E. & Wu, Y. 2017, The Astrophysical Journal, 847, 29

O'Brien, D. P., Walsh, K. J., Morbidelli, A., Raymond, S. N., & Mandell, A. M. 2014, Icarus, 239, 74

Parmentier, V., Fortney, J. J., Showman, A. P., Morley, C., & Marley, M. S. 2016, The Astrophysical Journal, 828, 22

Parmentier, V. & Guillot, T. 2014, Astronomy & Astrophysics, 562, A133

Parmentier, V., Line, M. R., Bean, J. L., et al. 2018, Astronomy & Astrophysics, 617, A110

Parmentier, V., Showman, A. P., & Lian, Y. 2013, Astronomy & Astrophysics, 558, A91

Pater, I. d., Sault, R. J., Butler, B., DeBoer, D., & Wong, M. H. 2016, Science, 352, 1198

Pearce, B. K. D., Ayers, P. W., & Pudritz, R. E. 2019, The Journal of Physical Chemistry A

Pearl, J. C. & Conrath, B. J. 1991, Journal of Geophysical Research: Space Physics, 96, 18921

Perez-Becker, D. & Showman, A. P. 2013, The Astrophysical Journal, 776, 134

Pinhas, A., Madhusudhan, N., Gandhi, S., & MacDonald, R. 2019, Monthly Notices of the Royal Astronomical Society, 482, 1485

Pino, L., Ehrenreich, D., Wyttenbach, A., et al. 2018, Astronomy & Astrophysics, 612, A53

Pirie, J. M. 1958, Platinum Metals Review, 2, 7

Piskunov, N. E., Kupka, F., Ryabchikova, T. A., Weiss, W. W., & Jeffery, C. S. 1995, Astronomy and Astrophysics Supplement Series, 112, 525

Podolak, M. & Helled, R. 2012, The Astrophysical Journal, 759, L32

Poling, B., Prausnitz, J., & Connell, J. O. 2000, The Properties of Gases and Liquids (McGraw Hill Professional), google-Books-ID: E920LnqY2woC

Poser, A. J., Nettelmann, N., & Redmer, R. 2019, Atmosphere, 10, 664, arXiv: 1911.01191

Prinn, R. G. & Barshay, S. S. 1977, Science, 198, 1031

Rayleigh, J. W. S. 1871, Philos. Trans., 161, 77

Raymond, S. N., Quinn, T., & Lunine, J. I. 2004, Icarus, 168, 1

Redfield, S., Endl, M., Cochran, W. D., & Koesterke, L. 2008, The Astrophysical Journal, 673, L87

Richard, C., Gordon, I. E., Rothman, L. S., et al. 2012, Journal of Quantitative Spectroscopy and Radiative Transfer, 113, 1276

Rimmer, P. B. & Helling, C. 2013, The Astrophysical Journal, 774, 108

Rimmer, P. B. & Helling, C. 2016, The Astrophysical Journal Supplement Series, 224, 9

Rimmer, P. B., Walsh, C., & Helling, C. 2013, Proceedings of the International Astronomical Union, 8, 303

Robinson, T. D. & Catling, D. C. 2014, Nature Geoscience, 7, 12

Rocchetto, M., Waldmann, I. P., Venot, O., Lagage, P.-O., & Tinetti, G. 2016, The Astrophysical Journal, 833, 120

Roman, M. T., Fletcher, L. N., Banfield, D. J., & Gierasch, P. J. 2018, AGU Fall Meeting Abstracts, 31

Rosenberg, H. 1910, Astronomische Nachrichten, 186, 71

Rossow, W. B. 1978, Icarus, 36, 1

Rothman, L. S., Gordon, I. E., Babikov, Y., et al. 2013, Journal of Quantitative Spectroscopy and Radiative Transfer, 130, 4

Rothman, L. S., Gordon, I. E., Barber, R. J., et al. 2010, Journal of Quantitative Spectroscopy and Radiative Transfer, 111, 2139

Salz, M., Czesla, S., Schneider, P. C., & Schmitt, J. H. M. M. 2016, Astronomy & Astrophysics, 586, A75

Samland, M., Mollière, P., Bonnefoy, M., et al. 2017, Astronomy & Astrophysics, 603, A57

Saumon, D., Geballe, T. R., Leggett, S. K., et al. 2000, The Astrophysical Journal, 541, 374

Saumon, D., Marley, M. S., Cushing, M. C., et al. 2006, The Astrophysical Journal, 647, 552

Saumon, D., Marley, M. S., Lodders, K., & Freedman, R. S. 2003, Symposium - International Astronomical Union, 211, 345

Scheucher, M., Grenfell, J. L., Wunderlich, F., et al. 2018, The Astrophysical Journal, 863, 6, arXiv: 1808.02347

Schiff, M. H., Jaffe, J. S., & Freundlich, B. 2014, Annals of the Rheumatic Diseases, 73, 1549

Schmid, H. M., Beuzit, J.-L., Feldt, M., et al. 2005, Proceedings of the International Astronomical Union, 1, 165

Schoell, M. 1988, Chemical Geology, 71, 1

Seager, S. 2010, ExoplanetAtmospheres: Physical Processes (Princeton University Press), google-Books-ID: XpaYJD7IE20C

Seager, S., Liang, M.-C., Parkinson, C. D., & Yung, Y. L. 2005a, Proceedings of the International Astronomical Union, 1, 491

Seager, S., Richardson, L. J., Hansen, B. M. S., et al. 2005b, The Astrophysical Journal, 632, 1122

Seager, S. & Sasselov, D. D. 2000, The Astrophysical Journal, 537, 916

Seiff, A., Kirk, D. B., Knight, T. C. D., et al. 1998, Journal of Geophysical Research: Planets, 103, 22857

Seinfeld, J. H. 1986, Atmospheric chemistry and physics of air pollution (Wiley), google-Books-ID: NAhSAAAAMAAJ

Seinfeld, J. H. & Pandis, S. N. 2012, Atmospheric Chemistry and Physics: From Air Pollution to Climate Change (John Wiley & Sons), google-Books-ID: YH2K9eWsZOcC

Selesnick, R. S. & Stone, E. C. 1991, Geophysical Research Letters, 18, 361

Selsis, F. 2002, in Earth-like Planets and Moons, Vol. 514, 251–258

Shabram, M., Fortney, J. J., Greene, T. P., & Freedman, R. S. 2011, The Astrophysical Journal, 727, 65

Shporer, A., O'Rourke, J. G., Knutson, H. A., et al. 2014, The Astrophysical Journal, 788, 92

Shulyak, D., Rengel, M., Reiners, A., Seemann, U., & Yan, F. 2019, Astronomy & Astrophysics, 629, A109

Simoes, F., Pfaff, R. F., Hamelin, M., et al. 2012, in Instrumentation for Planetary Missions, Vol. 1683, 1052

Sing, D. K. 2018, arXiv preprint arXiv:1804.07357

Sing, D. K., Fortney, J. J., Nikolov, N., et al. 2016, Nature, 529, 59

Skemer, A. J., Hinz, P. M., Esposito, S., et al. 2012, The Astrophysical Journal, 753, 14

Smith, A. J. R. W., Feng, Y. K., Fortney, J. J., et al. 2019, arXiv:1911.09211 [astro-ph], arXiv: 1911.09211

Smith, M. D. 1998, Icarus, 132, 176

Snellen, I. a. G., Albrecht, S., Mooij, E. J. W. d., & Poole, R. S. L. 2008, Astronomy & Astrophysics, 487, 357

Snellen, I. A. G., de Kok, R. J., de Mooij, E. J. W., & Albrecht, S. 2010, Nature, 465, 1049

Southworth, J., Mancini, L., Madhusudhan, N., et al. 2017, The Astronomical Journal, 153, 191

Steinrueck, M. E., Parmentier, V., Showman, A. P., Lothringer, J. D., & Lupu, R. E. 2019, The Astrophysical Journal, 880, 14

Stevenson, K. B. 2016, The Astrophysical Journal Letters, 817, L16

Stevenson, K. B., Bean, J. L., Seifahrt, A., et al. 2014, The Astronomical Journal, 147, 161

Stevenson, K. B., Harrington, J., Nymeyer, S., et al. 2010, Nature, 464, 1161

Stewart, P. H., Larson, C. W., & Golden, D. M. 1989, Combustion and Flame, 75, 25

Stokes, R. J. & Evans, D. F. 1997, Fundamentals of Interfacial Engineering (John Wiley & Sons), google-Books-ID: QuEeGZpjc9kC

Strobel, D. F., Meier, R. R., Summers, M. E., & Strickland, D. J. 1991, Geophysical Research Letters, 18, 689

Struve, O. 1952, The Observatory, 72, 199

Stubenrauch, C. J., Rossow, W. B., Kinne, S., et al. 2013, Bulletin of the American Meteorological Society, 94, 1031

Sudarsky, D., Burrows, A., & Pinto, P. 2000, The Astrophysical Journal, 538, 885

Suzuki, D., Bennett, D. P., Sumi, T., et al. 2016, The Astrophysical Journal, 833, 145

Swain, M. R., Tinetti, G., Vasisht, G., et al. 2009a, The Astrophysical Journal, 704, 1616

Swain, M. R., Vasisht, G., & Tinetti, G. 2008, Nature, 452, 329

Swain, M. R., Vasisht, G., Tinetti, G., et al. 2009b, The Astrophysical Journal Letters, 690, L114

Sánchez-López, A., Alonso-Floriano, F. J., López-Puertas, M., et al. 2019, Astronomy & Astrophysics, 630, A53

Tan, X. & Komacek, T. D. 2019, arXiv:1910.01622 [astro-ph], arXiv: 1910.01622

Tennyson, J. & Yurchenko, S. N. 2012, Monthly Notices of the Royal Astronomical Society, 425, 21

Thorngren, D. P., Fortney, J. J., Murray-Clay, R. A., & Lopez, E. D. 2016, The Astrophysical Journal, 831, 64

Thuillier, G., Floyd, L., Woods, T. N., et al. 2004, Advances in Space Research, 34, 256

Tinetti, G., A. Griffith, C., R. Swain, M., et al. 2010, Faraday Discussions, 147, 369

Todorov, K., Deming, D., Harrington, J., et al. 2009, The Astrophysical Journal, 708, 498

Torres, G., Fischer, D. A., Sozzetti, A., et al. 2012, The Astrophysical Journal, 757, 161

Trainer, M. G., Wong, M. H., McConnochie, T. H., et al. 2020, Journal of Geophysical Research: Planets

Tregloan-Reed, J., Southworth, J., Mancini, L., et al. 2017, Monthly Notices of the Royal Astronomical Society, 474, 5485

Tremblin, P., Amundsen, D. S., Mourier, P., et al. 2015, The Astrophysical Journal Letters, 804, L17

Triaud, A. H. M. J. 2014, Monthly Notices of the Royal Astronomical Society: Letters, 439, L61

Triaud, A. H. M. J., Lanotte, A. A., Smalley, B., & Gillon, M. 2014, Monthly Notices of the Royal Astronomical Society, 444, 711

Troe, J. 1983, Berichte der Bunsengesellschaft für physikalische Chemie, 87, 161

Tsai, S.-M., Lyons, J. R., Grosheintz, L., et al. 2017, The Astrophysical Journal Supplement Series, 228, 20

Tsiaras, A., Waldmann, I. P., Zingales, T., et al. 2018, The Astronomical Journal, 155, 156

Tsuji, T. & Nakajima, T. 2003, The Astrophysical Journal Letters, 585, L151

Uttenthaler, S., Meingast, S., Lebzelter, T., et al. 2016, Astronomy & Astrophysics, 585, A145

Velinov, P. 1968, Journal of Atmospheric and Terrestrial Physics, 30, 1891

Venot, O. 2012, thesis, Bordeaux 1

Venot, O. & Agúndez, M. 2015, Experimental Astronomy, 40, 469

Venot, O., Bounaceur, R., Dobrijevic, M., et al. 2019, Astronomy & Astrophysics, 624, A58

Venot, O., Drummond, B., Miguel, Y., et al. 2018, Experimental Astronomy, 46, 101

Venot, O., Hébrard, E., Agúndez, M., Decin, L., & Bounaceur, R. 2015, Astronomy & Astrophysics, 577, A33

Venot, O., Hébrard, E., Agúndez, M., et al. 2012, Astronomy & Astrophysics, 546, A43

Vuitton, V., Yelle, R. V., Klippenstein, S. J., Hörst, S. M., & Lavvas, P. 2019, Icarus, 324, 120

Vuitton, V., Yelle, R. V., Lavvas, P., & Klippenstein, S. J. 2011, The Astrophysical Journal, 744, 11

Wakeford, H. R. & Sing, D. K. 2015, Astronomy & Astrophysics, 573, A122

Wakeford, H. R., Sing, D. K., Deming, D., et al. 2017a, The Astronomical Journal, 155, 29

Wakeford, H. R., Sing, D. K., Kataria, T., et al. 2017b, Science, 356, 628

Wakeford, H. R., Visscher, C., Lewis, N. K., et al. 2017c, Monthly Notices of the Royal Astronomical Society, 464, 4247

Waldmann, I. P., Tinetti, G., Rocchetto, M., et al. 2015, The Astrophysical Journal, 802, 107

Wang, D., Miguel, Y., & Lunine, J. 2017, The Astrophysical Journal, 850, 199

Wang, J. & Fischer, D. A. 2014, The Astronomical Journal, 149, 14

Wang, L. V. & Wu, H.-i. 2012, Biomedical Optics: Principles and Imaging (John Wiley & Sons), google-Books-ID: EJeQ0hAB76gC

Wendt, J. 2008, Computational Fluid Dynamics: An Introduction (Springer Science & Business Media)

West, R. A. 2017, Nature, 551, 302

West, R. A. 2018, in Handbook of Exoplanets, ed. H. J. Deeg & J. A. Belmonte (Cham: Springer International Publishing), 265–283

West, R. A., Baines, K. H., Karkoschka, E., & Sánchez-Lavega, A. 2009, in Saturn from Cassini-Huygens, ed. M. K. Dougherty, L. W. Esposito, & S. M. Krimigis (Dordrecht: Springer Netherlands), 161–179

Wildt, R. 1934, Nature, 134, 418

Wildt, R. 1938, The Astrophysical Journal, 87, 508

Wildt, R. 1947, Monthly Notices of the Royal Astronomical Society, 107, 84

Wilson, D. J., Gänsicke, B. T., Farihi, J., & Koester, D. 2016, Monthly Notices of the Royal Astronomical Society, 459, 3282

Woitke, P., Helling, C., Hunter, G. H., et al. 2018, Astronomy & Astrophysics, 614, A1

Wolszczan, A. & Frail, D. A. 1992, Nature, 355, 145

Wong, I., Shporer, A., Morris, B. M., et al. 2019, arXiv:1910.01607 [astro-ph], arXiv: 1910.01607

Wright, J. T., Marcy, G. W., Howard, A. W., et al. 2012, The Astrophysical Journal, 753, 160

Yan, F., Casasayas-Barris, N., Molaverdikhani, K., et al. 2019, arXiv:1911.00380 [astro-ph], arXiv: 1911.00380

Yan, F. & Henning, T. 2018, Nature Astronomy, 2, 714

Yan, F., Pallé, E., Fosbury, R. a. E., Petr-Gotzens, M. G., & Henning, T. 2017, Astronomy & Astrophysics, 603, A73

Yung, Y. L., Allen, M., & Pinto, J. P. 1984, Astrophysical Journal Supplement Series, 55, 465

Zahnle, K. J. & Marley, M. S. 2014, The Astrophysical Journal, 797, 41

Zalesky, J. A., Line, M. R., Schneider, A. C., & Patience, J. 2019, arXiv:1903.11658 [astro-ph], arXiv: 1903.11658

Zapolsky, H. S. & Salpeter, E. E. 1969, The Astrophysical Journal, 158, 809

Zhang, M., Knutson, H. A., Kataria, T., et al. 2018, The Astronomical Journal, 155, 83

Zhang, X. & Showman, A. P. 2018a, The Astrophysical Journal, 866, 1

Zhang, X. & Showman, A. P. 2018b, arXiv:1808.05365 [astro-ph], arXiv: 1808.05365

Bibliography of own publications

A list of my publications as per requirement of the *HGSFP*.

Relevant publications published during this work:

Molaverdikhani, K., Henning, T., Molliere, P., *"From Cold to Hot Irradiated Gaseous Exoplanets: The role of Clouds"*, 2020, ready for submission to ApJ.

Molaverdikhani, K., Helling, Ch., Lew, B. W.P., MacDonald, R.J., Samra, D., Iro, N., Woitke, P., and Parmentier, V., *"Understanding the atmospheric properties and chemical composition of the ultra-hot Jupiter HAT-P-7b II. Mapping the effects of kinetic gas composition"*, 2019, submitted to A&A.

Pearce, F., et. al. (including Molaverdikhani K.), *"How HCN is Produced in Titan's Atmosphere"*, 2019, submitted to Icarus.

Yan, F., et. al. (including Molaverdikhani K.), *"LBT transmission spectroscopy of HAT-P-12b: confirmation of a cloudy atmosphere with no significant alkali features"*, 2019, submitted to A&A.

Lampon, F., et. al. (including Molaverdikhani K.), *"Modelling the He I triplet absorption at 10830 Angstroms in the atmosphere of HD 209458 b"*, 2019, submitted to A&A.

Casasayas-Barris, F., et. al. (including Molaverdikhani K.), *"Is there NaI in HD 209458b's atmosphere? The impact of the centre-to-limb variation and the Rossiter-McLaughlin effect in transmission spectroscopy studies"*, 2019, submitted to A&A.

Gibbs, F., et. al. (including Molaverdikhani K.), *"EDEN: Sensitivity Analysis and Transiting Planetary Detection Limits for Nearby Late Red Dwarfs"*, 2019, submitted to ApJ.

Yan, F., et. al. (including Molaverdikhani K.), *"Ionized calcium in the atmospheres of two ultra-hot exoplanets WASP-33b and KELT-9b"*, 2019, A&A, 632, A69.

Molaverdikhani, K., Henning, T., Molliere, P., *"From Cold to Hot Irradiated Gaseous Exoplanets: Fingerprints of chemical disequilibrium in atmospheric spectra"*, 2019, ApJ 883, 194.

Mollière, P., et. al. (including Molaverdikhani K.), *"petitRADTRANS: A Python radiative transfer package for exoplanet characterization and retrieval"*, 2019, A&A, 627, A67.

Helling, Ch., et. al. (including Molaverdikhani K.), *"Understanding the atmospheric properties and chemical composition of the ultra-hot Jupiter HAT-P-7b: I. Cloud and chemistry mapping"*, 2019, A&A, 631, A79.

Luque, R., et. al. (including Molaverdikhani K.), *"A planetary system around the nearby M dwarf Gl 357 including a transiting hot Earth-sized planet optimal for atmospheric characterization"*, 2019, A&A, 628 A39.

Molaverdikhani K., Henning, T., Mollière, P., *"From Cold to Hot Irradiated Gaseous Exoplanets: Toward an Observation-based Classification Scheme"*, 2019, ApJ 873, 32.

Nortmann, L., et. al. (including Molaverdikhani K.), *"Ground-based detection of an extended helium atmosphere in the Saturn-mass exoplanet WASP-69b"*, 2018, Science 362, 1388.

Salz, M., et. al., (including Molaverdikhani K.), *"Detection of He I 10830 Å absorption on HD 189733 b with CARMENES high-resolution transmission spectroscopy"*, 2018, A&A 620, A97.

Müller, A., et. al. (including Molaverdikhani K.), *"Orbital and atmospheric characterization of the planet within the gap of the PDS 70 transition disk"*, 2018, A&A 617, L2.

Other publications:

Bergemann, M., et. al. (including Molaverdikhani K.), *"Stellar Astrophysics and Exoplanet Science with the Maunakea Spectroscopic Explorer (MSE)"*, 2019, arXiv:1903.03157.

Fortney, J., et al. (including Molaverdikhani K.), *"The Need for Laboratory Measurements and Ab Initio Studies to Aid Understanding of Exoplanetary Atmospheres"*, 2019, arXiv:1905.07064.

Krissansen-Totton, J., et al. (including Molaverdikhani K.), *"Atmospheric disequilibrium as an exoplanet biosignature: Opportunities for next generation telescopes"*, 2019, 2019BAAS...51c.158K.

Rackham, B., et al. (including Molaverdikhani K.), 2019, *"Constraining Stellar Photospheres as an Essential Step for Transmission Spectroscopy of Small Exoplanets"*, arXiv:1903.06152.

Lopez, E., et al. (including Molaverdikhani K.), *"Understanding Exoplanet Atmospheres with UV Observations II: The Far UV and Atmospheric Escape"*, 2019, arXiv:1903.10669.

Albareti, F., et al. (including Molaverdikhani K.), *"The 13th Data Release of the Sloan Digital Sky Survey: First Spectroscopic Data from the SDSS-IV Survey Mapping Nearby Galaxies at Apache Point Observatory"*, 2017, ApJS, 233, 25.

Molaverdikhani K., Ajabshirizadeh, A., Davoudifar, P., Lashkanpour, M., *"Earth's space-atmosphere interaction region (SAIR) response to the solar flux at 10.7 cm through the evaluation of five solar cycle two-line element (TLE) records"*, 2016, ASR 58, 924.

Ajabshirizadeh, A., Ebadi, H., Vekalati, R. E., Molaverdikhani, K., *"The possibility of Kelvin-Helmholtz instability in solar spicules"*, 2015, Astrophys. Space Sci. 357, 7.

Metcalfe, T. S., et. al., (including Molaverdikhani K.), *"Properties of 42 Solar-type Kepler Targets from the Asteroseismic Modeling Portal"*, 2014, ApJS, 214, 27.

Gray, C. L., Chanover, N.J., Slanger, T., Molaverdikhani K., *"The effect of solar flares, coronal mass ejections, and solar wind streams on Venus'5577 Å oxygen green line"*, 2014, Icarus 233, 342.

Molaverdikhani K., McGouldrick, K., Esposito, L.W., *"The abundance and vertical distribution of the unknown ultraviolet absorber in the venusian atmosphere from analysis of Venus Monitoring Camera images"*, 2012, Icarus, 217, 2.

Molaverdikhani K., *"Common Radial Velocity vs. Rare Microlensing: Difficulties and Futures"*, 2010, arXiv:1002.4025

Molaverdikhani K., Tabeshian, M., *"Mapping the Probability of Microlensing Detection of Extra-Solar Planets"*, 2009, arXiv:0911.4424

Appreciation can make a day, even change a life. Your willingness to put it into words is all that is necessary.

— Margaret Cousins

Acknowledgements

It would have been unfair to name the ones who helped me through this research, as the list would exceed the page and words were inadequate to express my gratitude. Therefore I thank all people who assisted me during this time. I owe them the knowledge that I gained and will do my best to share it with all.

Everything in the universe is within you. Ask all from yourself.

— Rumi